Statistical Nano-Chemo-Mechanical Assessment of Shale by Wave Dispersive Spectroscopy and Nanoindentation

by

Amer Deirieh

B.S., Birzeit University (2008)

Submitted to the Department of Civil and Environmental Engineering
in partial fulfillment of the requirements for the degree of

Master of Science in Civil and Environmental Engineering

at the

MASSACHUSETTS INSTITUTE OF TECHNOLOGY

June 2011

Signature of Author ....
Department of Civil and Environmental Engineering
May 18, 2011

Certified by ....
Franz-Josef Ulm
Professor of Civil and Environmental Engineering
Thesis Supervisor

Accepted by ....
Heidi M. Nepf
Chair, Departmental Committee for Graduate Students

Statistical Nano-Chemo-Mechanical Assessment of Shale by Wave Dispersive Spectroscopy and Nanoindentation

by

Amer Deirieh

Submitted to the Department of Civil and Environmental Engineering
on May 18, 2011, in partial fulfillment of the
requirements for the degree of
Master of Science in Civil and Environmental Engineering

Abstract

Shale is a common type of sedimentary rock formed by clay particles and silt inclusions, and, in some cases, organic matter. Typically, shale formations serve as geological caps for hydrocarbon reservoirs. More recently, various shale formations have been identified as prolific sources of oil and natural gas and as host lithologies for the disposal of CO2 and nuclear waste. Despite its abundance, the characterization of shale rocks remains a challenging task due to their complex chemistry, heterogeneous microstructure, and multiscale mechanical behaviors. This thesis aims at establishing the link between the composition and mechanics of shale materials at grain scales. A comprehensive experimental program forms the basis for the characterization of the chemical composition and mechanical properties of shale at micrometer and sub-micrometer length scales. The chemical assessment was conducted through a novel experimental design involving grids of wave dispersive spectroscopy (WDS) spot analyses and statistical clustering of the chemical data generated by the experiments. This so-called statistical grid WDS technique was coupled with grid nanoindentation experiments as a means to assess the nanochemomechanics of shale rocks. The similar microvolumes probed by both methods ensure a direct relation between the local chemistry and mechanics response of shale materials. The results of this investigation showed that the grid WDS technique provides quantitative means to determine the chemistries of silt-size inclusions (mainly quartz and feldspars) and the clay matrix. The mineralogy assessments obtained by grid WDS analysis were validated through comparisons with results from X-ray image analysis and X-ray diffraction (XRD) experiments. The direct coupling of the grid WDS and indentation techniques revealed that the porous clay phase, previously inferred from the mechanistic interpretation of indentation experiments, corresponds to the response of clay minerals. The coupling technique also showed that clay minerals located nearby silt inclusions exhibit enhanced mechanical properties due to a composite action sensed by nanoindentation. The new understanding developed in this thesis provides valuable insight into the chemomechanics of shale at nano and microscales. This coupled assessment represents valuable information for the development of predictive models for shale materials which consider the intricate links of composition, microstructure, and mechanical performance.

Thesis Supervisor: Franz-Josef Ulm
Title: Professor of Civil and Environmental Engineering

Contents

List of Figures

Acknowledgments

First, I would like to express my deepest gratitude to my advisor Prof. Franz-Jozef Ulm for the continuous support of my Master study and research. I would also like to thank Dr. Alberto Ortega who mentored me throughout my studies for his continuous support, without which the outcome of this work may have been different. I also thank Prof. Younane Abousleiman, from the university of Oklahoma, who provided the financial support for the work presented in this thesis through the GeoGoenom Industry Consortium. I also thank my colleagues and friends who helped and supported me despite the enormous work pressures they were facing. Last but not the least, my deepest gratitude goes to my family for their unlimited love and support throughout my life; this achievement would have been impossible without them.

Part I

General Presentation

Chapter 1

Introduction

1.1 Industrial Context and Research Motivation

Shale constitutes 75% of the sedimentary rocks in the earth's crust. It is composed of highly consolidated clay particles, silt-size inclusions, and organic matter. Shale has progressively captured the attention of the geomechanics community. In conventional applications related to oil exploration and exploitation, shale formations serve as natural geological caps for hydrocarbon reservoirs. More recently, several shale formations have been identified as prolific sources of oil and natural gas and as lithologies for disposal of CO2 and nuclear waste. The engineering challenges associated with these applications such as horizontal drilling, enhanced recovery, and sequestration schemes require pushing beyond the boundaries of the conventional understanding of shale mechanics. In fact, industries such as oil and gas are actively moving towards adopting new predictive engineering models that do not rely heavily on empirical formulations.

In moving beyond phenomenology, the progress in mechanical modeling of shale has been closely associated with the implementation of the materials science approach. The paradigm in materials science is to resolve the intricate links between material composition, microstructure, and mechanical performance. Within this framework, the first generation of shale mechanical models employed empirical correlations between composition and mechanical behavior, such as bulk measurements of density or clay content against poromechanical data of stiffness and strength. The next improvement in the mechanical modeling of shale was developing detailed descriptions of microstructure. Over the past two decades, microstructural features such as nanopores and particle shape and orientation of clays have been characterized through several experimental techniques such as fluid porosimetry, scanning electron microscopy (SEM), transmission electron microscopy (TEM), and synchrotron X-ray analysis. However, upscaling models based on advanced definitions of microstructure have only been able to capture qualitatively the anisotropic behavior of shale, whereas quantitative predictions of stiffness and strength differ from macroscopic observations.

More recently, a novel approach was proposed by the MIT-OU GeoGenome Industry Consortium to model the poromechanics of shale. The approach aimed at the identification of fundamental material properties at nanoscales, which can be incorporated in upscaling micromechanical models that predict macroscopic responses for a wide range of shale lithologies. The nanomechanical information was derived from extensive material testing involving instrumented indentation experiments, which resolve load-deformation behaviors with high resolutions. The deployment of nanotechnologies resolved the in situ mechanical responses of the two main mechanical phases contributing to the nanomechanical signature of shale: the porous clay matrix and the silt inclusions. Their experimental identification, in combination with micromechanics modeling, revealed the sources of mechanical properties linked to intrinsic solid behaviors (e.g. particle anisotropy, solid elasticity and strength) and microstructural effects (e.g. particle geometry, fabric anisotropy). While the in situ assessments of these phases at grain-scales represented breakthroughs in the multiscale understanding of the mechanics of shale, the postulates for their identification were grounded on mechanical arguments. The relations between their mechanical responses and the corresponding local chemical compositions are missing. Shedding light on the chemistry and mechanics of shale at nanoscales will fulfill the materials science paradigm for this material, and therefore, enable the development of robust, physics-based micromechanics models.

1.2 Problem Statement and Approach

This thesis aims at establishing the link between composition and material performance at grain-scales for shale materials. The scientific challenge to be addressed in this work is:

What is the in situ chemo-mechanical signature of shale at nanometer length scales?

The research approach pursued in this study consists of determining the chemistry and mechanics of shale directly through experimental means capable of handling the highly heterogeneous nature of this rock material. The nanomechanics of shale is determined by grid nanoindentation, which represents an extension of instrumented indentation to the assessment of heterogeneous composites (cementitious materials, bone, metal alloys). In an original development and borrowing inspiration from the grid indentation technique, we develop a grid wave dispersive spectroscopy (grid WDS) methodology to address the complex chemical composition of shale. The extensive data sets of spot chemical analyses generated by this technique over representative sample areas are interpreted using multivariate statistics to yield the most likely chemical phases present in the shale sample. The grid WDS technique represents a stand-alone methodology for characterizing the chemical composition of shale with sub-micrometer resolutions. This methodology is then coupled with nanoindentation experiments performed over particular sample locations to probe in situ the chemical and mechanical signature of shale.

1.3 Research Objectives

An experimental approach is proposed to address the scientific challenge of linking the chemistry and mechanics of shale at nanometer length scales. The objectives of our chemo-mechanical investigation are the following:

- Review the multiscale and compositionally diverse natures of shale materials. Understanding the complex compositional make-up of shale from clay mineralogy and microstructural descriptions provides the adequate background for designing and interpreting the grid WDS experiments. The thorough literature review of shale mineralogy and microstructure yields information about the wide variety of chemical compositions and characteristic length scales of individual clays present in shale.
- Develop the grid WDS technique for the chemical assessment of shale materials. The WDS experimental setup is adapted for extensive testing of material surfaces in grid arrangements. The resulting data sets consisting of concentrations of chemical elements for each spot analysis are analyzed using multivariate statistical tools to infer the chemically distinct phases within shale. The grid WDS technique is validated using alternative

chemical assessment methods such as X-ray diffraction and X-ray mapping.

- Conduct an experimental program involving the chemical and mechanical characterizations of several shale samples through grid WDS and indentation experiments, respectively. The experiments are designed to probe similar material volumes. The grid WDS and indentation experiments are analyzed separately through multivariate clustering in order to independently evaluate the chemical and mechanical properties of shale at the proposed length scales.
- Couple the grid WDS and indentation experiments over specific areas in shale samples to reveal the chemo-mechanical signatures of the main material constituents. In particular, we seek to resolve the responses of the porous clay matrix, silt inclusions, and interfacial regions between the clay matrix and silt inclusions.

1.4 Outline of Thesis

This thesis is presented in four parts. Part I contains the introductory material and the presentation of the research topic.

Part II , Materials and Methods, consists of four chapters that describe the materials and experimental methods used in this study. Chapter 2 includes a presentation of the composition and mineralogy of shale, and introduces a multiscale thought model for shale that highlights the relevant length scales to this materials. Chapter 3 provides a description of the shale materials tested in this study. Chapter 4 describes electron probe microanalysis (EPMA) techniques and their applications to geology. It also includes the development of the grid WDS methodology for shale materials. Chapter 5 reviews the indentation technique as applied to homogeneous material, and presents its extension for the characterization of heterogeneous material.

Part III - Results and Discussion, includes the chemical characterization of shale materials using the grid WDS technique. Chapter 6 presents the results of the grid WDS experimental campaign on three shale materials, as well as the results of the multivariate cluster analysis applied to the WDS chemical data. The results of image analysis for X-ray maps, conducted as an alternative assessment of shale chemistry are presented in Chapter 7. Chapter 8 discusses the results of the grid WDS technique for shale materials, and the validation of the technique through comparisons with results from X-ray image analysis and X-ray diffraction (XRD) experiments.

Part IV deals with applications of the statistical grid WDS technique developed in this study. Chapter 9 describes a coupling methodology of the grid WDS and indentation experiments to access the chemo-mechanical signature of shale at nano and micrometer length scales.

Finally, Part V summarizes the main findings of this study and the scientific and industrial contributions.

Part II

Materials and Methods

Chapter 2

Shale Mineralogy and Multiscale Properties

Shale is a heterogeneous sedimentary rock composed of clay particles and silt-sized inclusions. The term mudrock refers to fine-grained sedimentary rocks, whereas shale is reserved for laminated fine-grained rocks. For the purpose of this study, all such materials are considered as shale. This chapter introduces shale materials with an emphasis on the chemical composition of non-clay minerals and clay minerals that are commonly found in shale. A compilation of chemical analyses for clay minerals from the literature is also included to account for their highly heterogeneous nature. This information will prove helpful in the interpretation of the chemical analysis of shale samples discussed later. Furthermore, this chapter addresses the multiscale thought model, originally presented by Ulm et al. [24], as a framework for investigation throughout this thesis.

2.1 Shale Mineralogy and Composition

Fine-grained , siliciclastic sedimentary rocks constitute approximately 75 percent of all sedimentary rocks, and are composed of particles smaller than hundreds of micrometers. This type of sedimentary rocks is known by several names such as lutite, siltstone, mudstone, mudrock, claystone, and shale. The terminologies commonly used to refer to this type of sedimentary rocks are not entirely clear and depend on the author or research field. Geologists use the terms mudrock and shale to describe two different rock occurrences: mudrock refers to fine-grained sedimentary rocks, whereas shale is reserved for laminated or fissile fine-grained rocks. Today, the terms mudstone, mudrock, and shale are still used as a group-name for fine-grained rocks; however, the reader must pay attention to the writer's terminology [62]. In this work, in which shale is studied from a geomechanics perspective, the term shale refers to sedimentary rocks that contain large amounts of clay minerals.

Shale is mostly composed of clay minerals, fine-size micas, quartz, and feldspar. Other minerals may exist in these rocks in minor amounts such as zeolite, iron oxides, carbonates, sulfates, and sulfides. Tables 2.1 and 2.2 list the principal constituents of shale. As a consequence of its heterogeneous nature, the average chemical composition of shale rocks varies based on the relative abundance of the principal shale constituents. This section is dedicated to the description of the chemical composition of the major constituents in shale, with an emphasis on clay minerals. The gathered information will be used in the interpretation of the chemical analysis from wave dispersive spectroscopy experiments conducted in this study.

2.1.1 Clay Minerals

Clay belong to the mineral family of phyllosilicates, which includes other silicates such as serpentine, pyrophyllite, talc, mica, and chlorite. Clay minerals are composed of combinations of two basic structural units: the silicon tetrahedron, and the aluminum or magnesium octahedron known as gibbsite and brucite, respectively. The silicon tetrahedron consists of SiO_4^{2-} connected at three corners in the same plane forming a hexagonal network. Gibbsite and brucite consist of octahedrally-coordinated aluminum and magnesium ions sandwiched between two planes of hydroxyl ions [12]. The chemical composition of the aluminum and magnesium octahedron is $Al_2(OH)_6$ and $Mg_3(OH)_6$, respectively. The stacking arrangement of sheets of these structural units and the manner in which two successive layers are held together determine different clay mineral groups [62]. Chemical composition may vary according to the extent of replacement of Si, Al, and Mg by other cations. This replacement is known as isomorphous substitution, which is responsible for the wide variation in chemical compositions within the same clay mineral group.

Various clay minerals are formed by different combinations of tetrahedron layers and oc-

Framework Silicates	
Quartz	Constitutes 20-30% of an average shale, and is most likely of detrital origin. Other varieties of silica include opal CT, chalcedony, and amorphous silica.
Feldspar	Commonly less abundant than quartz. Plagioclase is more abundant than alkali feldspars.
Zeolites	Commonly present as alterations of volcanic glass. Clinoptilolite and phillipsite are common zeolites in modern marine sediments.
Clay Minerals	
Kaolinite (7 Å)	Forms in soils developed under abundant rainfall, adequate drainage, and acid waters. Typically concentrated near shore in marine basins.
Smectite-Illite-Muscovite (10 Å and greater)	Members of this structurally complex group form in different ways. Smectite, a hydrated expandable clay, forms from volcanic glass (bentonites); it transforms to illite during burial. Illite, the most abundant clay mineral, derives from pre-existing shales, and it converts to muscovite during diagenesis. Muscovite also occurs as detrital particles in unaltered shale. A iron-rich variety of illite-smectite is glauconite.
Chlorite, Corrensite, and Vermiculite	Chlorite forms by burial diagenesis, especially in Mg-rich pore waters. It is commonly the second most abundant clay in Paleozoic and older shales. Vermeculite may convert to corrensite and finally to chlorite during diagenesis.
Sepiolite and Attapulgite	Magnesium-rich clays that form under special conditions, such as saline lakes.

Table 2.1: Principal constituents of shale and mudstone [59].

Oxides / Hydroxides	
Iron oxides and hydroxides	Present in shale mostly as coatings on clay minerals. In reducing environments, they convert into pyrite and siderite. Hematite is another common iron oxide in shales.
Gibbsite	It represents the product of acid leaching. May be associated with kaolinite in marine shale.
Carbonates	
Calcite	More common in marine than non-marine shales. As with quartz and feldspar, little is known about its distribution and form in shale.
Dolomite	Common in shale as a cementing agent.
Siderite and Ankerite	Occurs in shales commonly as concretions.
Sulfur Minerals	
Sulfates	Gypsum, anhydrite, and barite occur in shale as concretions and may indicate hypersalinity during or after deposition.
Sulfides	Shale typically exhibits iron sulfides such as pyrite and marcasite.
Other Constituents	
Apatite	A phosphatic mineral that forms nodules in slowly deposited marine muds.
Glass	Found in modern muds associated with volcanism. It converts into zeolites and smectites during burial.
Organic Materials	
Organic particles	Mostly either palynomorphs or small coaly fragments.
Kerogen	Amorphous organic material of complex chemical characterization that is present in almost all shales except red ones. It informs about gas and oil potential of a basin and its thermal history.

Table 2.2: Principal constituents of shale and mudstone [59] (*continued*).

tahedron layers as shown in Figure 2-1. The four major clay groups are: kaolinites, illites, smectites, and vermiculites. In this study, more emphasis will be given to the most common clay minerals in shale: kaolinites, illites, and smectites. Kaolinites belong to the 1:1 clay mineral group composed of alternating silica and octahedral sheets. The principal members of this group are kaolinite, dickite and nacrite, anauxite, and halloysite. Smectites belong to the 2:1 clay mineral group composed of an octahedral sheet sandwiched between two silica sheets. The major members of this family are: montmorillonite, hectorite, saponite, and sauconite. Illites are similar to smectites in that they possess the same structure, but they differ in composition. The major members of this family are: illite, hydro-mica, phengite, brammallite, glauconite, and celadonite [68]. The actual composition of clay minerals present in rocks deviates from the ideal compositions, reported in the literature in the form of chemical formulas. These differences are attributed to isomorphous substitutions and to the presence of other mineral. In our chemical analysis of shale, we will use the compositions of clay minerals published in several studies to account for the compositional variability of clay minerals. The chemical composition of the major clay minerals is discussed below.

Kaolinite Group

Kaolinites are 1:1 clay minerals consisting of alternating silica and octahedral sheets. The strong bonding between successive layers, dominated by van der Waals and hydrogen bonds, inhibits interlayer swelling due to the presence of water. The lateral and thickness dimensions of the kaolinite group are 0.1 - 4 μm and $0.05 - 2$ μm, respectively [47]. Compared to other clay minerals, the kaolinite group is the most restricted in composition and physical properties. This can be explained by the negligible isomorphous substitutions that may occur in this group of clay minerals. Kaolinite is by far the most abundant mineral in this group with an ideal composition of the form $Al_4[Si_4O_{10}](OH)_8$ as reported by [12] [68] [47] [1]. Variations of the stacking of layers result in different members of the kaolinite group such as dickite, nacrite, and halloysite.

The actual composition of kaolinites is slightly different from the ideal composition and little variation is expected among members of the group. The ideal composition for kaolinites is: 46.54 % SiO_2, 39.5 % Al_2O_3, 13.96 % H_2O. To capture the chemical variability of the kaolinite group,

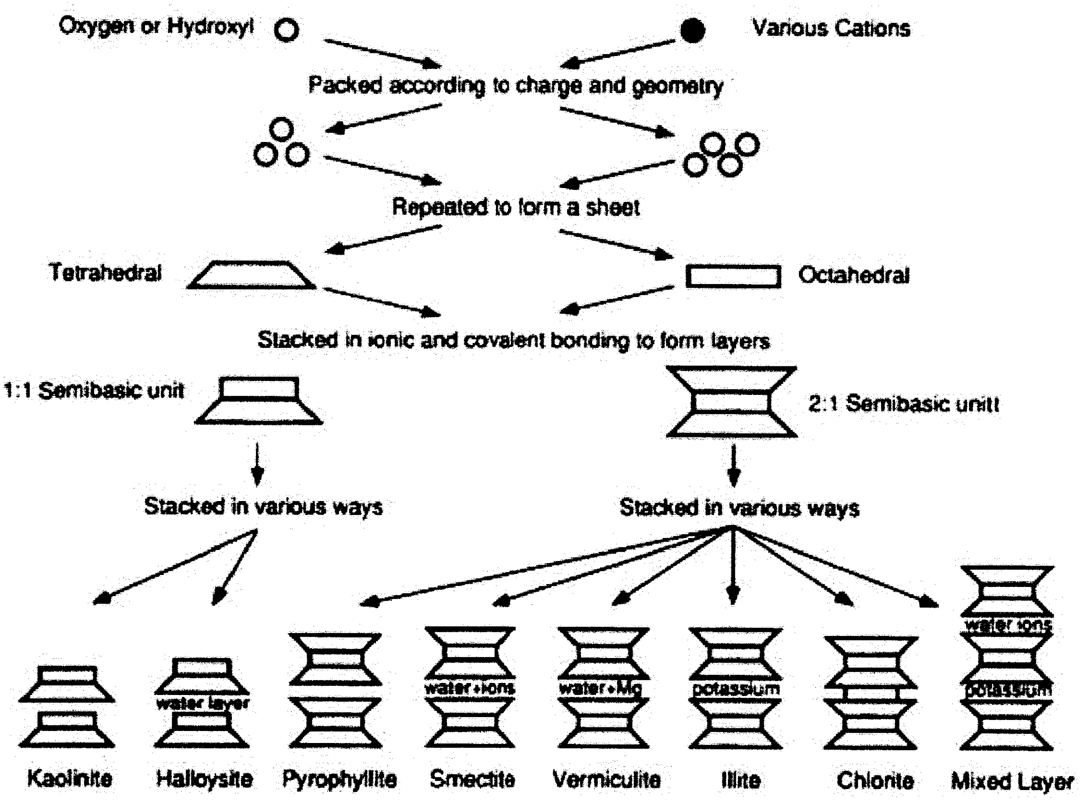

Figure 2-1: Synthesis pattern for clay minerals. Adapted from [47]

SiO_2	Al_2O_3	TiO_2	Fe_2O_3	FeO	MgO	CaO	Na_2O	K_2O	H_2O^+	H2O$^-$
46.6	39.5	0.0	0.0	0.0	0.0	0.0	0.0	0.0	14.0	0.0
46.4	39.5	0.0	0.1	0.0	0.2	0.2	0.1	0.0	13.9	
46.2	39.2	0.1	0.2		0.1	0.1	0.1	0.2	13.8	
45.2	39.2	1.2	0.2		0.1	0.1	0.0	0.0	13.3	
46.4	39.5		0.2		0.2		0.0	0.0	14.2	
46.2	39.9								13.9	
44.6	38.1	1.4	1.4		0.1	0.1	0.1		13.9	0.7
49.0	36.8	0.3	0.1			0.0	0.0		13.1	0.3
40.1	35.4				0.8	0.1			15.0	8.6
46.2	39.8	0.2	0.2		0.3	0.0	0.0		14.0	
44.7	28.1	12.8	12.8			1.7			13.3	
40.6	24.6	0.9	0.9		0.5	0.2	0.1		12.2	8.2

Table 2.3: Chemical analyses of kaolinite group minerals [1]. Blank spaces refer to either not determined or trace values.

Tables 2.3 and 2.4 display sets of published chemical analyses of kaolinites. While the chemical composition of Dickite and nacrite is identical to that of kaolinite, halloysite is characterized by higher content of water H_2O^+. Furthermore, small amounts of ions may be found in kaolinites, but the source of these ions cannot be traced due to the fine grained nature of clay minerals. The averages of the minor constituents found in the literature are as follows: $TiO_2 = 1.0$, $Fe_2O_3 = 0.5$, $FeO = 0.1$, $MgO = 0.15$, $CaO = 0.3$, $Na_2O = 0.3$, $K_2O = 0.5$ mass percent [68]. An extensive data set published by Weaver [12] was used to calculate the average composition for each member of the family as reported in Table 2.5. The chemical compositions gathered in Tables 2.3 through 2.5 in the above tables are quite similar and no striking differences were found.

Illite Group

Illite, a 2:1 type mineral, is the most commonly encountered clay mineral in engineering practice. The structure of illites is similar to that of muscovite mica, in which a layer of gibbsite is sandwiched between two layers of silica. Illites differ from muscovite in having more silica and less potassium, displaying randomness in the stacking of clay layers, and its smaller particle size. Charge deficiency that results mainly from isomorphous substitution is balanced by potassium between layers. Illite occurs as flaky particles with long direction that ranges from 0.1 μm to several micrometers, and thickness as of nanometers size [47].

SiO_2	Al_2O_3	TiO_2	Fe_2O_3	FeO	MgO	CaO	Na_2O	K_2O	H_2O^+	$H2O^-$
45.8	39.6		0.6	0.2	0.1	0.1		0.0	13.9	0.2
46.1	38.1	0.5	0.3		0.0	0.4	0.3	0.4	13.5	0.4
45.7	39.8	0.4	0.1				0.2	0.4	13.7	0.6
45.5	38.8	0.9	0.2		0.2	0.2	0.2	0.4	13.7	0.7
46.1	39.6								13.9	
44.9	38.0	0.6	1.7		0.3	0.2		0.1	14.4	
46.2	38.9				0.4	0.3			14.2	
46.0	39.2		0.3		0.1	0.2	0.1	0.3	13.7	
44.5	36.6	0.2	0.4	0.1	0.2	0.2	0.0	0.5	13.4	4.1
44.0	38.5	0.0		0.0		0.3	0.1	0.5	14.6	2.6

Table 2.4: Chemical analyses of kaolinite group minerals [68]. Blank spaces refer to either not determined or trace values.

Mineral	SiO_2	Al_2O_3	TiO_2	Fe_2O_3	FeO	MgO	CaO	Na_2O	K_2O	H_2O^+	$H2O^-$
Kaolinite	44.6	38.9	0.3	0.9		0.2	0.3	0.8	0.1	14.0	0.7
Nacrite	45.7	39.6		0.3		0.2	0.1			14.1	0.6
Dickite	46.1	39.4		0.1		0.1	0.2			13.9	1.3
Halloysite	43.4	38.5		0.4		0.1	0.2	0.1	0.1	14.9	3.1

Table 2.5: Chemical analyses of kaolinite group minerals. The reported values in this table correspond to the average of the chemical analyses reported in [12]. Blank spaces refer to either not determined or trace values.

	SiO_2	Al_2O_3	TiO_2	Fe_2O_3	FeO	MgO	CaO	Na_2O	K_2O	H_2O^+	$H2O^-$
illite	49.8	26.4	0.4	4.3	0.6	2.8	0.3	0.2	7.0	7.1	1.5
sericite	47.9	31.4	0.2	1.5	1.5	1.7	0.4	0.8	8.5	6.2	0.4
Glauconite	49.2	9.1		18.0	3.4	3.6	0.6	0.5	6.9	8.5	
Celadonite	53.2	8.0	0.2	13.4	3.6	6.1	0.8	0.8	7.1	6.0	3.3

Table 2.6: Chemical analyses of illite group minerals. The reported values in this table correspond to the average of the chemical analyses reported in [12]. Blank spaces refer to either not determined or trace values.

The extensive isomorphous substitution makes the composition of illite group very complex. The definition of this group is still not clear in the literature, and the terminology associated with members of this group is not consistent. Newman [1] considered the following minerals to be part of this group, which he referred to as clay micas: sericite, hydrous mica, illite, glauconite, and celadonite. This terminology agrees with the one used by Deer et al. [68] and Weaver [12] with minor differences. Given that the reported chemical formulas in the literature show significant variability, an attempt to compare different formulas would not advance the goal of understanding the chemical variability of illites. Instead, we rely on the detailed experimental chemical analyses published in the literature. Table 2.6 displays average compositions of members of the illite group calculated from several chemical analyses and published by Weaver [12].

The term illite is usually used for specimens where there is less potassium than mica and the major substitutions are aluminum for silicon. The chemical formula usually given for illite is of the form $K_yAl_4(Si_{8-y},Al_y)O_{20}(OH)_4$, where $y < 2$ and usually between 1 and 1.5 [68]. Sericite, usually referred to as phenigite, is an important member of the illite group, which doesn't have the potassium deficiency characterized by its fine-grained platy morphology. Hydrous mica is another member of the illite group characterized by its deficiency of potassium ions which is compensated either by $(H_3O)^+$ ions or $(OH)^-$ ions [68]. Table 2.7 contains a number of illites, sericite, and hydrous mica chemical analyses reported by Newman [1]. Glauconite and celadonites are iron-rich illites (Fe>1) that are considered as members of the illite group mainly due to their composition; these members are relatively rare. Table 2.8 displays the chemical analyses of glauconite and celadonites reported by Newman [1]. Finally, Table 2.9 contains additional chemical analyses for the entire illite group published by Deer [68]. The

SiO_2	Al_2O_3	TiO_2	Fe_2O_3	FeO	MgO	CaO	Na_2O	K_2O	H_2O^+	$H2O^-$
47.7	37.0	0.1	0.0		0.0		0.8	9.0	5.0	0.7
48.4	33.8		0.5	0.0	1.0	0.1	0.5	9.4	5.4	0.6
51.5	28.5	0.8	0.6	0.9	3.0	0.1	0.1	9.1	5.5	0.7
51.0	28.7	0.3	0.6	0.4	2.3	0.3	0.2	7.8	6.0	2.0
52.9	24.9	1.0	0.8	1.2	3.6	0.7	0.2	8.0	6.7	2.6
55.1	22.0	0.6	5.3	1.3	2.8	0.0	0.1	8.0	6.4	1.0
54.8	20.1	1.1	13.5		3.1	1.9		5.4		
60.4	16.4	1.4	11.8		3.7	2.3		4.0		
55.2	17.9	0.3	11.9	0.9	4.3	0.8	0.0	7.9		
47.5	27.7		3.8	1.5	1.5	0.4	4.3	4.4	6.4	2.6

Table 2.7: Chemical analyses of illites, sericite, and hydrous mica minerals reported in [1]. Blank spaces refer to either not determined or trace values .

SiO_2	Al_2O_3	TiO_2	Fe_2O_3	FeO	MgO	CaO	Na_2O	K_2O	H_2O^+	$H2O^-$
55.6	0.8		17.2	4.0	7.3	0.2	0.2	10.0	4.9	
53.4	2.5	0.0	15.9	3.5	6.5	0.1	0.1	10.3		
52.6	5.3	0.2	14.6	3.4	6.4	0.7	0.3	7.7		
50.1	2.4	0.0	20.3	2.1	6.4	0.2	0.0	8.2		
49.1	9.4	0.0	21.0	2.7	3.1	0.4	0.0	8.7		
51.2	9.3	0.1	18.2	1.8	3.3	0.6	0.0	8.0	5.2	2.0
57.0	13.3	0.1	8.8	7.1	5.4	0.1	0.2	8.2		
53.8	18.5	0.0	8.0		4.7	0.0	0.3	9.0		
49.0	17.9	1.1	13.1	1.3	2.8	0.4	0.1	7.8	6.0	

Table 2.8: Chemical analyses of glauconite, a member of illite group, reported in [1]. Blank spaces refer to either not determined or trace values.

data reported in this section clearly shows the chemical variability of the illite group.

Smectite Group

Smectite is a 2:1 clay mineral type, consisting of an octahedral sheet in between two silica sheets. Extensive isomorphous substitutions of aluminum by other minerals are expected in this type of clay minerals. These substitutions result in charge deficiencies which is balanced by exchangeable cations. The bonding between layers dominated by van der Waals and cations balancing charge deficiencies is relatively weak. These bonds are responsible for layer separation, water/liquid adsorption, and swelling. Smectites are divided into two groups according to the substitutions involved: di-octahedral and tri-octahedral. The tri-octahedral subgroup includes montmorillonite, beidellite, and nontronite. The tri-octahedral subgroup contains relatively less

SiO_2	Al_2O_3	TiO_2	Fe_2O_3	FeO	MgO	CaO	Na_2O	K_2O	H_2O^+	$H2O^-$
46.8	36.1	0.0		0.3	0.6	0.3	0.7	10.2	5.0	0.4
47.3	36.3		2.2				5.3	2.7	5.8	
45.3	31.4	0.2	0.5	1.6	2.7	0.4	1.1	9.1	6.1	1.1
46.3	28.8	0.0	5.7	1.5		1.1	0.0	9.3	5.8	0.4
46.5	36.4	0.2	0.7	0.4	0.5	0.2	0.5	8.1	6.3	0.5
47.6	32.5	0.6	0.8	1.9	1.7	0.1	1.1	6.2	7.7	0.0
46.8	32.4	1.2	3.0		1.0	1.0	0.9	5.7	8.0	0.0
51.3	30.2	0.1	2.4	0.6	1.4	0.0	0.1	7.8	6.3	0.0
56.9	18.5	0.8	5.0	0.3	2.1	1.6	0.4	5.1	6.0	2.9
50.1	30.1	0.1	1.5	0.4	2.5	0.0	2.0	9.8	3.6	
49.2	30.8			1.4	2.2		0.5	10.9	4.7	0.2
51.2	25.9	0.5	4.6	1.7	2.8	0.2	0.2	6.1	7.1	4.6
50.1	25.1	0.5	5.1	1.5	3.9	0.4	0.1	6.9	6.8	
49.3	3.2	0.1	21.7	3.2	3.9	0.7	0.1	6.0	7.2	
40.9	20.5	2.1	12.8		6.9	0.9	0.7	3.3	11.8	11.8

Table 2.9: Chemical analyses of illite group minerals reported in [68]. Blank spaces refer to either not determined or trace values.

Mineral	Formula
Montmorillonite	$(OH)_4\,Si_8(Al_{3.34}Mg_{0.66})O_{20}$
Beidellite	$(OH)_4(Si_{6.34}Al_{1.66})Al_{4.34}O_{20}$
Nontronite	$(OH)_4(Si_{7.34}Al_{0.66})Fe^{3+}O_{20}$
Hectorite	$(OH)_4\,Si_8(Mg_{5.34}Li_{0.66})O_{20}$
Saponite	$(OH)_4(Si_{7.34}Al_{0.66})Mg_6O_{20}$
Sauconite	$(OH)_4(Si_{8-y}Al_y)(Zn_{6-x}Mg_x)O_{20}$

Table 2.10: Minerals of the smectite group and their chemical formulas [47]

common minerals including saponite, hectorite, and sauconite. Table 2.10 lists the chemical formula of some of the smectites. Table 2.11 contains chemical analyses of the smectite group, which include both the tri-octahedral and di-octahedral smectites.

Similar to other clay minerals, because of the variability of composition that can exist within the same group of clay minerals, the chemical formulas listed in Table 2.10 must be considered indicative, but not absolute. Montmorillonite is the most common smectite mineral; it occurs as film-like, equi-dimensional structures with particle thickness in the nanometer range, and a characteristic long dimension of 1-2 μm [47]. Beidellites differ from montmorillonites in that the charge in the former arises from Al^{3+} in tetrahedral sites, whereas in montmorillonite it originates from divalent cations in octahedral sites. Minerals in between these two end-members

SiO_2	Al_2O_3	TiO_2	Fe_2O_3	FeO	MgO	CaO	Na_2O	K_2O	H_2O^+	$H2O^-$
54.0	16.0	0.1	1.0	0.2	4.5	2.3	0.1	0.1	9.1	13.1
51.1	19.8		0.8		3.2	1.6	0.1	0.0	8.0	14.8
51.5	17.2	0.5	5.7	0.3	2.8	1.7	0.2	0.9	8.6	11.2
49.9	20.2		1.2	0.2	2.2	2.4	0.3	0.1	8.8	14.6
51.9	18.6	0.2	2.8	1.0	3.3	3.5	0.6	1.6	6.1	10.4
59.8	24.4		3.7		3.1	3.4	1.4		3.9	
45.3	27.8		0.7		0.2	2.8	0.1	0.1	14.5	8.2
45.8	22.8	0.5	5.7	0.3	0.9	1.4	0.2	0.1	9.8	12.6
47.3	20.3		8.7		0.7	2.8	1.0			13.1
39.9	5.4	0.1	29.5	0.3	0.9	2.5				14.4
40.3	5.5	0.0	29.4	0.0	0.5	2.3	0.0	0.0	7.3	15.1
53.9	4.5	0.3	0.6		31.6		0.0	0.1	9.3	
43.6	5.5	0.0	0.7		24.3	2.9	0.1	0.0	5.5	17.4
50.0	3.9	0.0	0.2		25.6	1.3			12.0	7.3
40.5	10.2		3.6	4.9	20.7	1.9	0.3	0.3	4.2	13.3
54.0	0.1		0.0		25.9	0.2	3.0	0.2	5.6	9.3

Table 2.11: Chemical analyses of tri-octahedral and di-octahedral smectites reported in [68]. Blank spaces refer to either not determined or trace values.

are expected, and they are usually described as montmorillonite or beidellites based on the origin of the charge [1]. Nontronite is the iron-rich di-octahedral smectite. Tables 2.12 and 2.13 provide chemical analyses for montmorillonite and beidellites/nontronites, respectively.

The composition of the tri-octahedral smectites is quite variable. Stevensite, the magnesium-rich end member, contains little aluminum in either the octahedral or tetrahedral sheet. Hectorite resembles stevensite in having little tetrahedral substitution, but its octahedral sheet has significant lithium content. Hectorite and stevensite contain uncommon elements such as Cr, Ni, and Zn, but will not be considered in this study. Table 2.14 shows chemical analyses of saponite, another member of the tri-octahedral smectites. Average compositions of some of the smectites calculated from several analyses published by Weaver [12] are presented in Table 2.15. The chemical data presented in this section highlights the variability in composition of the smectite group.

Other Clay Minerals

Chlorite, a clay mineral that consists of alternating mica-like and brucite-like layers, occurs in almost all types of sedimentary rocks. The structure of chlorite contains two octahedral sheets;

SiO_2	Al_2O_3	TiO_2	Fe_2O_3	FeO	MgO	CaO	Na_2O	K_2O	H_2O^+	$H2O^-$
64.7	18.6		8.1	0.3	4.3		3.3	0.0		
57.5	20.6	0.1	3.9		2.5		2.9			
59.6	22.2	0.1	4.3		2.7	0.1	3.2	0.0	6.0	
54.1	21.0	0.1	3.7		2.1		2.8			
55.7	19.4	0.8	6.5		2.3		2.5			
52.8	17.9		0.1		3.6		3.2			
62.6	18.4	0.1	1.2		7.3	0.1	3.4	0.0	6.5	
56.6	17.2	0.2	2.8		4.9		3.6			
66.3	22.4		3.3		4.1	0.0	3.7	0.1		
56.6	21.2	0.0	2.0		3.5		3.7			
60.4	20.4	0.4	3.7		4.5	0.1	3.7	0.0	6.4	
55.6	22.5	0.0	0.2		3.3		3.6			

Table 2.12: Chemical analyses of montmorillonites, members of the smectite group, reported in [1]. Blank spaces refer to either not determined or trace values.

SiO_2	Al_2O_3	TiO_2	Fe_2O_3	FeO	MgO	CaO	Na_2O	K_2O	H_2O^+
59.3	36.1		0.5		0.1	0.0	4.0	0.1	9.7
55.8	28.6	0.3	0.4		2.0	2.2	0.1	0.5	
64.0	29.0		0.2		3.0		4.0	0.1	
53.1	0.4	0.1	29.7		2.5	1.5		0.3	12.5
42.4	5.6		32.5		0.3			5.1	14.0
45.8	0.7		45.3		0.3		3.6		4.3
52.3	4.4	0.1	22.7		2.2	1.2	1.3	0.1	15.8
49.3	13.5	0.1	13.5		2.1	2.1	0.1	0.7	18.6

Table 2.13: Chemical analyses of beidellites and nontronites, members of the smectite group, reported in [1]. Blank spaces refer to either not determined or trace values.

SiO_2	Al_2O_3	TiO_2	Fe_2O_3	FeO	MgO	CaO	Na_2O	K_2O	H_2O^+	$H2O^-$
53.88	4.47	0.25	0.60		31.61		0.01	0.05	9.28	
43.62	5.50	0.00	0.66		24.32	2.85	0.08	0.04	5.48	17.42
50.01	3.89	0.04	0.21		25.61	1.31			12.02	7.28
54.74	8.93		0.43	4.80	33.28	2.65			9.93	9.17
51.40	9.00		5.40	7.83	26.10	3.20	0.04	0.12		
39.64	9.05		7.32	1.24	15.80	2.93	0.71	0.00	4.90	12.31
48.96	7.30	0.20	11.93	1.12	23.39	2.42	0.04	0.06	4.45	
39.68	3.93	0.37	19.82		11.21	2.37			6.16	15.11
55.86	0.13	0	0.03	0.70	25.03		2.68	0.10	7.24	9.90

Table 2.14: Chemical analyses of saponite, member of the smectite group, reported in [1]. Blank spaces refer to either not determined or trace values.

	SiO_2	Al_2O_3	TiO_2	Fe_2O_3	FeO	MgO	CaO	Na_2O	K_2O	H_2O^+	$H2O^-$
Montmor.	59.5	21.9	0.3	3.8	0.2	3.5	1.2	0.8	0.3	8.4	
nontronite	44.1	11.3	0.9	20.2	0.4	2.1	2.1	0.1	0.6	10.8	12.0
saponite	43.2	7.8	0.1	4.9	2.7	20.8	2.2	0.3	0.2	7.1	11.8

Table 2.15: Chemical analyses of smectite group minerals. The reported values in this table correspond to the average of the chemical analyses reported in [12]. Blank spaces refer to either not determined or trace values.

SiO_2	Al_2O_3	TiO_2	Fe_2O_3	FeO	MgO	CaO	Na_2O	K_2O	H_2O^+	$H2O^-$
36.1	10.6		1.0	1.8	38.6				11.9	0.4
24.9	25.9	0.1	3.4	7.3	26.2				10.4	1.7
24.0	23.2	0.1	3.1	15.8	18.9	0.1			12.8	
27.6	19.7		0.7	20.7	18.4				11.4	0.3
30.8	12.1		9.1	22.8	12.4				9.8	1.8
27.9	15.8		1.8	31.9	9.5	0.2			12.0	0.2
20.8	17.6		8.7	38.0	4.2				10.3	0.1
21.9	15.7		9.0	41.7					11.1	

Table 2.16: Chemical analyses of tri-octahedral chlorites reported in [1]. Blank spaces refer to either not determined or trace values.

one in the 2:1 layers and another between them. There are two types of chlorite minerals: tri-octahedral and di-octahedral. In tri-octahedral and di-octahedral chlorites, the two octahedral sheets are tri-octahedral and di-octahedral, respectively. In di,tri-octahedral chlorites, however, octahedral sheets are di-octahedral in the 2:1 layers, and tri-octahedral in the interlayer sheets [1]. Tri-octahedral chlorites are the most abundant among chlorite minerals, and their composition is usually represented by the following general formula [1]:

$$[(R^{2+},R^{3+})_6(Si,Al)_8O_{20}(OH)_4][(R^{2+}R^{3+})_6(OH)_{12}]$$

where R^{2+} and R^{3+} represent the sum of divalent and trivalent cations, respectively. Published chemical analyses of tri-octahedral, di-octahedral, di,tri-octahedral chlorites are provided in Tables 2.16, 2.17, and 2.18, respectively. Accessory elements, such as Mn, Li, Ni, were ignored in this presentation.

Vermiculite, another 2:1 clay mineral, consists of an octahedral sheet centered between two tetrahedral sheets. Vermiculite may well be considered as a member of the tri-octahedral smectites; however, its different characteristics makes its description as a different group necessary.

SiO_2	Al_2O_3	TiO_2	Fe_2O_3	FeO	MgO	CaO	Na_2O	K_2O	H_2O^+	$H2O^-$
34.4	38.8		0.5		10.2	0.1	0.1	0.1	14.0	0.8
33.7	38.0		2.7	2.4	12.1	1.5			13.1	
33.1	37.4	0.3	0.9		13.1		0.2	0.3	13.3	2.1
36.1	32.4		2.0		15.9		0.4		13.1	
32.8	35.7	0.2	2.7	1.1	13.5	0.0		0.0	13.0	
33.0	35.7		2.7	0.2	14.1				13.8	
33.8	31.9	0.3	0.3	0.4	18.9	1.8	0.6	0.0	12.1	

Table 2.17: Chemical analyses of di-octahedral chlorites reported in [1]. Blank spaces refer to either not determined or trace values.

SiO_2	Al_2O_3	TiO_2	Fe_2O_3	FeO	MgO	CaO	Na_2O	K_2O	H_2O^+
35.1	48.2					0.6	2.0		14.0
34.7	46.0		0.6		1.6	1.8	1.1		14.0
35.4	47.4		0.5	0.1	0.7	0.5	0.4		14.3
38.0	47.4				0.8				13.8
36.7	49.5				0.0				13.8
29.5	52.0	1.2	0.5	0.3		1.6			13.9
39.0	32.2	0.5	0.9	0.1	10.1	0.5	0.1	1.5	14.2

Table 2.18: Chemical analyses of di,tri-octahedral chlorites reported in [1]. Blank spaces refer to either not determined or trace values.

The composition of vermiculite is very similar to that of tri-octahedral smectites, and it is given by the following general form [68]:

$$(Mg,Ca)_{0.7}(Mg,Fe^{+3},Al)_{6.0}[(Al, Si)_{8.0}O_{20}](OH)_4.8H_2O$$

The most common inter-layer ions in smectites are sodium and calcium, although magnesium sometimes can be found. Furthermore, vermiculites possess some characteristics of smectite; for instance, it can absorb liquids between its layers and, hence, it has the property of swelling.

Another type of clay minerals is the mixed-layer or interstratified clay minerals. In this type of clay minerals, the individual crystals consist of layers of more than one type. The layers may be regularly or randomly stacked. Mixed-layer clay minerals are usually named according to the types and proportions of the layers involved in the stacking. There are several mixed-layer clay minerals described in the literature such as illite-smectite, chlorite-montmorillonite, and kaolinite-smectites. Illite-smectite is the most common type of mixed-layer clays followed in order of abundance by chlorite-montmorillonite. There is a variety of other types of mixed-

SiO_2	Al_2O_3	TiO_2	Fe_2O_3	FeO	MgO	CaO	Na_2O	K_2O	H_2O^+	$H2O^-$
41.2	12.1	0.0	1.7	0.4	22.0	1.4	0.1	0.2	15.4	6.8
43.1	16.6	0.7	6.3		17.7	0.9	0.5	2.7	7.4	
37.2	15.5	0.4	6.7		18.9	1.0	0.2	1.4	18.4	
36.1	13.7	0.2	2.1	6.9	25.2	1.7	0.4	0.1	9.3	4.8
33.4	14.3		1.7	3.7	22.4	2.8	0.2		8.2	5.5
39.9	33.2	0.7	1.3	0.2	6.4	1.3	0.5	0.2	11.6	4.4
42.1	37.4		0.3		0.1	1.7	0.2	1.4	11.2	6.2

Table 2.19: Chemical analyses of chlorite-smectite mixed-layer clay minerals reported in [12]. Blank spaces refer to either not determined or trace values.

SiO_2	Al_2O_3	TiO_2	Fe_2O_3	FeO	MgO	CaO	Na_2O	K_2O	H_2O^+	$H2O^-$
54.5	39.5	0.0	0.1		0.4	2.5	2.0	2.0		
55.1	35.7	1.0	0.3		0.4	1.4	0.4	5.9		
58.6	25.0		7.2		2.9	0.0	2.8	3.6		
53.7	19.0	0.1	3.0		3.9	0.8	1.9	2.3	14.7	3.3
55.7	21.8	0.2	2.2		4.1	0.5	1.3	4.6	7.6	4.3
56.0	24.4	0.3	1.0		4.1	0.2	1.0	6.5	7.0	1.7
54.9	18.6	0.7	14.9	0.1	5.4	1.0	1.6	1.8		
50.8	6.3	0.2	17.9	1.6	4.5	1.3	0.1	6.0	6.8	3.9
55.2	16.7	0.7	17.2		4.1	0.1	0.6	4.8		
59.3	14.4	0.4	12.1	1.4	6.9	0.2	0.4	6.7		

Table 2.20: Chemical analyses of illite-smectite mixed-layer clay minerals reported in [1]. Blank spaces refer to either not determined or trace values.

layer clays; however, the available chemical analyses are scarce. A detailed discussion of the chemistry and structure of all types of mixed-layer clays is beyond the scope of this study. Instead, published chemical analyses for chlorite-montmorillonite, illite-smectite, and kaolinite-smectite are presented in Tables 2.19, 2.20, and 2.21, respectively.

2.1.2 Non-Clay minerals

Shales include non-clay minerals such as quartz, feldspars, carbonates, sulfates, and sulfides. Among these minerals, quartz and feldspars are the most abundant, while other minerals occur in minor quantities. This section provides a brief description of some of these minerals with a focus on the chemical composition.

SiO_2	Al_2O_3	TiO_2	Fe_2O_3	FeO	MgO	CaO	Na_2O	K_2O	H_2O^+	$H2O^-$
41.9	30.1	0.4	2.4	0.2	1.5	0.3			11.1	12.9
47.0	35.3	0.0	0.6	0.0	1.0	0.4	0.1	0.1	13.0	2.5
44.5	27.3	0.4	4.3	0.0	1.6	0.4	0.5	1.0	20.0	
43.3	28.0	0.4	4.2	0.1	1.2	0.9	0.2	0.6	21.0	
45.0	26.3	0.3	4.3	0.0	1.8	0.6	0.5	0.5	20.5	
46.5	29.9	0.4	0.9	0.3	1.0	0.8	0.4	0.6	12.8	6.9
48.7	19.5	0.3	2.1	0.1	3.0	0.7	0.3	0.3	8.7	15.6

Table 2.21: Chemical analyses of kaolinite smectite mixed-layer clay minerals reported in [12]. Blank spaces refer to either not determined or trace values.

Quartz

Quartz is one of the most common minerals on earth. It occurs in igneous, sedimentary, and metamorphic rocks. The composition of quartz contains 100 % SiO_2. Small amounts of other oxides may be found in quartz due to to the presence of either small inclusions of other minerals or liquid fillings within cavities in the quartz grain.

Feldspar

Feldspars are the most common minerals in the igneous rocks. They also occur in metamorphic and sedimentary rocks such as schists, gneissess, and arenaceous sediments. Different feldspars are classified based on their composition and structure. In this study, we focus on the chemical composition of feldspars. Feldspars can be classified chemically based on the ternary system: $NaAlSi_3O_8$ - $KAlSi_3O_8$ - $CaAl_2 Si_2O_8$. These end-members are usually called sodium, potassium, and calcium feldspars, respectively. In this ternary system, members of the alkali feldspars are those between $NaAlSi_3O_8$ and $KAlSi_3O_8$, while members of the series between $NaAlSi_3O_8$ and $CaAl_2 Si_2O_8$ are called plagioclase [69].

Chemical composition of alkali feldspars ranges from $NaAlSi_3O_8$ to $KAlSi_3O_8$. The members of this group are anorthoclase, sanidine, orthoclase, and microcline. They all possess the chemical formula $(Na,K)AlSi_3O_8$ with minor amounts of $CaAl_2 Si_2O_8$ (generally less than 5 %). The potassium feldspars are polymorphs, i.e., they have the same chemistry, $KAlSi_3O_8$, but exhibit different structures resulting in different minerals. Plagioclase feldspars, on other hand, are ubiquitous minerals with chemical compositions that range from a sodium-rich end member

Mineral	Chemical formula
Calcite	$CaCO_3$
Magnesite	$MgCO_3$
Siderite	$FeCO_3$
Dolomite	$CaMg(CO_3)_2$
Ankerite	$Ca(Mg,Fe)(CO_3)_2$

Table 2.22: Some carbonates mineral along with their chemical formula[70].

(albite) with the chemical composition $NaAlSi_3O_8$, to a calcium-rich end member (anorthite) with the chemical composition $CaAl_2Si_2O_8$. Members of the plagioclase feldspar series are albite, oligoclase, andesine, labradorite, bytownite, and anorthite. The intermediate members between albite and anorthite are differentiated based on their anorthite mole percentages $0-10$, $10-30$, $30-50$, $50-70$, $70-90$, $90-100$, respectively [69]. Varying amounts of $KAlSi_3O_8$ may be found in plagioclase feldspars.

Other Non-Clay minerals

Other non-clay minerals can be found in shale in minor amounts including carbonates, pyrite, and hematite. In carbonates, the basic unit is the $(CO_3)^{2-}$ ion. Around 150 minerals have been identified as carbonates; however, many of them are relatively uncommon. The most common carbonate minerals are grouped as calcite-, aragonite-, and dolomite-types [70]. Calcite, the most abundant and important mineral in the carbonate group, consists of alternate layers of Ca and CO_3 groups. In dolomite-type carbonates, however, dolomite and ankerite are the most common. Table 2.22 lists the most important carbonates and their chemical formula.

Hematite and pyrite are other minor minerals that may be found in shale. Fe_2O_3 is the expected ideal composition of hematite; however, small quantities of MnO and FeO may be found. The presence of SiO_2 and Al_2O_3 indicate the presence of impurities. Pyrite, however, has the chemical formula FeS_2. Minor amounts of other elements can be found in pyrite, but they probably represent impurities.

2.2 Multiscale Structure Thought Model for Shale

Shale is a highly heterogeneous sedimentary rock, with compositional and microstructural features that manifest themselves at different length scales. These heterogeneities range from fine-grained clay minerals and nanoscale pores to silt-size inclusions. In conventional laboratory experiments, intact rock specimens display characteristic sizes in the centimeter range. At this length scale, shale specimens can be considered homogeneous. Hence, laboratory experiments such as acoustic measurements and triaxial testing can capture overall macroscopic elasticity and strength behaviors, respectively.

Aiming at simplifying the multiscale investigation of shale, Ulm and co-workers [24] introduced a thought-model that establishes three characteristic length scales of observation. The model, which is discussed in details hereafter, will guide our chemo-mechanical investigation[1].

2.2.1 Level 0: Elementary Clay Particles

Level 0 corresponds to the scale of individual clay particles that constitute the solid clay phase in shale; and it is sometimes referred to as the fundamental scale of clay mineralogy. Figure 2-2 shows electron transmission microscope (TEM) images with sub-micrometer resolution of clay particles. Figure 2-2 shows a TEM section of clay composite with details of the aggregation of clay minerals forming equidimensional particles of one micron diameter. Figure 2-2 (b) displays a TEM section of individual clay platelets.

2.2.2 Level 1: Porous Clay Composite

Level 1 refers to the scale of the porous clay, a composite of clay particles and porosity, on the order of 10^{-7} to 10^{-6} m. Advanced observational methods are used to study clay structure at this scale, such as environmental scanning electron microscope (ESEM) and conventional scanning electron microscope (SEM). These techniques provide visual description of the surface morphology of a sample. Figure 2-3 displays three images obtained by ESEM for shale samples. These images are taken parallel to the bedding direction where the flaky structure of clay

---

[1] The presentation of the multiscale though-model of shale is inspired from the works of J. A. Ortega and C. Bobko [40] [9].

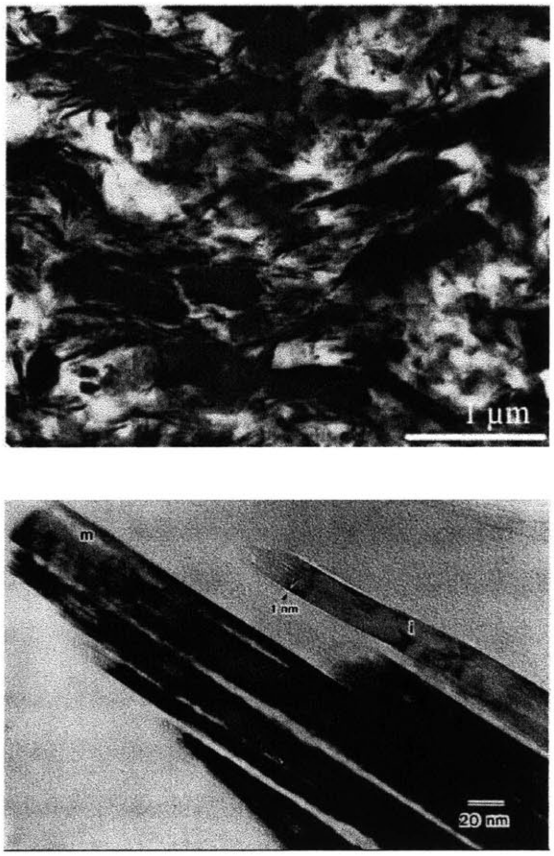

Figure 2-2: TEM images of (top) natural clay composite [67] and (bottom) individual clay platelet particles in shale [73].

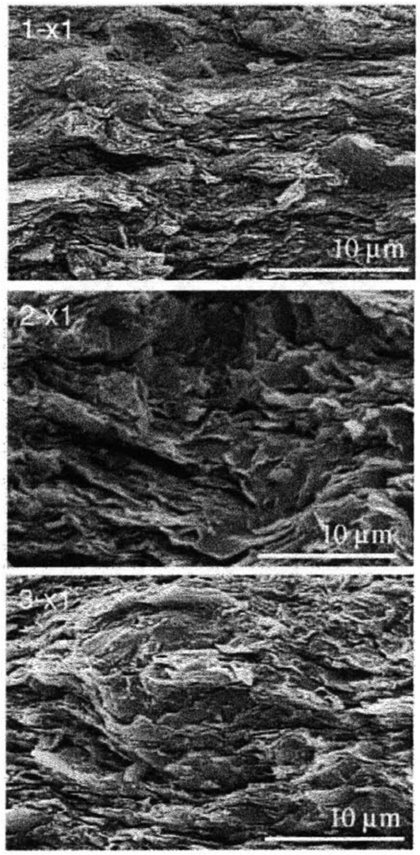

Figure 2-3: Environmental SEM of three shale samples taken parallel to the bedding direction. In these images the flaky structure and the alignment of particles in the direction of bedding are clearly observed [2].

minerals is evident, showing the tendency of particles and porosity to align in the direction of bedding. This trend is also visible in Figure 2-4 obtained for one of the investigated shale samples in this work (sample S7). Several authors have attempted to link the microstructure of clay minerals to the macroscopic anisotropic behavior of shale [7] [17]. Regarding the porosity in shale,

Level 1 is of particular importance. First, we consider the porous clay composite as the main driver of macroscopic behavior of shale. Ulm and co-workers. [25] [10] [41] suggested that shale's elastic anisotropy is, in first order, a function of the packing of clay conglomerates, and much less dependent of the particular clay mineralogy. The proposed model links the macroscopic mechanical properties of shale to the particle-to-particle contact forces of the clay fabric rather

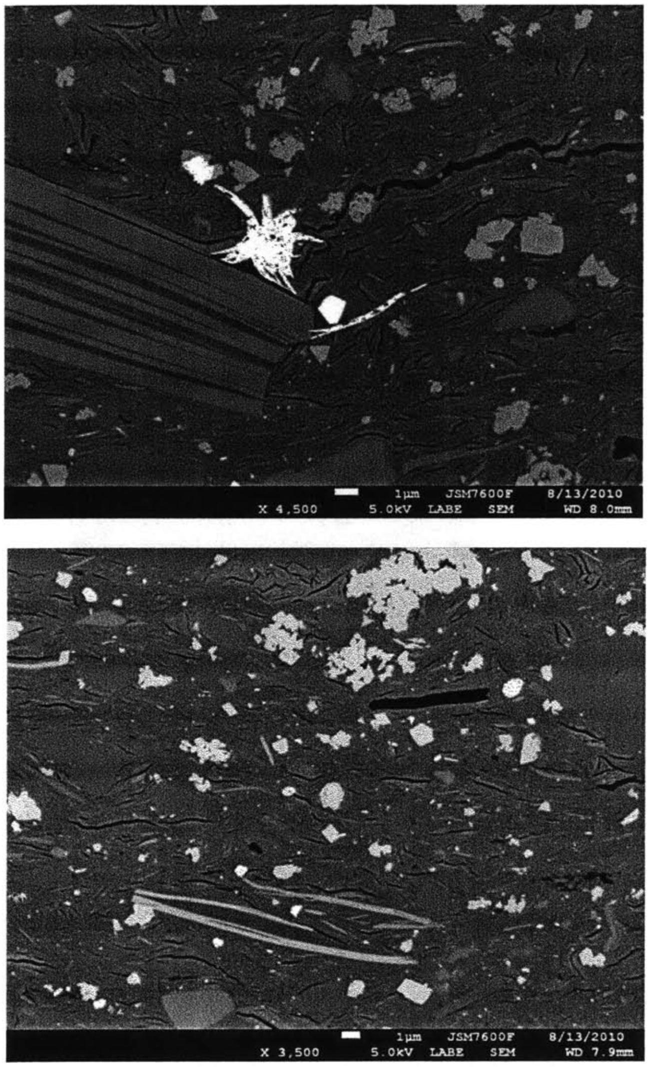

Figure 2-4: Backscattered images for one of the studied shale samples in this work (sample S7). In these images the flaky structure and the alignment of particles in the direction of bedding are clearly observed.

than the properties of individual clay minerals. This definition of the effective behavior of porous clay composite agrees with several studies. Sayers [17], quoting Terzaghi, stated that groups of parallel particles separated by a fluid behave as single particles in suspension, whose properties are controlled by the fluid chemistry. Aylore et al. [50] defined an arrangement of clay particles as "domains", and considered the clay volume as a group of separated crystals. Bandyopadhyay [49] called the agglomeration of clay particles "clay domains", while Hornby [7] called them "bundles".

In addition to being the driver of the macroscopic properties, the porous clay composite defines the scale of experimental measurements in this study; namely nanoindentation and wave dispersive spectroscopy (WDS). In nanoindentation tests, the experimental parameters are designed to probe the length scale of porous clay composite. WDS, on the other hand, probes a volume of material of a few micrometers; a length scale that matches that of the porous clay composite. These techniques and the characteristic material volumes associated with shale rock samples will be discussed at length later on.

2.2.3 Level 2: Composite of Porous Clay and Silt Inclusions

Level 2, at the scale of 10^{-5}– 10^{-4} m, is considered as the scale of porous clay composite intermixed with poorly sorted detrital grains (mainly quartz and feldspar inclusions). This scale is that of intact rock specimens used in the laboratory to determine mechanical properties. Figure 2-5 shows an example of an SEM image obtained for one of the studied shale samples in this work (S7), where the random distribution of silt/sand inclusions is observed.

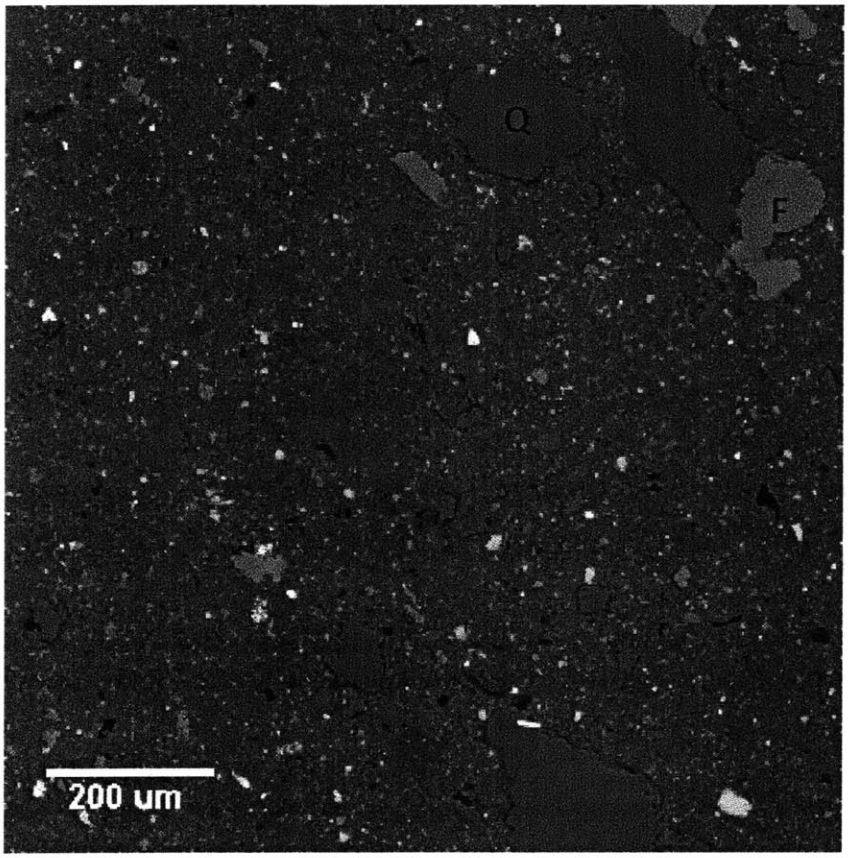

Figure 2-5: SEM image in backscattered electron mode of sample S7 studied in this work. The image shows the random distribution of inclusions. Q and F correspond to the color intensity of quartz and feldspar inclusions, respectively.

2.2.4 Chapter Summary

This chapter began with an introduction of shale mineralogy, followed by a detailed discussion of the chemical composition of clay and non-clay mineral components of shale. In particular, the heterogeneous nature of clay mineral compositions has been demonstrated through a database collected from the open literature. The discussion in Chapter 6 about the interpretation of the chemical analyses performed on shale materials will make extensive use of this database. This Chapter also introduced a multiscale thought model for the structure of shale. This model will provide the framework to explore the mineralogy and length scales relevant to shale, as well as to guide our experimental investigation.

Chapter 3

Shale Materials

This chapter provides detailed information, including mineralogy and porosity data, about each of the shale samples studied in this thesis in the context of the multiscale thought-model. The last section of this chapter introduces the surface preparation protocol followed in this work to obtain flat material surfaces appropriate for chemical and mechanical testing.

3.1 Shale Materials

In this work we investigate a set of shale samples known as the GeoGenome shales, as they were the materials selected for consideration in the GeoGenome industrial consortium. A total of twelve samples were originally supplied for characterization in this consortium, from which we choose three samples that provide the sufficient diversity in both chemical and mechanical properties. These samples were provided by Chevron, Norsk Hydro (now StatoilHydro), and the University of Oklahoma. Detailed experimental information was disclosed for all samples, although information about their geologic origin was not generally provided. The samples are identified by a reference number: S7, S3, and S1.

3.2 Mineralogy Data

The mineralogy data for the studied shale samples was obtained by X-ray diffraction method (XRD). This technique is the most widely used method for characterization of fine-grained soil

Sample	Inclusions	Total clay	Kaolinite	Illite/Smectite	Other clay	Amorphous
S7	31	67	37	21	9	-
S3	30	70	9	54	7	-
S1	22	76	36	38	2	-

Table 3.1: Mineralogy information of shale samples (in mass percent) provided by the GeoGenome industry Consortium. The mineralogy data was obtained by X-ray diffraction. Inclusions refer to quartz, feldspar, and carbonates. Other clays refer to minerals such as chlorite, glauconite, biotite, serpentine, and berhierine. Amorphous refers mainly to kerogen content.

materials, although other methodologies can be used, such as infrared spectroscopy and energy dispersive spectroscopy. Table 3.1 summarize the mineralogy data of the studied shale samples.

3.3 Porosity and Bulk Density

Three different methods are used to determine porosity in this study. The first method consists of the combination of experimental bulk density and measurements and mineralogy data:

$$\overline{\rho}^{sat} = \frac{1-\phi_0}{\sum_{i=1}^{N} m_i/\rho_i} + \phi_0\rho^{fl} \Longrightarrow \phi_{0,\rho} = \frac{\overline{\rho}^{sat} - \left[\sum_{i=1}^{N}(m_i/\rho_i)\right]^{-1}}{\left[\sum_{i=1}^{N}(m_i/\rho_i\right] - \rho^{fl}} \tag{3.1}$$

where ϕ_0 is the porosity, $\overline{\rho}^{sat}$ is the saturated bulk density and ρ^{fl} is the density of fluid saturating the pore space. Another convenient way of determining porosity is by comparing the density of a saturated and dried sample:

$$\phi_{0,d} = \frac{\overline{\rho}^{sat} - \overline{\rho}^{sat}}{\rho^{fl}} \tag{3.2}$$

where $\overline{\rho}^{sat} = M^{sat}/V_0$ and $\overline{\rho}^{dry} = M^{dry}/V_0$ are the mass densities of the fully saturated and the oven-dried sample, respectively (M^{sat} and M^{dry} are the masses of the fully saturated and the oven-dried samples, respectively). Finally, fluid intrusion or gas expansion techniques, provide independent measurements of the porosity, among which mercury intrusion porosimetry (MIP) is the most prominent test. MIP consists of forcing mercury into a porous solid by means of applying high pressures on mercury. It is well known that MIP tends to underestimate the actual porosity [64], while porosity measurements using bulk density and mineralogy information

Sample	MIP porosity(%)	Drying porosity (%)	Bulk density (g/cm^3)
S7	7	11.5	2.51
S3	7	13	2.55
S1	26	26	2.20

Table 3.2: Porosity and bulk density data for the tested shale samples.

provide a higher value of porosity. The results of porosity estimates for the investigated shale samples are shown in Table 3.2.

3.4 Volume Fractions

With the multiscale thought-model of shale in hand, the mineralogy and porosity of the studied shale samples are transformed into volumetric parameters. These parameters become critical for micromechanics experimentation and modeling. In view of the multiscale thought-model discussed in section 2.2, we define two important volumetric parameters associated with shale: the clay packing density, and the inclusion volume fraction.

At the macroscopic level, shale is classically divided into three characteristic components, non-clay minerals, clay minerals, and porosity[1]:

$$\text{Level II: } f^{inc} + f^{c} + \phi_0 = 1 \tag{3.3}$$

where f^{inc} is the volume occupied by non-clay mineral (NCM) components (quartz, feldspars, carbonates, etc.) in the macroscopic sample volume, f^{c} is the volume fraction occupied by the clay mineral (CM) components (Kaolinite, illite, smectite, etc.) in the macroscopic sample volume, and ϕ_0 is the porosity. The inclusion volume fraction and the clay volume fraction are calculated as:

$$f^{inc} = (1-\phi_0)\frac{\sum_{i=1}^{i=NCM}(m_i/\rho_i)}{\sum_{i=1}^{N}(m_i/\rho_i)} \tag{3.4}$$

$$f^{c} = (1-\phi_0)\frac{\sum_{i=1}^{i=CM}(m_i/\rho_i)}{\sum_{i=1}^{N}(m_i/\rho_i)} \tag{3.5}$$

---

[1] The presentation of this section follows the work of J. A. Ortega [40].

		Density, ρ_i (g/cm^3)
Inclusion	Quartz	2.65
	Kspar	2.57
	Plagioclase	2.68
	Calcite	2.71
	Dolomite	2.90
	Pyrite	5.00
	Siderite	3.74
	Ankerite	3.00
	Hematite	2.90
Clay minerals	Kaolinite	2.64
	Illite / Smectite	2.65
	Chlorite	2.95

Table 3.3: Density information of some minerals present in shale.

where m_i is the mass fraction of the solid constituents of shale determined by XRD, and ρ_i the mineral densities (see Table 3.3). The volume fraction associated with Level I is the clay packing density and is given by:

$$\eta = \frac{f^c}{1 - f^{inc}} = \frac{(1-\phi_0)\sum_{i=1}^{i=CM}(m_i/\rho_i)}{\sum_{i=1}^{i=CM}(m_i/\rho_i) + \phi_0 \sum_{i=1}^{i=NCM}(m_i/\rho_i)} \tag{3.6}$$

The value of volume fraction of non-clay minerals (f^{inc}) and the packing density depend on the method with which the porosity was measured. As discussed in section 3.3, several methods can be used to determine porosity including mercury intrusion porosimetry, drying experiments, and estimation from mineralogy density. These techniques may yield different measures for porosity which result in variability in the estimation of clay packing density and the inclusion volume fraction. Table 3.4 summarizes the volume fractions of clay minerals and non-clay inclusions derived from the provided XRD mineralogy information and porosity measurements. Since the mineralogy information was derived form XRD, which provides solid mass fractions, the obtained volume fractions represent the solid volume fractions of the clay minerals and non-clay inclusions. To obtain the volume fraction of the porous clay composite (see Section 2.2.2), which defines the scale of measurements in this study, the measured porosity is added to the solid volume fraction of clay minerals calculated from XRD mineralogy information. Also, Table 3.5 lists the solid volume fractions of clay minerals separated into 1:1 and 2:1 clay

	Porosity		Solid clay	Quartz	Feldspar	Other inclusions	Porous clay
S7	max	7	65	17	7	4	72
	min	11	62	17	7	3	73
	dry	12	61	17	7	3	73
S3	max	7	65	20	3	4	72
	min	7	65	20	3	4	72
	dry	13	60	20	3	2	73
S1	max	26	58	13	2	1	84
	min	29	55	13	2	1	84
	dry	26	58	13	2	1	84

Table 3.4: Volume fraction and porosity information of shale samples provided by the GeoGenome Consortium. The volume fraction data was derived from X-ray diffraction (XRD) mineralogy results. Porous clay refers o the summation of solid clay and porosity. Minimum volume fractions were calcuated using mineralogy and bulk density information. Maximum volume fractions were calculated using using mineralogy and MIP porosity measurements.

Sample	1:1 Clays	2:1 Clays	1:1 - 2:1 Clay ratio
S7	36	29	1.30
S3	8	57	0.14
S1	28	30	0.93

Table 3.5: Solid volume fractions of clay minerals reported in Table 3.4 separated into 1:1 and 2:1 clays derived from XRD mineralogy results and porosity measurements.

minerals.

3.5 Sample Preparation

An appropriate surface preparation protocol, which minimizes surface roughness and sample disturbance, is crucial for a correct experiment. This task is particularly challenging for shale due to its heterogeneous nature. The wide range of hardness of particles embedded in a soft matrix complicates surface polishing for shale. As we will discuss later in this study, the scale of the performed experiments in this study (indentation and electron microprobe) is around 2 μm, the surface roughness must be well below this scale. Shale samples were trimmed with a diamond saw to create a sample which is easily handled and fits the machines nicely (around 10 mm in diameter and 5 mm in height). Subsequently, samples are mounted on an AFM steel disk (Ted Pella) 15 mm in diameter, and are ultrasonically cleaned. Next, the sample polishing proceeds in two steps:

- The first step is a coarse polishing step designed to make the surface of the sample parallel to the mounting disk. A hard, perforated non-woven pad (TexMet P, by Buehler) is mounted on a lapping wheel where the sample is held in place using a jig that contains a specially designed opening to fit the outer diameter of the outer disk (see Figure 3-1). A light weight is applied to the sample through a cylinder that fits inside the jig. 0.5 mm of 9 μm oil-based diamond suspension is added under the sample. Oil-based polishing is necessary to prevent any reaction with clay minerals. With the sample held on the pad by the jig, the polishing table is turned on and allowed to spin underneath the sample. This step lasts for 5 to 10 minutes. Once this step is done, the sample is ultrasonicated in n-decane solution, which does not react with shale minerals, for 5 minutes.

- The second and final step is the fine polishing step necessary to make the surface of the sample flat. Polishing is performed in dry conditions using 9 μm, 3 μm, and 1 μm FibrMet (by Buehler) aluminum oxide abrasive disks. The grain size of the abrasive is progressively decreased to reduce damage and to obtain a scratch free surface. A glass plate is used underneath the abrasive disks to provide a flat surface appropriate for polishing. After each pass, the sample is ultrasonically cleaned before advancing any further. Figure 3-2 shows the experimental setup in this step. The above procedure produced a flat surface, appropriate for chemical and mechanical testing, which can be visually inspected. The surface was evaluated using secondary electron microscope (SEM) under the backscattered electron mode. Figure 3-3 shows the flat surface of the shale samples investigated in this study using the above polishing protocol.

Atomic force microscopy (AFM) was used to measure the surface roughness obtained from the application of this polishing protocol on different shale samples. Several areas were scanned to determine the root mean square roughness (RMS) of each area. Three small areas of 1 μm area showed that the measured RMS ranges from 10 nm to 30 nm. To avoid sampling issues, a larger area of 40 μm size was scanned yielding a RMS value of 30 nm. Bobko [9], following

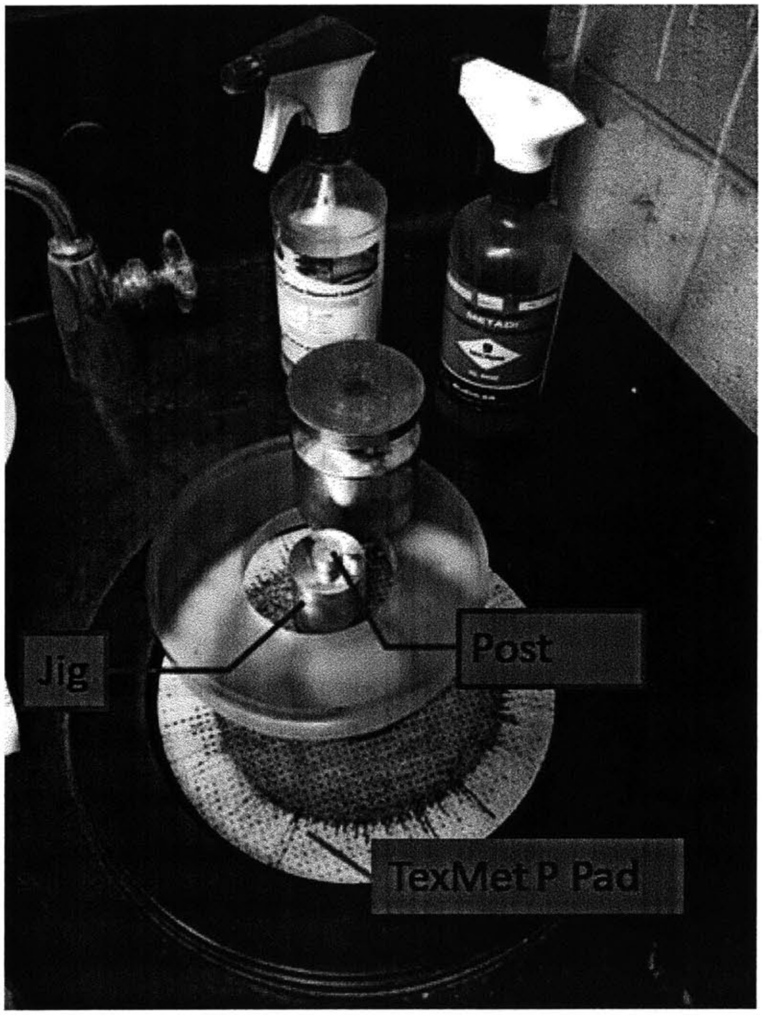

Figure 3-1: Polishing equipment used in step 1.

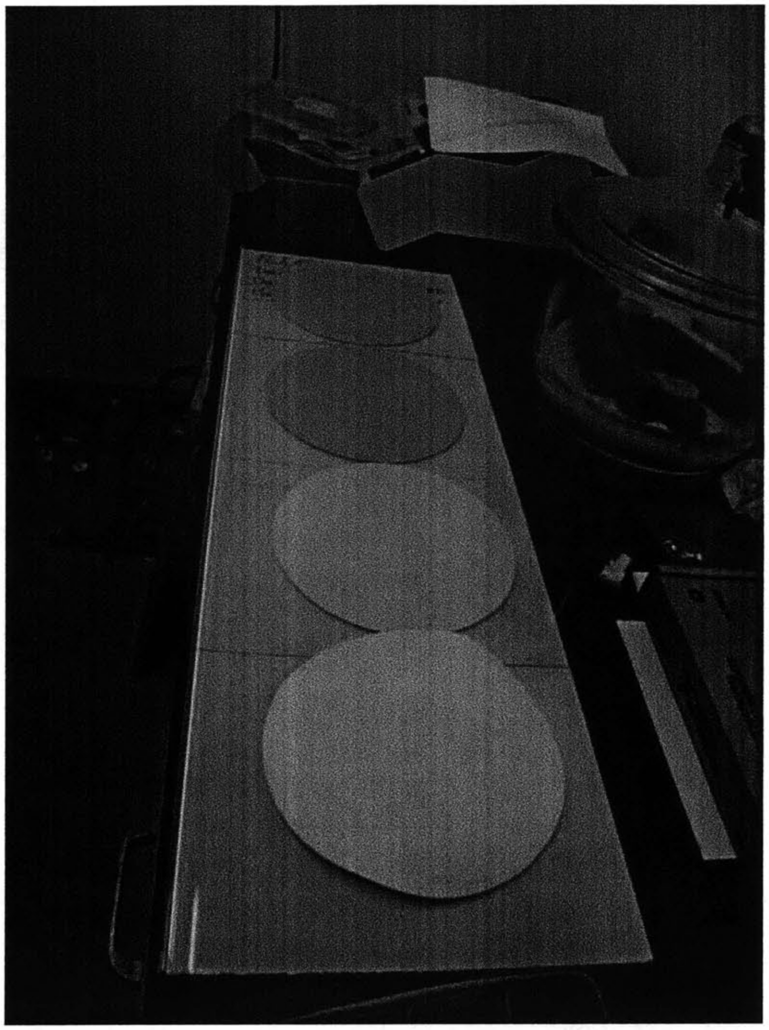

Figure 3-2: Polishing equipment used in step 2. Different colors for the abrasive disks correspond to different abrasive grain sizes.

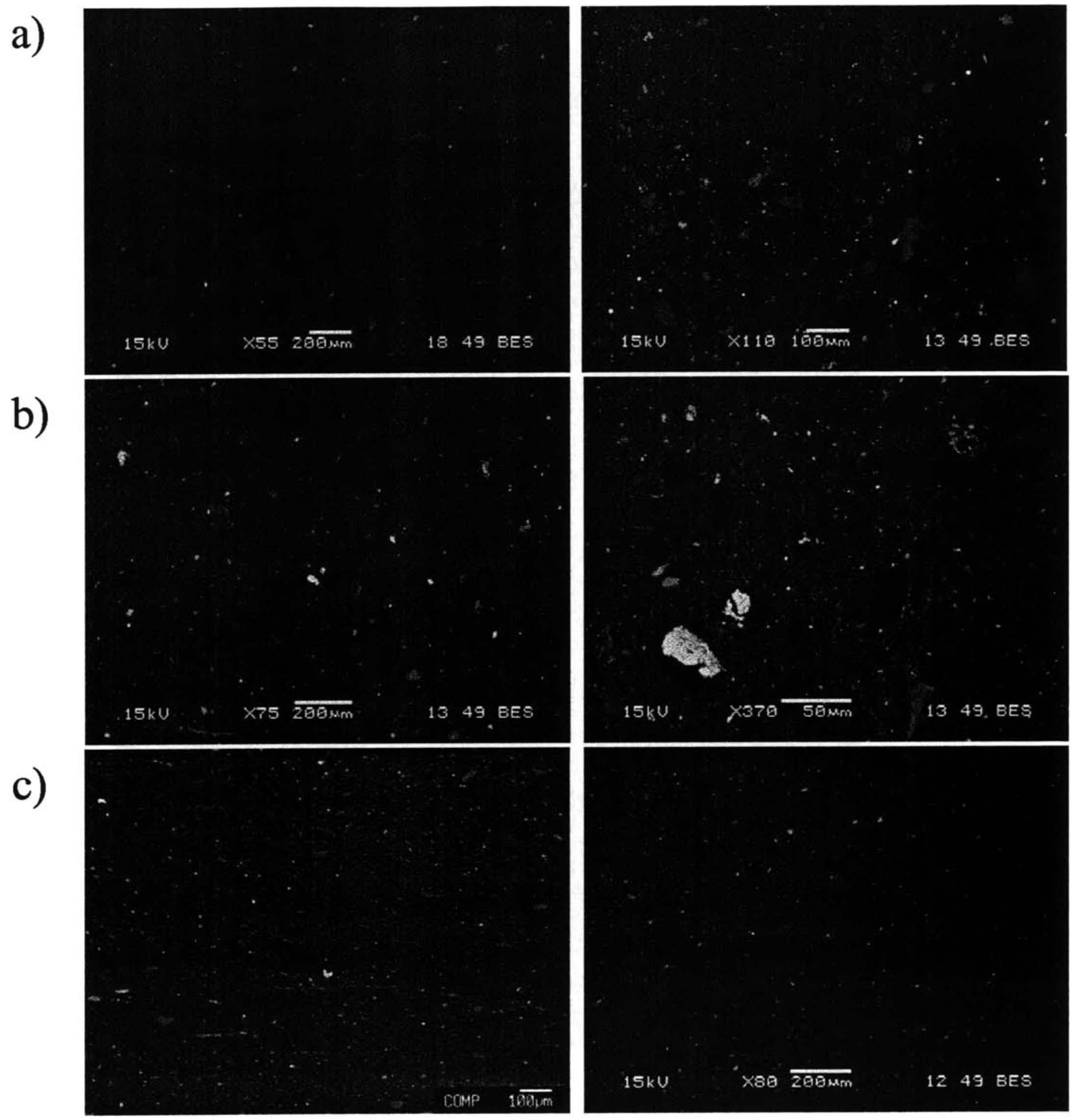

Figure 3-3: Backscattered electron (BSE) images for the studied shale samples: a) S7, b) S3, and c) S1. The images show the flat surface obtained using the polishing protocol described in this section.

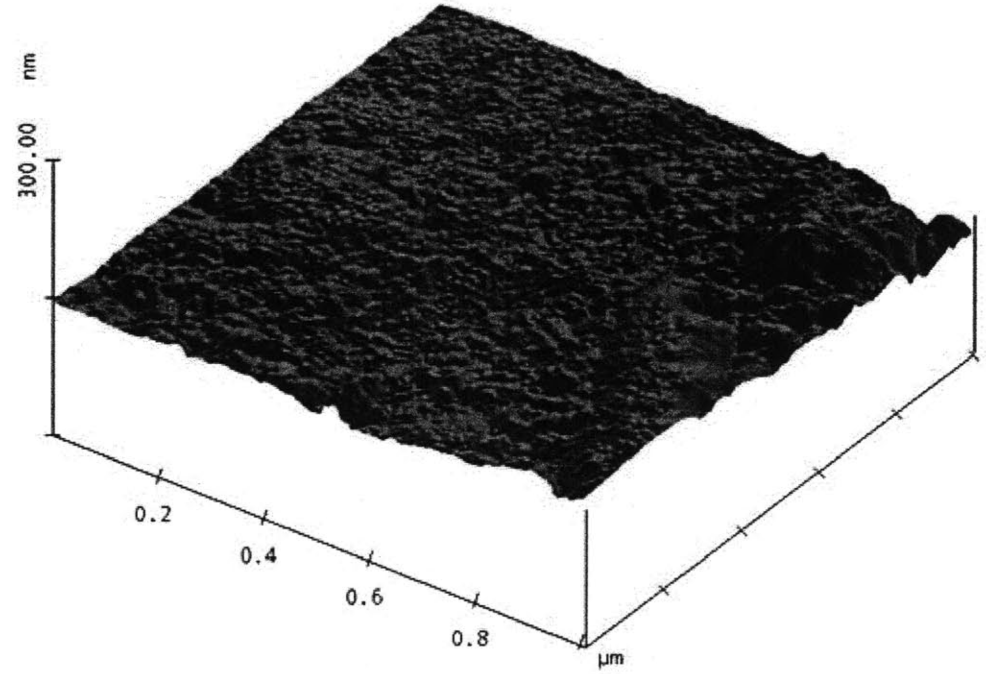

Figure 3-4: AFM image of a shale sample over 1 μm area. The root-mean-square roughness is 10 nm.

a different polishing protocol, found that the RMS of the studied shale materials ranges from 150 to 200 nm. We expect that the RMS of the investigated shale materials using the polishing protocol will be between the two mentioned values (30 and 150 nm).

3.6 Chapter Summary

This chapter provided a summary of the mineralogy and microstructural information of the shale samples investigated in this work. X-ray diffraction (XRD) mineralogy information is provided in terms of the solid mass percents of shale constituents. The porosity information was obtained through different methods, providing an upper and lower estimates for the measured porosity. The XRD and porosity data were combined to derive volume fraction estimates for shale mineral components. The volumetric mineralogy information will be used to validate the wave dispersive spectroscopy (WDS) experiments presented later in this thesis. Finally, this chapter provided a description of the surface preparation protocol used to obtain polished flat surfaces appropriate for the chemical and mechanical testing conducted in this work.

Chapter 4

Statistical Grid WDS Analysis

This chapter deals with the application of electron probe microanalysis to shale materials. We begin with a presentation of background information about EPMA that is necessary to understand the basics of this technique. A brief review of the use of this technique in geology is also provided. The next section of this chapter introduces the grid WDS technique as an adaptation of this classical method for the measurements of heterogeneous materials. The discussion of grid WDS technique starts with an introduction of the cluster analysis method used in the analysis of the grid WDS chemical data. We then discuss the experimental parameters involved in the design of grid WDS technique and their effects on the chemical measurements. Finally, the analysis methodology adopted in this work along with a sample application on shale materials is presented.

4.1 Electron Probe Microanalysis and Scanning Electron Microscopy

Electron probe microanalysis (EPMA) is an experimental technique used to determine the chemistry of a specified region in a sample. Electrons and X-rays are emitted as a result of the interaction between a beam of electrons and a sample. Emitted electrons are then used to produce images of the surface of interest, while x-rays, which are a characteristic of the elements from which they are emitted, provide qualitative and quantitative measure of the elements present in the sample. The specimen-beam interactions are discussed below. Imaging capabilities of EPMA are primarily used for locating regions of interest for point analysis, which makes it an invaluable technique in materials science. Scanning electron microscope (SEM), on the other hand, is a close relative of EPMA. SEM is primarily made for imaging purposes where different detection modes of electrons can be used to produce topographic and compositional images. Furthermore, SEM is usually equipped with x-ray detector enabling x-rays of selected elements to be collected and analyzed. The function of the two equipment, however, overlap considerably with different priorities.

EPMA and SEM are widely used in many branches of geology: planetology, sedimentology, mineralogy, and petrology. In mineralogy and petrology, for instance, EPMA and SEM are used for elemental quantification at the micrometer scale, and for generating images of polished samples that reveal a wealth of microstructural details [66]. The wide use of both techniques stems from the relatively easy sample preparation, high accuracy of elemental analysis, small volume of interaction (on the order of 1 micrometer), and the non-destructive nature of the technique (the sample can be reserved for other tests). The two main aspects of the EPMA and SEM techniques, the interaction between electron beam and a sample and the methods for detection of emitted radiations, are discussed below.

4.1.1 Specimen Beam Interactions

In EPMA and SEM experiments, a beam of electrons is accelerated onto the surface of the material to excite radiations which are a function of the topography and composition of the sample. These interactions cause various types of emissions, mainly elastic and inelastic scattering and X-ray emissions.

Elastic Scattering

In elastic scattering the total kinetic energy of the collision of electrons is conserved. This type of scattering mainly describes the interaction between an electron and nuclei of the specimen. It involves large deflections in which the angular deflection angle γ, derived by Rutherford, is given by:

$$\tan(\frac{\gamma}{2}) = \frac{Z}{1.4pE} \tag{4.1}$$

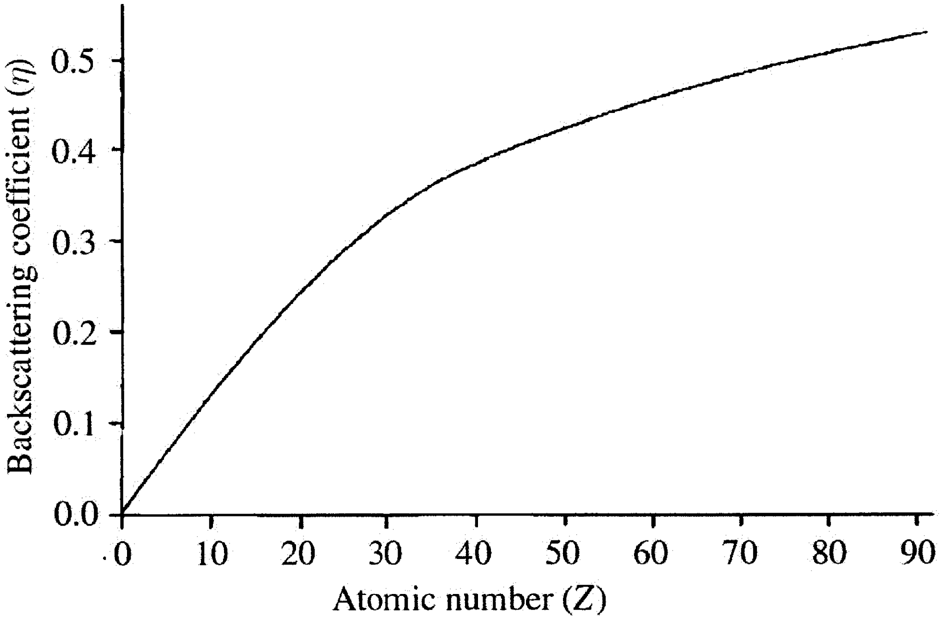

Figure 4-1: Backscattering coefficient versus atomic number. The figure shows the strong relation between these two parameters [66].

where Z is the average atomic number, p is the minimum distance between the undeflected electron path and the nucleus, and E is the energy of the beam of electrons. Elastic scattering is responsible for electron backscattering, where an electron is deflected through an angle greater than 90°. Backscattered electrons are, by convention, electrons with energies greater than 50 eV (1 eV $=1.6\times10^{-19}$ Joules). The fraction of the beam electrons that are deflected through angles greater than 90°represents the backscattering coefficient η, and it is strongly dependent on the atomic number Z as shown in Figure 4-1. Hence, backscattering electrons provide information about the composition of the sample.

Inelastic Scattering

The energy of the beam of electrons that is dissipated through various types of interactions with bound electrons is known as inelastic scattering. This type of scattering is responsible for the emission of secondary electrons, which by convention possess energy less than 50 eV. During inelastic scattering, electrons receive sufficient energy to leave the sample surface. Similar to the backscattering coefficient η, the secondary electron coefficient η_{SE} represents the ratio of the number of secondary electrons produced to the number of incident electrons. The secondary electron coefficient does not vary smoothly with atomic number. As a result of their low energy, secondary electrons that are within a few nanometers from the surface are able to leave. Consequently, secondary electrons provide information about the topography of a specimen.

Characteristic X-ray Emission

X-ray produced by beam electron-sample interactions is a characteristic of the elements from which they are emitted. X-ray emissions are produced by electron transition between the bound orbits which possess energy governed by the quantum number (n). These orbits are usually designated as K(n=1), L(n=2), and M(n=3). Each of these orbits contains subshells with slight energy differences as shown in Figure 4-2. For an x-ray to be produced the incident beam energy must exceed the critical excitation energy required to ionize the sample.

The energies of the relevant energy shells are schematically shown in Figure 4-3. The energy of x-ray is equal to the difference between the initial and final energy in the transition process. The lines are designated as K, L, and M based on the energy level from which the electron is ejected. In each shell, lines are labelled based on intensity: α being the most intense line, β the second most intense line, and so on [66]. Since x-ray emissions are characteristic of the elements from which they are emitted, they can be used to identify the composition of a specimen.

4.1.2 X-ray Detection

Two types of x-ray detectors are commonly employed in EPMA testing: energy dispersive spectrometers (EDS), which characterize the emitted X-rays based on their energy; and wave dispersive spectrometers (WDS), which sort the X-rays based on their wavelengths. In this section we briefly discuss the two detection techniques and state some of their comparative advantages and disadvantages.

Energy Dispersive Spectroscopy (EDS)

Energy dispersive spectroscopy classifies X-rays based on their energy. The major component of an EDS system is a solid state detector, which could be made of lithium-drifted silicon,

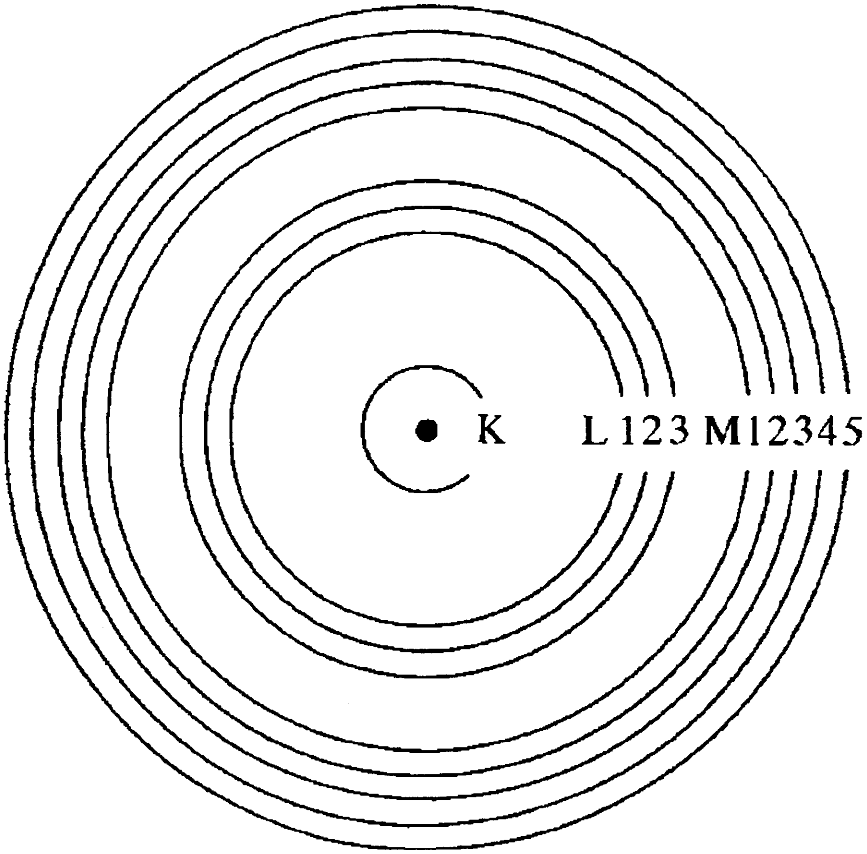

Figure 4-2: Schematic of the inner atomic shells. X-rays are produced by electron transitions between these shells [66].

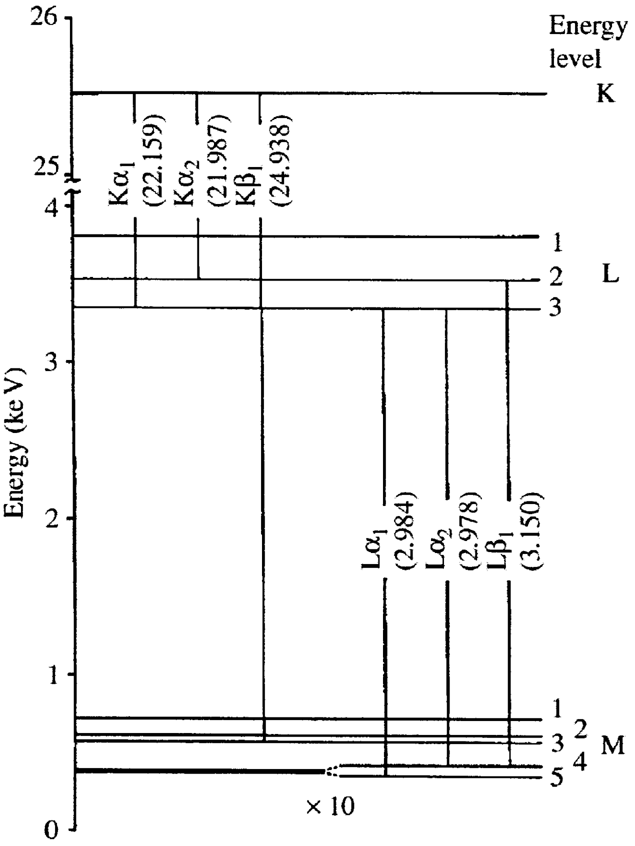

Figure 4-3: Schematic of the energy levels of a silver atom. The energy of X-ray is equal to the difference between the initial and final energy levels in the transition process [66].

lithium drifted germanium, or mercuric iodide. The detector absorbs the X-ray photons and forms a charge pulse, which is then converted into a voltage pulse that is amplified and passed to a computer X-ray analyzer. The data is displayed as a histogram of intensity by voltage, which provides information about all elements with X-ray emissions in the range of voltage being analyzed. Hence, one detector is sufficient to measure all chemical elements within the probed material volume that generate detectable radiations.

Wave Dispersive Spectroscopy (WDS)

In WDS, X-rays are classified based on their wavelengths and making use of the Bragg reflection phenomenon associated with the experiment. In Bragg reflection, X-rays of a given wavelength λ are diffracted by the atomic layers of crystal of interplanar spacing d at a certain angle of incidence θ (see Figure 4-4). The relationship between these variables is known as Bragg's law, and is given by:

$$n\lambda = 2d \sin\theta \tag{4.2}$$

where n is an integer ($n = 1, 2, 3, ..$) representing the order of reflection. In WDS testing, the first order of reflection ($n = 1$) is usually used since it produces the most intense reflections. For $n = 1$ and a given value of interplanar spacing $2d$ the wavelength range is limited. Hence, several crystals of different interplanar spacing are needed to cover the entire range of X-rays. A typical WDS system can have up to five detectors allowing up to five elements to be measured simultaneously. Source, detectors, and analyzing crystals are usually positioned in the imaginary Rowland circle, see Figure 4-5. This geometrical arrangement ensures that the Bragg angle is the same for all points.

Once a x-ray has been emitted and diffracted by the crystals, a proportional counter is used to detect the radiation. The proportional counter consists of a tube filled with gas and a coaxial wire held at a positive potential between 1 and 2 kV. X-rays enter the detector through a window, which could be thin or thick depending on the wavelength, causing the gas atoms to ionize. This ionization generates electrons and ions that are attracted to the anode wire and to the cathode, respectively. The electrons cause further ionization resulting in a pulse that appears in the anode. The analysis of the pulse enables measuring the X-ray intensities [66].

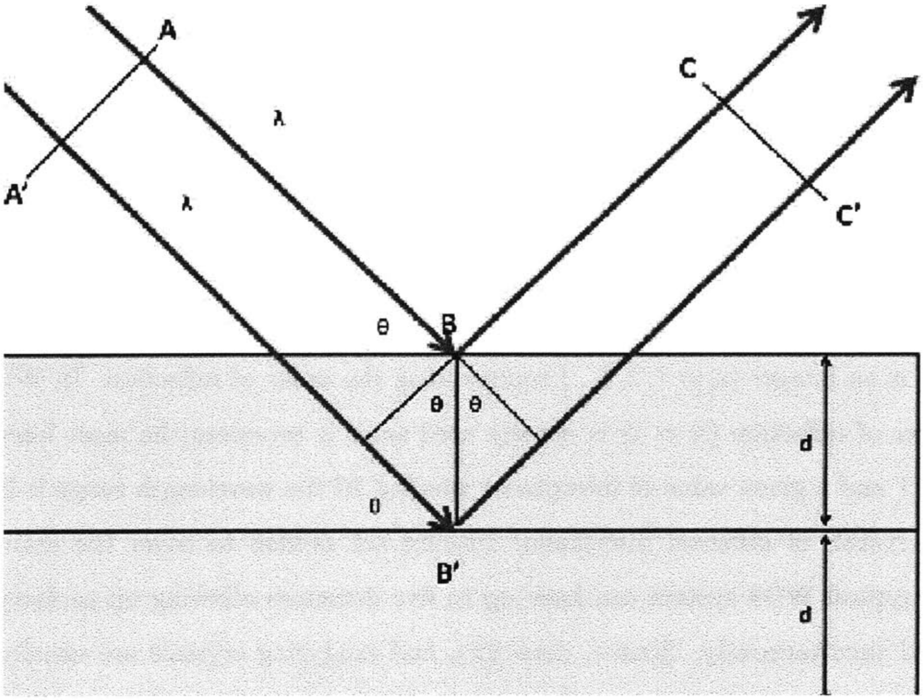

Figure 4-4: Bragg reflection: X-ray diffraction pattern of a certain wavelength by a crystal of interplanar spacing *d*. Adapted from [48].

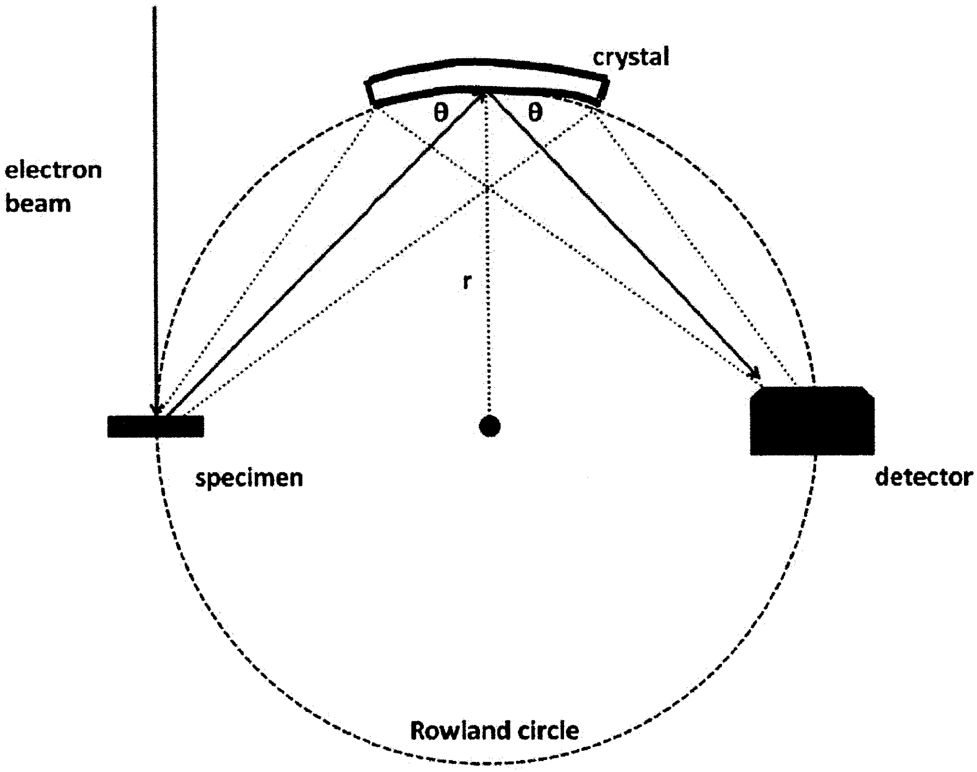

Figure 4-5: Schematic of the imaginary Rowland circle geometry used to locate the specimen, crystals, and detectors in EPMA [66]

Quantitative Analysis of X-rays

Two types of X-ray spectrometers can be used to collect emitted X-rays. The EDS technique is better suited for qualitative chemical analysis owing to its ability to record complete spectra in short experimental times. The WDS technique, in contrast, is used for quantitative analysis given its better resolution. In this study, we have chosen to use the WDS method since it has the potential of producing quantitative measurements of elements concentrations.

The intensity of a characteristic X-ray is proportional to the mass concentration of the element of interest. Hence, for a given sample, once the X-ray intensities of each element of interest are measured, the intensities are compared to those of standards containing known values of the elements of interest. The uncorrected elemental concentrations are calculated by the following relation [66]:

$$C'_A(sp) = \frac{I_A(sp)}{I_A(st)} C_A(st) \tag{4.3}$$

where $C'_A(sp)$ is the uncorrected mass concentration of element A in the specimen, and $C_A(st)$ is the mass concentration of element A in the standard. $I_A(sp)$ and $I_A(st)$ are the intensities measured in the specimen and standard, respectively. Several corrections are required to ensure that the WDS measurements and data analysis provide quantitative chemical data. The measured peak intensities require background and overlap corrections. Background corrections eliminate background contributions to the measured peak intensities. Overlap corrections take into account the fact that peak intensities are enhanced by overlaps with neighboring peaks. In addition, uncorrected mass concentrations must be corrected for matrix effects. This correction is known as matrix correction, and sometimes referred to as ZAF, an acronym for the different matrix effects: atomic number (Z), absorption (A), and fluorescence (F). The ZAF correction is applied iteratively since it depends on the composition of the specimen, which is a priori unknown. This correction procedure is implemented within a computer environment that processes measured X-ray intensities, compares them to standards, computes the ZAF correction, and outputs the results as mass concentrations of elements or oxides.

WDS is generally used to generate high resolution wavelength spectra and X-ray compositional maps, but the most common application of WDS is for quantitative spot analysis. The results of WDS spot analysis are presented as mass concentrations of each element or as mass concentrations of the appropriate oxides. In this study, the elemental mass concentration representation will be adopted because it is most suited for the data processing employed herein.

X-ray Mapping

X-ray maps provide the spatial distribution of a specific element by recording a map of X-ray intensities resulting from beam of electrons-sample interactions. Unlike EPMA spot analysis, the beam of electrons is scanned in a rectangular raster or the specimen is moved while holding the beam position fixed. X-ray maps are generated by converting X-ray intensities recorded for each pixel to gray levels. In this method of recording the data, the information about elements concentrations are lost. If a quantitative X-ray map is required, it is then necessary to apply background and ZAF corrections [66]. Similar to EPMA spot analysis, X-ray maps can be acquired by WDS or EDS. In this work, we use the WDS method for the reasons discussed above.

4.2 EPMA in Geology

During the past three decades EPMA and SEM have become established experimental tools in the study of geological materials. EPMA and SEM are versatile techniques that have been successfully applied to studies including investigation of individual minerals, age determination, and elemental mapping of major constituents in rocks [46] [66]. Backscattered electron (BSE) imaging is by far the most widely used imaging mode. The ability of BSE microscopy provide images on the basis of atomic number contrast has made it an invaluable technique in the study of the relations between composition and grain morphology. Krinsley [21] provided a summary of this technique and its applications to sedimentary rocks, including shale. He showing how the technique can be used to obtain textural information. WDS spot analysis, on the other hand, is conventionally used in conjunction with imaging capabilities in order to isolate a particular grain or phase of interest and provide quantitative compositional data. Image analysis of backscattered images and X-ray maps is another application typically used to obtain quantitative information about earth materials. In this technique, the analysis of a set of BSE micrographs and X-ray maps of representative surfaces of the specimen can deliver microstructural information such as volume fractions of constituents and pore/grain size distributions (see e.g., [21]). The image analysis technique has been successfully applied to shale rocks and other sedimentary rocks [4] [57] [58].

In EPMA and SEM applications previously discussed, the experimental setup primarily targets the chemical assessment of a specific location in the material surface. A few studies reported in the literature of geological materials resorted to statistical treatment of large data sets of EPMA measurements in order to assess overall composition and chemical variability of material samples. Statistical clustering methods for multivariate data help assigning each experimental event to the most probable cluster, within the framework that the entire data set can be decomposed into clusters with similar properties.

In studies of atmospheric aerosol samples, cluster analysis techniques were applied to investigate the composition of aerosol particles and determine the most abundant particle types [18] [16] [71]. These studies were based on EDS measurements of hundreds of particles. In a different application, Bondarenko et al. [37] employed cluster analysis of EDS data of ceramic samples to address the effect of temperature on chemical composition and phase homogeneity. EDS experiments performed on samples before and after thermal treatment, showed enhanced chemical homogeneity, as well as, the production of new chemical phases. Finally, Klepka et al. [55] used cluster analysis of EPMA data combined with X-ray diffraction (XRD) to decode the phase composition of an iliminite mineral.

These first applications of cluster statistics to model EPMA data open the possibility to potentially deal with highly heterogeneous materials. In the following section, we design a systematic implementation of EPMA to tackle the highly complex chemistry of shale materials.

4.3 Grid WDS Technique

Shale is a highly heterogeneous sedimentary rock, which consists of clay minerals, quartz, feldspar, and other minerals with minor amounts. This heterogeneous nature of shale makes its mineralogy and chemistry more complex than other sedimentary rocks. In this study, an experimental protocol to assess the chemical make-up of shale is proposed based on a combination of EPMA testing and multivariate statistics to interpret large sets of chemical data.

The proposed approach borrows inspiration from the so-called statistical grid indentation developed by Ulm and co-workers [33] [26] [34], which addresses the mechanical characterization of heterogeneous porous composites. With the appropriate experimental setup, each WDS experiment of the hundreds performed over a sample surface is treated as an independent statistical event, and clustering algorithms can be implemented to infer the chemical composition of the main constituents of the material. The statistical grid WDS has already been developed for the assessment of cementitious materials. Vanzo and Ulm [48] implemented the grid WDS technique to characterize the effect of carbonation on the chemical composition of oil cements at grain scale. In our study, we adapt the principle of grid WDS to the characterization of shale materials. Our original contribution to the chemical assessment of shale composition is the implementation of multivariate clustering method to resolve the main material constituents at micrometer length scales, as well as to design and validate the appropriate experimental protocols. In what follows, the principles of grid WDS technique, the statistical treatment of WDS data, and the implementation of the proposed methodology to shale rocks are detailed.

4.3.1 Principle of Grid WDS Technique

The grid WDS concept can be illustrated by considering the following thought experiment of a heterogeneous sample containing more than one material of different chemical composition. A random WDS spot on the sample surface provides access to the chemical composition of any of the material phases given that the volume of the material probed by WDS (interaction volume) is smaller than the characteristic size of the individual phases. In contrast, a larger volume of interaction compared to the characteristic size of the individual phases provides access to the average chemical composition of the individual phases. Another instance of such response is when the beam of electrons in WDS lands at the boundary of two phases. Figure 4-6 schematically illustrates the concept of grid WDS. This thought experiment shows how the conventional WDS spot analysis can be applied to heterogeneous materials. This requires a large array of WDS spot results followed by statistical analysis of the data to separate the chemical properties of individual phases.

The grid WDS technique introduces a new length scale to the problem. The grid size must be chosen properly to achieve statistical independence in the sampling process. The grid size L

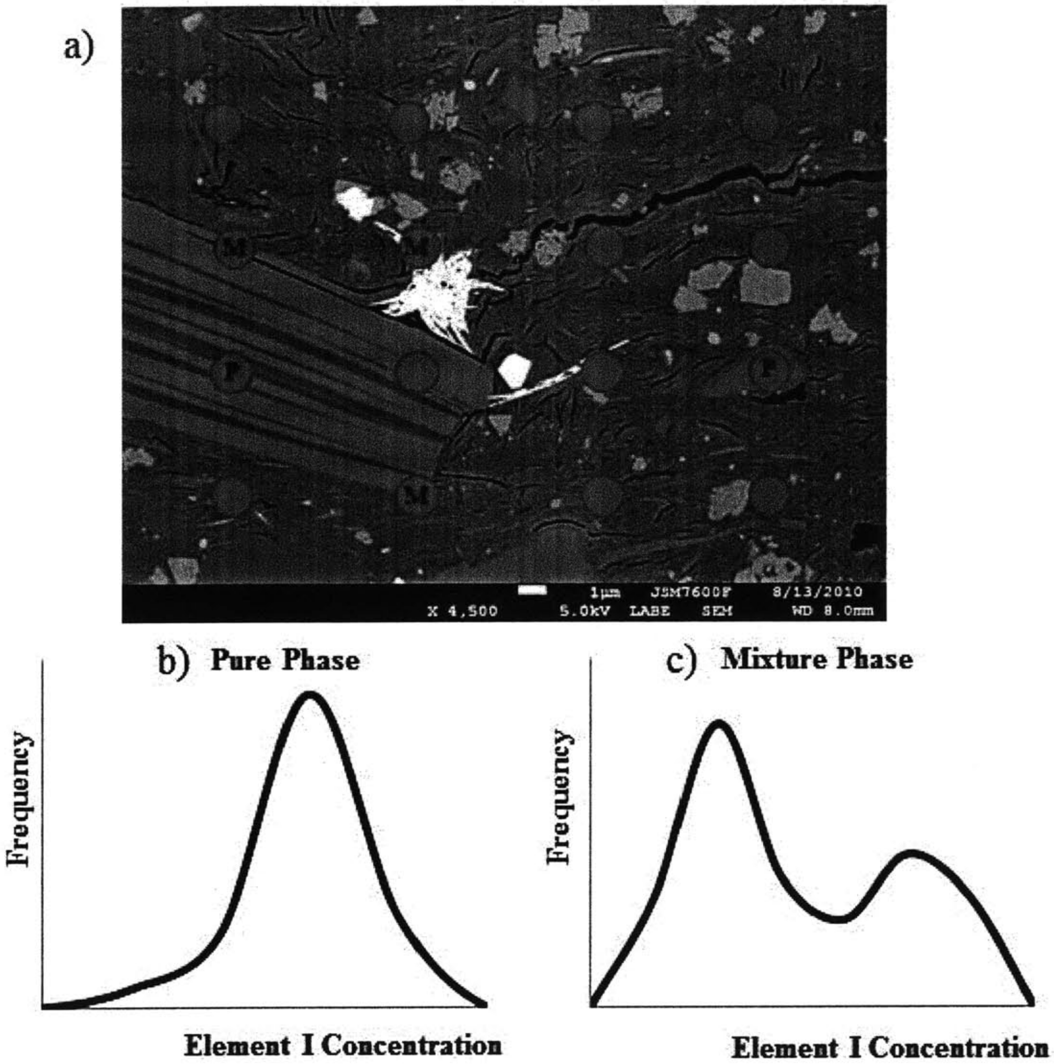

Figure 4-6: a) Schematic of the proposed grid WDS technique showing an array of WDS spot analyses on a heterogeneous material. The background corresponds to a backscattered image of shale S7. The contrast in color intensity corresponds to different chemical composition. The beam of electrons in WDS may probe pure chemical phases (P) or the mixture of more than one phase (M). b) and c) Probability distribution functions of the pure chemical phase and the mixture chemical phase, respectively.

must be much larger than the interaction volume of the WDS test. To avoid sampling effects, a large number of tests N is necessary. Furthermore, to obtain the properties of individual phases, the characteristic size of interaction volume v must be smaller than the length scale of individual phases D. These conditions can be summarized as:

$$v^{1/3} << D << L\sqrt{N} \tag{4.4}$$

4.3.2 Statistical Analysis of WDS Data-Clustering Analysis

Clustering analysis is the automated identification of groups of related observations in a data set. The strength of this technique stems from its ability to determine the number of clusters in a data set and the uncertainty of observations belonging to a cluster based on statistical criteria. In this investigation we apply this technique using the R package Mclust, a contributed package for normal mixture modeling and model-based clustering [13]. It provides functions for model based approaches assuming a variety of data models and implement maximum likelihood estimation and Bayesian criteria to identify the most likely model and the number of clusters. The provided functions in Mclust package identifies the optimal model based on Bayesian criteria (BIC) for Expectation Maximization algorithm (EM) initialized by hierarchical clustering for various parameterization of the Gaussian model [13] [14] [15].

In model-based clustering the data are considered as a mixture density $f(x) = \sum_{k=1}^{G} \tau_k f_k(x)$, where $f_k(x)$ is the probability density function of the observations in group k, and τ_k is the probability that an observation belongs to the k-th component ($\sum_k^G \tau_k = 1$). Each component is usually represented by Gaussian or normal distribution which is characterized by the mean μ_k and the covariance matrix Σ_k with the probability density function:

$$\phi(x_i, \mu_k, \Sigma_k) = \frac{\exp\{-\frac{1}{2}(x_i - \mu_k)^T \sum_k^{-1}(x_i - \mu_k)\}}{\sqrt{\det(2\pi\Sigma_k)}}. \tag{4.5}$$

The likelihood for data consisting of n observations assuming Gaussian mixture model with G components is given by:

$$\prod_{i=1}^{n} \sum_{k=1}^{G} \tau_k \phi(x_i; \mu_k, \sum_k). \tag{4.6}$$

For a fixed number of components G, the model parameters $\tau_{k,}$ μ_k, and Σ_k are estimated via the EM algorithm initialized by hierarchical model based clustering [5]. EM iterates between two steps: the expectations step (E-step), and the maximization step (M-step). In the E-step, matrix z is calculated such that z_{ik} is the conditional probability that reading i belongs to group k given the current parameter estimates. In the M-step, the maximum likelihood of the parameters is estimated given z. Geometric features (shape, volume, orientation) are identified by the covariance matrix Σ_k, which may be parameterized to impose constraints across components. Geometric constraints in multivariate normal mixtures can be imposed through eigenvalue decomposition of the covariance matrix Σ_k in the following form [44]:

$$\Sigma_k = \lambda_k D_k A_k D_k^T \tag{4.7}$$

where D_k is the orthogonal matrix of eigenvectors, A_k is a diagonal matrix whose elements are proportional to the eigenvalues, and λ_k is a constant of proportionality. D_k governs the orientation of the k-th mixture component, while A_k identifies its shape, and λ_k determines its volume which is proportional to λ^d $\det(A_k)$. These parameters (λ_k, D_k, A_k) are considered as independent sets of parameters, and can be constrained to be the same for each component or allowed to vary among components. Various model options are available in R package Mclust. In one dimension, two models are available: E for equal volume and V for varying variance. In more than one dimension, the model identifiers refer to the geometric characteristics of the model. For example, EVI denotes a model in which the volumes of all clusters are equal, the shapes of the clusters are allowed to vary, and the orientation is the identity matrix.

The best model can be identified by fitting models with differing parameterization and/or number of components to the data by maximum likelihood determined by the EM algorithm, and then implementing a statistical criterion for model selection. Mclust uses the Bayesian statistical criterion (BIC) as the model selection criterion. To illustrate the concept of cluster analysis, Figure 4-7 shows an example of clustering results of WDS chemical data.

Experimental Parameters

The main experimental parameters that can be varied during and an EPMA investigation are accelerating voltage, beam current, and coating. Accelerating voltage is by far the most

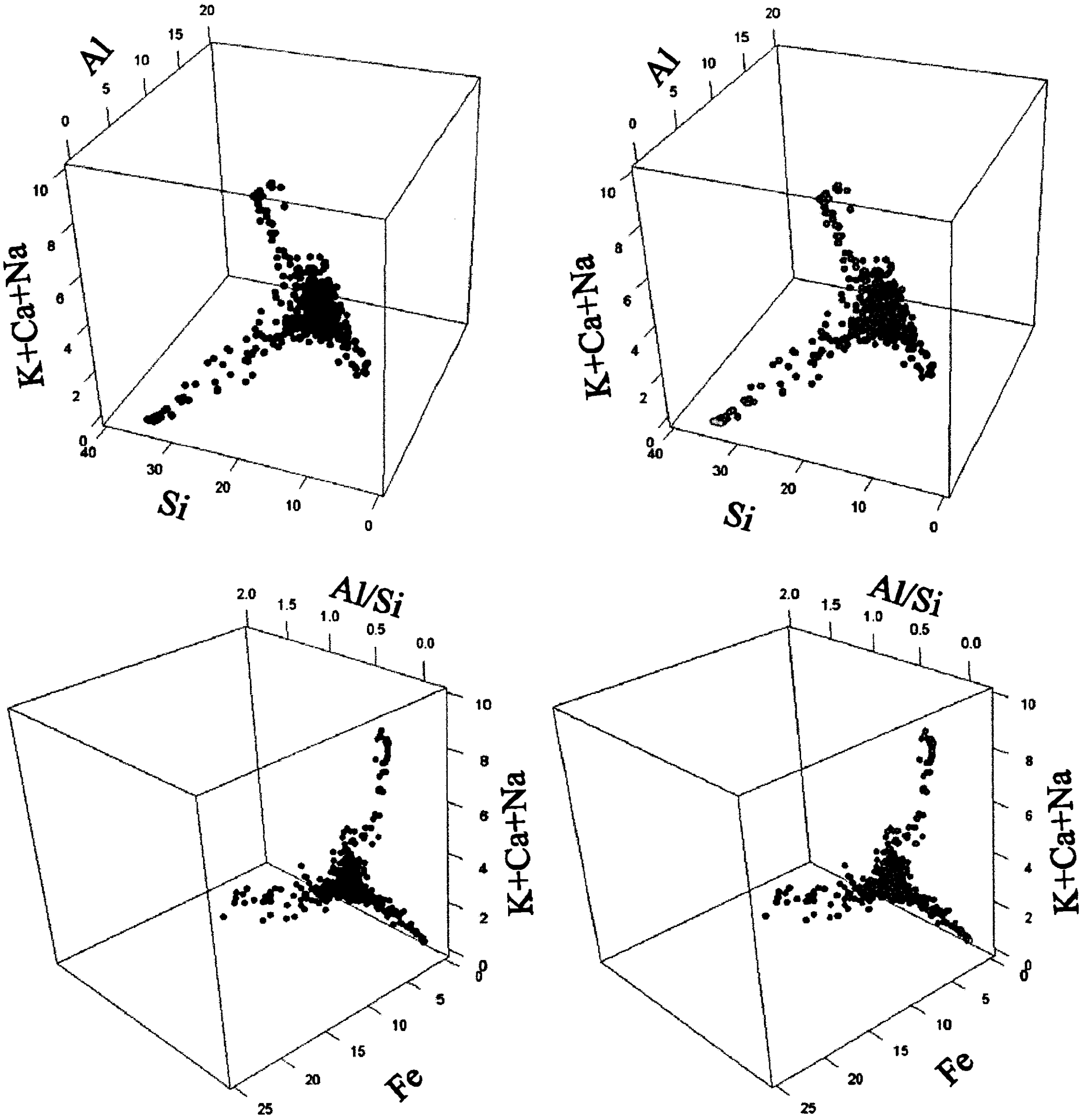

Figure 4-7: Illustration of the cluster analysis applied to WDS chemical data. The data in this figure corresponds to the WDS chemical data before clustering (left) and after clustering (right). Each color corresponds to a different phase identified by the cluster analysis.

important parameter since it controls the probed volume of material (volume of interaction) by EPMA. Increasing the accelerating voltage increases the interaction volume. Hence, the choice of accelerating voltage defines the scale of measurements in EPMA. The accelerating voltage is limited by the critical excitation energy, and must be high enough to excite the characteristic X-rays of the elements of interest. To satisfy this condition, an accelerating voltage of around 2 times the critical excitation energy is recommended [66]. For example, iron with a critical excitation energy of 7.1 keV for the Kα shell, requires an accelerating voltage approximately 15 kV [6] [66]. Since shale materials may contain iron, an accelerating voltage less than 15 kV may underestimates iron and produce unreasonable chemical data. Operating at high accelerating voltage, on the other hand, increases the X-ray intensities and peak to background ratios, which improves the experimental conditions; however, at the expense of increasing the spatial resolution. For these reasons, the accelerating voltage adopted in this study is 15 kV.

To find the volume of interaction associated with the chosen accelerating voltage (15 kV), Monte Carlo (MC) simulation of a WDS experiment was performed using CASINO [19]. The average density for the simulated shale material is around 2.55 g/cm^3 (see Table 3.2). Figure 4-8 displays a cross-section of the material and the computed electron trajectories. The MC simulation shows an interaction volume of approximately 2 μm. Interaction volume is an important parameter since only minerals with characteristic size larger than the interaction volume can be identified by WDS. As the size of clay minerals is less than two microns, it is not possible to resolve individual clay minerals. Instead, the WDS technique measures an on-average composition of clay minerals.

Beam current is less important and varying this parameter does not affect measurements significantly. Increasing the beam current gives high X-ray intensities; however, the extent to which the beam current can be increased is limited by sample damage. For instance, high beam current may heat up the sample causing the loss of carbon dioxide from carbonates and water from hydrous minerals [66] [45]. In WDS analysis, a current in the range 10–100 nA is reasonable for most materials. In this study we use a beam current of 10 nA.

Coating is another experimental parameter that needs consideration. Coating is necessary to prevent electrical charge built-up of the specimen during electron bombardment; however, the measured X-rays are affected by coating. Coating reduces X-ray intensities since incident

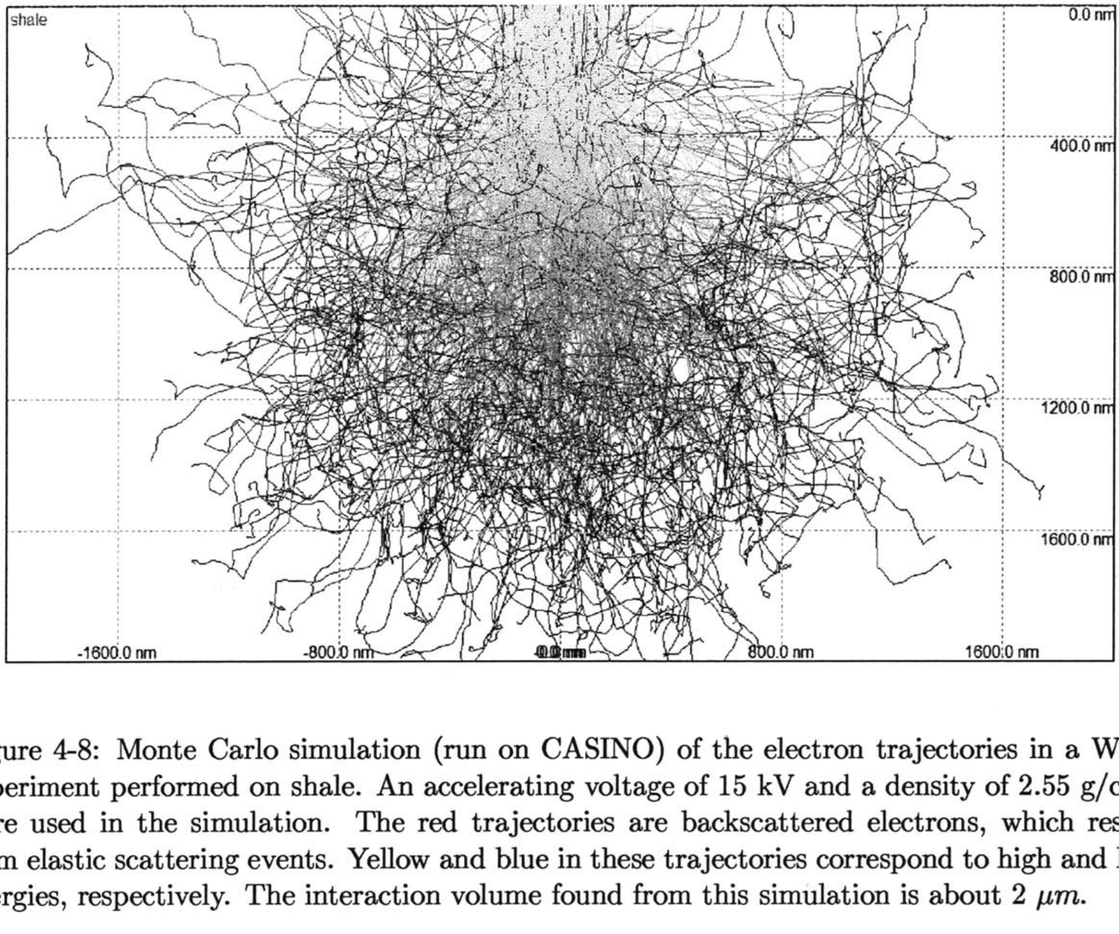

Figure 4-8: Monte Carlo simulation (run on CASINO) of the electron trajectories in a WDS experiment performed on shale. An accelerating voltage of 15 kV and a density of 2.55 g/cm^3 were used in the simulation. The red trajectories are backscattered electrons, which result from elastic scattering events. Yellow and blue in these trajectories correspond to high and low energies, respectively. The interaction volume found from this simulation is about 2 μm.

electrons lose energy when passing through the coating, and X-rays are attenuated within the coating film [66] [45]. For X-ray measurements, carbon coating is commonly used in EPMA testing since it has minimal effects on the emitted X-rays [66] [45]. Coating thickness must be optimized in order to obtain maximum information from the specimen. Too thick coating obscures sample details, while too thin coating may not prevent charge built up. Coating thickness of 20 nm is optimum for x-ray measurements [66]. For this reason, shale samples were coated with a 20 nm layer of carbon.

4.3.3 WDS Data Processing

Once the sample is ready for testing, it is mounted in the EPMA chamber, which is subsequently pumped to create vacuum. The surface of the sample is then scanned under the backscattered electron mode to choose a surface suitable for testing. Once the surface is chosen, the x, y, and z coordinates are generated for the WDS grid with a specific size (number of points and spacing). The z is the focus distance, an important parameter in obtaining a consistent WDS signal. The focus distance is usually calculated for the first point and assumed constant for the rest. For this reason, a flat surface is necessary to ensure that the variations in the focus distance is minimal and will not affect the measurements.

In WDS testing, each element is assigned to a crystal-detector. Since the particular machine that we use in this study has 5 detectors, only five elements can be measured simultaneously in one run. Hence, for the ten elements we measure, two runs are required. The test is run and x-ray intensities are collected by the WDS detector. Quantification of the WDS results is then performed on the computer attached to the EPMA and the results are output as weight percentages of the measured elements as shown in Table 4.1.

Analysis total is an important experimental parameter that requires careful considerations. It represents the sum of elements weight percents in each spot and must be close to 100 percent. In practice, however, the WDS technique deviates from the given mark due to several reasons: the presence of water, an element not included in the analyses, surface roughness, or deviations from the analytical conditions because of instrumental error. The elements used in this analysis insure that all elements that exist in shale are analyzed for, except carbon and hydrogen. Carbon cannot be measured since the samples are carbon-coated. Hydrogen, on the other hand, is a

Spot No.	Al	O	P	Fe	Na	Si	S	Mg	Ca	K	Analysis total
1	12.13	48.12	0.04	5.20	0.91	24.80	0.01	1.28	0.05	3.06	95.59
2	5.47	35.76	0.02	40.37	0.84	11.84	0.03	1.41	0.05	0.82	96.60
3	9.97	48.25	0.07	2.54	5.84	28.64	0.00	0.44	0.35	1.05	97.15
4	10.77	51.44	0.01	7.73	0.77	24.72	0.03	1.31	0.07	3.21	100.06
5	10.36	47.43	0.01	6.61	1.00	25.77	0.00	1.62	0.02	2.84	95.65
6	9.11	49.07	0.00	6.10	0.70	28.28	0.00	1.23	0.02	2.40	96.91
7	10.72	50.88	0.02	5.87	0.77	24.85	0.00	1.81	0.02	3.28	98.22
8	8.46	50.35	0.00	5.78	1.43	28.84	0.00	1.23	0.04	2.09	98.23
9	10.54	51.46	0.00	5.75	1.11	26.94	0.00	1.32	0.08	3.21	100.41
10	9.92	45.91	0.03	6.55	1.01	26.46	0.01	1.34	0.06	2.85	94.13

Table 4.1: Typical WDS spot analysis results for a shale sample. The data is presented in the form of weight percentage of each element.

light element for which special capabilities of EPMA are required. Hence, the analysis total for clay minerals is expected to be less than 100 as they contain water. Furthermore, carbonates which contain large amounts of carbon, are expected to have as low analysis totals as 60 %. Special care must be given when filtering the data to make sure that no mineral is excluded. In this study, filtering of the data is done based on whether the sample contains carbonates or not. If carbonates are found in the sample, the threshold limit, that is the analysis total below which the data is discarded, is set to 60 %, otherwise, the threshold limit is set to 80 %. The presence of carbonates can be easily found by looking at the elemental concentrations of Ca, Mg, and Fe. Another reason for low analysis total results from the assumption that Fe is divalent when it is trivalent [66]. An attempt to predict the amount of Fe^{3+} based on ratios published in the literature has not been made, since such a step complicates data analysis rather than simplifying it. Another issue related to analysis total is its large variability, particularly in clay minerals. This is an expected trend, since the ZAF correction applied to the measured X-ray intensities assumes homogeneous composition over the interaction volume. This condition is violated if composite composition or clay minerals are measured.

Chemical Data Interpretation

Multivariate cluster analysis is used to analyze the chemical data obtained through grid WDS technique. The clustering algorithm presented in section 4.3.2 helps through cluster modeling in synthesizing a large data set to a reduced number of components, which are clustered based

Spot No.	Al	O	P	Fe	Na	Si	S	Mg	Ca	K
1	9.76	65.29	0.02	2.02	0.86	19.17	0.00	1.14	0.03	1.70
2	5.48	60.40	0.01	19.54	0.99	11.39	0.03	1.57	0.03	0.56
3	7.76	63.35	0.05	0.96	5.34	21.42	0.00	0.38	0.18	0.56
4	8.31	66.91	0.01	2.88	0.70	18.32	0.02	1.12	0.03	1.71
5	8.41	64.90	0.01	2.59	0.95	20.09	0.00	1.46	0.01	1.59
6	7.24	65.76	0.00	2.34	0.65	21.59	0.00	1.09	0.01	1.32
7	8.35	66.80	0.01	2.21	0.71	18.59	0.00	1.56	0.01	1.76
8	6.59	66.14	0.00	2.18	1.31	21.58	0.00	1.06	0.02	1.12
9	8.04	66.24	0.00	2.12	0.99	19.75	0.00	1.12	0.04	1.69
10	8.22	64.18	0.02	2.62	0.98	21.07	0.01	1.23	0.03	1.63

Table 4.2: Atomic ratios of the elements presented in Table 4.1 .

on their chemical signature. For the implementation for shale materials, atomic ratios of the collected elements are employed instead of elemental mass concentrations. The atomic ratio representation provides more contrast between phases , making the identification of shale chemistry through cluster modeling viable. Table 4.2 shows an example of atomic ratio calculations for the chemical data reported in Table 4.1. The elements used in WDS testing must be carefully chosen to represent all minerals that may exist in the material of interest. The elements suitable for the characterization of shales are Si, Al, Fe, K, Mg, Ca, Na, S. This set of elements covers the major and minor minerals that can be found in shale, and provides the sufficient contrast between chemical phases. Cluster analysis involves a set of mathematical procedures that aims at classifying the data into chemical phases with similar composition. Each chemical test is represented as a point in a multidimensional space with the base dimensions being the atomic ratios of elements. Thus, points with different compositions will be located in different regions in this space, while points with similar composition will be located in a particular region (see Figure 4-7)

The chemical composition of common minerals known to be present in shale aids in interpreting the results of EPMA testing and cluster analysis (see Section 2.1). Table 4.3 reports the chemical composition of the non-clay minerals, presented in terms of chemical formulas and atomic ratios of important elements. Different elemental projections can be used to provide a visual interpretation of the data analysis. These projections must be carefully designed to deliver the required information. In the case of silicates such as quartz, feldspar and clay minerals, the projections in the space Al–Si and Al/Si–K+Ca+Na are found to be useful, as shown

Mineral	Chemical formula	Si	Al	Al/Si	Ca+Na+K
Quartz	SiO_2	33.33	0		0
Alkali feldspars	$(Na,K)AlSi_3O_8$	23	7.7	0.33	7.7
Plagioclase feldspar	$NaAlSi_3O_8$ - $CaAl2Si_2O_8$	23 - 15.4	7.7 - 15.4	0.33 - 1	7.7
Mineral	Chemical formula	Ca	Mg	Fe	
Calcite	$CaCO_3$	20	0	0	
Magnesite	$MgCO_3$	0	20	0	
Siderite	$FeCO_3$	0	0	20	
Dolomite	$CaMg(CO_3)_2$	10	10	0	

Table 4.3: Chemical composition of non-clay minerals expressed through chemical formulas and atomic ratios of elements. Atomic ratios provide sufficient contrast between different minerals.

in Figure 4-9. The Al–Si space mainly helps in locating quartz phases. The Al/Si–K+Ca+Na space provides the necessary contrast between quartz, feldspar and clay minerals. The rationale behind using the summation of elements K, Na, and Ca is that they add up to a specific value (7.7 in the atomic ratios representation) in the case of feldspars, and appear in variable amounts for clay minerals. The use of Ca, Mg, and Fe elements is helpful to characterize carbonates minerals. Figure 4-9 shows two projections that can be used for the analysis of carbonates: Ca–Mg, and Fe–Si. The former representation shows the the regions of calcite, magnesite, and dolomite; the latter marks the location of siderite and hematite.

Clay minerals pose major challenges in the application of grid WDS technique. The state-of-the-art of EPMA experiment cannot be used to study compositional variations across the small clay flakes, given that their characteristic size is less than the interaction volume probed by the experiment. Furthermore, the actual composition of clay minerals in rocks deviates from the ideal compositions reported in the literature as discussed in Section 2.1.1. For these reasons, the chemical compositions of clay minerals reported in Section 2.1.1 are considered to aid in identifying the signature of clays and their variability in the proposed atomic ratio projections. The atomic ratios are first calculated using the chemical information provided in Tables 2.3 through 2.21. The data is displayed in the projections adopted for silicates; Si–Al and Al/Si–Ca+K+Na as shown in Figures 4-10 through 4-13 for the different types of clay minerals. Figure 4-15 synthesizes the data provided in Figures 4-10 through 4-13 , showing the particular regions associated with each mineral. From the information presented graphically

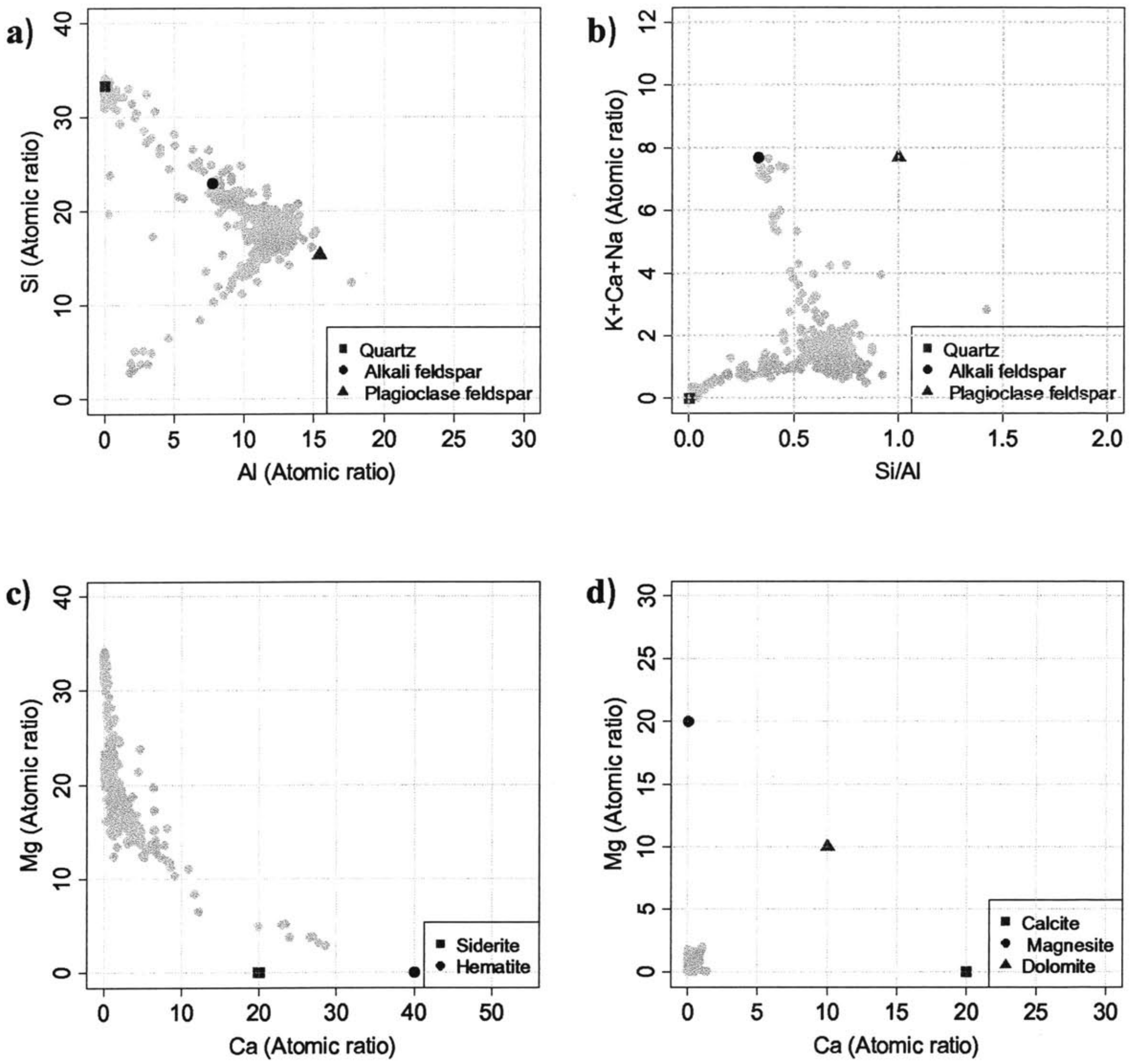

Figure 4-9: Elemental projections used to provide a visual interpretation for the results of cluster analysis of WDS chemical data. a) and b) are the projections used to discriminate between quartz, feldspars, and clay minerals. c) and d) are the projections used to discriminate between different carbonate minerals such as calcite, magnesite, dolomite, and siderite.

in Figure 4-15, all clay minerals types present in shale display a broad chemical signature in the chosen atomic ratio representation. Less tractable differences are inferred from projections based on elemental mass concentrations. To further reduce complexity, Figure 4-15 represents the chemical composition of the most common clay minerals encountered in sedimentary rocks. As presented in Section 2.1.1 , the most common clays in sedimentary rocks, given in the order of relative abundance, are: illite, montmorillonite, mixed-layer illite-montmorillonite, chlorite and kaolinite [12]. The data presented in this section , in particular the information in Figure 4-16, will assist in the analysis and interpretation of the results of cluster analysis.

4.3.4 Sample Application of Grid WDS to Shale

The previous section outlines the analysis and interpretation of grid WDS data. This procedure is illustrated in detail in this section using as a reference the results of experiment S7-b. This experiment was performed over a grid of 1 mm× 1 mm. Figures 4-17 and 4-18 display the cluster analysis results of experiment S7-b. Tables 6.4 and 6.5 provide the detailed numerical description of the results. From these sample results, we can identify two visible types of features in the projections of clustered WDS data: poles and ligands.

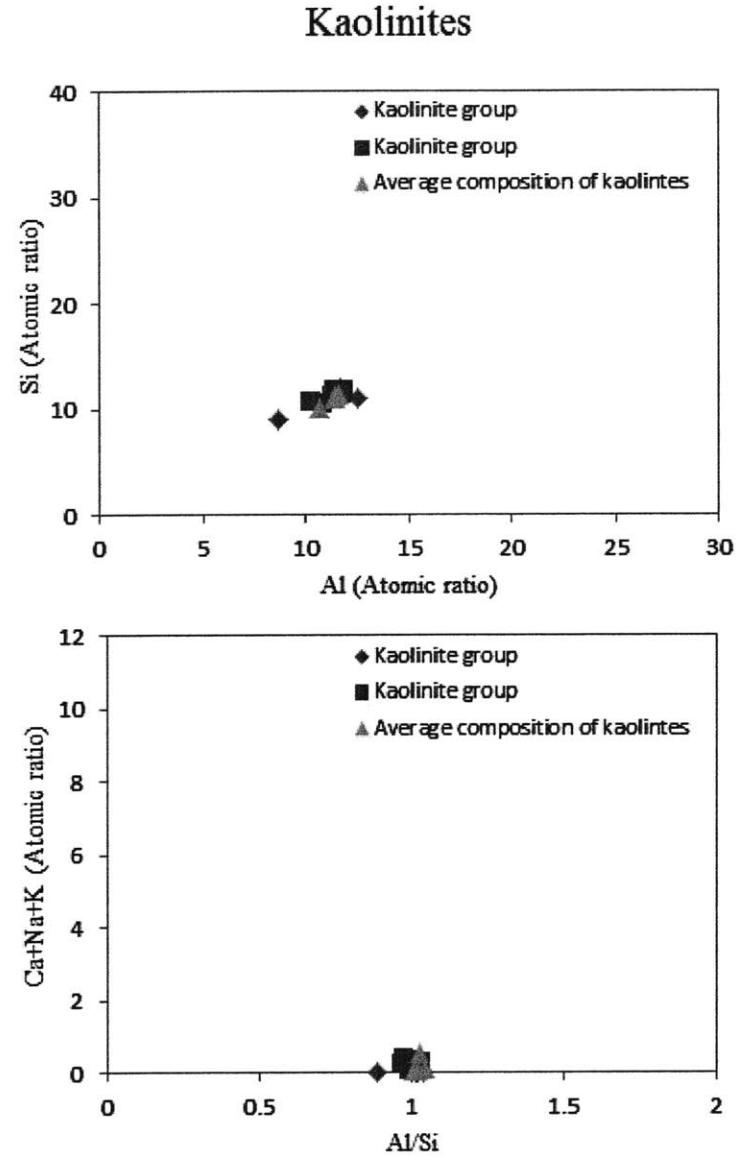

Figure 4-10: Atomic ratios of kaolintes based on the chemical analyses reported in Tables 2.3 through 2.5. The data are displayed on the adopted projections for clay minerals: (top) Al–Si and (bottom) Al/Si–K+Ca+Na.

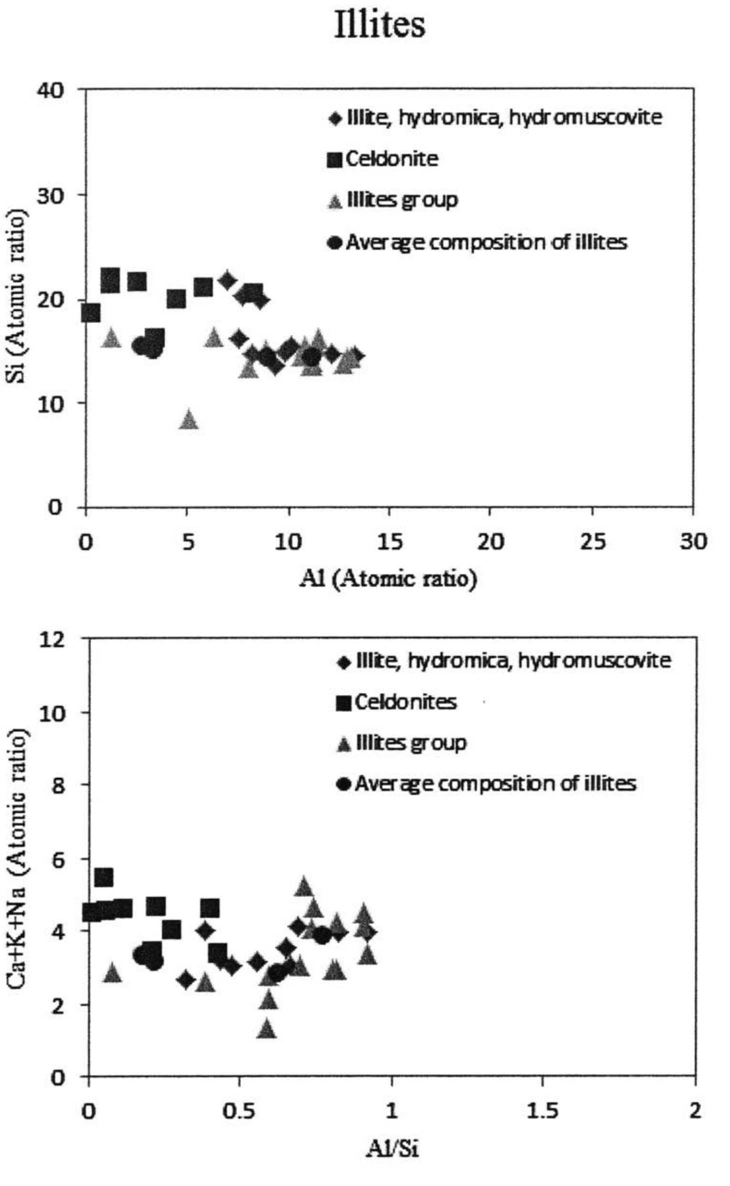

Figure 4-11: Atomic ratios of illites chemical analyses reported in Tables 2.6 through 2.9. The data is displayed on the adopted projections for clay minerals: (top) Al–Si and (bottom) Al/Si–K+Ca+Na.

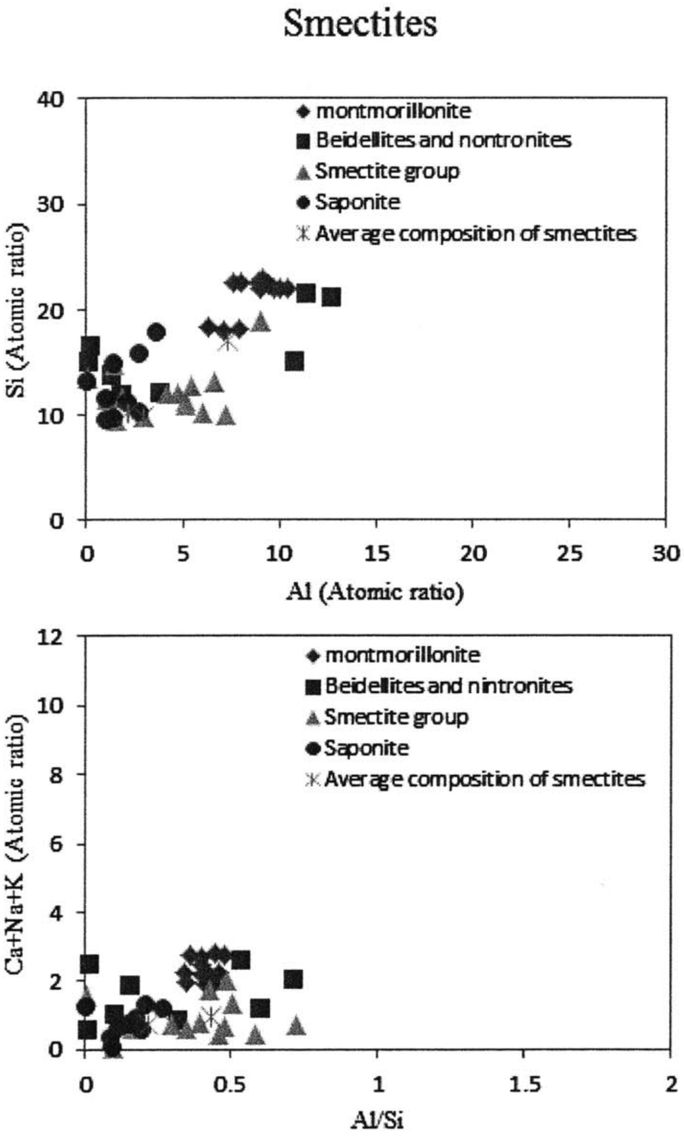

Figure 4-12: Atomic ratios of smectites based on the chemical analyses reported in Tables 2.11 through 2.15. The data are displayed on the adopted projections for clay minerals: (top) Al–Si and (bottom) Al/Si–K+Ca+Na.

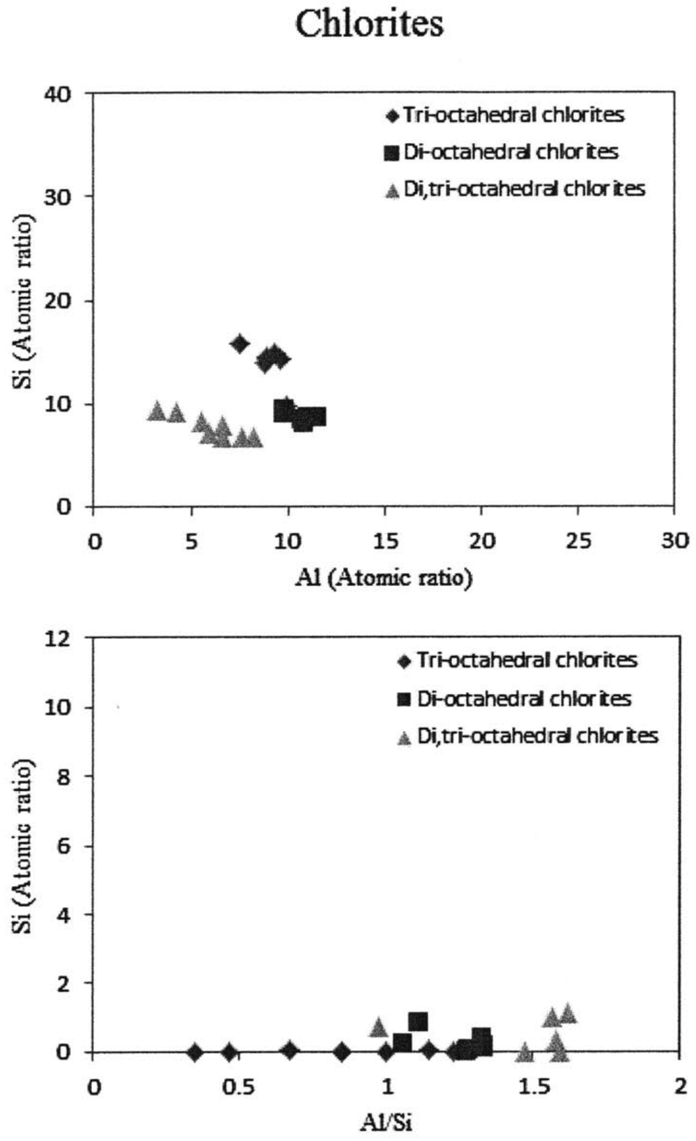

Figure 4-13: Atomic ratios of chlorites based on the chemical analyses reported in Tables 2.16 through 2.18. The data are displayed on the adopted projections for clay minerals: (top) Al–Si and (bottom) Al/Si–K+Ca+Na.

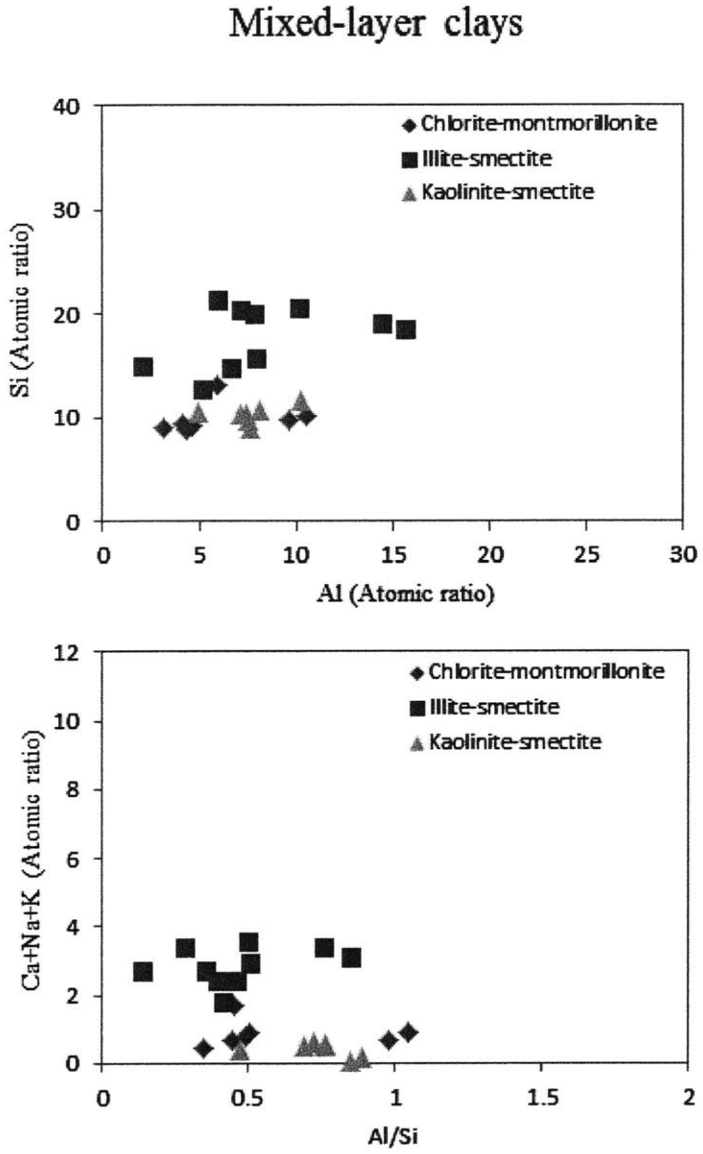

Figure 4-14: Atomic ratios of mixed-layer clays based on the chemical analyses reported in Tables 2.19 through 2.21. The data are displayed on the adopted projections for clay minerals: (top) Al–Si and (bottom) Al/Si–K+Ca+Na.

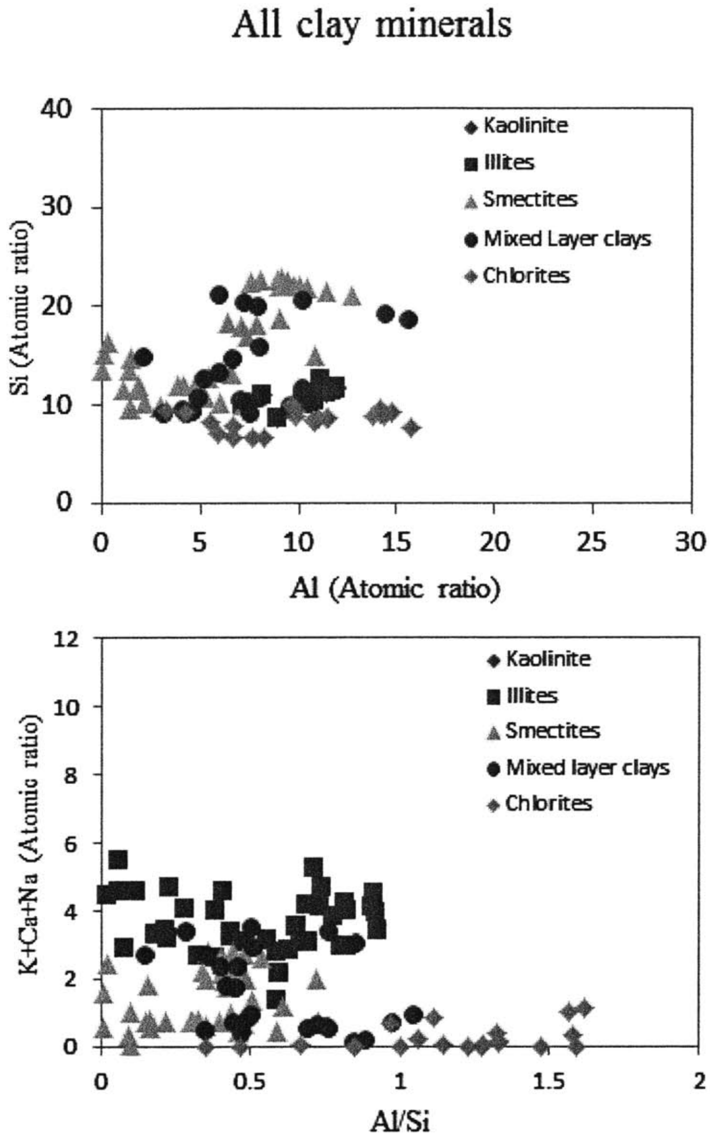

Figure 4-15: Atomic ratios of clay minerals based on the chemical analyses reported in Figures 4-10 through 4-14. This figure shows that clay minerals types present in shale display a broad chemical signatures in the chosen atomic ratio representation: (top) Al–Si and (bottom) Al/Si–K+Ca+Na.

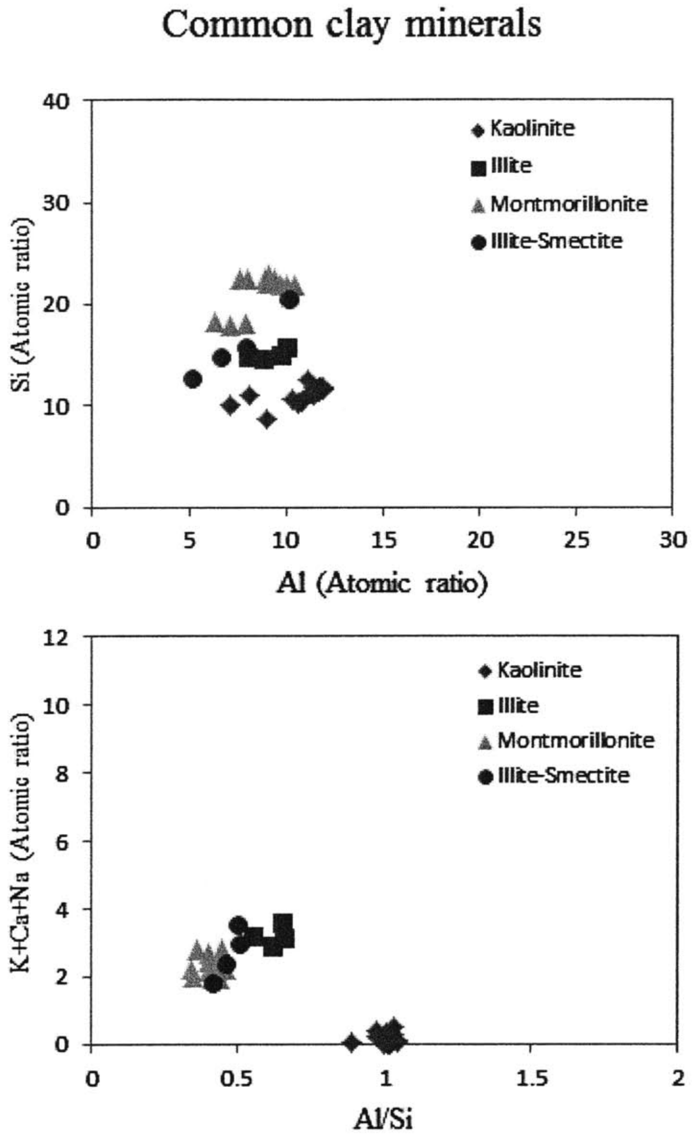

Figure 4-16: Atomic ratios of the most common clay minerals encountered in sedimentary rocks. This chemical data was derived from Figures 4-10 through 4-14 and displayed on the adopted projections for clay minerals: (top) Al–Si and (bottom) Al/Si–K+Ca+Na.

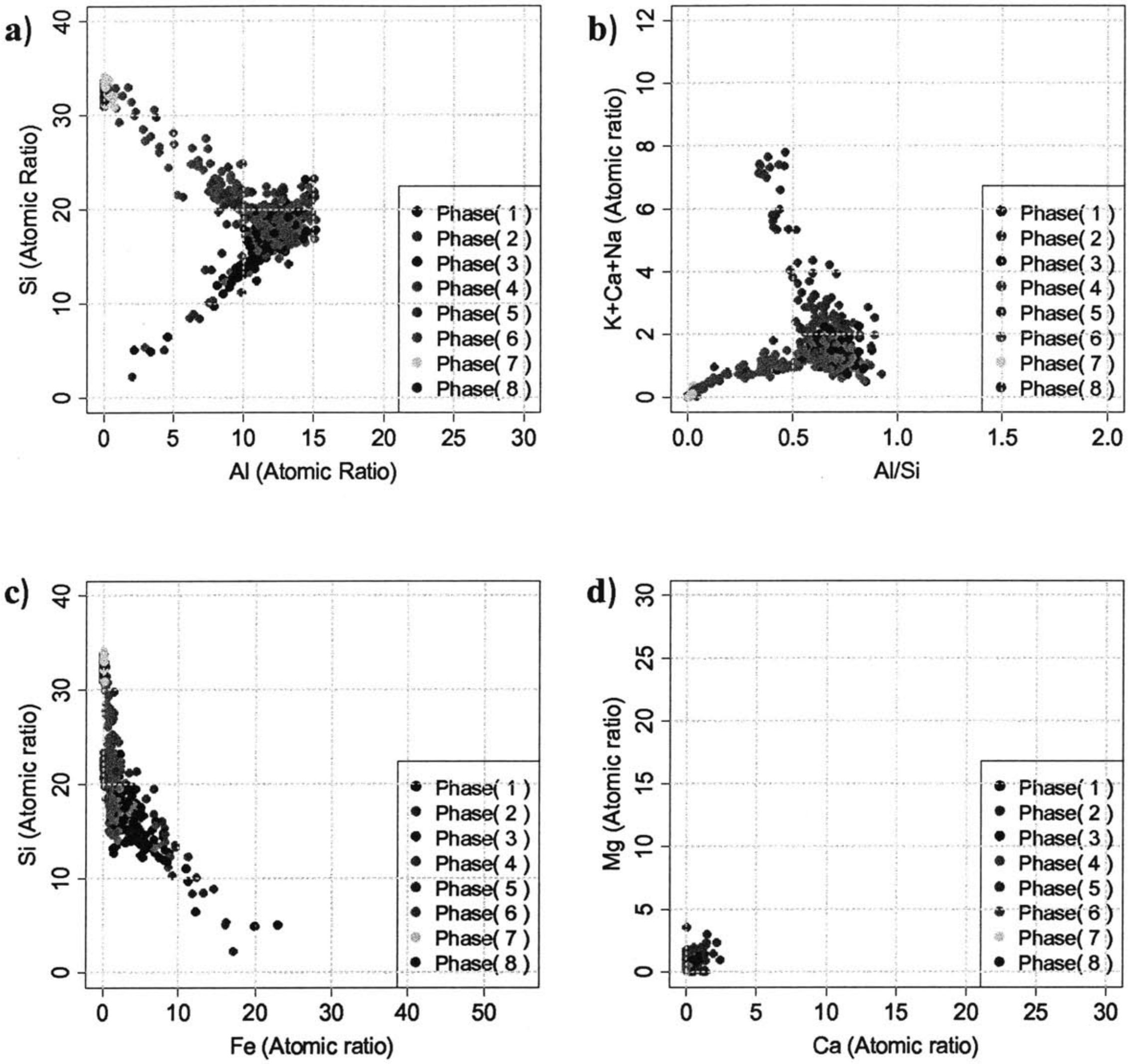

Figure 4-17: Multivariate cluster analysis of the grid WDS data for experiment S7-b. The identified phases are presented on 2-D projections for visual interpretation of the data: a) Al-Si space and b) Ca+Na+K-Al/Si space separate quartz, feldspars, and clay minerals. c) Fe-Si space and d) Ca-Mg space separate carbonate minerals; siderite, calcite, magnesite, ankerite, and dolomite.

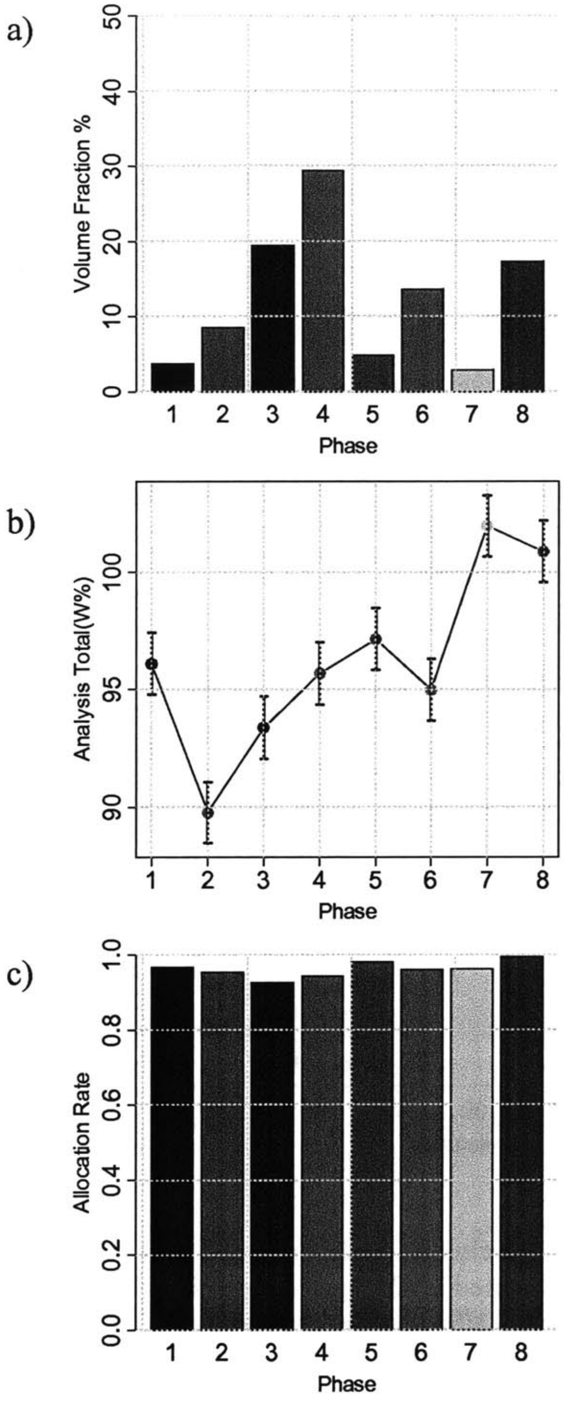

Figure 4-18: Graphical representation of clustering results presented in Table 6.5 for experiment S7-b. a) volume fractions, b) mean and standard deviation values of the analysis totals, and c) allocation rates for each of the phases displayed in Figure 4-17.

Phase		1	2	3	4	5	6	7	8
Si	μ	15.36	16.30	16.89	18.02	21.16	21.52	32.78	32.82
	σ	3.65	3.81	1.96	1.14	2.66	4.04	0.79	0.66
Al	μ	11.12	10.94	11.91	12.63	9.64	9.78	0.24	0.02
	σ	2.80	2.40	1.20	0.81	2.51	3.54	0.24	0.01
K	μ	0.53	0.99	0.58	0.67	1.92	0.47	0.01	0.00
	σ	0.23	0.76	0.12	0.19	2.30	0.19	0.01	0.00
Ca	μ	0.20	0.43	0.26	0.06	0.22	0.08	0.00	0.00
	σ	0.25	0.52	0.19	0.03	0.34	0.05	0.01	0.00
Na	μ	0.65	0.76	0.68	0.62	2.10	0.60	0.04	0.01
	σ	0.15	0.30	0.17	0.13	2.24	0.27	0.07	0.01
Fe	μ	4.52	4.42	2.99	1.41	1.00	1.39	0.08	0.02
	σ	4.94	4.01	1.55	0.24	0.87	0.58	0.03	0.02
Mg	μ	0.62	1.11	0.76	0.57	0.31	0.47	0.01	0.00
	σ	0.32	0.61	0.20	0.12	0.25	0.19	0.01	0.00

Table 4.4: Summary of the make up of chemical phases identified by cluster analysis for experiment S7-b. The notations μ and σ correspond to the mean and standard deviation of the given property. The standard deviation corresponds to the square root of the variance.

Phase	1	2	3	4	5	6	7	8
Volume fraction (%)	3.80	8.60	19.41	29.30	4.94	13.64	2.96	17.35
Analysis total μ	96.11	89.75	93.37	95.69	97.14	94.98	101.97	100.88
Analysis total σ	1.32	1.32	1.32	1.32	1.32	1.32	1.32	1.32
Allocation	0.97	0.95	0.93	0.94	0.98	0.96	0.96	0.99

Table 4.5: Volume fractions, analysis totals, and allocation rates for the chemical phases identified by cluster analysis for experiment S7-b. The notation σ corresponds to the standard deviation of the given property.

Poles

A pole represents a component with relatively small standard deviation; that is an intense clustering of data points around a mean position. The pole is interpreted as an approximately homogeneous phase, and defines composition and volume fraction of this phase. In Figure 4-17, the phases identified as poles are 1, 3, 4, 7 and 8. Referring to Figure 4-9, which shows the regions of non-clay minerals on the relevant projections, we note that phases 7 and 8 are situated in the region expected for quartz, for which reason we identify them as quartz phases. The silicon content of these components (Si = 32.78 and 32.82, respectively) is very close to the ideal composition of quartz (Si = 33.33), and their volume fractions are 2.96 and 17.36 percent, respectively. Phases 1, 3, and 4, however, are located in the region expected for clay minerals (e.g., Figure 4-15), hence, we interpret them as clay minerals phases. It is worth noting that clay minerals are far from being homogeneous which may be taken to contradict our definition of the pole. However, if we remind ourselves that the characteristic size of clay minerals is less than the interaction volume, we note that WDS probes the on-average composition of clay minerals which is homogenous at the scale of our measurements (2 μm).Few points of the clay cloud (Figure 4-17) show tendency towards kaolinite composition (Al/ Si = 1). This indicates the presence of pure kaolinite minerals with sizes larger than the interaction volume, which is not peculiar since kaolinite is known for its large size that can exceed two microns [47]. Analysis total can further help solidifying the above conclusions. Analysis total less than 100 % could be due to missing elements or due to experimental issues. We note that clay phases exhibit lower analysis totals (around 95 %) compared to the quartz phases (around 100 %). This difference in behavior is attributed to hydrogen element present in clay minerals in the form of water or OH^-. Hydrogen is not measured in the WDS experiments because its low atomic number is outside the range of resolution of EPMA equipment. Consequently, the clay-like phases consistently displays lower yield totals compared to the quartz phases.

Ligands

A ligand, which approximates a straight line between two compositions, is a component that represents a mixture between two phases. These components can be identified visually as a component spans between two anchor points. The composition of these anchor points can be identified based on knowledge of the chemical phases which are found in the sample. This can either come from the identification of poles (as discussed above) or the knowledge of the stoichiometry of the phases present in the sample. Referring to Figure 4-17 the following components are identified as ligands:

- Component 6 represents a mixture of quartz (Si = 33.33) and clay minerals.
- Component 2 represents a mixture of siderite (Fe = 20) and clay minerals.
- Component 5 represents a mixture of feldspar (K+Ca+Na = 7.7) and clay minerals.

In the above cases, we identified clay minerals based on the discussion above. A discussion of the mixture phases is discussed below.

Mixture Phases

To explain the concept of mixture phases, consider a hypothetical sample that contains two phases: phase I and phase II. Statistically speaking, a beam of electrons in WDS moving with no guidance, may sample phase I, phase II, or both (see Figure 4-6). The latter case results in what we call a mixture phase. The composition of mixture phases probed by WDS can be considered as a linear combination of the compositions of the individual components; i.e., phase I and Phase II. Consider an element X measured by WDS, the concentration of X can be expressed as:

$$X_{mix} = \lambda X_I + (1 - \lambda) X_{II} \tag{4.8}$$

where λ is the proportion of phase I in the mix, X_{mix} is the measured concentration of element X by WDS, X_I and X_{II} are the concentrations of element X in phases I and II, respectively. Given that the composition of the chemical components in the sample is known, the analysis of the mixture phases reduces to finding λ.

Applying the above mixture model to shale is challenging due to its heterogenous nature. First, we assume that each mixture phase is a mixture of two phases only. Referring to Figure 4-17, we note that all mixture phases represent a mixture of clay and other non-clay minerals; quartz, feldspar, and siderite. This behavior is expected since shale is composed of a dominant clay phase and other less abundant inclusions, such as quartz, feldspar, and carbonates. Second, the element used in the analysis of the mixture phases, X in equation 4.8, must be carefully chosen to provide sufficient contrast between phases that are part of the mix. For quartz mixture phases (phase 6 in Figure 4-17), the element silicon, with atomic ratios that range from 33.33 for quartz to around 18 for clay minerals, provides the sufficient contrast for phase separation. Similarly, for siderite mixture phases (phase 2 in Figure 4-17), the element iron, with atomic ratios that range from 20 for siderite to around 2 for clays, provides the required contrast between phases. In the case of feldspars, however, the use of either silicon or aluminum in the mixture analysis does not deliver the required results, as these elements are present in both clay and feldspar minerals in comparable amounts. Instead, the combination K+Ca+Na, with atomic ratios that range from 7.7 for feldspars to around 2 for clays, proves to be helpful as they provide the sufficient contrast for phase separation.

Next, we illustrate the analysis of mixture phases using as a reference the quartz mixture phase (phase 6 in Figure 4-17). Applying the above mixture model on quartz, equation 4.8 can be written as follows:

$$\mathrm{Si}_{mix} = \lambda\, \mathrm{Si}_q + (1-\lambda)\, \mathrm{Si}_c \tag{4.9}$$

where λ is the proportion of quartz in the mix, Si_q and Si_c are the atomic ratios of Si in quartz and clay, respectively. While Si_q can be readily calculated from quartz composition as 33.33, the determination of Si_c is challenging given the chemical variability of clay minerals. This value is obtained form the weighted average of silicon in clay phases identified in the cluster analysis; namely phases 1, 3, and 4 in Figure 4-17. The above can be summarized by the following formula:

$$\mathrm{Si}_c = \mathrm{Si}_i\, \mathrm{V}_i \tag{4.10}$$

where Si_i and V_i are the silicon content and volume fraction of phase i, that are identified as clay phases. Following the above procedure, the λ values are calculated for each point in the quartz mixture phase. Figure 4-19a shows the distribution of λ values for the quartz mixture phase (phase 6 in 4-17). The calculated λ values are then clustered using the Mclust algorithm in which one variable was used in this case, λ. Two components are found to fit the data as shown in Figure 4-19a. The interpretation of the λ clustering results is similar to that of the multivariate results; narrow peaks are poles which we interpret as materials of relatively homogeneous composition. Flat curves are ligands and correspond to disordered mixing of the two phases. Finally, the pure quartz and clay proportions of the mixture phase are separated according to the following formula:

$$V_q = \lambda_i v_{f,i} \tag{4.11}$$

$$V_c = (1-\lambda_i) v_{f,i} \tag{4.12}$$

where V_q and V_c are the pure volume fractions of quartz and clays, respectively. λ_i and $v_{f,i}$ are the mean value and the volume fraction of component i identified in the clustering of $\lambda-$values. Similarly, other mixture phases are analyzed using the same procedure. Table 4.6 shows the mixture analysis results for the mixture phases identified for sample S7-b.

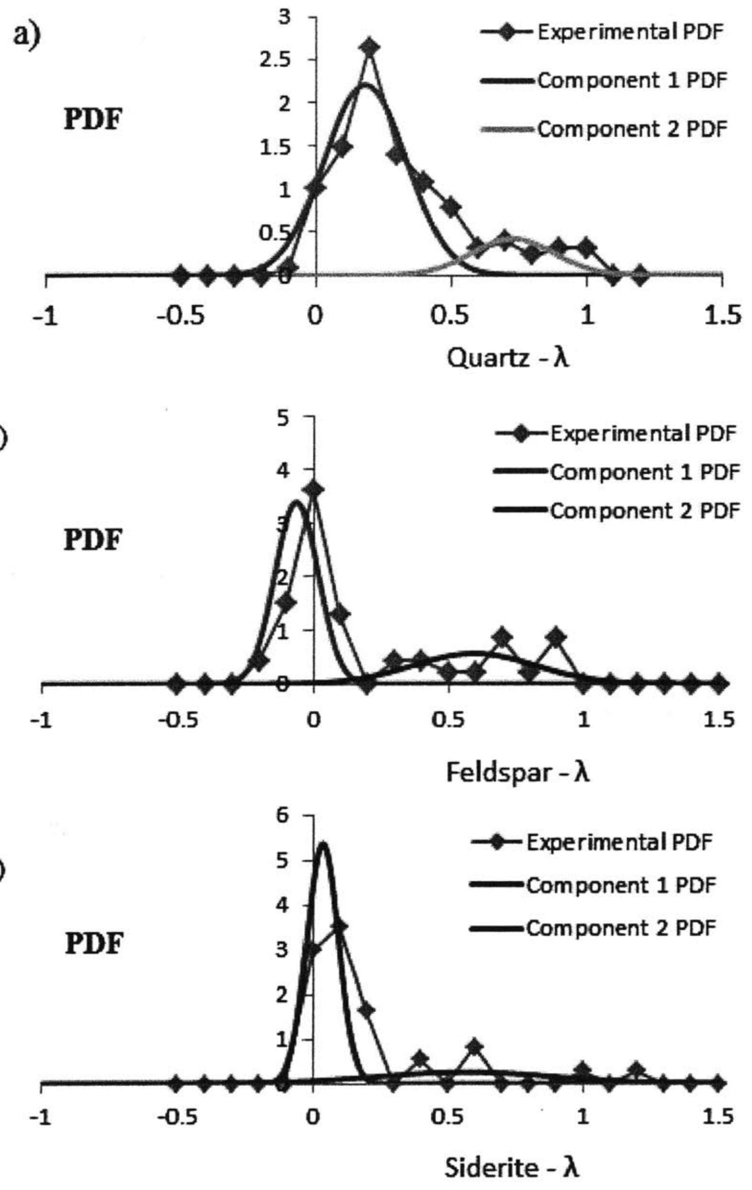

Figure 4-19: The distribution of λ values found in the analysis of the mixture phases of sample S7-b. The λ values were clustered using the Mclust algorithm to find the proportions of each phase involved in the mixture. a) quartz mixture analysis, b) feldspar mixture analysis, c) siderite mixture analysis.

Mixture phase	Component 1 λ_1	 $v_{f,1}$	Component 2 λ_2	 $v_{f,2}$
Quartz mixture	0.18	0.84	0.72	0.16
Feldspar mixture	-0.06	0.68	0.59	0.32
Siderite	0.04	0.78	0.56	0.22
Mixture phase	**Quartz**	**Feldspar**	**Siderite**	**Clay**
Quartz mixture	0.27			0.73
Feldspar mixture		0.19		0.81
Siderite			0.15	0.85

Table 4.6: Results of the analysis of mixture phases for sample S7-b. This table displays the clustering results and the calculated volume fractions of each of the phases involved in the mixture.

4.4 Chapter Summary

The tools presented in this chapter provide a methodology for accessing and interpreting compositional information of shale materials. This chapter began with an introduction of the experimental technique which we employed to investigate shale chemistry, namely electron probe microanalysis (EPMA). For this study, we adopted wave dispersive spectroscopy (WDS) for the detection of the characteristic X-ray signals given its accuracy and ability to provide quantitative chemical information. The second part of this chapter introduced the grid WDS technique as a method for in situ characterization of shale mineralogy. In particular, we discussed the experimental parameters used in the design of this technique, the cluster analysis methodology used to analyze the generated chemical data, and a methodology for data interpretation. Finally, the application of the grid WDS technique to shale materials was illustrated through a detailed example. We showed how the method of data interpretation can be used to identify clay and non-clay mineral components. We also proposed a methodology for the analysis of two-phase mixture models.

Chapter 5

Statistical Nanoindentation

This chapter provides a brief introduction to general concepts of nanoindentation. The first part of this chapter reviews background information that aims to link quantities measured by nanoindentation to the mechanical properties of a homogeneous solid. A discussion of the grid indentation technique which deals with the application of the classical indentation test to heterogeneous materials, is then presented. The last section of this chapter discusses the application of grid indentation technique to shale materials[1].

5.1 Overview of Indentation Experiment

The aim of instrumented indentation is to extract the elastic and hardness properties of materials. An indentation test consists of pushing orthogonally an indenter of known geometry and mechanical properties onto the surface of the material of interest. During the indentation test, the load P applied to the indenter tip and the depth h of the indenter with respect to the indented surface are continuously recorded, as shown in Figure 5-1. The resulting $P-h$ curve defines the characteristic mechanical behavior of the material and can be used to extract elastic, strength, and creep properties. The indentation data is traditionally summarized in two parameters; the indentation modulus M and indentation hardness H. Using contact mechanics models, the indentation modulus relates to elastic properties of the material, whereas the in-

---

[1] The presentation of the instrumented indentation experiments and analysis is inspired from the work of M. Vandamme [56].

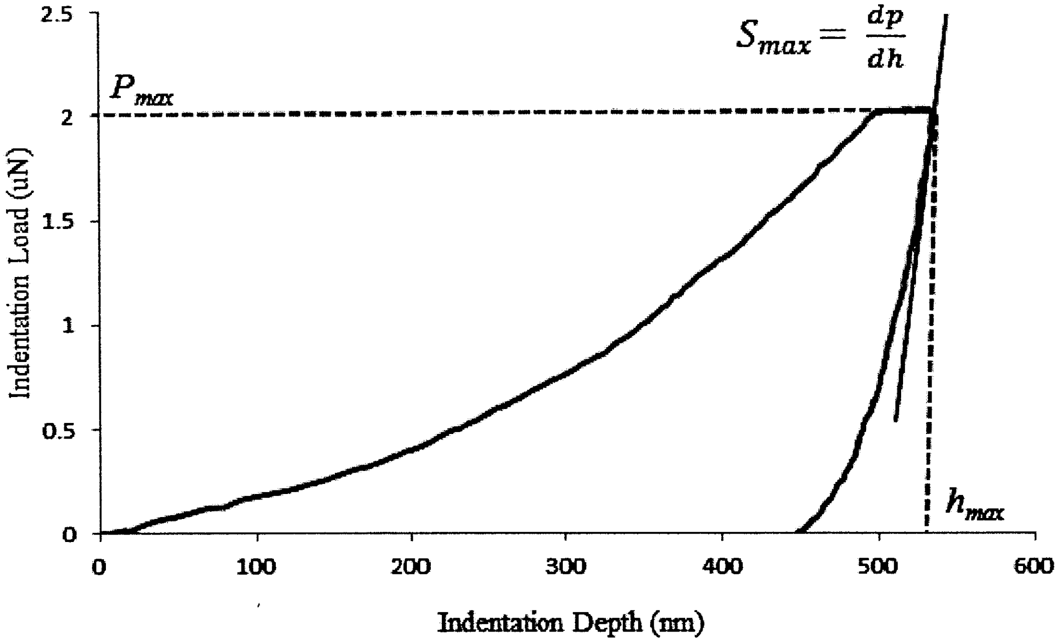

Figure 5-1: Typical $P - h$ curve of an indentation test. $P_{\max}$ is the maximum load, $h_{\max}$ the maximum depth, and S_{max} the contact stiffness at maximum depth.

dentation hardness relates to strength properties. The following sections review the theoretical background of the indentation technique.

5.2 Self-Similarity of Indentation Tests

Self-similarity is one of the important features of the indentation test, which allows linking measured parameters to material properties. A time-developing phenomenon is referred to as self-similar if the spatial distributions of its properties at different times can be obtained from one another by a similarity transformation [35]. Self-similarity implies that the displacement fields at any load P can be inferred from the displacement fields at a different load P_0. Self similarity depends on three criteria [27]. First, the constitutive relations of the indented material must be homogeneous functions with respect to stresses or strains. Second, the shape of the

Probe type	d	B
Flat punch	$\rightarrow \infty$	$1/(a^n)$
Spherical	2	$1/2R$
Conical	1	$\cot\theta$
Pyramidal	1	$\cot\theta^{eq}$

Table 5.1: Degree d of the homogeneous function and proportionality factor B for various indenter probes.

indenter probe must be described by a homogeneous function of degree greater than or equal to unity. Finally, the loading at any point must be increasing during the contact process. The criteria for the self-similarity of indentation tests are detailed hereafter.

5.2.1 Indenter Shape and Geometric Similarity

The most common indenter probes are shown in Figure 5-2. In practice the pyramidal indenters, such as the Berkovich, Vickers, and Cube-Corner probes, are the most used indenter shapes. Their sharp geometries allow for the testing of volumes of material smaller than what other geometries can probe. However, this sharp geometry generates stress concentrations so that the material is solicited plastically even at low load magnitudes. For any given probe described in a Cartesian coordinate system, $O(x_1, x_2, x_3)$, where the probe tip is at the origin, and x_3 directed into the depth of the indenter, the height z of the surface of the probe verifies:

$$z(\lambda x_1, \lambda x_2) = \lambda^d z(x_1, x_2) \quad \text{with } \lambda > 0 \tag{5.1}$$

where d is the degree of the homogeneous function. For axisymmetric probes, equation 5.1 simplifies to

$$z(r) = Br^d \tag{5.2}$$

where r is the radius of the probe at a given height z, and B is a proportionality factor that represents the depth z at $r = 1$ (Figure 5-3). The degree d and the proportionality factor B for the probes shown in Figure 5-2 are provided in Table 5.1.

Two objects that can be transformed into each other by dilation or contraction are geometrically similar. Applied to the considered indenter geometries in Figure 5-2, all flat indenters are

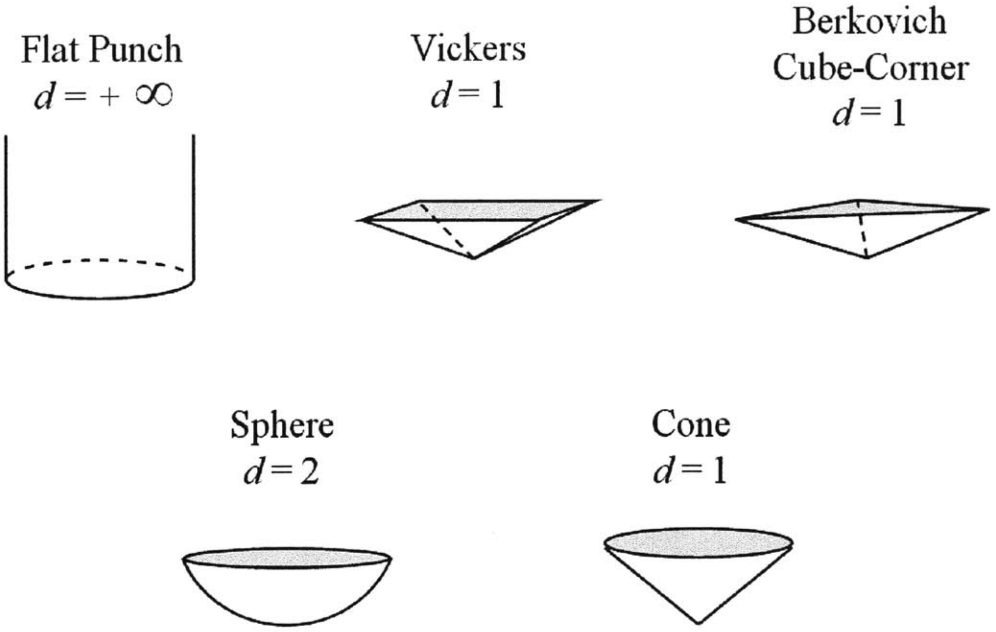

Figure 5-2: Indenter probes of different geometries.

Probe type	Equivalent half-cone angle, θ^{eq}
Berkovich	70.32°
Vickers	70.32°
Cube corner	42.28°

Table 5.2: Equivalent half-cone angle for various pyrimidal probes.

geometrically similar. In contrast, all pyramidal indenter probes are invariant when contracted or dilated. That is, pyramidal and conical indenters are similar to themselves, and said to be geometrically self-similar. Making use of this geometric self-similarity, the non-axisymmetric pyramidal probes are often approximated by axisymmetric cones of same degree $d = 1$, which greatly simplifies the analysis of the indentation experiment. This approximation is obtained by the implementation of an equivalent half-cone angle θ^{eq}, whose cone gives the same projected contact area for a given depth as the original indenter. The equivalent half-cone angles for common pyramidal probes are provided in Table 5.2

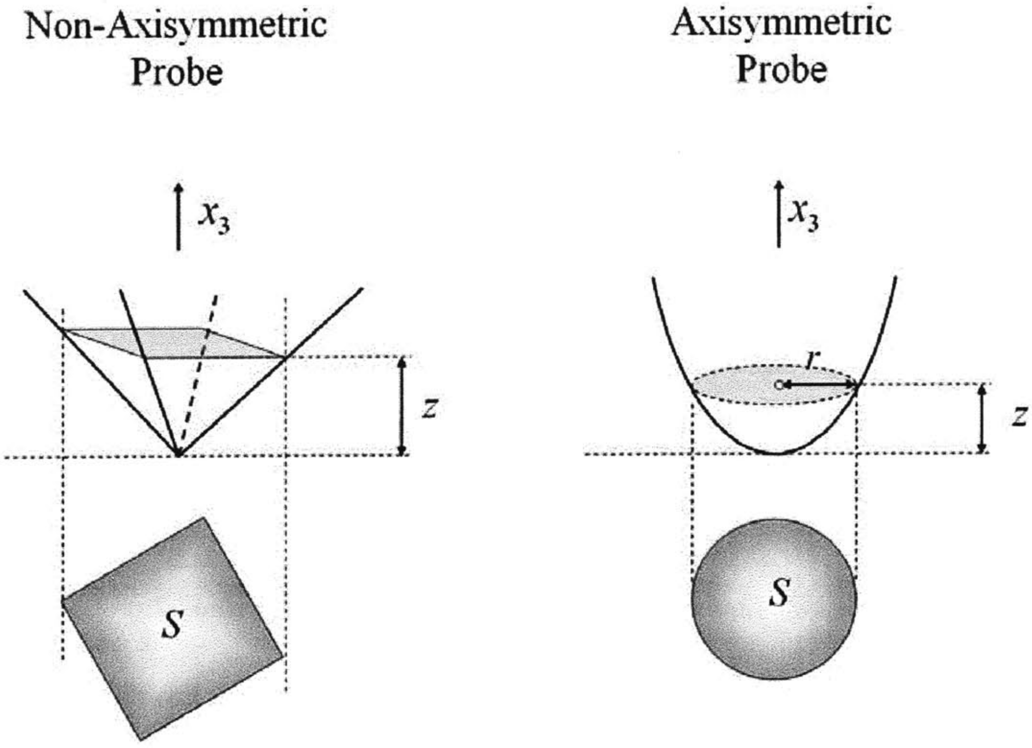

Figure 5-3: Parameters defining the geometry of an indenter probe. z is the indentation height, and S is the cross sectional area. For an axisymmetric probe, r is the radius. Adapted from [56].

5.2.2 Material Behavior

The self-similarity of an indentation experiment requires that the constitutive relations of the indented material are homogeneous with respect to the resulting strains (or strain rates) or stresses. This means that the operator of constitutive relations F, and thus the stress tensor $\boldsymbol{\sigma}(\boldsymbol{\varepsilon})$, must scale as:

$$F(\lambda\boldsymbol{\varepsilon}) = \lambda^{\kappa} F(\boldsymbol{\varepsilon}) \tag{5.3}$$

where $\boldsymbol{\varepsilon}$ is the strain tensor, and κ the degree of the homogeneous constitutive function F. Linear and nonlinear-elasticity satisfy this requirement provided that [29]:

$$\boldsymbol{\sigma} = \mathbb{C}(\boldsymbol{\varepsilon}) : \boldsymbol{\varepsilon} \tag{5.4}$$

$$\mathbb{C}(\lambda\boldsymbol{\varepsilon}) = \lambda^{\kappa-1}\mathbb{C}(\boldsymbol{\varepsilon}) \tag{5.5}$$

where $\mathbb{C}(\boldsymbol{\varepsilon})$ is the secant stiffness tensor. $\kappa = 1$ corresponds to the case of linear elasticity. Equation (5.3) is also satisfied for the case of rigid plastic limit behavior, for which the stress derives from the dissipation (or support) function $\boldsymbol{\sigma} : \boldsymbol{\varepsilon} = \pi(\mathbf{d})$ [52]:

$$\boldsymbol{\sigma} = \frac{\partial \pi}{\partial \mathbf{d}}(\mathbf{d}) \tag{5.6}$$

where $\pi(\mathbf{d})$ is a homogeneous function of degree 1 with respect to the strain rate $\mathbf{d}$, such that:

$$\pi(\lambda\mathbf{d}) = \lambda\pi(\mathbf{d}) \tag{5.7}$$

Hence, the yield design solution applied to indentation analysis satisfies self-similarity condition with $\kappa = 0$.

But not all materials satisfy self-similarity conditions (5.3). One example of such materials is a linear-elastic perfectly-plastic material, for which $\kappa = 1$ within the elastic domain, and $\kappa = 0$ at the limit of the elastic domain, corresponding to the strength limit. Hence, there is no unique value of parameter κ for which condition 5.3 holds for all strain levels eventually present in the indentation test. Therefore, indentation testing performed on linear-elastic perfectly-plastic materials are not self-similar. In general, whenever the material response of the indented half-space is not governed uniformly by the same class of material behavior characterized by the parameter κ, the non-homogeneous stress distribution within the indented half-space may imply the loss of self-similarity of the indentation test.

5.2.3 Self-Similar Scaling Relations

Provided that conditions (5.1) and (5.3) are satisfied, the loading phase of an indentation test possesses self-similarity. That is, given a known indentation response represented by load P_0, indentation depth h_0, contact depth $(h_c)_0$, and projected area of contact $(A_c)_0$ (see Figure 5-4), the indentation response (P, h, h_c, A_c) is obtained from a similarity transformation [30]:

$$\frac{P}{P_0} = \left(\frac{h}{h_c}\right)^{\frac{2+\kappa(d-1)}{d}} \tag{5.8}$$

For example, for an elastic material ($\kappa = 1$), $P \propto h$ for flat punch, and $P \propto h^{3/2}$ for a spherical indenter. For conical and pyramidal indenters ($d = 1$), $P \propto h^2$ irrespective of the material behavior. This provides a strong argument in favor of using the Berkovich indenter, as self-similarity will prevail irrespective of the constitutive material relations.

Another relation obtained from the self-similarity of the indentation test is [30]:

$$\frac{h}{h_0} = \left(\frac{A_c}{(A_c)_0}\right)^{\frac{d}{2}} \tag{5.9}$$

A combination of the previous two scaling relations readily shows that the average pressure below the indenter , i.e. the indentation hardness $H = P/A_c$, scales as:

$$\frac{H}{H_0} = \left(\frac{h}{h_0}\right)^{\frac{\kappa(d-1)}{d}} \tag{5.10}$$

As a result, the hardness H is constant throughout the loading process and does not depend on the applied load for any rigid plastic behavior ($\kappa = 0$) or for any pyramidal or conical indenter ($d = 1$).

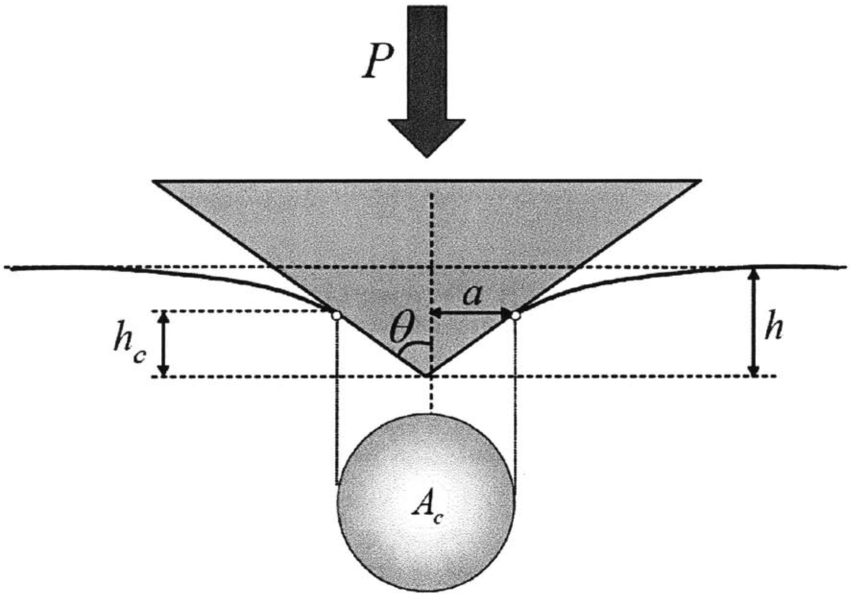

Figure 5-4: Geometric description of a conical indentation test. P is the indentation load, h the indentation depth, h_c the contact depth, A_c the projected area of contact, and a the contact radius [56].

Finally, given that $A_c = \pi a^2$, where a is the contact radius, equation 5.9 can be written as:

$$\frac{a^d}{h} = cst \tag{5.11}$$

For axisymmetric probes, for which the contact radius a and the contact depth h_c are linked by $h_c = Ba^d$, an equivalent expression is given by:

$$\frac{h_c}{h} = cst \tag{5.12}$$

Hence, provided self-similarity of the indentation test, the contact height to indentation depth ratio h_c/h does not depend on the indentation load. This result is of critical importance for indentation analysis and forms the basis of indirect methods of determining the projected area of contact A_c.

5.3 Elastic and Strength Properties In Indentation

5.3.1 Indentation Modulus

The indentation modulus M of an indentation test is given by:

$$M = \frac{\sqrt{\pi}}{2}\frac{S}{\sqrt{A_c}} \tag{5.13}$$

where $S = dP/dh$ is the measured initial slope of the unloading branch of the $P - h$ curve, and A_c the projected area of contact between the indenter tip and the indented material (see Figure 5-4). This definition of indentation modulus was introduced by Bulychev, Alekhin and Shorshorov, and equation (5.13) is called the BASh formula [65]. The application of this solution is challenging since the indentation modulus is measured from the unloading portion of an indentation test, after the plastic domain of the material has already been solicited. However, recent developments have shown that the initial part of the indentation curve measures the elastic properties of the probed material (e.g., [74], [75]).

Another important parameter in BASh formula is the area of contact A_c. While elastic indentation solutions provide a direct means to determine the contact area A_c from the contact depth-to-indentation depth relation h_c/h (the Galin-Sneddon solution [51], [38]), the contact area for other material behaviors, such as elasto-plastic materials, is a priori an unknown of the contact problem. To circumvent this problem, indirect methods have been developed to determine the contact area in terms of the maximum indentation depth measured in the indentation experiment. One of these methods is the Oliver and Pharr method [72]. Making use of the self-similarity of the indentation problem, in which the contact depth-to-indentation depth ratio is constant, Oliver and Pharr found that:

$$\frac{hc}{h_{\max}} = 1 - \varepsilon \frac{P_{\max}}{S h_{\max}} \tag{5.14}$$

where $\varepsilon = 3/4$. The contact area is linked to the contact radius a by:

$$A_c = \pi a^2 \tag{5.15}$$

The contact radius can be determined from the contact depth by equation (5.2). Hence, we have the sufficient parameters (A_c and S), which can be obtained from an indentation test, to determine the indentation modulus.

In this context, it is worth introducing the link between the indentation modulus and meaningful mechanical properties of the indented material. For the case of isotropic materials, the indentation modulus corresponds to the plane-stress modulus [39] [51]:

$$M = \frac{E}{1 - v^2} \tag{5.16}$$

where E is the Young's modulus, and v the Poisson's ratio of the indented isotropic material. The case of transversely isotropic materials, which is an attribute of shale materials, is of particular importance in this investigation. For such materials with the material symmetry oriented in the x_3 direction, the indentation moduli $M_i = M(x_i)$ are related to the five independent constants defining the material [3]:

$$M_1 = M(x_1) = M(x_2) \approx \sqrt{\sqrt{\frac{C_{11}}{C_{33}}} \frac{C_{11}^2 - C_{12}^2}{C_{11}} M_3} \tag{5.17}$$

$$M_{3=}M(x_3) = 2\sqrt{\frac{C_{11}C_{33} - C_{13}^2}{C_{11}} \left(\frac{1}{C_{44}} + \frac{2}{\sqrt{C_{11}C_{33}}+C_{13}} \right)^{-1}} \tag{5.18}$$

where the Voigt notation was used to denote the elastic constants $C_{11} = C_{1111}, C_{12} = C_{1122}, C_{13} = C_{1133}, C_{33} = C_{3333}, C_{44} = C_{1313} = C_{2323}$.

5.3.2 Indentation Hardness

The indentation hardness H is defined as the average pressure below the indenter:

$$H = \frac{P_{\max}}{A_c} \tag{5.19}$$

where $P_{\max}$ is the maximum load applied to the indenter and A_c is the projected area of contact between the indenter tip and the indented material, as determined by the Oliver and Pharr method. Hardness is often related to strength properties of materials. For metals, Tabor suggested a rule-of-thumb relation between hardness H and tensile strength σ_y [23]:

$$\frac{H}{\sigma_y} \approx 3 \tag{5.20}$$

However, indentation hardness is not a material property, and its physical meaning is still subject to debate [76]. The main limitation to using indentation hardness to back-calculate plastic or strength properties is the non-uniqueness of the solution of the reverse analysis. In fact, for cohesive materials with work-hardening, very different material properties (yield strength-to-Young's modulus ratio and work-hardening exponent) can yield identical indentation hardness values, and even identical loading curves. For the case of cohesive-frictional elasto-plastic material, Ganneau et al. [32] developed a dual indentation approach that allows the determination of cohesion and friction of a Mohr-Coulomb solid from the dependence of the hardness-to-cohesion ratio on the cone angle θ :

$$\frac{H}{C} = \Pi_H(\mu, \theta) \tag{5.21}$$

where $\mu = \tan\varphi$ is the Coulomb friction coefficient. Recent developments by Cariou and Ulm [63] and Gathier and Ulm [8] provide a similar solution for a cohesive-frictional material whose strength behavior is governed by a Drucker-Prager strength model. The method of Gathier and Ulm provides the means for establishing explicitly the relations between measured hardness H, porosity (expressed as one minus the packing density η), and the solid's cohesion and friction properties (c^s, α). These micromechanics developments illustrate the link between the measured indentation hardness, and the intrinsic strength properties of the solid skeleton, and the presence of porosity in the microstructure.

5.4 Indentation Analysis of Heterogeneous Materials

5.4.1 Grid Indentation Technique

The application of the indentation technique to assess a heterogeneous material is challenging, as it is difficult to choose to indent on a specific material phase with sufficient repeatability. To address this challenge, Ulm and co-workers [33] [26] [34] developed the so-called grid indentation technique, which consists of performing a large number of indentations over the surface of the heterogeneous material of interest. Provided the adequate choices for the indentation depth and grid size, each indentation experiment could be considered as statistically independent, and statistical techniques can be applied to interpret the results.

The grid indentation concept can be illustrated by considering the following thought experiment of two materials of different mechanical properties as shown in Figure 5-5. A random indentation on the sample surface provides access to the properties of either of the phases given that the indentation depth is much smaller than the characteristic size of the two phases. In contrast, a much deeper indentation depth compared the characteristic size of the phases provides access to the homogenized response of the two phases. This thought experiment shows how the classical indentation test can be applied to heterogeneous materials provided an adequate choice of indentation depth. This requires a large array of indentations followed by statistical analysis of the data to separate the mechanical properties of individual phases.

5.4.2 Scale Separability

The grid indentation technique introduces a new length scale to the problem. The grid size must be chosen properly to achieve statistical independence in the sampling process. The grid size L must be much larger than the imprint of the indentation test. To avoid sampling effects, a large number of tests N are necessary. Furthermore, to obtain the properties of individual phases, the indentation depth h must be much smaller than the length scale of individual phases. These

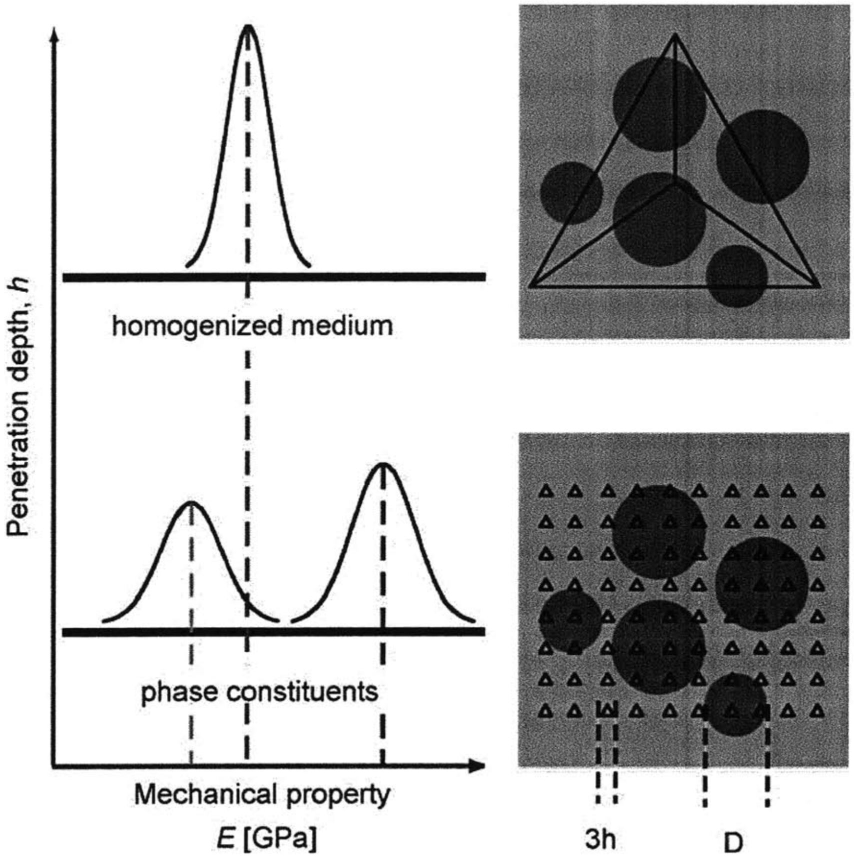

Figure 5-5: Schematic of the proposed grid indentation technique showing massive array of indentations on a heterogeneous material. Top: indentations with large depth ($h >> D$) gives the homogenized response of the material. Bottom: indentations with low depths ($h << D$) gives the properties of individual constituents. Adapted from [56].

conditions can be summarized as:

$$h << D << L\sqrt{N} \tag{5.22}$$

In addition, because the analysis of the indentation tests depends on continuum mechanics, the indentation test must conform to the scale separability of continuum mechanics:

$$d << l << h \tag{5.23}$$

where l is the characteristic size of the representative elementary volume, which must be larger than the characteristic size of the largest heterogeneity d contained in the representative elementary volume (rev), and smaller than the indentation depth h.

5.5 Experimental Parameters

The grid Indentation technique described in section 5.4 aims at measuring the mechanical properties of heterogeneous materials. In this study, we use this technique to probe the porous clay composite (see section 2.2.2), which requires an appropriate length scale that satisfies scale separability conditions described in Section 5.4.

The identification of the sought length scale starts by identifying the length scales in equations (5.22) and (5.23) above parameters for the porous clay composite. A candidate for the largest heterogeneity d is the pore throat radius which can be obtained from porosimetry. For shale materials, this parameter is on the order of 10 nm [9]. Information obtained from TEM and SEM images, along with the information about clay mineralogy (see section 2.1.1) reveals the maximum dimension of a solid clay, on the order of one micron, as another possible candidate for d. To resolve the porous clay composite from the inclusions (non-clay minerals), the characteristic size of inclusions D must be incorporated in the scale separability conditions. From experimental testing, characteristic size of inclusions D obtained from imaging techniques can be as small as 20 nm. Combining the lower limit d and the upper limit D, an indentation depth greater than 750 nm and less than 3 μm is appropriate. Bobko [9] conducted a massive indentation campaign and found that the experimental parameters listed in Table 5.3 solicit the

Maximum load	4.8 mN
Loading rate	10 mN/s
Unloading rate	10 mN/s
Holding time	10 s

Table 5.3: Experimental parameters used in indentation experiments.

porous clay composite. Another important experimental parameter related to the indentation test is the size of the material probed during the test. Finite element simulations for indentation testing using Berkovich indenter show that the probed elastic response corresponds to a material volume that is roughly 3 times the depth of indentation [33] [60]. This parameter will be discussed later in the context of the chemo-mechanical coupling technique.

5.6 Indentation Equipment

Nanoindentation experiments for this study were performed using a nanohardness tester from CSM Instruments (Peseux, Switzerland) available in the Department of Civil and Environmental Engineering at MIT. A schematic of the key components of the nanohardness tester is provided in Figure 5-6. The indentation load is applied electromagnetically by passing a current through a coil mechanically connected to the tip. The displacement is measured via the change in voltage of a parallel plate capacitor. The indentation depth is measured with respect to the thermal calibration ring. The indenter is supplied with an optical microscope so that the surface may be visually identified before being indented. The sample and the indenter is housed in a sealed box to minimize temperature drifts and mechanical and acoustic noise. The apparatus is capable of applying a maximum load of 300 mN with a resolution of 40 nN. The maximum displacement allowed by the equipment is 20 μm with a resolution 0.04 μm.

5.6.1 Calibration Parameters

Several calibrations are required to ensure that the measured loads and displacements provide meaningful results about the mechanical properties of the indented material.

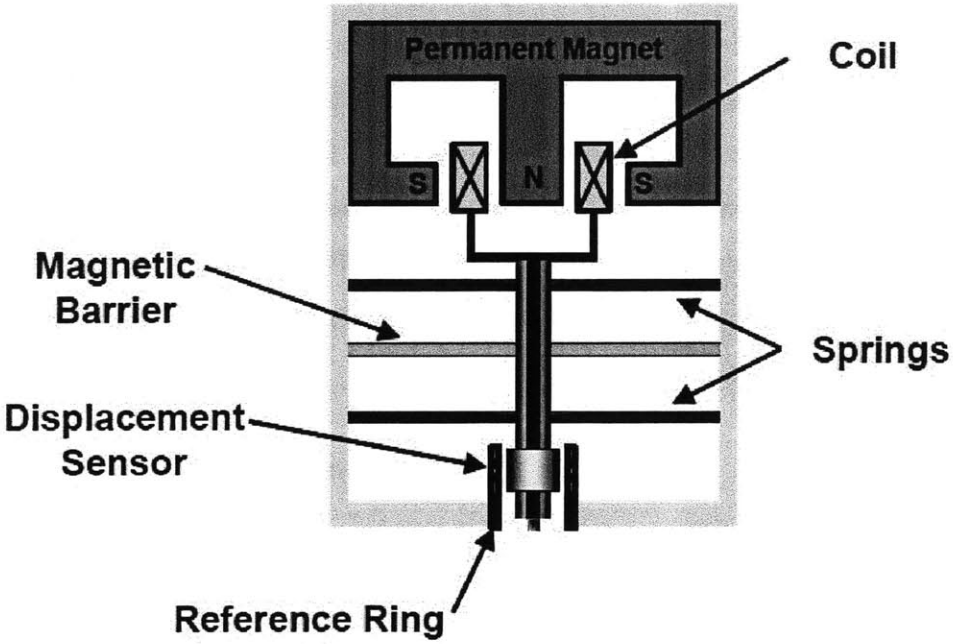

Figure 5-6: The CSM Instruments SA nano-hardness tester (courtesy from Dr. N. Randall).

Shape Area Function

In indentation testing, the projected area of contact is a crucial parameter to ensure that subsequent data analysis provides meaningful results. The projected area of contact $A_c(h_c)$, required to calculate indentation properties (M and H), is obtained by the Oliver and Pharr method (see Section 5.3.1), which provides an estimate of the contact depth h_c and, hence, the function $A_c(h_c)$ can be precisely determined. For a perfectly sharp Berkovich tip, the area function is well defined. In practice, however, the Berkovich indenter exhibits some bluntness, usually a radius of curvature greater than 30 nm. This bluntness can have significant effects on the interpretation of results, especially for shallow indentations. For this reason, the area function $A_c(h_c)$ must be carefully calibrated. One approach to determine $A_c(h_c)$ is by visual assessment methods such as atomic force microscopy (AFM) or scanning electron microscopy [33]. However, these methods are time consuming. Instead, $A_c(h_c)$ is typically determined indirectly by indentation on a material whose mechanical properties are known (e.g., fused silica, which has an indentation modulus M = 72 GPa). A_c can then be determined by the BASh formula (equation (5.13)) and h_c with the Oliver and Pharr method. A function is then fit to the measured h_c and A_c values, of the form:

$$A_c(h_c) = C_1 h_c^2 + C_2 h_c + C_3 h_c^{1/2} + C_4 h_c^{1/4} + ... \tag{5.24}$$

where C_1 is usually fixed to the area-to-depth constant of the perfectly sharp indenter (C_1 = 24.58 for a Berkovich indenter) and $\{C_i\}>1$ are the factors that capture the bluntness of the tip.

Electronic-Mechanical Interface

The interface between mechanical parts and electronics must be calibrated frequently. In particular, the relations of load–applied current and the depth–change in capacitance require special attention. The load applied to the specimen is proportional to the current passed through the loading coil. The proportionality factor is calibrated every two years by hanging weights of known mass on the indenter and then measuring the current necessary to bring the indenter back to its initial position. The displacement of the indenter is measured by a change in capacitance in a parallel plate capacitor. The proportionality factor between changes in depth and in capacitance must be calibrated every two years by indentation on a calibrated piezoelectric crystal with a spherical indenter.

Frame Compliance

The frame of the indenter deforms in response to the load applied to the sample. The measured indentation depth $h_{\max}$ is a linear combination of the real displacement in the sample (h) and the deformation of the frame (h_{frame}) :

$$h_{meas} = h + h_{frame} \tag{5.25}$$

The frame compliance can be modeled as a linear spring of compliance C_f :

$$h_{frame} = PC_f \tag{5.26}$$

where P is the applied load. Due to the specific design of the CSM indenter, the frame compliance is fixed, $C_f = 0.1$ nm/mN and requires no calibration.

Thermal Drift

Thermal drift is the variation in the depth measurements in an indentation test resulting from thermal expansion or contraction of the sample or indentation apparatus during the indentation. The CSM indenter is designed such that it does not require a thermal drift correction, given that the depth is measured with reference to a thermal ring sitting on the sample surface, and hence, acting as a floating reference. This results in the movement of the reference ring being the same as the thermal drift of the sample. This can be easily accounted for in the measured displacement.

5.7 Sample Application to Shale Materials

The application of grid indentation technique to shale materials involves performing a large grid of indentations followed by cluster analysis of the measured indentation modulus M and

Phase	1	2	3	4
M_3, μ [GPa]	13.76	21.29	37.91	103.96
M_3, σ [GPa]	2.53	4.51	7.49	6.88
H_3, μ [GPa]	0.46	0.93	2.74	17.48
H_3, σ [GPa]	0.12	0.30	1.21	3.49
$h_{\max}$, μ [nm]	812.30	557.73	359.46	166.21
$h_{\max}$, σ [nm]	111.20	72.75	102.92	6.80
Vol. fraction	59.85	31.79	5.32	3.03
No. data	187	87	15	9

Table 5.4: Cluster analysis results of the grid indentation experiment performed on sample S3. The notations μ and σ correspond to the mean and standard deviation of the given property. The values for the number of measured data (No. data), indentation depth, volume fraction are also listed.

indentation hardness H to assess the types of mechanically active phases at the scale of measurements. Similar to the grid WDS, we use the Mclust cluster analysis algorithm presented in Section 4.3.2 to analyze the indentation data. The interpretation of the cluster analyses of grid indentation experiments on shale samples is pursued herein solely based on mechanics arguments. This approach, previously pursued in [10] [25], brings together elements of mechanical behaviors of constituents, length scale considerations, and overall material composition known a priori from mineralogy tests (see Table 3.1) to evaluate the mechanical responses of shale measured in grid indentation, and in particular that of the porous clay phase. The discussion of the application of grid indentation technique to shale material is pursued based on the results presented in Figure 5-7, and listed in Table 5.4, for a grid indentation experiment performed on sample S3. This experiment was performed perpendicular to the direction of bedding planes (x_3) of the shale sample.

Three main types of mechanically active phases are identified, whose on-average properties are graphically displayed in Figure 5-7. The first type corresponds consistently to a phase with large M, H values, (Phase 4 in Figure 5-7) whose response is expected due to the presence of a dominant quartz inclusion phase determined from XRD mineralogy experiments. In Figures 5-7a, this so-called inclusion (INC) phase exhibits average indentation modulus and hardness values of approximately $M = 104$ GPa, $H = 18$ GPa. Such observation matches, in first order. the expected properties of quartz ($M = 80 - 100$ GPa, $H = 12 - 14$ GPa) [20] [61] [53]. The second type of mechanical response corresponds to the phases with lower M, H

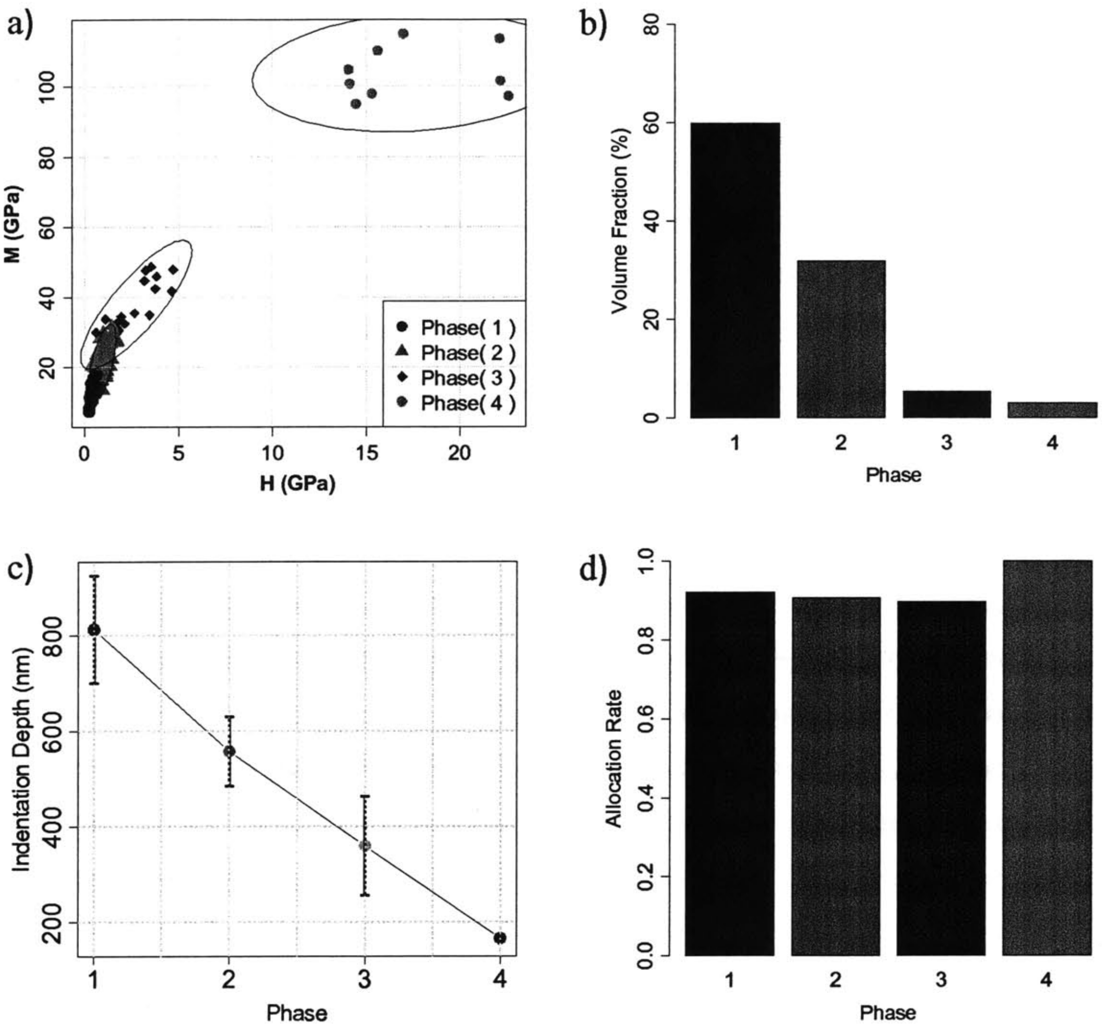

Figure 5-7: Cluster analysis results of the grid indentation experiment performed on sample S3. a) Cluster analysis of the indentation modulus M and hardness H showing four mechanical phases. b) Volume fractions for each of the mechanical phases described by the cluster modeling in (a). c) Mean and standard deviation values of the maximum indentation depths for each mechanical phase measured in the grid indentation experiment.

values (phases 2 and 3 in Figure 5-7) compared to the inclusion phase type , and with low volume fractions (Figure 5-7b). These so-called composite phases exhibit low allocation rates. Finally, the third phase type corresponds to the porous clay phase (phase 1 in Figure 5-7), identified in first instance from the notoriously large volume fraction (Figure 8b) expected from the XRD mineralogy assessment. The porous clay phase is consistently identified with high allocation rates (Figure 5-7d), and exhibits lower M, H values compared to the inclusion and composite phases. Figure 5-8 illustrates typical indentation responses measured for the porous clay phase (phase 1) and the hard inclusion phase (phase 4). The indentation load-depth curve for the phase 1 data exhibits a larger maximum depth, a significant creep during the holding phase regime of the applied load, and a large plastic deformation upon unloading. In contrast, the deformation response of the experiments linked to phase 4 displays less plastic behavior upon unloading and relatively little creep. The average indentation depth for the data grouped in phase 1 is $h_{\max} = 812 \pm 111$ nm. For phases 2 through 4, the indentation depths are lower, reaching 166 ± 7 nm for phase 4. The corresponding standard deviations to those estimates decrease drastically from phase 1 to 4. Finally, consolidating the understanding of the porous clay phase from indentation considerations calls for an evaluation of the length scale associated with the indentation experiments. With average maximum indentation depths of approximate $h_{\max} \approx 800$ nm, the interaction volumes in indentation experiments associated with the porous clay phase access a length scale in shale which encompasses the clay minerals and the nanoporosity (Section 2.2.2). At such indentation depths, the condition of scale separability (see Section 5.4.2) underlying the definition of porous clay as a mechanical composite is justified. The interpretation of the porous clay and silt inclusion phases in shale from mechanical arguments will be discussed later in the context of coupled chemo-mechanical analysis of shale.

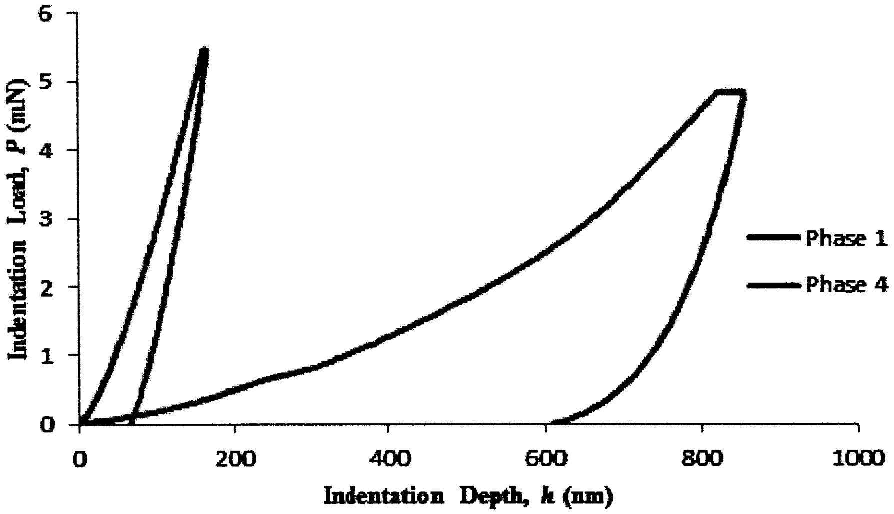

Figure 5-8: Representative indentation responses measured in the indentation experiment presented in Figure 5-7. The load-depth curves were recorded for experiments that are associated with data clustered in phases 1 and 4. The indentation modulus and hardness inferred from these experimental curves are $M_3 = 116$, $H_3 = 15.4$ GPa for the experiment assigned to phase 4, and $M_3 = 11.4$, $H_3 = 0.35$ GPa for the experiment assigned to phase 1.

5.8 Chapter Summary

This chapter introduced the general concepts related to nanoindentation on homogeneous solids. We also showed the implementation of the grid indentation technique to determine the mechanical and microstructural properties of our highly heterogeneous shale materials. The descriptions of the experimental equipment, calibrations, and limitations of the technique were presented. The interpretation of the cluster analysis results of indentation data was explained through a sample application.

Part III

Results and Discussion

Chapter 6

Grid WDS Results

This chapter is the first of two devoted to the presentation of the mineralogy assessment of shale materials. Both chapters show the implementation of wave dispersive spectroscopy (WDS) to characterize the chemical signature of shale materials. This chapter presents the results of chemical assessment of shale materials performed through the grid WDS technique. The main goal is to provide quantitative evaluation of shale mineralogy presented in terms of the volume fractions of the major constituents at sub-micrometer scale. We begin with a presentation of the cluster analysis results of the grid WDS experiments performed on the investigated shale materials. We then present the analysis methodology used to interpret the results. The next chapter of this part presents supplementary mineralogy information obtained through image analysis of X-ray maps and backscattered electron (BSE) images that is employed to validate the grid WDS results.

6.1 Grid WDS Experimental Program

In this section we present the results of grid WDS chemical analysis of the shale samples investigated in this work. Three different samples (S7, S3, S1) described in Chapter 3 were tested. These samples represent a diverse sample of shale composition. Two grid designs were conducted: massive grids performed on a relatively large areas, and more focussed grids performed on relatively small areas. The terminology associated with grid size will be discussed later. Table 6.1 summarizes the grids that were performed on each sample. Five tests with

Sample name	Grid size	Spacing (μm)	No. of points
S3-a	32x32	30	1024
S3-b	32x32	3	1024
S3-c	20x20	10	400
S3-d	20x20	10	400
S3-e	20x20	10	400
S7-a	32x32	100	1024
S7-b	32x32	30	1024
S7-c	33x33	3	1160
S7-d	20x20	10	400
S7-e	20x20	10	400
S1-a	32x32	0	1024

Table 6.1: Experimental program showing the WDS grids that were performed on the shale samples investigated in this work.

different grid sizes were run on samples S7 and S3, whereas one test was run on sample S1. The results of these grids will be used to investigate the mineralogy of each sample quantitatively. The chemical results of these grids are presented in Figures 6-1 through 6-21. The interpretation of these results follows in the next section.

Phase		1	2	3	4	5	6	7
Si	μ	13.48	18.29	18.60	20.02	20.86	32.26	33.70
	σ	6.65	3.91	1.69	2.92	4.30	0.66	0.12
Al	μ	9.79	12.85	13.23	11.14	10.24	0.92	0.03
	σ	4.61	2.28	1.00	2.01	4.39	0.55	0.03
K	μ	0.51	0.78	0.56	0.50	3.00	0.03	0.00
	σ	0.58	0.39	0.12	0.17	5.97	0.07	0.00
Ca	μ	0.76	0.16	0.07	0.16	0.24	0.00	0.00
	σ	0.99	0.20	0.04	0.14	0.58	0.01	0.00
Na	μ	0.79	0.93	0.68	0.68	1.77	0.09	0.00
	σ	0.32	0.42	0.17	0.27	2.65	0.13	0.01
Fe	μ	6.71	2.47	1.52	1.83	0.83	0.18	0.05
	σ	7.15	2.13	0.31	0.75	1.33	0.11	0.03
Mg	μ	1.07	0.71	0.57	0.59	0.34	0.04	0.00
	σ	0.85	0.31	0.11	0.22	0.64	0.03	0.01

Table 6.2: Summary of the make up of the chemical phases identified by cluster analysis and displayed in Figure 6-1 for experiment S7-a. The notations μ and σ correspond to the mean and standard deviation of the given property. The standard deviation corresponds to the square root of the variance.

Phase	1	2	3	4	5	6	7
Volume fraction (%)	7.40	19.43	37.14	20.93	6.35	2.42	6.34
Analysis total μ	91.26	87.91	90.93	90.64	93.72	97.81	97.82
Analysis total σ	8.05	8.72	6.77	7.70	8.61	2.10	0.95
Allocation	0.99	0.93	0.95	0.92	0.98	1.00	1.00

Table 6.3: Volume fractions, analysis totals, and allocation rates for the chemical phases identified by cluster analysis and displayed in Figure 6-1 for experiment S7-a. The notations μ and σ correspond to the mean and standard deviation of the given property.

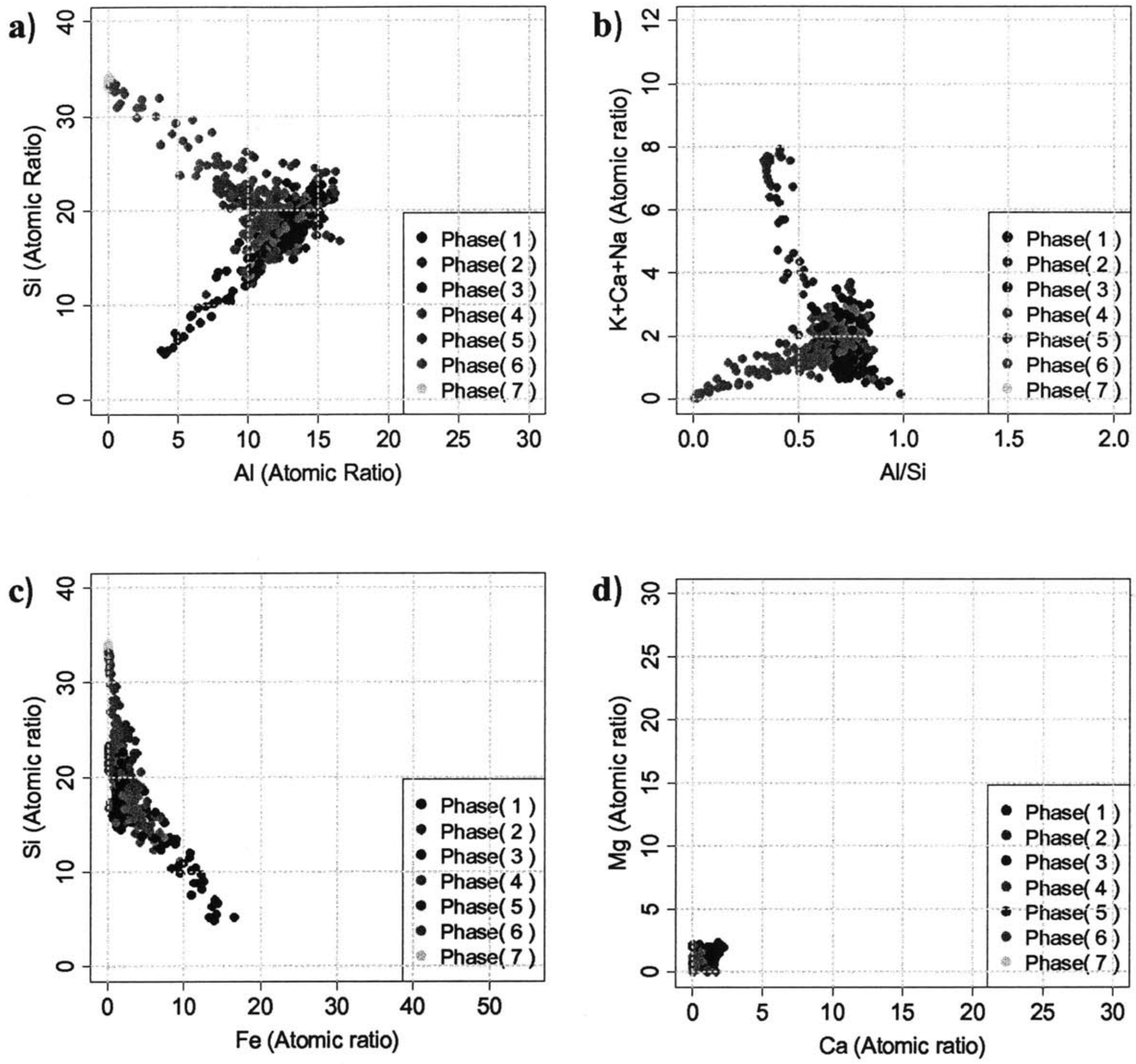

Figure 6-1: Multivariate cluster analysis of the grid WDS data for experiment S7-a. The identified phases are presented on 2-D projections for visual interpretation of the data: a) Al-Si space and b) Ca+Na+K-Al/Si space separate quartz, feldspars, and clay minerals. c) Fe-Si space and d) Ca-Mg space separate carbonate minerals; siderite, calcite, magnesite, ankerite, and dolomite.

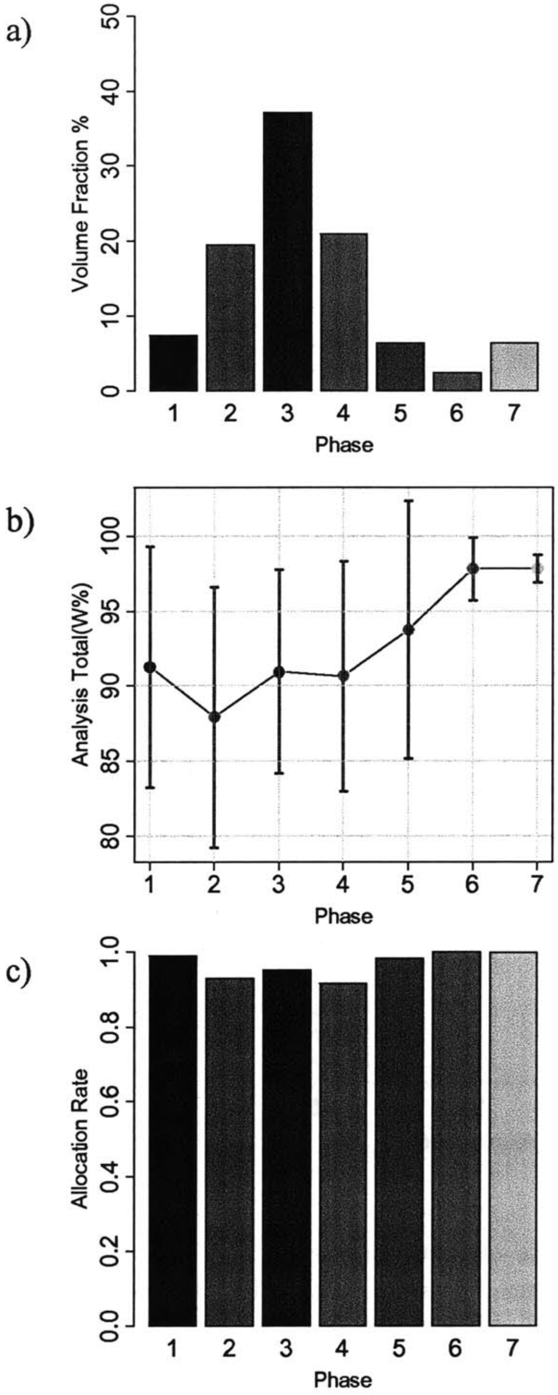

Figure 6-2: Graphical representation of clustering results presented in Table 6.3 for experiment S7-a. a) volume fractions, b) mean and standard deviation values of the analysis totals, and c) allocation rates for each of the phases displayed in Figure 6-1.

Phase		1	2	3	4	5	6	7	8
Si	μ	15.36	16.30	16.89	18.02	21.16	21.52	32.78	32.82
	σ	3.65	3.81	1.96	1.14	2.66	4.04	0.79	0.66
Al	μ	11.12	10.94	11.91	12.63	9.64	9.78	0.24	0.02
	σ	2.80	2.40	1.20	0.81	2.51	3.54	0.24	0.01
K	μ	0.53	0.99	0.58	0.67	1.92	0.47	0.01	0.00
	σ	0.23	0.76	0.12	0.19	2.30	0.19	0.01	0.00
Ca	μ	0.20	0.43	0.26	0.06	0.22	0.08	0.00	0.00
	σ	0.25	0.52	0.19	0.03	0.34	0.05	0.01	0.00
Na	μ	0.65	0.76	0.68	0.62	2.10	0.60	0.04	0.01
	σ	0.15	0.30	0.17	0.13	2.24	0.27	0.07	0.01
Fe	μ	4.52	4.42	2.99	1.41	1.00	1.39	0.08	0.02
	σ	4.94	4.01	1.55	0.24	0.87	0.58	0.03	0.02
Mg	μ	0.62	1.11	0.76	0.57	0.31	0.47	0.01	0.00
	σ	0.32	0.61	0.20	0.12	0.25	0.19	0.01	0.00

Table 6.4: Summary of the make up of the chemical phases identified by cluster analysis and displayed in Figure 6-3 for experiment S7-b. The notations μ and σ correspond to the mean and standard deviation of the given property. The standard deviation corresponds to the square root of the variance.

Phase	1	2	3	4	5	6	7	8
Volume fraction (%)	3.80	8.60	19.41	29.30	4.94	13.64	2.96	17.35
Analysis total μ	96.11	89.75	93.37	95.69	97.14	94.98	101.97	100.88
Analysis total σ	1.32	1.32	1.32	1.32	1.32	1.32	1.32	1.32
Allocation	0.97	0.95	0.93	0.94	0.98	0.96	0.96	0.99

Table 6.5: Volume fractions, analysis totals, and allocation rates for the chemical phases identified by cluster analysis and displayed in Figure 6-3 for experiment S7-b. The notations μ and σ correspond to the mean and standard deviation of the given property.

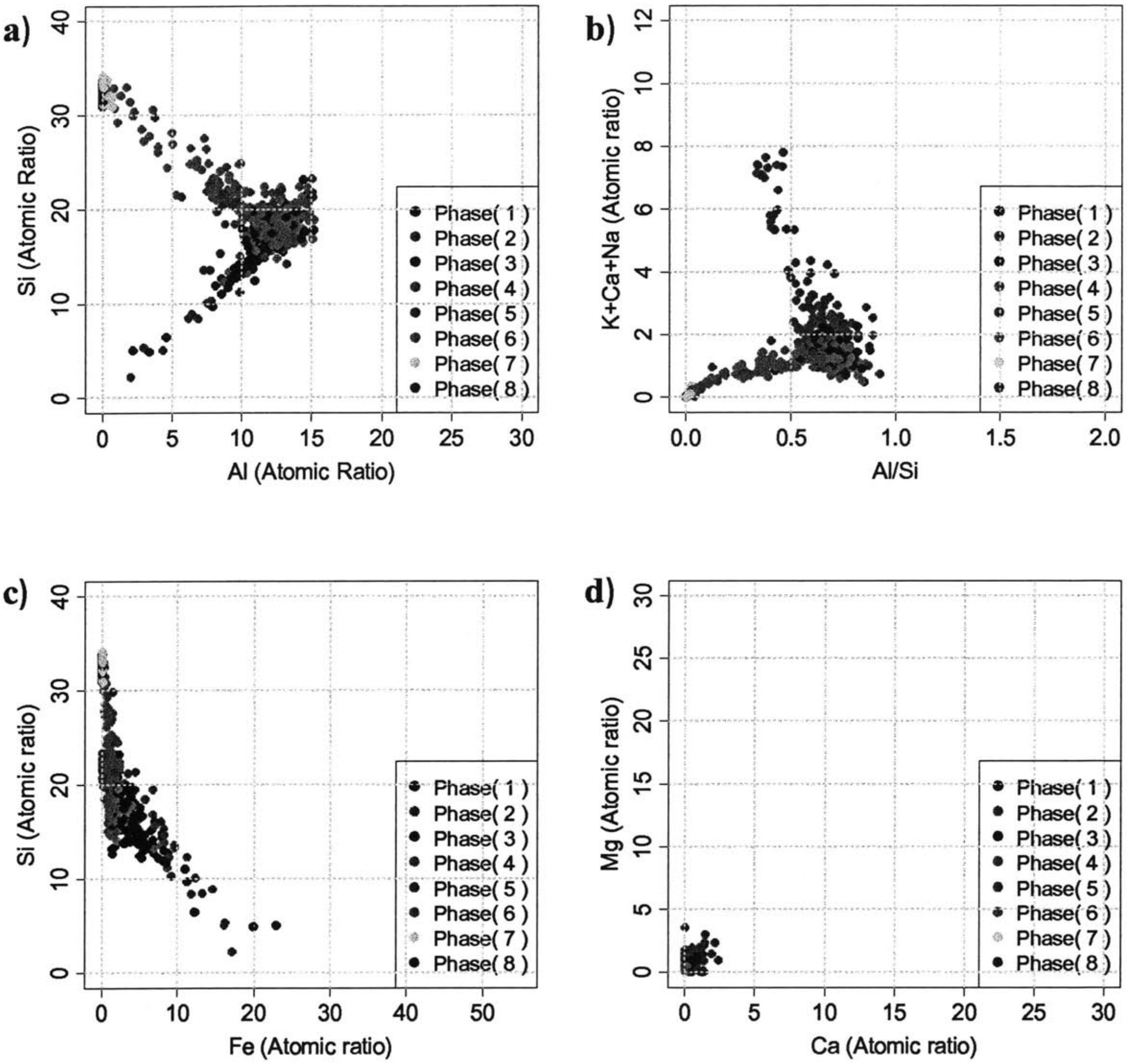

Figure 6-3: Multivariate cluster analysis of the grid WDS data for experiment S7-b. The identified phases are presented on 2-D projections for visual interpretation of the data: a) Al-Si space and b) Ca+Na+K-Al/Si space separate quartz, feldspars, and clay minerals. c) Fe-Si space and d) Ca-Mg space separate carbonate minerals; siderite, calcite, magnesite, ankerite, and dolomite.

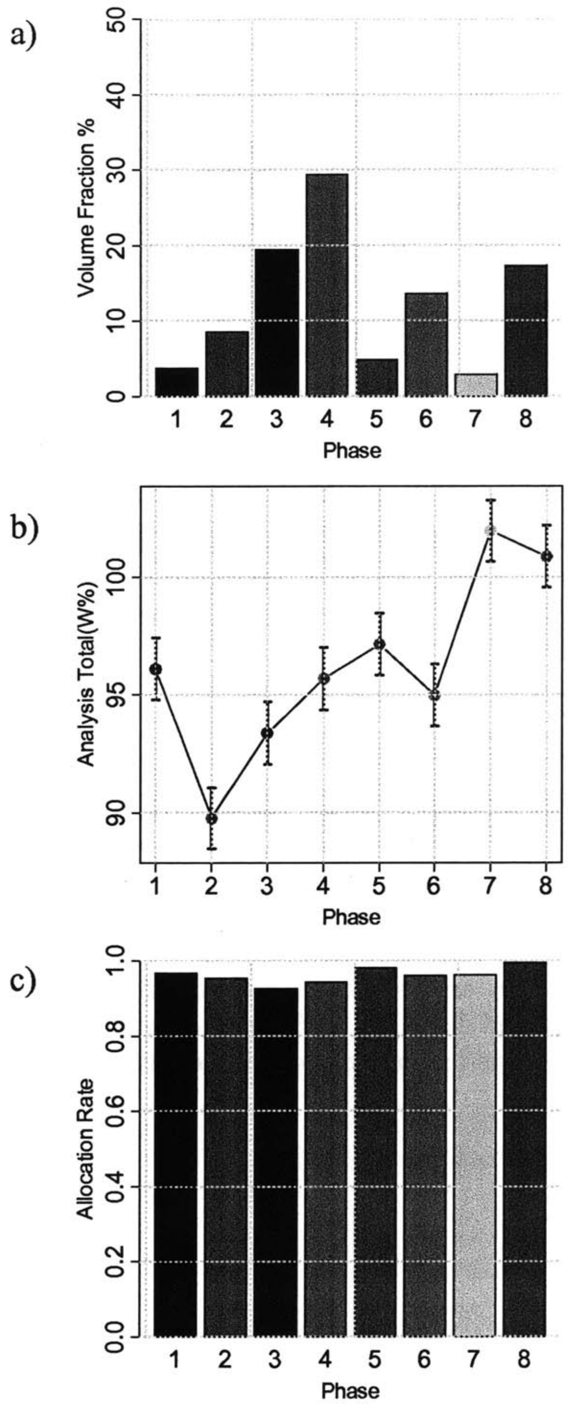

Figure 6-4: Graphical representation of clustering results presented in Table 6.5 for experiment S7-b. a) volume fractions, b) mean and standard deviation values of the analysis totals, and c) allocation rates for each of the phases displayed in Figure 6-3.

Phase		1	2	3	4	5	6	7	8
Si	μ	11.96	13.37	15.53	15.93	16.71	19.80	23.81	31.36
	σ	3.47	2.54	1.25	2.33	0.94	2.61	4.90	1.55
Al	μ	8.25	8.78	10.87	10.24	11.92	9.59	6.54	0.31
	σ	2.39	1.97	0.99	1.64	0.76	1.86	3.96	0.32
K	μ	0.35	1.00	0.43	0.56	0.45	1.32	0.27	0.02
	σ	0.19	0.50	0.10	0.26	0.12	1.36	0.15	0.02
Ca	μ	0.41	0.53	0.13	0.06	0.04	0.03	0.08	0.11
	σ	0.30	1.08	0.08	0.04	0.02	0.02	0.11	0.19
Na	μ	1.27	1.29	0.71	0.59	0.56	0.42	0.31	0.03
	σ	0.56	0.92	0.17	0.20	0.13	0.18	0.17	0.04
Fe	μ	6.41	2.81	2.37	1.59	1.32	0.89	0.75	0.12
	σ	3.32	1.83	1.13	0.54	0.26	0.30	0.37	0.07
Mg	μ	0.63	0.64	1.20	0.38	0.50	1.01	0.19	0.02
	σ	0.71	0.50	1.11	0.19	0.28	1.06	0.11	0.02

Table 6.6: Summary of the make up of the chemical phases identified by cluster analysis and displayed in Figure 6-5 for experiment S7-c. The notations μ and σ correspond to the mean and standard deviation of the given property. The standard deviation corresponds to the square root of the variance.

Phase	1	2	3	4	5	6	7	8
Volume fraction (%)	8.17	2.63	19.77	17.42	26.77	8.00	10.27	6.97
Analysis total μ	81.29	79.89	87.30	83.57	88.74	92.65	92.98	96.88
Analysis total σ	7.76	9.74	3.88	8.57	3.01	4.46	4.35	4.18
Allocation	0.95	0.99	0.90	0.88	0.90	0.96	0.94	1.00

Table 6.7: Volume fractions, analysis totals, and allocation rates for the chemical phases identified by cluster analysis and displayed in Figure 6-5 for experiment S7-c. The notations μ and σ correspond to the mean and standard deviation of the given property.

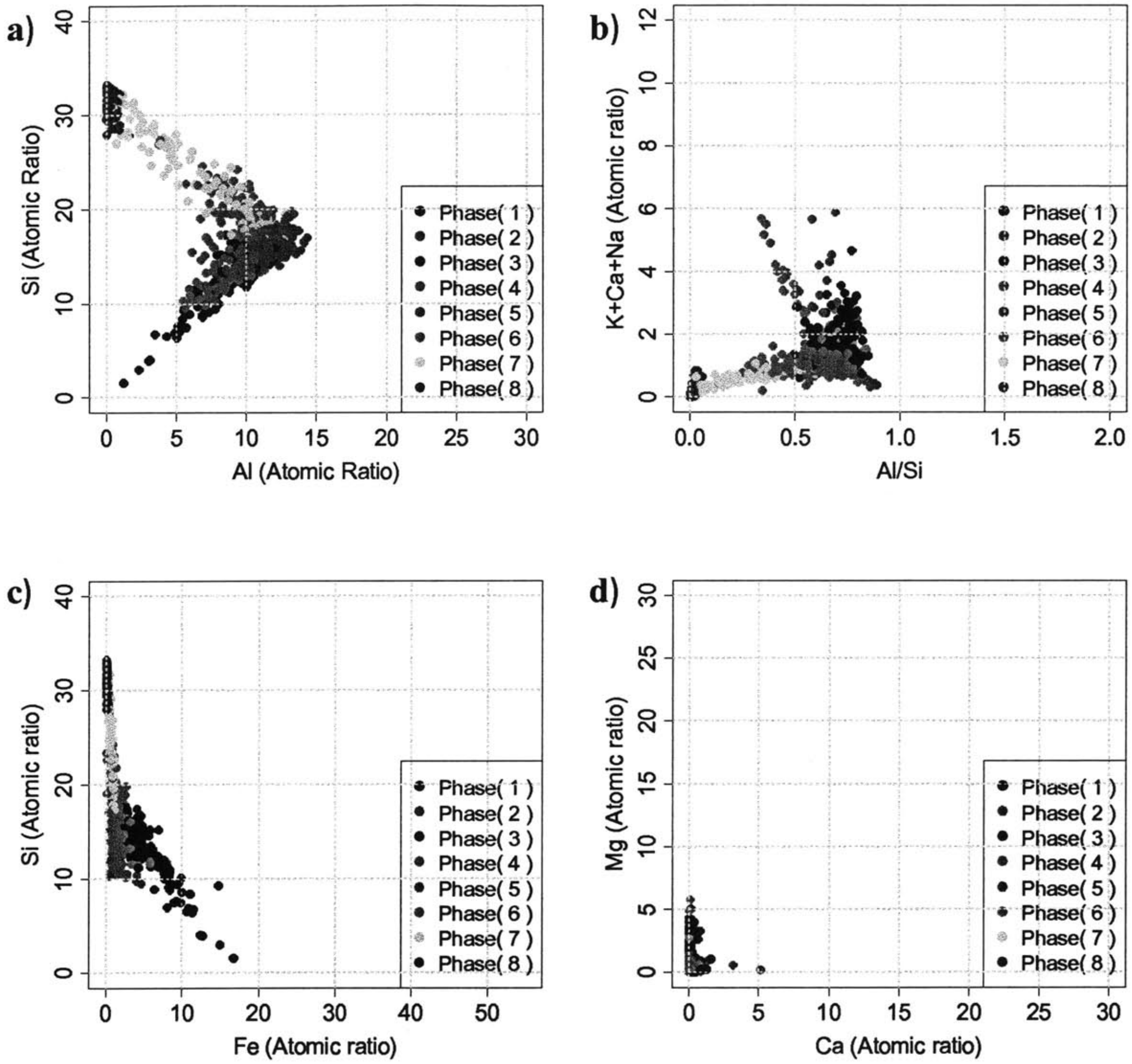

Figure 6-5: Multivariate cluster analysis of the grid WDS data for experiment S7-c. The identified phases are presented on 2-D projections for visual interpretation of the data: a) Al-Si space and b) Ca+Na+K-Al/Si space separate quartz, feldspars, and clay minerals. c) Fe-Si space and d) Ca-Mg space separate carbonate minerals; siderite, calcite, magnesite, ankerite, and dolomite.

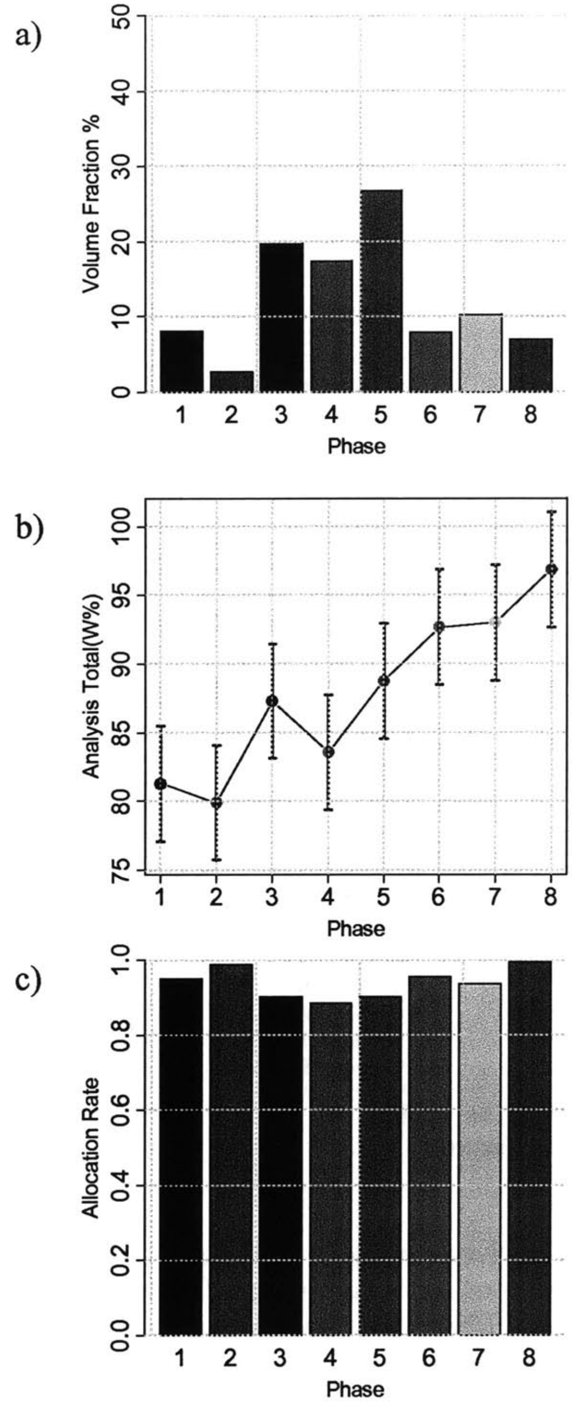

Figure 6-6: Graphical representation of clustering results presented in Table 6.7 for experiment S7-c. a) volume fractions, b) mean and standard deviation values of the analysis totals, and c) allocation rates for each of the phases displayed in Figure 6-5.

Phase		1	2	3	4	5	6	7	8
Si	μ	12.98	15.60	16.59	17.28	17.94	19.56	28.45	32.61
	σ	3.15	2.23	1.09	0.70	2.15	3.45	1.70	0.68
Al	μ	8.19	10.29	11.44	12.08	10.84	8.25	3.86	0.38
	σ	1.95	1.08	0.62	0.51	1.51	2.25	1.69	0.33
K	μ	0.03	0.02	0.03	0.02	0.02	0.10	0.00	0.00
	σ	0.03	0.01	0.02	0.01	0.01	0.12	0.00	0.00
Ca	μ	0.84	0.34	0.13	0.07	0.07	0.09	0.03	0.00
	σ	1.14	0.18	0.05	0.02	0.02	0.10	0.02	0.00
Na	μ	1.50	0.96	0.75	0.70	0.54	0.23	0.22	0.03
	σ	0.95	0.34	0.18	0.10	0.10	0.19	0.09	0.03
Fe	μ	4.95	3.08	1.58	1.31	1.13	0.68	0.50	0.12
	σ	3.23	1.42	0.31	0.14	0.13	0.44	0.16	0.03
Mg	μ	2.13	1.79	2.43	2.29	1.45	1.45	0.32	0.03
	σ	1.77	0.96	1.92	0.89	0.96	1.65	0.24	0.03

Table 6.8: Summary of the make up of the chemical phases identified by cluster analysis and displayed in Figure 6-7 for experiment S7-d. The notations μ and σ correspond to the mean and standard deviation of the given property. The standard deviation corresponds to the square root of the variance.

Phase	1	2	3	4	5	6	7	8
Volume fraction (%)	7.35	16.20	22.59	21.68	18.13	5.73	3.90	4.42
Analysis total μ	83.63	89.10	90.90	93.25	90.26	87.53	99.60	102.11
Analysis total σ	3.04	3.04	3.04	3.04	3.04	3.04	3.04	3.04
Allocation	0.98	0.96	0.91	0.89	0.89	0.97	1.00	1.00

Table 6.9: Volume fractions, analysis totals, and allocation rates for the chemical phases identified by cluster analysis and displayed in Figure 6-7 for experiment S7-d. The notations μ and σ correspond to the mean and standard deviation of the given property.

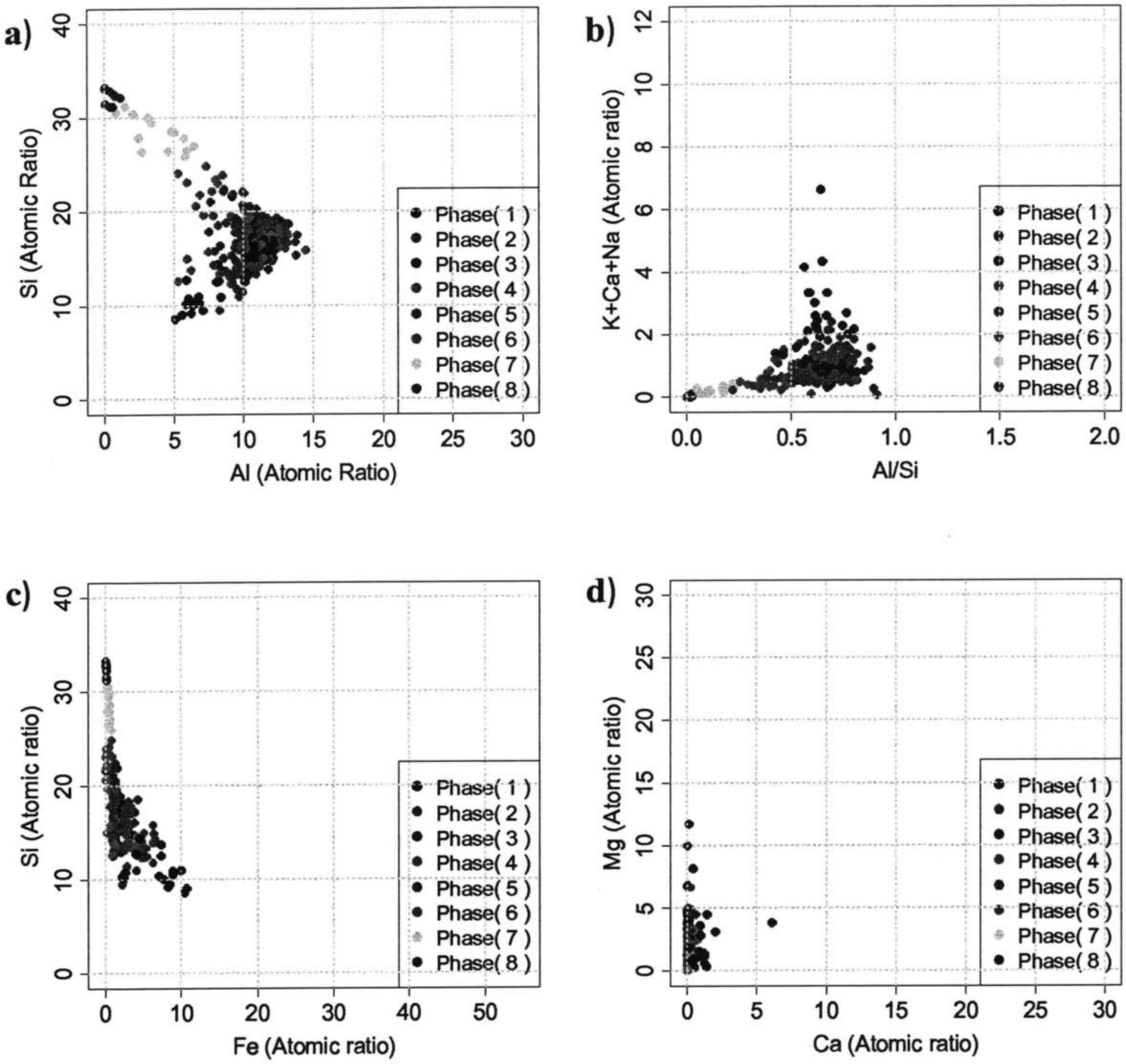

Figure 6-7: Multivariate cluster analysis of the grid WDS data for experiment S7-d. The identified phases are presented on 2-D projections for visual interpretation of the data: a) Al-Si space and b) Ca+Na+K-Al/Si space separate quartz, feldspars, and clay minerals. c) Fe-Si space and d) Ca-Mg space separate carbonate minerals; siderite, calcite, magnesite, ankerite, and dolomite.

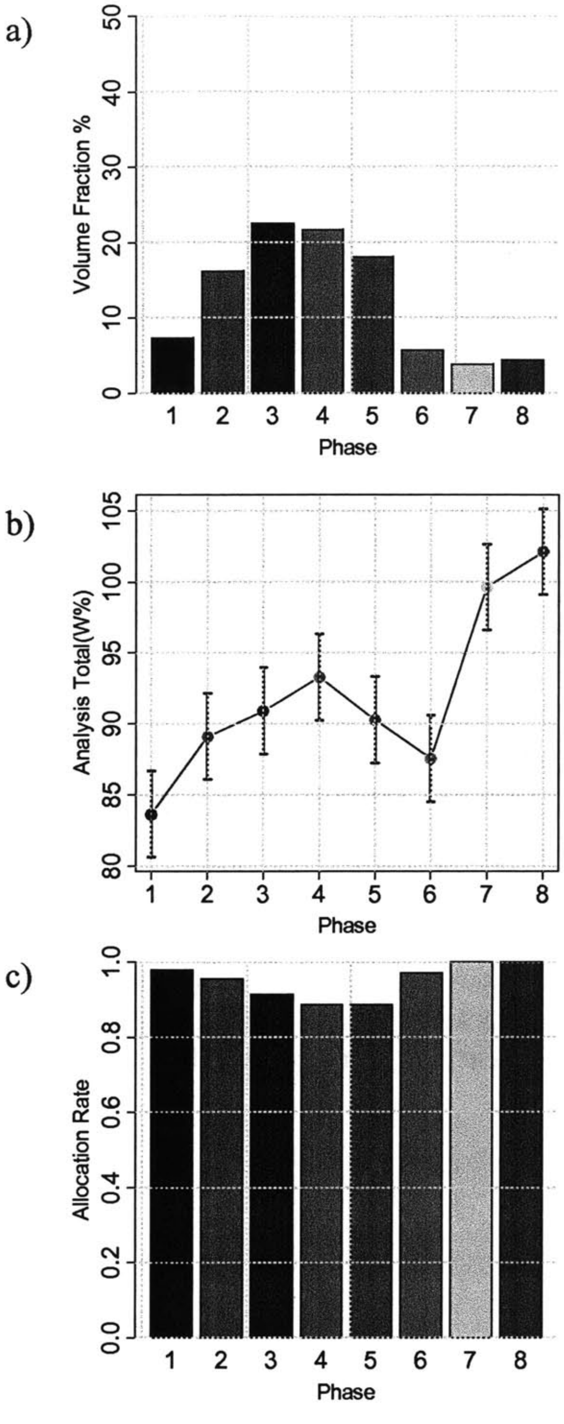

Figure 6-8: Graphical representation of clustering results presented in Table 6.9 for experiment S7-d. a) volume fractions, b) mean and standard deviation values of the analysis totals, and c) allocation rates for each of the phases displayed in Figure 6-7.

Phase		1	2	3	4	5	6	7
Si	μ	8.76	15.17	15.86	16.72	17.47	19.72	30.27
	σ	2.51	2.04	1.13	1.26	0.83	3.19	2.00
Al	μ	6.06	9.53	11.11	11.24	12.12	9.49	1.99
	σ	1.67	1.63	0.70	0.94	0.61	2.04	1.61
K	μ	0.03	0.06	0.07	0.05	0.05	0.13	0.01
	σ	0.01	0.04	0.02	0.02	0.02	0.18	0.02
Ca	μ	0.77	0.46	0.08	0.20	0.07	0.05	0.01
	σ	0.45	0.32	0.03	0.08	0.02	0.03	0.01
Na	μ	1.94	1.05	0.75	0.78	0.65	0.41	0.14
	σ	0.84	0.43	0.18	0.13	0.12	0.18	0.11
Fe	μ	10.29	3.36	1.40	2.10	1.29	0.93	0.31
	σ	2.29	1.92	0.22	0.52	0.15	0.35	0.17
Mg	μ	0.94	2.32	3.30	2.13	2.30	1.16	0.22
	σ	0.57	1.91	1.95	1.33	1.04	1.08	0.36

Table 6.10: Summary of the make up of the chemical phases identified by cluster analysis and displayed in Figure 6-9 for experiment S7-e. The notations μ and σ correspond to the mean and standard deviation of the given property. The standard deviation corresponds to the square root of the variance.

Phase	1	2	3	4	5	6	7
Volume fraction (%)	3.21	10.05	15.38	14.24	38.57	13.49	5.06
Analysis total μ	81.17	87.69	89.49	91.90	93.58	90.77	98.89
Analysis total σ	3.97	3.97	3.97	3.97	3.97	3.97	3.97
Allocation	1.00	0.98	0.85	0.95	0.92	0.95	1.00

Table 6.11: Volume fractions, analysis totals, and allocation rates for the chemical phases identified by cluster analysis and displayed in Figure 6-9 for experiment S7-e. The notations μ and σ correspond to the mean and standard deviation of the given property.

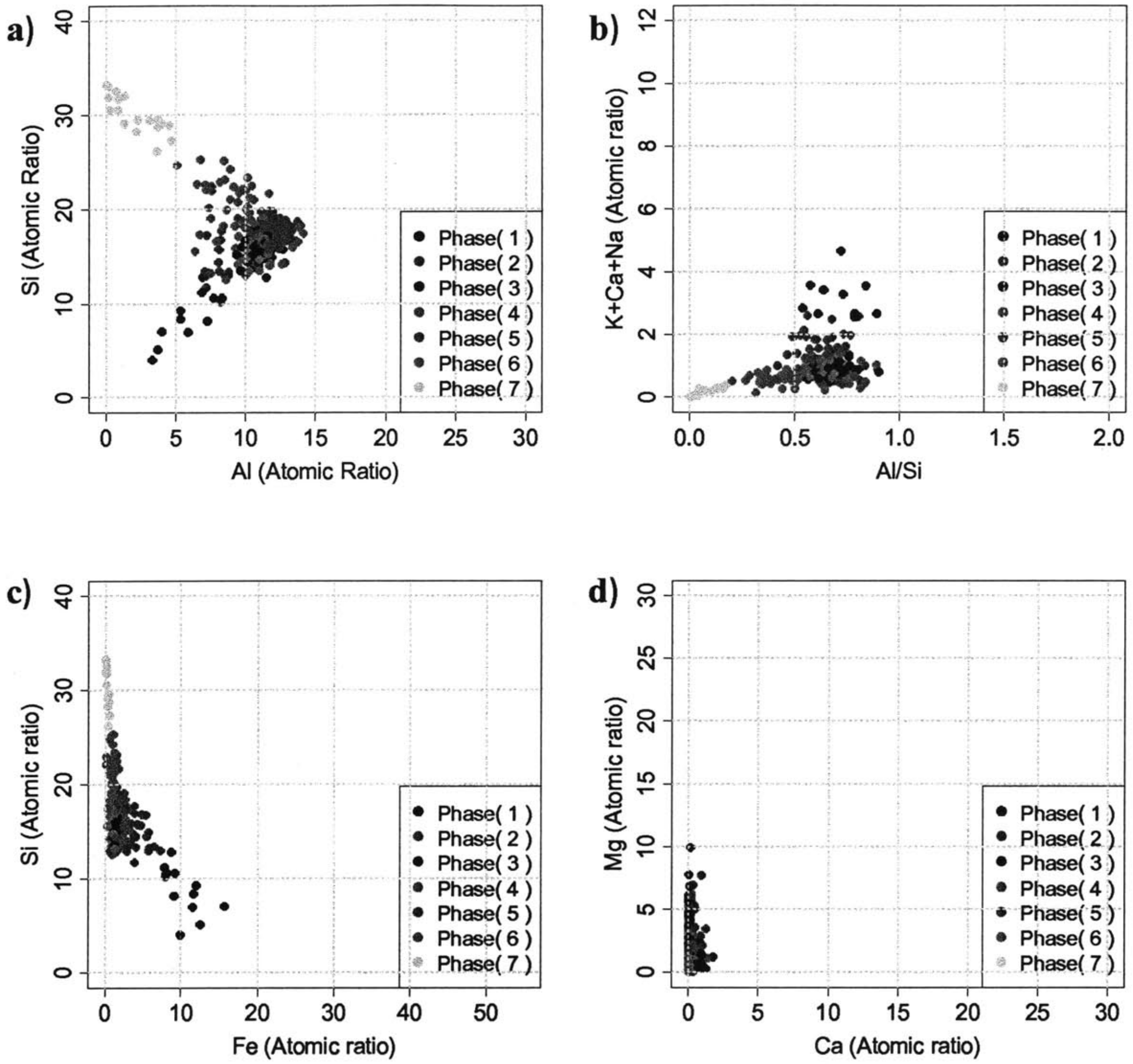

Figure 6-9: Multivariate cluster analysis of the grid WDS data for experiment S7-e. The identified phases are presented on 2-D projections for visual interpretation of the data: a) Al-Si space and b) Ca+Na+K-Al/Si space separate quartz, feldspars, and clay minerals. c) Fe-Si space and d) Ca-Mg space separate carbonate minerals; siderite, calcite, magnesite, ankerite, and dolomite.

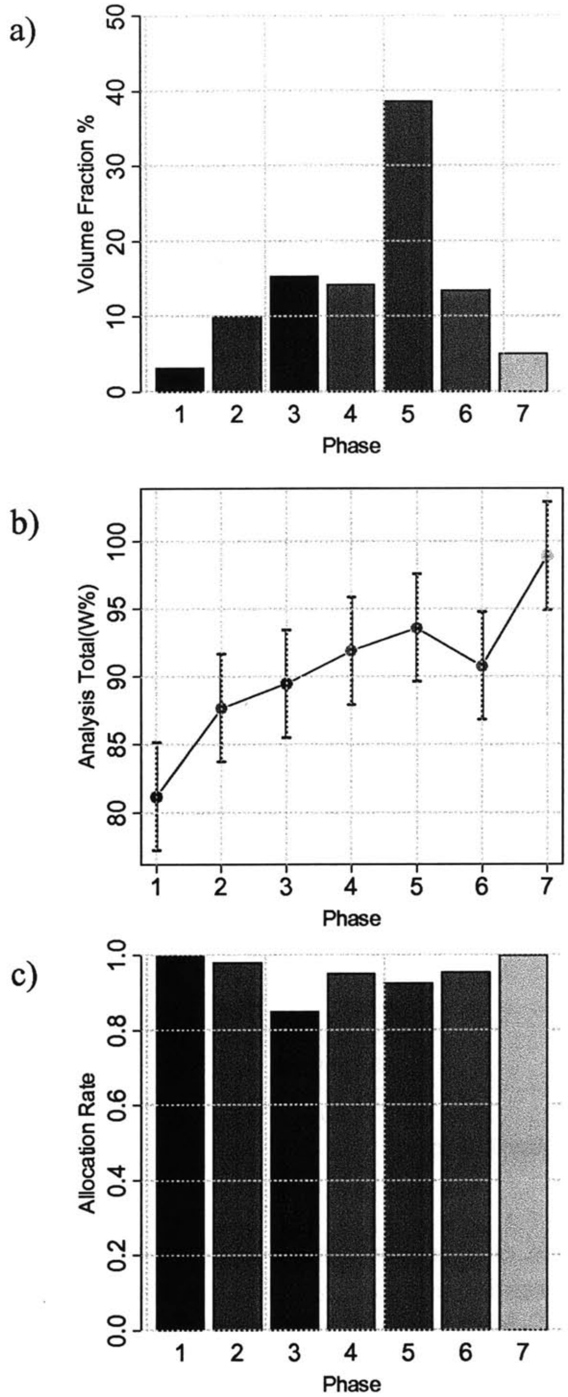

Figure 6-10: Graphical representation of clustering results presented in Table 6.11 for experiment S7-e. a) volume fractions, b) mean and standard deviation values of the analysis totals, and c) allocation rates for each of the phases displayed in Figure 6-9.

Phase		1	2	3	4	5	6	7	8	9	10
Si	μ	18.77	19.68	20.67	20.89	21.08	21.24	24.33	24.39	29.43	33.46
	σ	3.00	1.12	1.52	3.27	1.85	1.17	1.17	1.54	0.94	0.44
Al	μ	8.91	9.28	9.05	8.53	8.28	8.54	6.22	6.36	3.17	0.24
	σ	1.35	1.57	1.33	1.72	1.01	0.71	0.80	1.14	0.71	0.24
K	μ	1.48	1.89	1.58	1.52	1.61	1.71	1.23	1.10	0.60	0.04
	σ	0.54	0.62	0.39	2.51	0.31	0.25	0.26	0.22	0.20	0.07
Ca	μ	0.06	0.02	0.02	0.34	0.03	0.02	0.02	0.10	0.01	0.00
	σ	0.06	0.02	0.02	0.63	0.02	0.01	0.01	0.22	0.01	0.01
Na	μ	0.89	0.79	0.87	3.07	1.24	0.91	0.71	1.53	0.46	0.05
	σ	0.31	0.15	0.20	5.26	0.42	0.13	0.12	0.73	0.20	0.11
Fe	μ	4.18	2.95	2.41	1.92	2.80	2.60	2.01	1.76	1.07	0.14
	σ	1.97	0.90	0.42	2.98	0.52	0.34	0.42	0.39	0.31	0.11
Mg	μ	1.94	1.62	1.26	0.87	1.26	1.36	1.01	0.92	0.53	0.03
	σ	1.04	0.44	0.24	1.15	0.22	0.19	0.21	0.20	0.18	0.05

Table 6.12: Summary of the make up of the chemical phases identified by cluster analysis, and displayed in Figure 6-11 for experiment S3-a. The notations μ and σ correspond to the mean and standard deviation of the given property. The standard deviation corresponds to the square root of the variance.

Phase	1	2	3	4	5	6	7	8	9	10
Volume fraction (%)	7.36	10.30	12.95	4.21	14.17	33.65	9.50	1.61	3.46	2.80
Analysis total μ	97.04	98.27	98.02	98.09	97.16	97.10	99.04	97.73	98.59	100.67
Analysis total σ	4.06	3.25	4.48	6.04	5.02	4.01	3.68	3.09	2.46	1.44
Allocation	0.95	0.91	0.94	1.00	0.90	0.89	0.91	0.96	0.98	1.00

Table 6.13: Volume fractions, analysis totals, and allocation rates for the chemical phases identified by cluster analysis and displayed in Figure 6-11 for experiment S3-a. The notations μ and σ correspond to the mean and standard deviation of the given property.

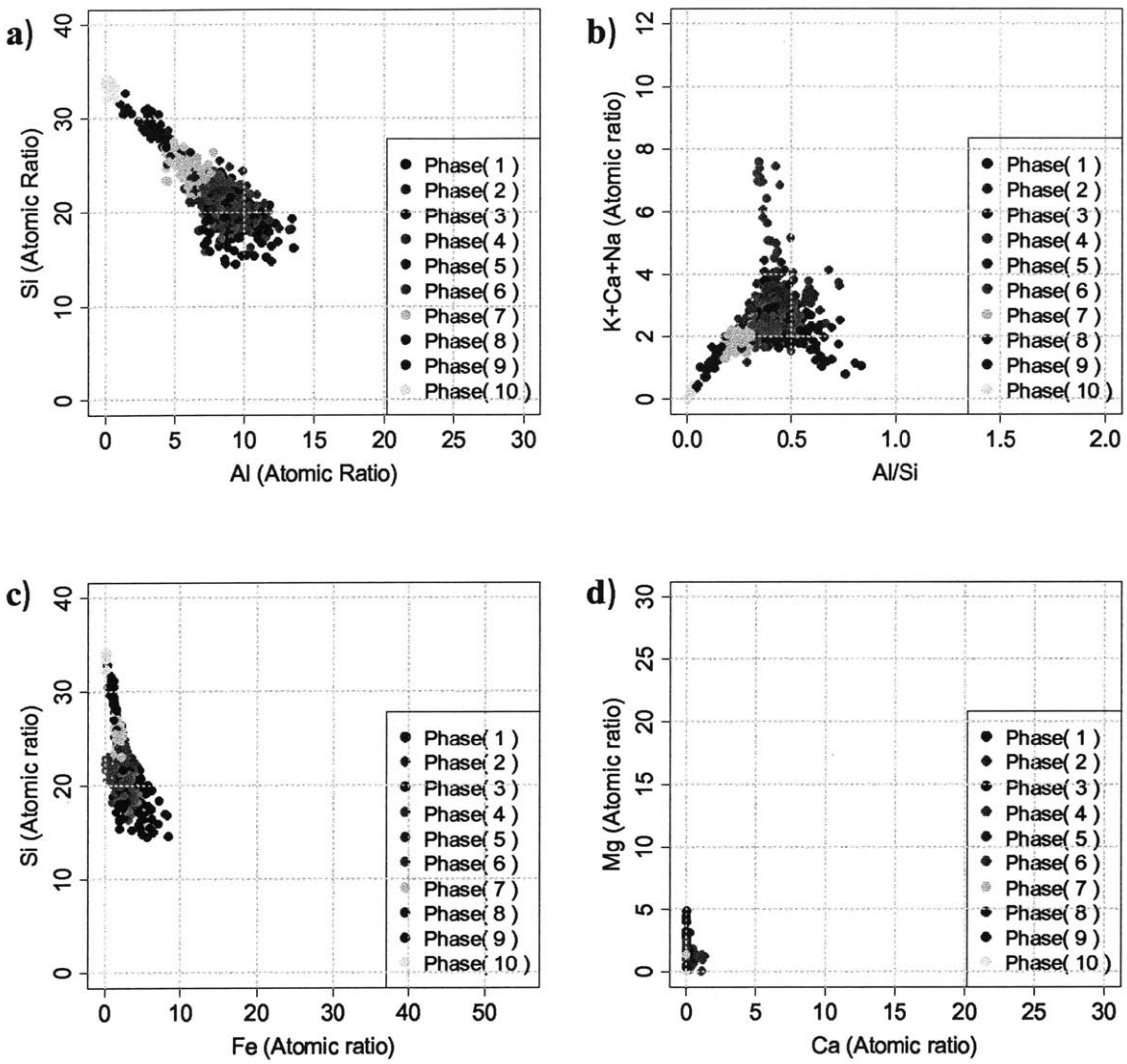

Figure 6-11: Multivariate cluster analysis of the grid WDS data for experiment S3-a. The identified phases are presented on 2-D projections for visual interpretation of the data: a) Al-Si space and b) Ca+Na+K-Al/Si space separate quartz, feldspars, and clay minerals. c) Fe-Si space and d) Ca-Mg space separate carbonate minerals; siderite, calcite, magnesite, ankerite, and dolomite.

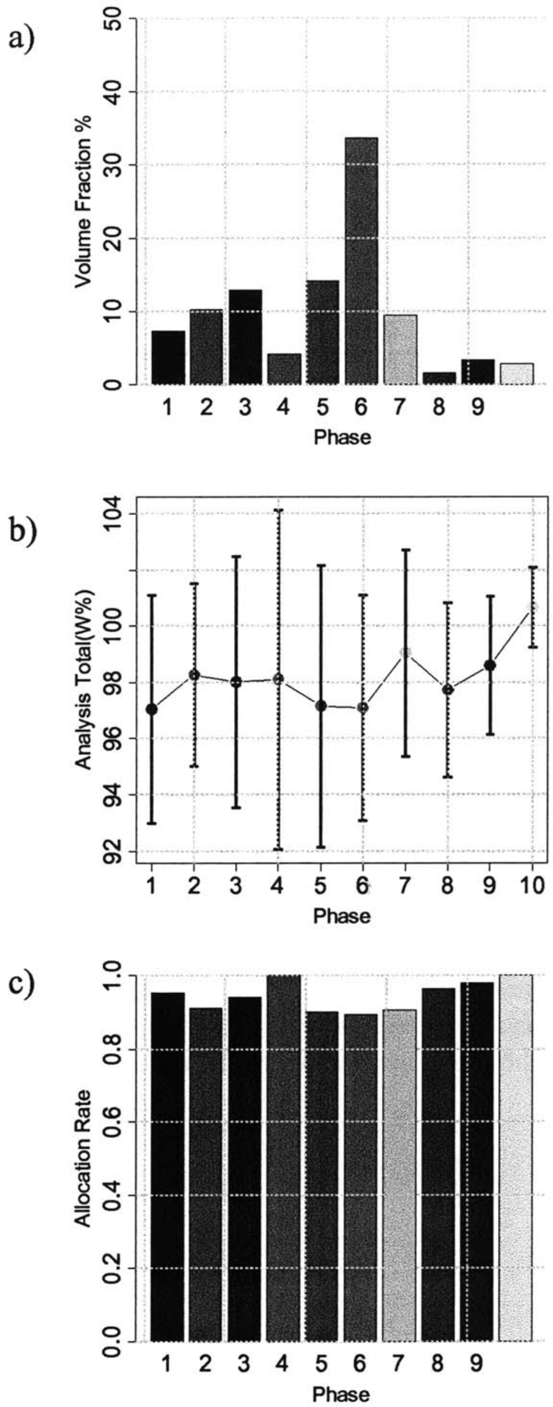

Figure 6-12: Graphical representation of clustering results presented in Table 6.13 for experiment S3-a. a) volume fractions, b) mean and standard deviation values of the analysis totals, and c) allocation rates for each of the phases displayed in Figure 6-11.

Phase		1	2	3	4	5	6	7	8	9
Si	μ	17.91	18.98	19.57	19.78	20.25	21.89	22.72	24.79	33.03
	σ	1.56	1.31	1.35	2.08	2.88	1.29	0.15	3.50	0.25
Al	μ	9.86	9.04	8.17	7.52	7.41	7.65	7.80	5.09	0.13
	σ	1.70	0.94	0.83	1.21	1.35	0.47	0.09	2.45	0.16
K	μ	2.00	1.62	1.68	1.48	1.34	2.39	7.28	1.01	0.02
	σ	1.31	0.34	0.30	0.36	0.45	2.28	0.20	0.51	0.02
Ca	μ	0.01	0.04	0.01	0.01	0.36	0.03	0.00	0.01	0.00
	σ	0.01	0.02	0.01	0.01	0.46	0.04	0.00	0.01	0.00
Na	μ	0.53	0.72	0.65	1.24	0.89	4.45	0.30	0.43	0.03
	σ	0.20	0.36	0.17	0.89	0.70	2.24	0.08	0.20	0.04
Fe	μ	2.61	2.07	2.17	2.38	1.93	0.52	0.14	1.34	0.10
	σ	1.16	0.40	0.33	0.80	0.60	0.45	0.07	0.61	0.03
Mg	μ	1.56	1.16	1.34	1.30	1.01	0.28	0.03	0.83	0.02
	σ	0.66	0.28	0.20	0.46	0.34	0.29	0.05	0.41	0.04

Table 6.14: Summary of the make up of the chemical phases identified by cluster analysis and displayed in Figure 6-13 for experiment S3-b. The notations μ and σ correspond to the mean and standard deviation of the given property. The standard deviation corresponds to the square root of the variance.

Phase	1	2	3	4	5	6	7	8	9
Volume fraction (%)	11.62	10.15	34.23	14.69	2.75	4.61	2.38	14.08	5.49
Analysis total μ	92.94	92.30	92.35	92.36	91.67	97.82	99.94	95.48	100.68
Analysis total σ	1.28	1.28	1.28	1.28	1.28	1.28	1.28	1.28	1.28
Allocation	0.91	0.87	0.85	0.89	0.98	1.00	1.00	0.93	1.00

Table 6.15: Volume fractions, analysis totals, and allocation rates for the chemical phases identified by cluster analysis and displayed in Figure 6-13 for experiment S3-b. The notations μ and σ correspond to the mean and standard deviation of the given property.

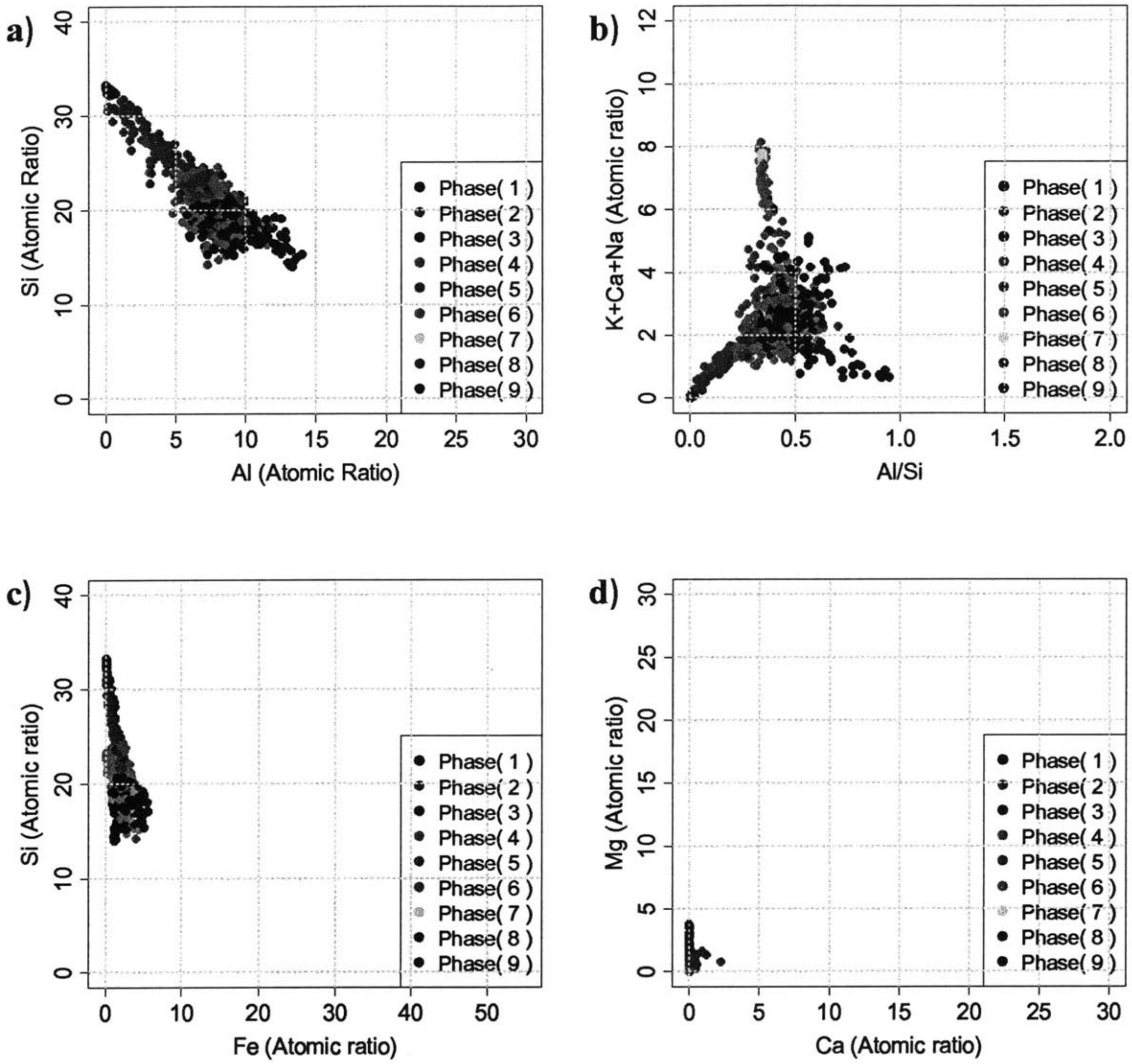

Figure 6-13: Multivariate cluster analysis of the grid WDS data for experiment S3-b. The identified phases are presented on 2-D projections for visual interpretation of the data: a) Al-Si space and b) Ca+Na+K-Al/Si space separate quartz, feldspars, and clay minerals. c) Fe-Si space and d) Ca-Mg space separate carbonate minerals; siderite, calcite, magnesite, ankerite, and dolomite.

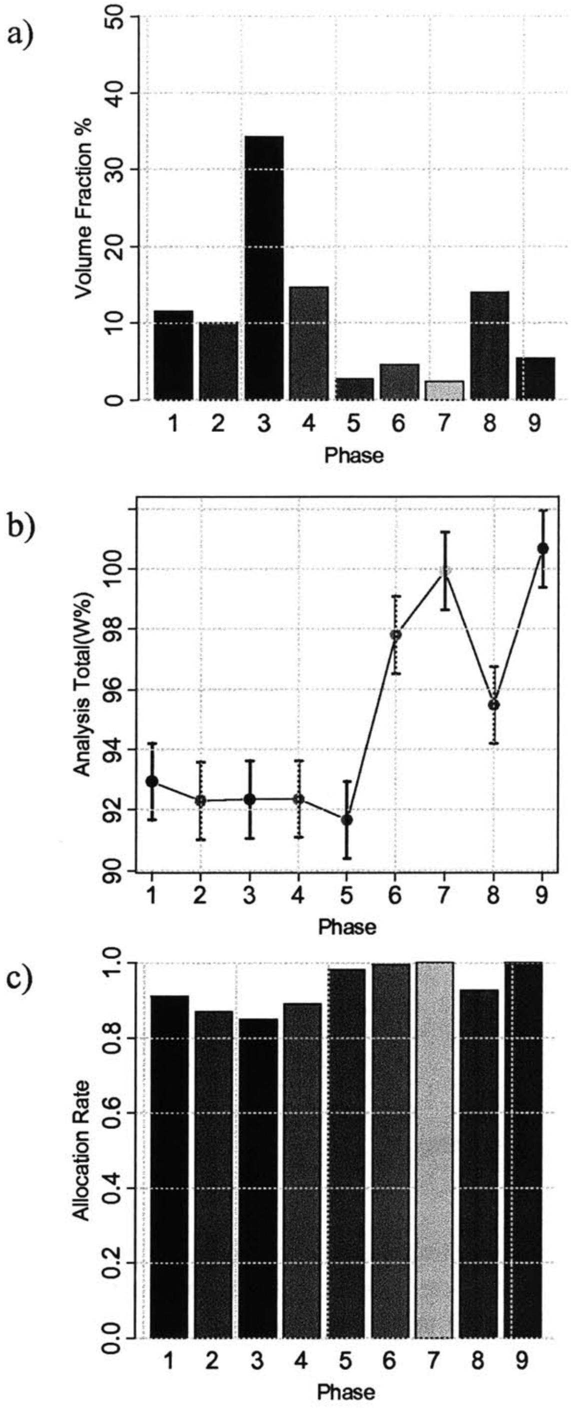

Figure 6-14: Graphical representation of clustering results presented in Table 6.15 for experiment S3-b. a) volume fractions, b) mean and standard deviation values of the analysis totals, and c) allocation rates for each of the phases displayed in Figure 6-13.

Phase		1	2	3	4
Si	μ	18.08	19.97	21.92	26.90
	σ	1.90	1.92	2.11	3.73
Al	μ	9.51	8.21	6.79	4.78
	σ	1.86	1.19	1.56	3.00
K	μ	1.32	1.54	1.11	0.88
	σ	0.59	0.37	0.36	0.58
Ca	μ	0.27	0.08	0.08	0.05
	σ	0.41	0.02	0.04	0.03
Na	μ	0.33	0.41	0.99	0.25
	σ	0.27	0.14	0.75	0.17
Fe	μ	2.99	2.47	1.73	1.52
	σ	0.91	0.60	0.51	0.91
Mg	μ	1.41	1.22	0.87	0.67
	σ	0.85	0.27	0.27	0.46

Table 6.16: Summary of the make up of the chemical phases identified by cluster analysis and displayed in Figure 6-15 for experiment S3-c. The notations μ and σ correspond to the mean and standard deviation of the given property. The standard deviation corresponds to the square root of the variance.

Phase	1	2	3	4
Volume fraction (%)	12.61	61.61	6.91	18.87
Analysis total μ	92.46	93.44	93.81	101.87
Analysis total σ	4.54	4.94	5.87	4.35
Allocation	0.97	0.96	0.96	0.92

Table 6.17: Volume fractions, analysis totals, and allocation rates for the chemical phases identified by cluster analysis and displayed in Figure 6-15 for experiment S3-c. The notations μ and σ correspond to the mean and standard deviation of the given property.

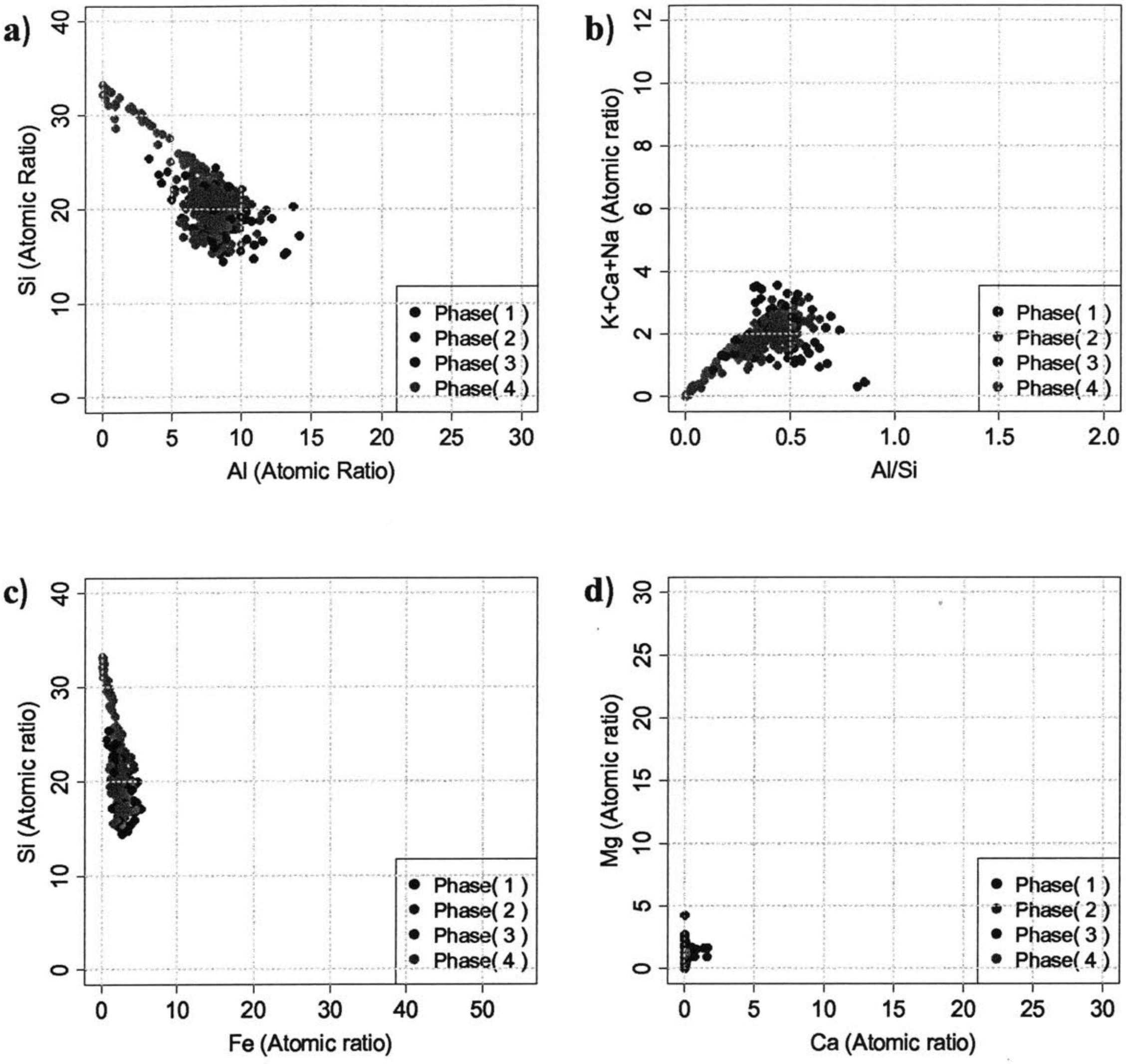

Figure 6-15: Multivariate cluster analysis of the grid WDS data for experiment S3-c. The identified phases are presented on 2-D projections for visual interpretation of the data: a) Al-Si space and b) Ca+Na+K-Al/Si space separate quartz, feldspars, and clay minerals. c) Fe-Si space and d) Ca-Mg space separate carbonate minerals; siderite, calcite, magnesite, ankerite, and dolomite.

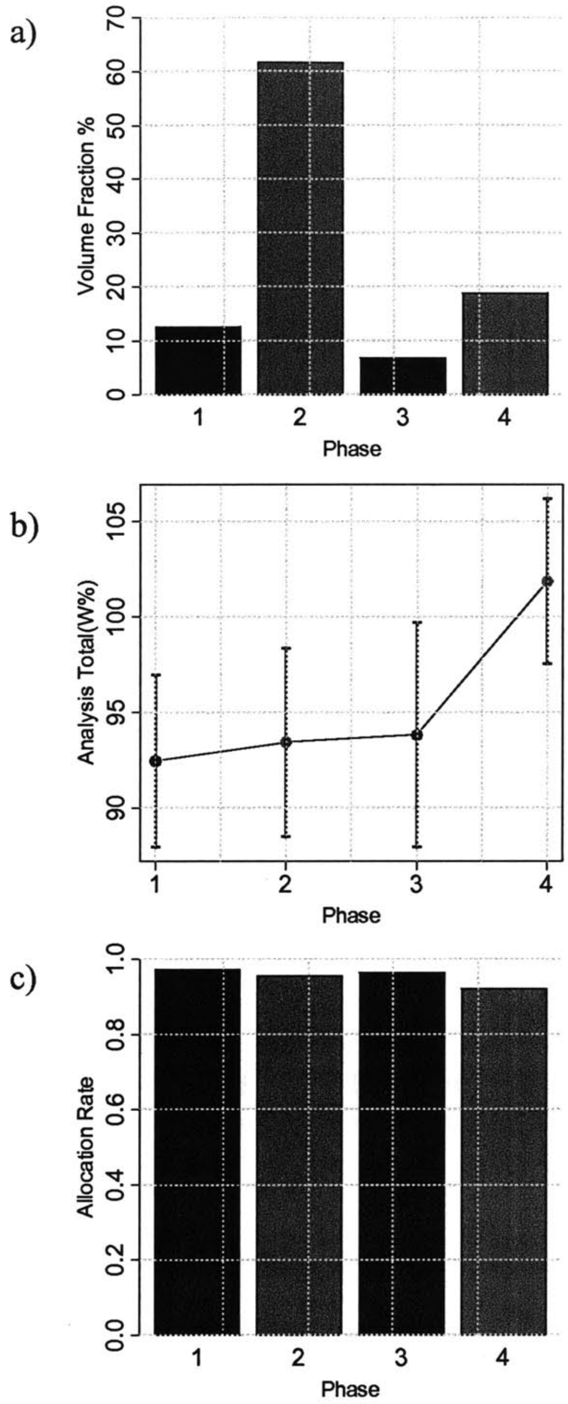

Figure 6-16: Graphical representation of clustering results presented in Table 6.17 for experiment S3-c. a) volume fractions, b) mean and standard deviation values of the analysis totals, and c) allocation rates for each of the phases displayed in Figure 6-15.

Phase		1	2	3	4	5
Si	μ	18.54	19.99	21.21	22.03	29.40
	σ	1.33	1.19	1.16	1.83	2.98
Al	μ	9.49	8.98	8.79	7.76	2.64
	σ	1.31	1.00	0.96	1.34	2.28
K	μ	1.68	1.61	1.50	1.53	0.54
	σ	0.80	0.34	0.51	0.29	0.48
Ca	μ	0.14	0.06	0.12	0.07	0.05
	σ	0.16	0.01	0.09	0.02	0.10
Na	μ	0.45	0.42	1.70	0.47	0.24
	σ	0.25	0.10	1.27	0.14	0.23
Fe	μ	2.79	2.81	2.02	2.31	0.72
	σ	0.97	0.68	0.79	0.47	0.62
Mg	μ	1.41	1.49	1.06	1.22	0.39
	σ	0.51	0.41	0.40	0.28	0.36

Table 6.18: Summary of the make up of the chemical phases identified by cluster analysis and displayed in Figure 6-17 for experiment S3-d. The notations μ and σ correspond to the mean and standard deviation of the given property. The standard deviation corresponds to the square root of the variance.

Phase	1	2	3	4	5
Volume fraction (%)	7.98	34.62	8.69	40.71	7.99
Analysis total μ	101.58	100.44	99.13	100.05	103.21
Analysis total σ	4.42	3.49	7.80	4.44	4.90
Allocation	0.96	0.92	0.97	0.92	1.00

Table 6.19: Volume fractions, analysis totals, and allocation rates for the chemical phases identified by cluster analysis, and displayed in Figure 6-17 for experiment S3-d. The notations μ and σ correspond to the mean and standard deviation of the given property.

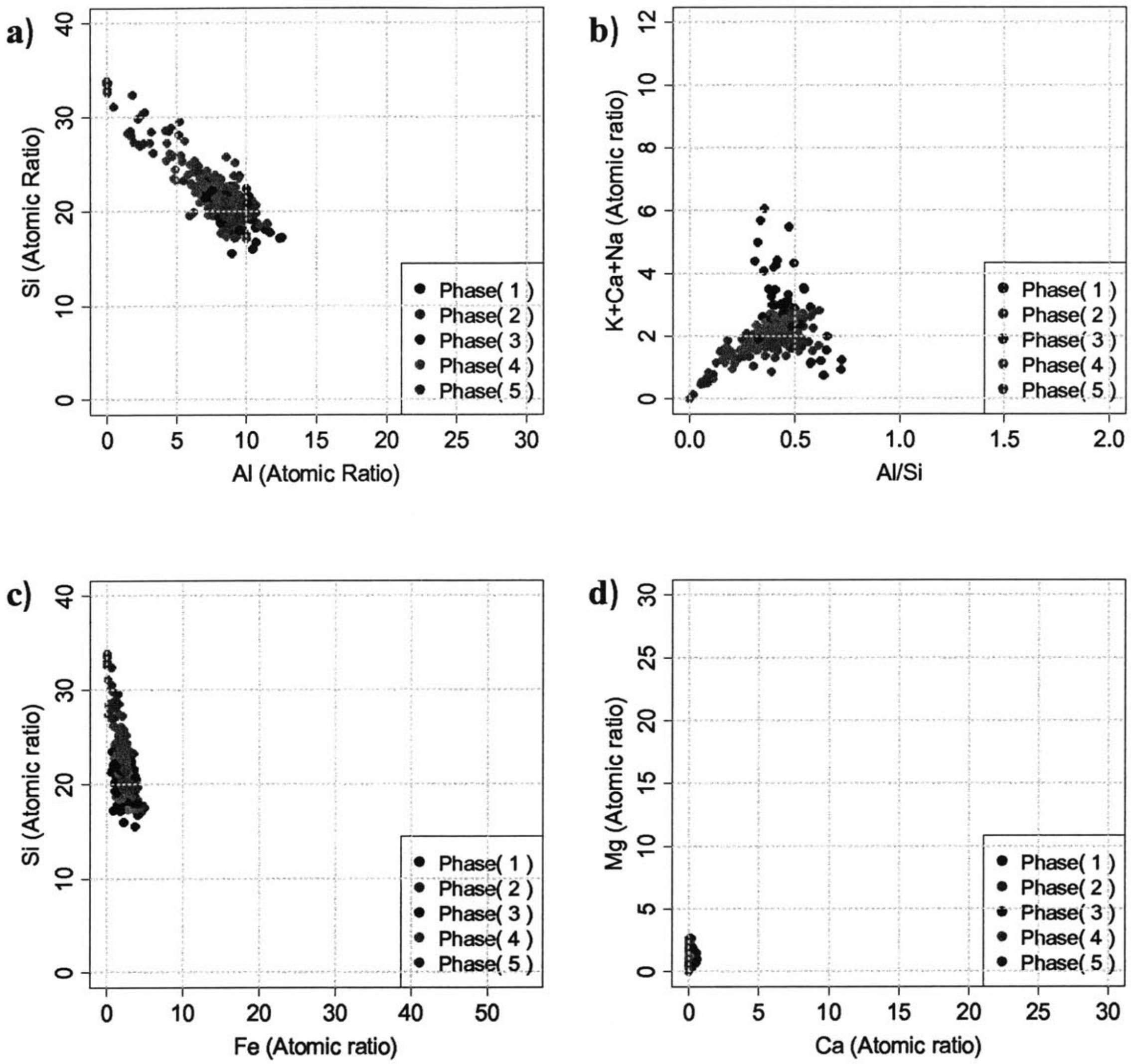

Figure 6-17: Multivariate cluster analysis of the grid WDS data for experiment S3-d. The identified phases are presented on 2-D projections for visual interpretation of the data: a) Al-Si space and b) Ca+Na+K-Al/Si space separate quartz, feldspars, and clay minerals. c) Fe-Si space and d) Ca-Mg space separate carbonate minerals; siderite, calcite, magnesite, ankerite, and dolomite.

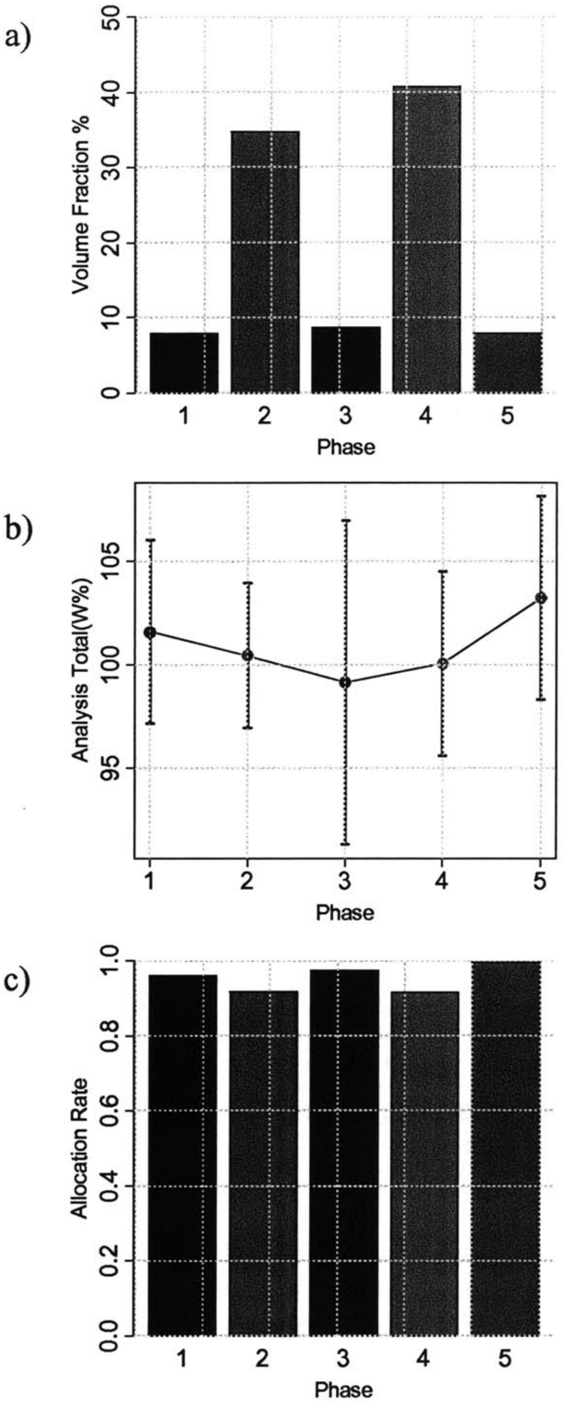

Figure 6-18: Graphical representation of clustering results presented in Table 6.19 for experiment S3-d. a) volume fractions, b) mean and standard deviation values of the analysis totals, and c) allocation rates for each of the phases displayed in Figure 6-17.

Phase		1	2	3	4	5	6	7	8	9
Si	μ	20.00	20.26	20.37	21.17	21.21	21.30	23.84	28.39	31.84
	σ	1.01	0.71	1.47	2.23	1.99	1.17	2.02	0.97	1.15
Al	μ	9.05	8.41	8.28	7.94	7.05	8.22	6.13	3.38	0.90
	σ	0.77	0.32	0.75	0.88	0.67	0.58	1.75	0.70	0.73
K	μ	1.77	2.00	1.60	2.02	1.40	1.66	1.16	0.72	0.24
	σ	0.31	0.47	0.18	0.95	0.16	0.15	0.22	0.24	0.25
Ca	μ	0.06	0.78	0.11	0.10	0.06	0.07	0.05	0.04	0.00
	σ	0.01	0.53	0.05	0.20	0.01	0.01	0.02	0.04	0.00
Na	μ	0.51	0.36	0.81	1.34	0.55	0.48	0.35	0.22	0.05
	σ	0.14	0.08	0.33	1.14	0.18	0.09	0.08	0.13	0.06
Fe	μ	2.88	3.13	2.53	1.54	2.29	2.46	1.73	0.95	0.22
	σ	0.42	0.63	0.37	0.46	0.26	0.19	0.37	0.25	0.12
Mg	μ	1.46	1.19	1.26	0.96	1.15	1.25	0.91	0.43	0.12
	σ	0.33	0.26	0.17	0.27	0.17	0.12	0.16	0.14	0.10

Table 6.20: Summary of the make up of the chemical phases identified by cluster analysis and displayed in Figure 6-19 for experiment S3-e. The notations μ and σ correspond to the mean and standard deviation of the given property. The standard deviation corresponds to the square root of the variance.

Phase	1	2	3	4	5	6	7	8	9
Volume fraction (%)	18.29	1.16	11.59	5.53	15.83	33.24	7.37	3.37	3.61
Analysis total μ	96.86	97.12	95.20	96.91	93.48	96.84	96.86	101.78	103.27
Analysis total σ	3.48	0.67	4.85	7.35	5.68	3.03	4.50	5.40	4.47
Allocation	0.91	1.00	0.93	0.97	0.87	0.87	0.94	1.00	1.00

Table 6.21: Volume fractions, analysis totals, and allocation rates for the chemical phases identified by cluster analysis and displayed in Figure 6-19 for experiment S3-e. The notations μ and σ correspond to the mean and standard deviation of the given property.

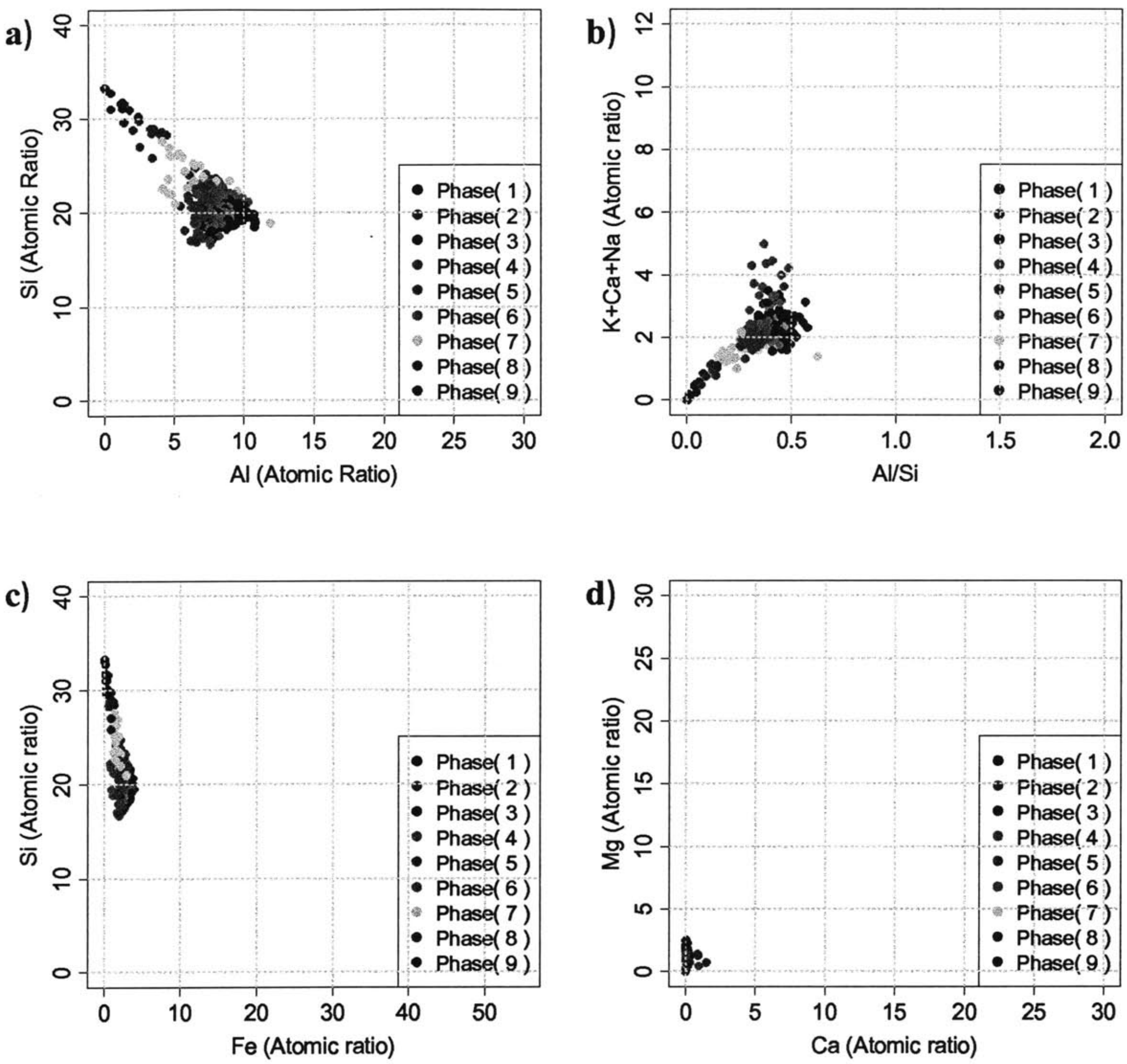

Figure 6-19: Multivariate cluster analysis of the grid WDS data for experiment S3-e. The identified phases are presented on 2-D projections for visual interpretation of the data: a) Al-Si space and b) Ca+Na+K-Al/Si space separate quartz, feldspars, and clay minerals. c) Fe-Si space and d) Ca-Mg space separate carbonate minerals; siderite, calcite, magnesite, ankerite, and dolomite.

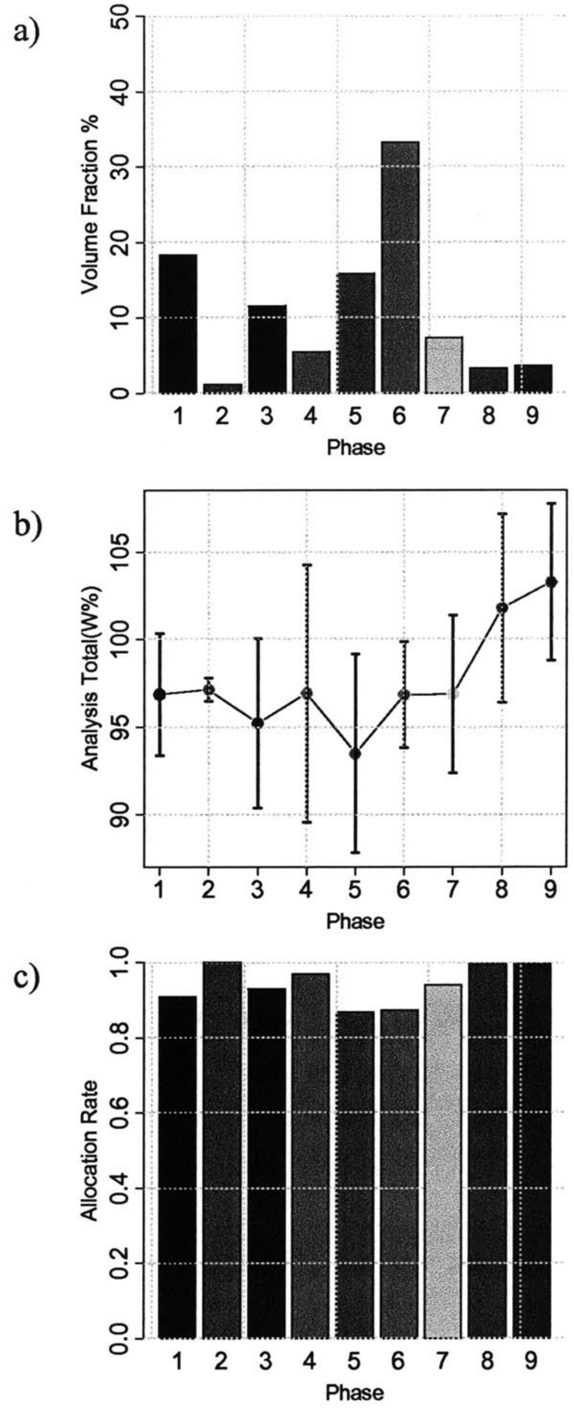

Figure 6-20: Graphical representation of clustering results presented in Table 6.21 for experiment S3-e. a) volume fractions, b) mean and standard deviation values of the analysis totals, and c) allocation rates for each of the phases displayed in Figure 6-19.

Phase		1	2	3	4	5	6	7	8	9	10	11
Si	μ	16.86	17.47	17.53	17.56	17.78	17.87	18.08	19.61	21.20	27.49	32.94
	σ	1.52	2.19	1.42	1.79	1.47	2.44	1.43	3.03	2.40	2.68	0.66
Al	μ	12.86	12.34	13.28	12.97	13.74	12.41	13.79	11.70	9.50	4.78	0.38
	σ	0.90	1.38	1.07	1.86	0.94	1.00	0.92	2.25	1.98	2.06	0.49
K	μ	0.93	0.92	0.81	1.81	0.86	0.84	0.88	0.61	2.51	0.31	0.02
	σ	0.32	0.46	0.18	1.01	0.19	0.50	0.22	0.17	2.77	0.21	0.02
Ca	μ	0.10	0.08	0.07	0.03	0.11	0.29	0.04	0.05	0.10	0.02	0.01
	σ	0.04	0.04	0.02	0.02	0.05	0.24	0.01	0.02	0.16	0.01	0.01
Na	μ	0.45	0.38	0.40	0.37	0.43	0.59	0.38	0.27	2.85	0.16	0.02
	σ	0.09	0.14	0.07	0.23	0.08	0.37	0.08	0.06	2.70	0.06	0.02
Fe	μ	3.29	2.97	1.92	1.04	1.36	1.34	1.22	1.20	0.32	0.51	0.09
	σ	1.15	1.08	0.54	0.46	0.27	0.37	0.23	0.41	0.22	0.21	0.05
Mg	μ	0.75	0.69	0.62	0.52	0.66	0.51	0.57	0.38	0.13	0.19	0.01
	σ	0.14	0.45	0.09	0.35	0.15	0.15	0.08	0.07	0.11	0.08	0.02

Table 6.22: Summary of the make up of the chemical phases identified by cluster analysis and displayed in Figure 6-21 for experiment S1-a. The notations μ and σ correspond to the mean and standard deviation of the given property. The standard deviation corresponds to the square root of the variance.

Phase	1	2	3	4	5	6	7	8	9	10	11
Volume fraction (%)	10.79	3.39	18.18	11.95	6.92	2.73	20.25	15.01	1.57	5.21	4.0
Analysis total μ	91.02	92.86	92.37	97.20	89.55	93.77	92.86	94.96	98.39	98.56	100.
Analysis total σ	3.38	3.38	3.38	3.38	3.38	3.38	3.38	3.38	3.38	3.38	3.3
Allocation	0.89	0.97	0.84	0.94	0.84	0.95	0.86	0.91	1.00	0.99	1.0

Table 6.23: Volume fractions, analysis totals, and allocation rates for the chemical phases identified by cluster analysis and displayed in Figure 6-21 for experiment S1-a. The notations μ and σ correspond to the mean and standard deviation of the given property.

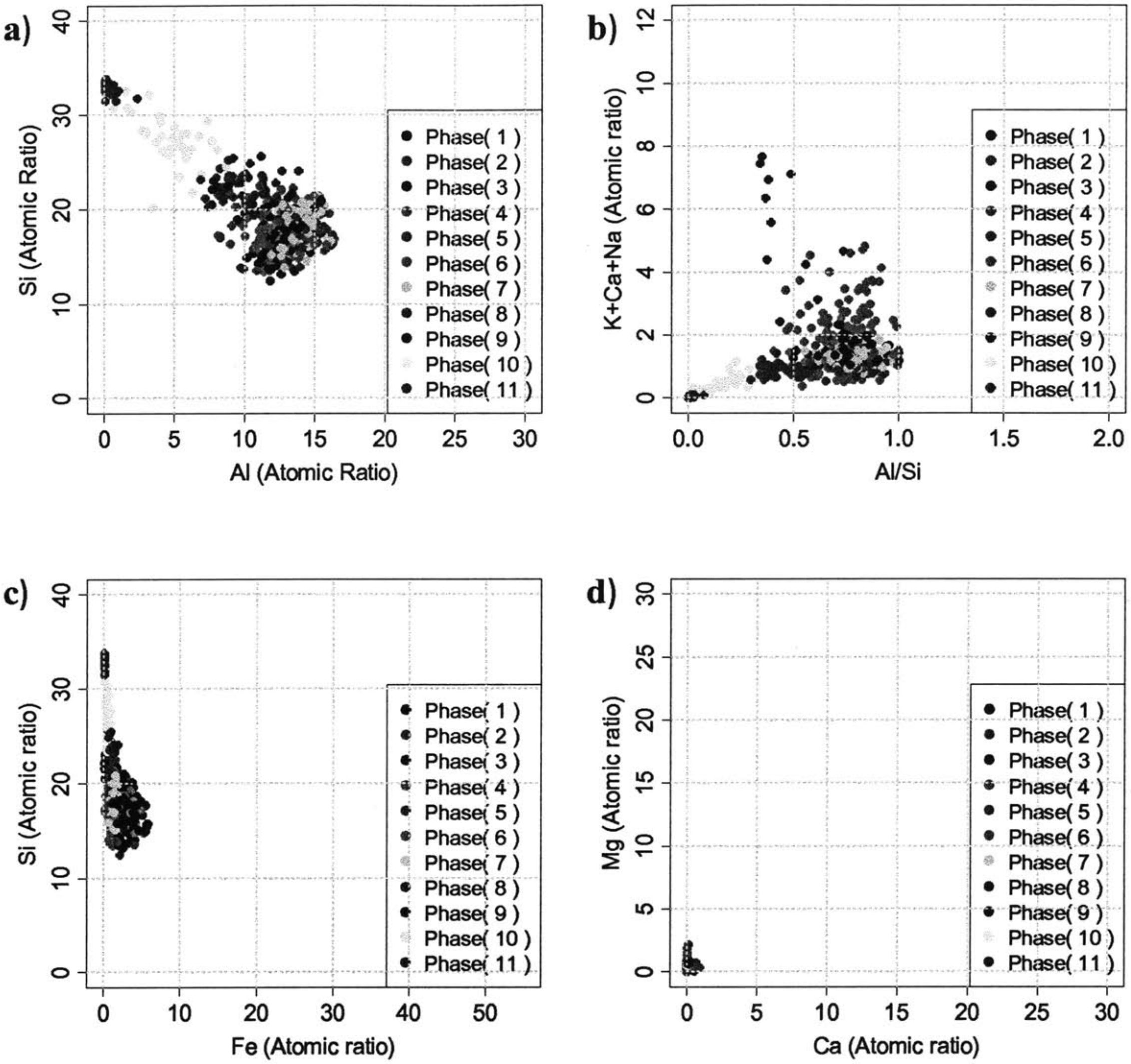

Figure 6-21: Multivariate cluster analysis of the grid WDS data for experiment S1-a. The identified phases are presented on 2-D projections for visual interpretation of the data: a) Al-Si space and b) Ca+Na+K-Al/Si space separate quartz, feldspars, and clay minerals. c) Fe-Si space and d) Ca-Mg space separate carbonate minerals; siderite, calcite, magnesite, ankerite, and dolomite.

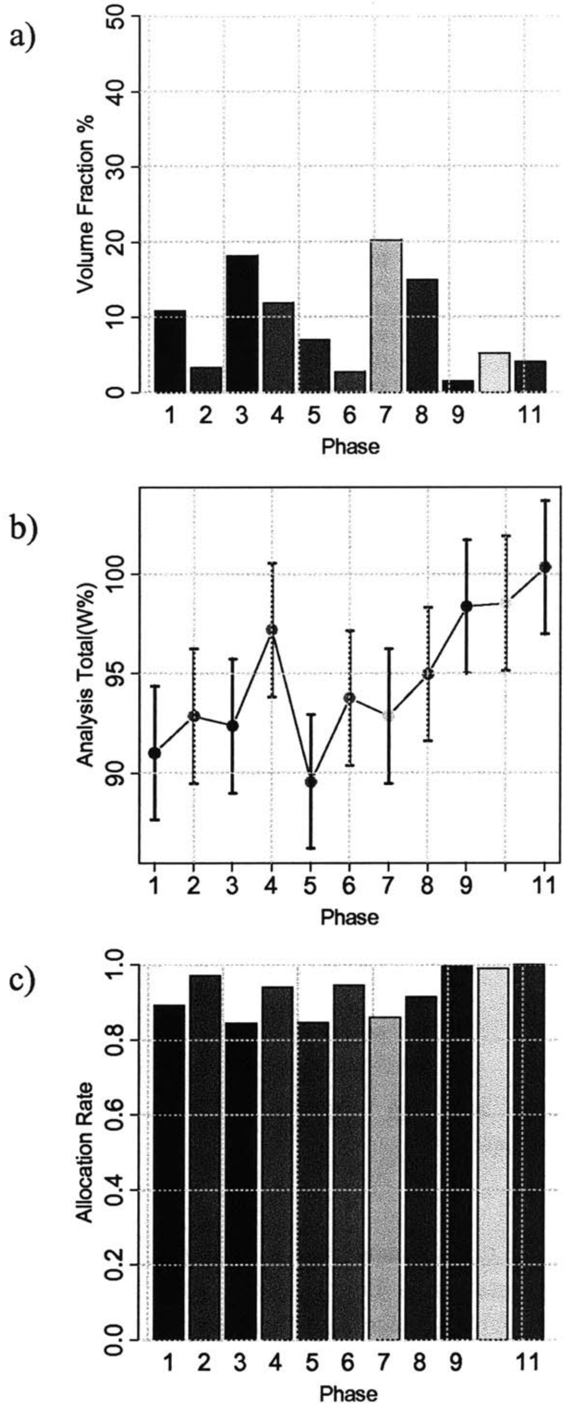

Figure 6-22: Graphical representation of clustering results presented in Table 6.23 for experiment S1-a. a) volume fractions, b) mean and standard deviation values of the analysis totals, and c) allocation rates for each of the phases displayed in Figure 6-21.

6.2 Data Interpretation

The chemical assessment of the shale samples using the grid WDS technique follows the procedure outlined in Section 4.3.3. The chemical data collected by WDS spot analysis is interpreted using the multivariate clustering, in which the atomic ratios of the measured elements are used to find the most probable chemical families present in the sample. The elements necessary to describe the mineralogy of shale are: silicon, aluminum, iron, potassium, magnesium, calcium, sodium, and sulphur. These elements provide the sufficient contrast between minerals that can be found in shale materials with minimum organic content. Once the data is clustered, the results are presented on 2-D elemental projections that provide means for visual interpretation of the data. The projections adopted in this study differentiate between silicates and carbonates. In the case of silicates, such as quartz, feldspar, and clay minerals, the projections Al–Si, and Al/Si–K+Ca+Na are adopted. The projections that can be used for the analysis of carbonates are: Ca–Mg, and Fe–Si. These projections help in identifying calcite, magnesite, dolomite, and siderite (see Figure 4-9 for an illustration of the identification process). The remainder of this section presents the interpretation of clustering results defined for experiments in Table 6.1, which are displayed in Figures 6-1 through 6-21. The objective is to identify the poles and ligands associated with the main chemical components derived from the grid WDS experiments and provide quantitative assessment of the mixture phases, and finally, determine the properties and volume fractions of the dominant chemical components present in the studied shale materials.

6.2.1 The Clay and Quartz Poles

A pole is defined as a component with a relatively small standard deviation; that is an intense clustering of data points around a mean position, and, hence, interpreted as an approximately homogeneous phase (see Section 4.3.4). One of the strongest commonalities between the chemical analyses of the shale samples presented in Section 6.1 is the presence of a quartz pole. The simple chemical composition of quartz makes its identification straightforward. Quartz phases are situated in the region expected for quartz mineral (Figure 4-9), for which reason we interpret phases such as phases 6 and 7 in Figure 6-1, for example, as quartz mineral phases.

The analysis of clay minerals, in contrast, is more complex due to their highly heterogeneous chemical composition. The task is simplified using the chemical database gathered from the literature and reported in Section 2.1.1. This database is used to account for chemical variability in clay minerals due to isomorphous substitution. Figures 4-10 through 4-13 show the chemical composition of clay minerals derived from the gathered chemical data and displayed on the adopted elemental projection; Al-Si and Al/Si - Ca+K+Na. This data set aids in identifying the chemical signature of clays in the proposed atomic projections.

Chemical data that are located in the regions expected for clay minerals such as e.g., phases 2 and 3 in Figure 6-1 are interpreted as clay dominated phases. These clay phases possess the characteristic of a pole, that is a material of a homogeneous composition (intense clustering of data points). Contrary to quartz phases, the data for clay phases show more spread due to the expected heterogeneity of clay minerals. Furthermore, the definition of clay minerals as poles (homogeneous) does not contradict the heterogeneous nature of clay minerals, given that the WDS technique probes an on-average composition of clay minerals, which is homogeneous at the scale of measurements (approximately 2 μm).

Another experimental parameter that can be used to separate clay and quartz phases is the analysis totals, which represents the sum of elements weight percents in each WDS spot. As explained in Section 4.3.3, the analysis total should be equal to 100. However, the application of the WDS technique deviates from the given mark due to some minor elements not being measured and other experimental issues. We note that the analysis totals corresponding to clay phases consistently display lower values (95 %) compared to that of quartz phases (100 %). This behavior is attributed to hydrogen, which are present in clay minerals in the form of water or OH^-, and which are not measured in the WDS experiments because its low atomic number is outside the range of resolution of EPMA. Referring to Figure 6-2, for example, quartz phases (phases 7 and 6) have analysis totals of approximately 98 %, while clay phases (phases 2 and 3) have analysis totals in the range of 90-93 %. Table 6.24 compiles the chemical phases identified as clay and quartz in Figures 6-1 through 6-21.

Sample	Grid Size	Clay phases	Quartz phases
S7-a	32x32	2, 3	7, 6
S7-b	32x32	1, 3, 4	8, 7
S7-c	33x33	3, 4, 5	8
S7-d	20x20	2, 3, 4, 5	8
S7-e	20x20	2, 3, 4, 5	
S3-a	32x32	1, 2, 3, 5, 6, 8	10
S3-b	32x32	1,2, 3, 4, 5	9
S3-c	20x20	1, 2, 3	
S3-d	20x20	1,2, 4	
S3-e	20x20	1, 2, 3, 5, 6	9
S1-a	32x32	1, 2, 3, 5, 6, 7, 8	11

Table 6.24: Identification of clay and quartz phases based on cluster modeling of grid WDS experiments outlined in Table 6.1 and Figures 6-1 through 6-21.

6.2.2 The Ligands

Another feature that is consistent throughout the chemical analyses presented in this Chapter is the presence of ligands between clays and other non-clay minerals (quartz, feldspars, and siderite). Ligands are clearly visible, for example, in the chemical analysis of sample S7-a presented in Figure 6-1, where three ligands were identified. These ligands are identified visually based on their end anchor points. Phase 4 connects the clays and quartz phases in the Al–Si projection shown in Figure 6-1a. This mixture phase spans between quartz anchor point (Si = 33.33 and Al = 0) and clay anchor point (Si $\approx$ 15 - 20, and Al $\approx$ 5-10). Phase 5 connects the clay and feldspar phases in the Al/Si–K+Ca+Na projection shown in Figure 6-1b. This mixture phase spans between feldspar anchor point (K+Ca+Na = 7.7, Al/Si = 0.33 – 1) and clay anchor point (K+Ca+Na $\approx$ 2–4, Al/Si = 0.3-1). Finally, Phase 1 connects the clays and siderite phases in the Fe–Si projection shown in Figure 6-1c. This mixture phase spans between siderite anchor point (Fe = 20, Si = 0) and clay anchor point (Fe $\approx$ 2, Si $\approx$ 15 - 20). As can be seen in Figure 6-1c, the siderite mixture phase is incomplete as the data points do not reach siderite anchor point (Fe = 20, Si = 0). Such phases are still important as they represent a mixture of two phases, either because the adjacency of two phases cause the electron beam to sample from both of them, or because of the presence of cavities in some of the grains. Table 6.25 lists the mixture phases identified in the chemical analyses presented in Figures 6-1 through 6-21. In the following section, we seek to find the volume fractions of individual phases involved

Sample	Phase No.	Classification
S7-a	1	Siderite-clay
	4	Quartz-clay
	5	Feldspar-clay
S7-b	2	Siderite-clay
	5	Feldspar-clay
	6	Quartz-clay
S7-c	1	Siderite-clay
	6, 2	Feldspar-clay
	7	Quartz-clay
S7-d	1*	Feldspar-clay
	6, 7	Quartz-clay
S7-e	1*	Feldspar-clay
	6	Quartz-clay
S3-a	4	Feldspar-clay
	7, 9	Quartz-clay
S3-b	6	Feldspar-clay
	8	Quartz-clay
S3-c	4	Quartz-clay
S3-d	3	Feldspar-clay
	5	Quartz-clay
S3-e	4	Feldspar-clay
	7, 8	Quartz-clay
S1-a	4, 9	Feldspar-clay
	10	Quartz-clay

Table 6.25: Identification of mixture phases found in the chemical analyses of the experiments outlined in Table 6.1 and displayed in Figures 6-1 through 6-21.
* Minor amount of siderite was ignored in phase 1.

in the mix. For this, we follow the mixture modeling outlined in Section 4.3.4.

6.2.3 Mixture Analysis

To analyze mixture phases, we assume that each mixture phase is a linear combination of the phases involved in the mix. This requires a careful identification of the element to be used in the mixture model described in Section 4.3.4 (variable X in equation (4.8)), which must provide sufficient contrast between phases involved in the mix. Three types of mixture phases were identified and summarized in Table 6.25: quartz-, feldspar-, and siderite-clay mixture phases. The elements chosen to analyze each of these mixture phases are: silicon, the combination K+Ca+Na, and iron, respectively. Considering the quartz-clay mixture phases as example, equation (4.8) can be written as:

$$\mathrm{Si}_{mix} = \lambda\,\mathrm{Si}_q + (1-\lambda)\,\mathrm{Si}_c \tag{6.1}$$

where λ is the proportion of quartz in the mix, Si_q and Si_c are the atomic ratios of Si in quartz and clay, respectively. Si_q is determined from the well know chemical formula of quartz SiO_2 ($\mathrm{Si}_q = 33.33$). Si_c, on the other hand, is more complex due to the chemical variability of clay minerals. Thus, Si_c is calculated based on the weighted average of silicon in clay phases identified in the cluster analysis, e.g., phases 2 and 3 for experiment S7-a listed in Table 6.24. The above description is summarized by the following formula:

$$\mathrm{Si}_c = \mathrm{Si}_i\,\mathrm{V}_i \tag{6.2}$$

where Si_i and V_i are the mean silicon contents and volume fractions of phases i that are identified as clay phases. With the mixture model at hand, the λ values are calculated for each point in the quartz-clay mixture phase. The calculated values are clustered using the Mclust, in which one variable was used; in this case λ. Finally, the pure quartz and clay proportions of the mixture phase are separated according to the following formula:

$$V_q = \lambda_i v_{f,i} \tag{6.3}$$

$$V_c = (1-\lambda_i) v_{f,i} \tag{6.4}$$

where V_q and V_c are the pure volume fractions of quartz and clays, respectively. λ_i and $v_{f,i}$ are the mean value and volume fraction of component i identified in the clustering of λ values. The proposed model is applied to each of the mixture phases, and the volume fractions of each phase involved in the mix are calculated accordingly. To illustrate this procedure, Figure 6-23 shows the distribution of λ values for the mixture phases identified for experiment S3-a (see Figure 6-11) along with the clustering results of the calculated λ values. The interpretation of the $\lambda-$clustering results is similar to that of the multivariate results; narrow peaks are poles which we interpret as materials of relatively homogeneous composition. Flat curves are ligands and correspond to disordered mixing of the two phases. Table 6.26 contains the results of mixture

Sample	Phase No.	Classification	Quartz	Feldspar	Clay	Siderite
S7-a	1	Siderite-clay			0.73	0.27
	4	Quartz-clay	0.07		0.93	
	5	Feldspar-clay		0.35	0.65	
S7-b	2	Siderite-clay			0.85	0.15
	5	Feldspar-clay		0.19	0.81	
	6	Quartz-clay	0.27		0.73	
S7-c	1	Siderite-clay			0.73	0.27
	6, 2	Feldspar-clay		0.19	0.81	
	7	Quartz-clay	0.53		0.47	
S7-d	1	Feldspar-clay		0.32	0.68	
	6, 7	Quartz-clay	0.76		0.24	
S7-e	1	Feldspar-clay		0.84	0.16	
	6	Quartz-clay	0.13		0.87	
S3-a	4	Feldspar-clay		0.46	0.54	
	7, 9	Quartz-clay	0.72		0.28	
S3-b	6	Feldspar-clay		0.85	0.15	
	8	Quartz-clay	0.44		0.56	
S3-c	4	Quartz-clay	0.51		0.49	
S3-d	3	Feldspar-clay		0.10	0.90	
	5	Quartz-clay	0.69		0.31	
S3-e	4	Feldspar-clay		0.16	0.84	
	7, 8	Quartz-clay	0.60		0.40	
S1-a	4, 9	Feldspar-clay		0.16	0.84	
	10	Quartz-clay	0.63		0.37	

Table 6.26: Breakdown of mixture phases into pure end phases. The values in this table correspond to the proportions of each phase involved in the mix.

modeling applied to the mixture phases listed in Table 6.25.

6.3 Chapter Summary

In our study of the chemical make up of shale, we set out to assess the mineralogy of the studied samples by determining the volume fractions of the different constituents. The volume fractions associated with the results for pole-identification in Table 6.24 and mixture modeling of ligands detailed in Table 6.26 enabled the identification of volume fractions of shale constituents. Table 6.27 summarizes the volume fractions of the minerals identified in each sample. These values obtained through the grid WDS technique will be compared with results obtained by XRD and porosity measurements detailed in Chapter 3. In the next Chapter, supplementary mineralogy

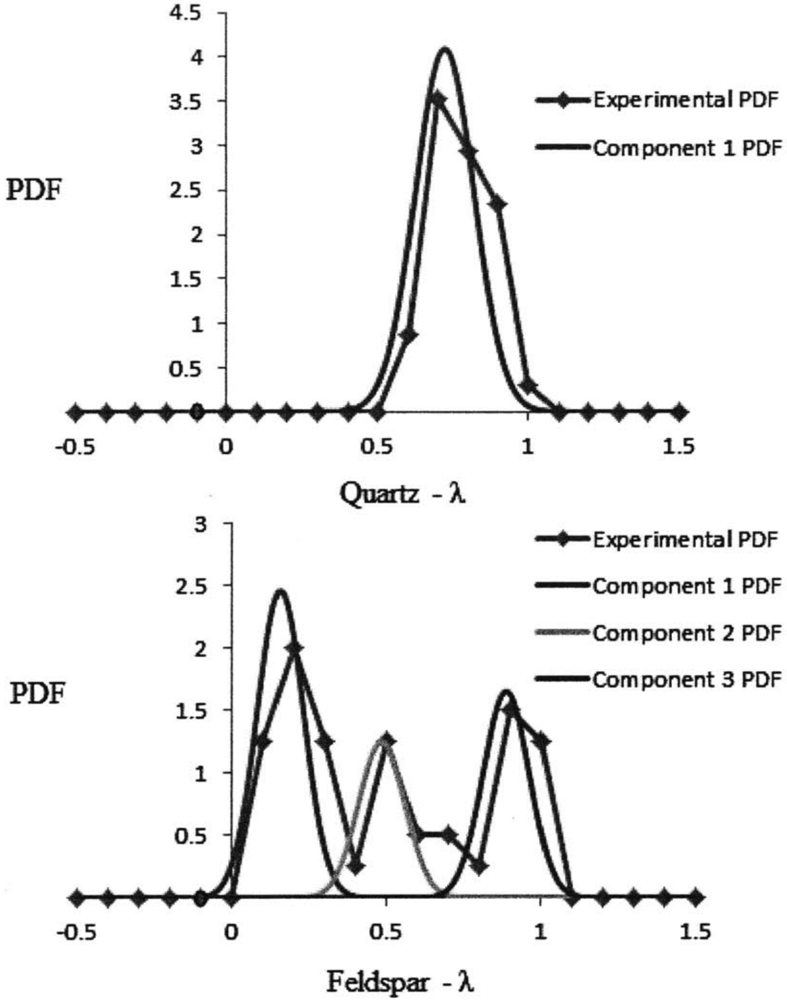

	Component 1		Component 2		Component 3	
Mixture phase	λ_1	v_{f1}	λ_2	v_{f2}	λ_3	v_{f3}
Quartz - clay	0.72	1.00	-	-	-	-
Feldspar - clay	0.16	0.46	0.48	0.23	0.89	0.31

Figure 6-23: The distribution of λ values found in the analysis of the mixture phases of sample S3-a. The λ values were clustered using the Mclust algorithm to find the proportions of each phase involved in the mixture. a) Quartz mixture analysis, b) feldspar mixture analysis. The results are also provided in tabular format.

Sample	Quartz (%)	Feldspar (%)	Clay (%)	Siderite (%)
S7-a	10	2	86	2
S7-b	24	1	75	1
S7-c	12	3	83	2
S7-d	7	2	90	1
S7-e	6	2	90	2
S3-a	5	2	93	0
S3-b	12	6	82	0
S3-c	10	0	90	0
S3-d	5	1	94	0
S3-e	6	1	93	0
S1-a	7	3	89	0

Table 6.27: Identification of mixture phases inferred from the chemical analyses of the experiments outlined in Table 6.1 and displayed in Figures 6-1 through 6-21.

information of the investigated shale samples obtained through image analysis of X-ray maps and backscattered images is presented.

Chapter 7

Image Analysis of Backscattered Electron and X-ray Images

This chapter deals with the assessment of shale mineralogy obtained through image analysis of X-ray maps and backscattered electron (BSE) images. We begin by describing the analysis methodology that lead to the mineralogical characterization of shale materials. The obtained mineralogy information will be used later to validate the grid WDS technique. Finally, this chapter presents the results of grain size analysis of the silt inclusions found in the investigated shale materials. This information will be used later to study the effect of the WDS grid size on the mineralogy results.

7.1 Image Analysis in Geology

Image analysis is the characterization of images to obtain quantitative information about materials. It involves the identification and evaluation of image features as means to extract chemical and geometrical information of interest. Images required for analysis can be acquired by experimental setups, such as EPMA and SEM. Images produced by particular modes of EPMA and SEM such as backscattered electron (BSE) images and x-ray maps are of particular importance to this study as they provide mineralogical and chemical information. The technique of image analysis has been successfully applied in several applications in the field of sedimentology including quantitative mineralogical analysis of materials, and the assessment of grain size, particle shape, pore size, and the nature of boundaries between grains [21]. This chapter describes the implementation of this technique to obtain mineralogical and morphological information about the shale samples studied in this work. The software used to analyze images, ImageJ, is a free open-source imaging software. The information generated through image analysis will be used as an independent dataset to be compared with the grid WDS technique applied for shale materials

7.2 Mineralogy Assessment

One of the important applications of image analysis in geology is the mineralogical assessment of materials. The careful analysis of specific image features can be used to obtain the volume fractions of minerals that are found in a sample, and several references in the literature document the application of image analysis to shale and other sedimentary rocks [21] [4] [57] [58]. In this section, we report the application of this technique to the shale samples considered in this work to determine the mineralogy of the samples.

Before testing, sample were prepared and polished according to the protocol described in Section 3.5. This is an essential step to obtain a flat surface appropriate for imaging through EPMA. Each sample was coated with a 20 nm thin carbon layer to prevent charging. A set of backscattered electron (BSE) images and X-ray maps were then acquired for the area of interest for each sample. Similar to the grid WDS experiments, images were collected on a JEOL JXA-733 superprobe equipped with a WDS spectrometer operating at an accelerating voltage of 15 kV, and a beam current of 10 nA. For X-ray maps, the dwell-time was 30 ms. In BSE images, mineral phases are distinguished based on their gray color scale, since minerals with different compositions exhibit different backscattered coefficients (see Section 4.1.1). Figure 7-1 displays a BSE image of an area of 1mm×1mm for sample S7. In contrast, X-ray maps show the distribution of a chemical element on the surface of a sample, as well as the relative amount of the particular element (the dark-to-light transition corresponds to a low-to-high concentration gradient). Several elements were selected for mapping including silicon, aluminum, magnesium, potassium, sulphur, iron, sodium, and calcium. Figure 7-2 shows a set of X-ray maps obtained for the same area displayed in Figure 7-1. The X-ray maps for Mg and Ca, show little contrast,

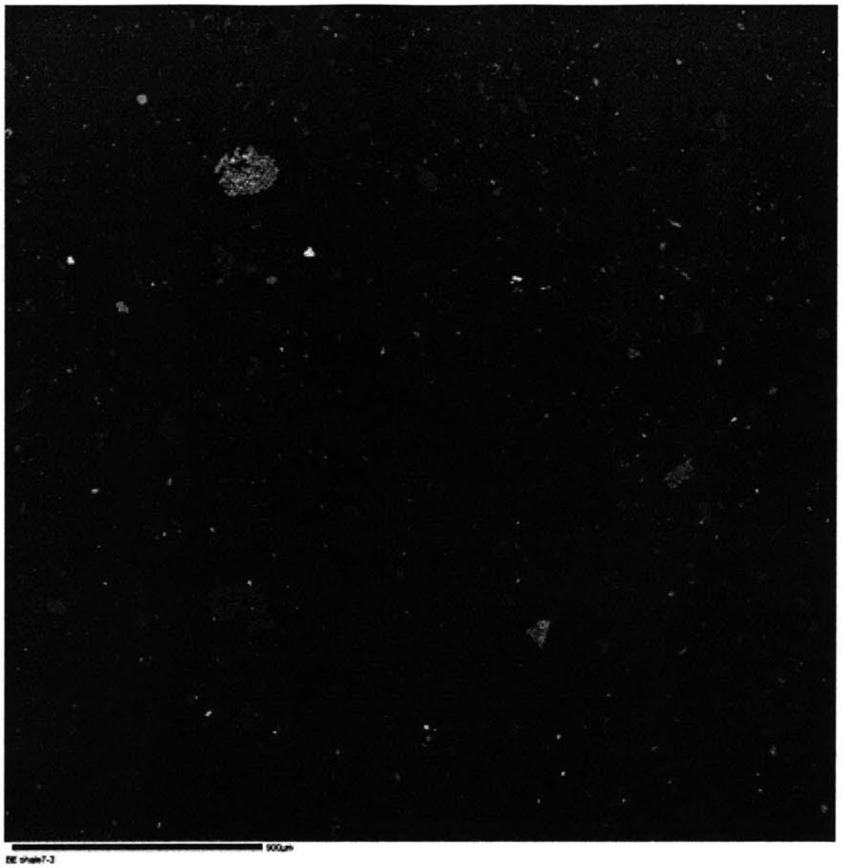

Figure 7-1: Backscattered electron (BSE) image of an area of sample S7 (Area 4 in Table 7.1). The composition of the sample can be inferred from the contrast in color intensities. The scale bar in the image corresponds to 900 μm.

for which reason they are not presented.

The next step in the image analysis technique is the thresholding of the backscattered electron (BSE) images and X-ray maps, which involves separating gray-level images into binary images for each gray level, and identifying the mineral corresponding to each grey level. In principle, BSE images which show contrast in color intensity for different minerals, could be used to separate each mineral by selecting the relevant gray level. However, BSE images are rarely appropriate for such analysis when applied to shale materials, as the color intensity may change within the same mineral due to compositional variations, or because the color intensities of two minerals are very close [21]. Instead, X-ray maps are better suited for separating different

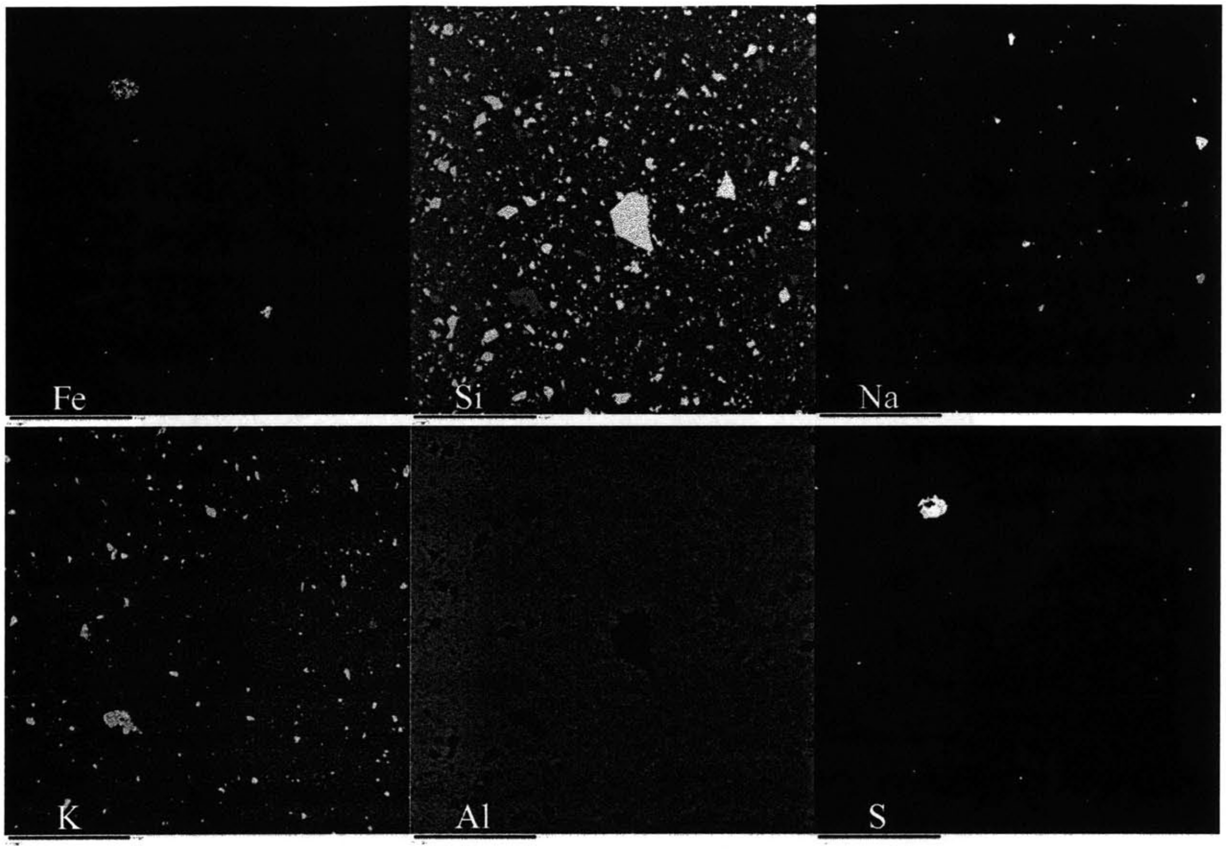

Figure 7-2: X-ray maps showing the distribution of elements of the image shown in Figure 7-1 obtained for sample S7. The X-ray maps display the relative amount of the particular element in the material surface: the dark-to-light transition corresponds to a low-to-high concentration gradient. The scale bar in the images corresponds to 900 μm.

minerals in shale. As observed in Figure 7-2, quartz corresponds to regions with high silicon concentration and an absence of other elements. Na- and K-feldspars are identified in regions with high concentration of Na or K, respectively, and moderate concentrations of Al and Si (see Figure 7-2). Figure 7-3 displays the thresholded images and the identified minerals for sample area shown in Figure 7-1. Besides the identification of quartz and feldspars, the matrix of clay minerals cannot be resolved by neither BSE imaging nor X-ray maps. The resolution of the techniques exceeds the sizes of clay minerals. Given this characteristically small length scale issue, the matrix of fine clays is established as the remainder of the image after separating the minerals found in the sample.

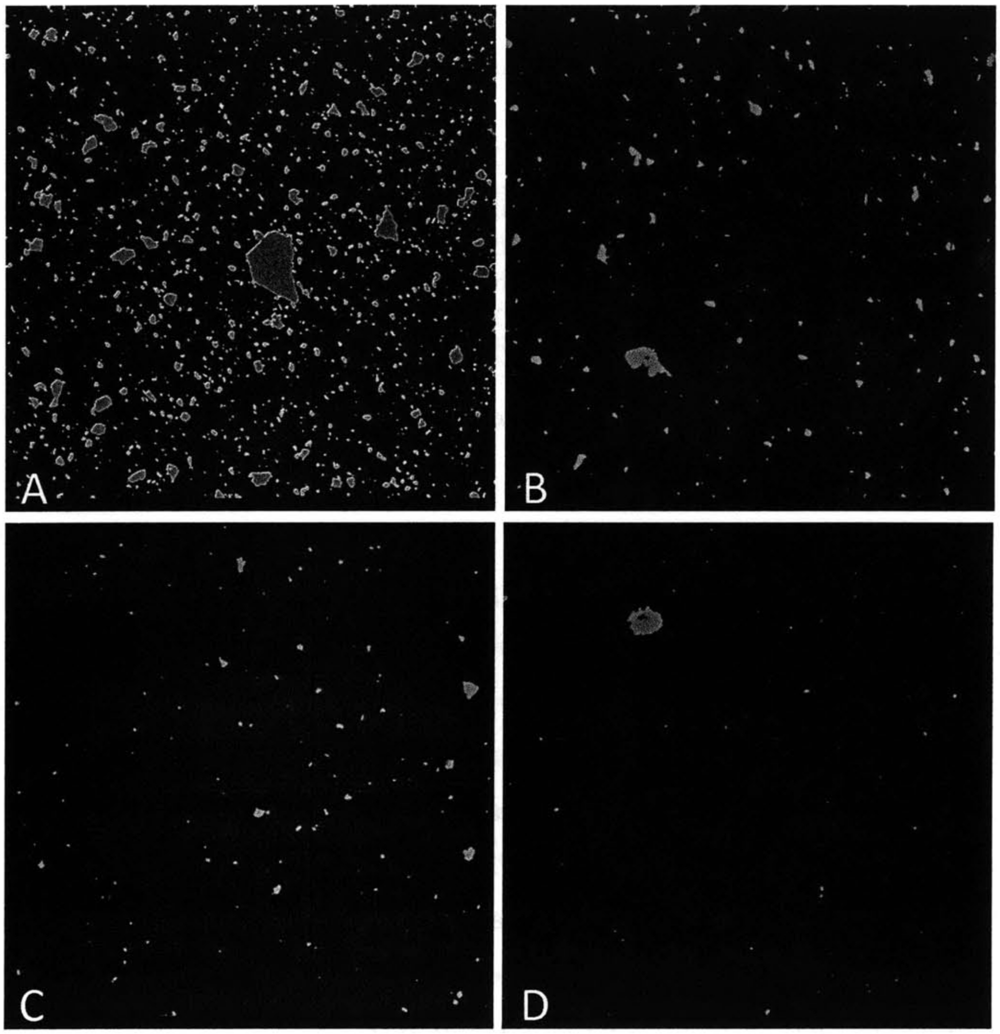

Figure 7-3: Thesholded images based on the X-ray maps shown Figures 7-1 and 7-2. A) Thresholding for quartz from Si map, B) K-feldspar from K map, C) Na-feldspar from Na map, and D) pyrite from S map.

Location	Area (mm^2)	Quartz	Feldspar	Voids	Other Inclusions	Fine Matrix
1	1x1	6.50	4.00	0.50	1.00	89.00
2	1x1	6.00	2.50	0.30	0.50	91.20
3	1x1	10.00	3.10	0.20	0.60	86.70
4	3x3	8.00	2.50	0.60	0.80	88.90
Mean, μ		7.63	3.03	0.40	0.73	88.95

Table 7.1: Compositional analyses in volume percent of four areas in sample S7. Other inclusions include pyrite and siderite.

Location	Area (mm^2)	Quartz	Feldspar	Voids	Other Inclusions *	Fine Matrix
1	1x1	5.50	2.00	0.20	0.50	92.30
2	1x1	5.20	2.60	0.10	1.00	92.10
3	1x1	4.50	1.50	0.20	0.60	93.80
4	1x1	4.70	2.70	0.30	1.10	92.30
Mean, μ		4.98	2.20	0.20	0.80	92.63

Table 7.2: Compositional analyses in volume percent of four areas in sample S3. Other inclusions include hematite and calcite.

In this study, we analyzed four areas in each of the S7 and S3 shale samples. The imaging was performed on random spots in the samples covering large areas to ensure that the analysis provides chemical information representative of the sample. Tables 7.1 and 7.2 summarize the results of the image analysis for samples S7 and S3, respectively. In addition, Figure 7-4 displays the image analysis results in Tables 7.1 and 7.2 graphically. The image analysis shows consistent assessment of the main chemical components in shale across the different spots. This confirms that the chosen area for EPMA testing of 1×1 mm^2 (or larger) is sufficient to characterize the composition of the shale samples (i.e., the proportions of silt-size inclusions and the fine-grained clay matrix). This chemical information derived from EPMA and image analysis will be used for bench marking the grid WDS methodology developed in this thesis.

7.3 Grain Size Characterization

In addition to mineralogy, image analysis can characterize microstructural features of the specimen including the size, shape, and orientation of particles exposed in the material surface. The image analysis technique has been previously applied to morphological features of shale samples [58]. The application of image analysis to study grain size distribution of samples S7 and S3

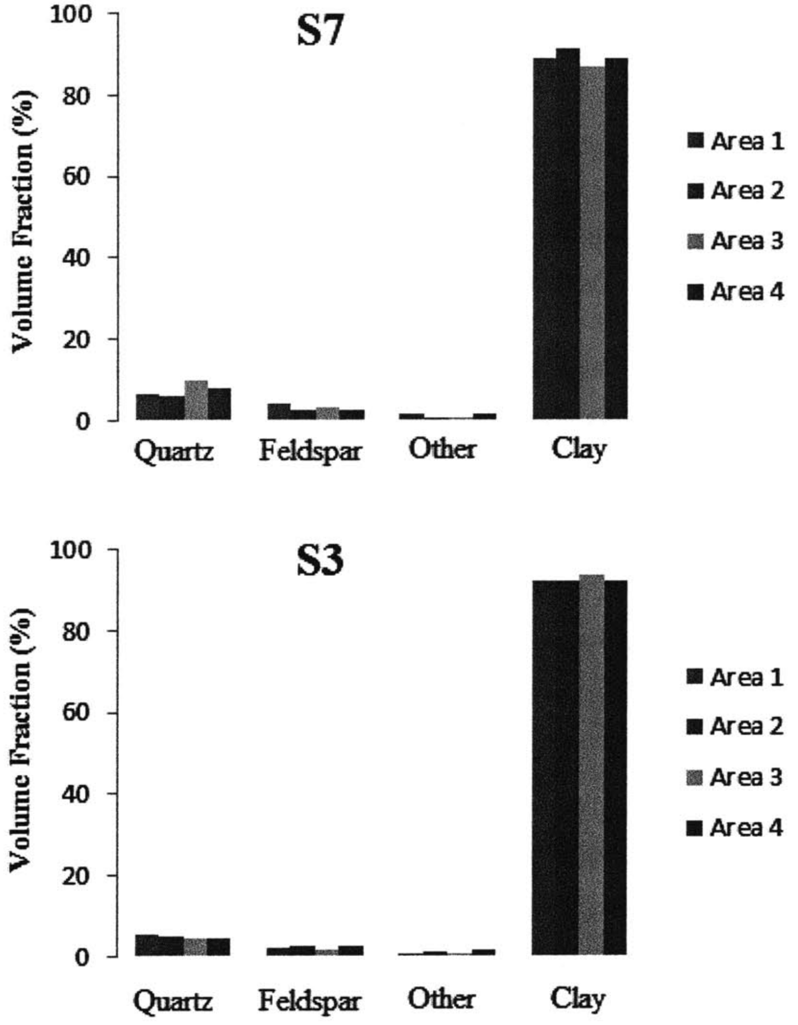

Figure 7-4: Graphical representation of the image analysis results in Tables 7.1 and 7.2 for samples S7 and S3. Other include pyrite and siderite for sample S7 and hematite and calcite for sample S3.

Phase	1	2	3	4	5	6
Mean (μm)	5	7	10	15	27	59
Std. dev.	0.5	1.1	2.2	4.2	9.2	28.1
Vol. fraction (%)	19	21	21	22	13	4

Table 7.3: Clustering results of the grain sizes of sample S7. The clustering of grain sizes was performed using Mclust algorithm.

Phase	1	2	3	4
Mean (μm)	3	5	8	19
Std. dev.	0.1	0.8	2.4	8.4
Vol. fraction (%)	23	24	36	17

Table 7.4: Clustering results of the grain sizes of sample S3. The clustering of grain sizes was performed using Mclust algorithm.

begins by isolating binary images for each mineral as already shown in Figure 7-3. In this study we are interested in the size distribution of all minerals existing in the studied shale samples. Hence, the particles of each mineral were isolated and analyzed to determine their area. The characteristic size of each particle was calculated as the diameter of a circle of equivalent surface area. With the assessment of particle sizes associated with non-clay minerals (mostly quartz and feldspar) at hand, statistical analysis can provide a quantitative information about the relevant length scales encountered in the microstructures of shales S3 and S7. Figure 7-5 display the calculated particle size distribution for both shale samples. The particle distribution for samples S7 and S3 was constructed from the bulk analysis of the results presented in Tables 7.1 and 7.2, respectively. The grain size distribution in sample S3 ranges from 4 to 50 μm, whereas, for sample S7, it ranges from 4 to 200 μm. To further explore the data sets of particle sizes for non-clay minerals, statistical clustering was conducted on the single parameter defined by the equivalent diameter. Tables 7.3 and 7.4 report the means and standard deviations of the most likely groups of particles associated by their size, and the corresponding volume fraction for each group. The cumulative size distributions were constructed for the set of all minerals. Furthermore, the grain sizes found according to the above procedure were clustered to define the main grain size families present in both samples.

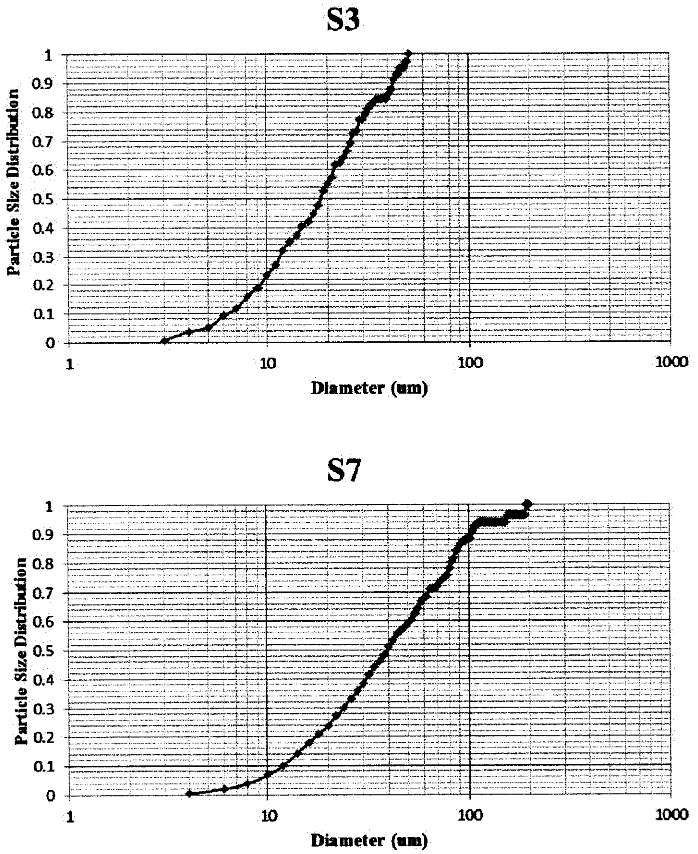

Figure 7-5: Cumulative size distribution curves constructed for all minerals (mostly quartz and feldspars) found in samples a) S3 and b) S7. The data used to generate the curves correspond to all areas described in Tables 7.1 and 7.2.

7.4 Chapter Summary

In this Chapter, mineralogy information about the studied shale samples was obtained through image analysis of X-ray maps and backscattered (BSE) images. Analysis of grain sizes for silt inclusions found in our shale samples was also presented. The mineralogy information obtained in this Chapter will be used to validate the grid WDS technique.

Chapter 8

Discussion

Determining the composition and relative abundance of minerals in shale rocks is crucial for the adequate characterization of their mechanical behavior. In this thesis, we propose the grid WDS technique as a quantitative method to determine the composition and mineralogy of shale. This chapter presents the validation of the grid WDS technique based on comparisons with two independent methodologies used for mineralogy assessment. In addition, we explore the capabilities of the statistical treatment of grid WDS data to resolve the clay mineralogy in different shale rocks. Finally, the effect of grid size on the assessment of volumetric proportions of mineral components in shale is evaluated.

8.1 Validation of the Grid WDS Technique

The statistical grid WDS method developed in Chapter 4, and applied to shale materials in Chapter 6, requires validation. The fine-grained nature of clay minerals in shale, which limits the resolution of our WDS experimental setup, imposes a validation procedure aiming at the identification of the clay matrix and silt-size inclusions. This compositional assessment of shale materials needs to consider the highly heterogeneous microstructure and composition. Two independent techniques are used to validate the grid WDS method: image analysis and X-ray diffraction (XRD). Our implementation of the image analysis technique for the shale materials investigated in this thesis was presented in Chapter 7. XRD mineralogy assessments were conducted through the work of the GeoGenome Industry Consortium, and the results were presented in Chapter 3. This chapter begins with critical analyses of the two independent techniques used for benchmarking the grid WDS technique, with a focus on relative advantages and disadvantages in their implementation for shale materials. The comparisons of experimental results of these techniques and those obtained through grid WDS are then presented and evaluated.

8.1.1 Evaluation of Image Analysis

Image analysis is one of the techniques that we have employed to characterize the microstructure, and more importantly, the composition of the shale materials considered in our investigation. As shown in Chapter 7, the technique involves the identification and evaluation of image features as a means to extract the chemical and geometrical information of interest. Similarly to the grid WDS technique, the images used for analysis are acquired using EPMA, which relies on emitted X-rays resulting from interactions between the beam of electrons and the specimen to determine the chemical composition of a specimen. However, the grid WDS technique and the standard X-ray imaging mode differ in two important aspects. One difference between them is related to the particular setups of the two experiments: the grid WDS technique provides compositional information at specific spots (of few micrometers in size, see Section 4.3.2), whereas X-ray imaging provides a continuous description of the chemistry of a sample. The second difference comes form the way the results are presented. X-ray intensities are presented in the form of maps for the corresponding elements with color intensity contrast (see Section 4.1.2), whereas in WDS spot analysis, the quantitative elemental concentrations are provided.

The set of X-ray maps and backscattered electron (BSE) images obtained for samples S7 and S3 were properly analyzed for the major mineral families present in the shale samples. Image analysis results were presented in Tables 7.1 and 7.2, respectively, and displayed in Figure 7-4. As explained in Section 7.2, the separation of minerals through thresholding was performed using computer imaging software. Each mineral is separated from the appropriate X-ray map by thresholding the relevant gray level relative to the image: e.g. quartz is separated from the silicon X-ray map, whereas K-feldspar and Na-feldspar are separated from the potassium and sodium X-ray maps, respectively. Other inclusions could be identified similarly from other X-ray maps. The thresholding procedure requires the intervention of an operator to assess the gray level associated with the mineral of interest. This intervention may result in the variabilities of calculated volume fractions of minerals. Based on our experience on image analysis, the color intensity contrast between different minerals in shale was sufficient to differentiate major inclusion families (quartz, feldspars) from the matrix. The sensitivity of the threshold for the different silt-size minerals was minor (less than 1% for estimated volume fractions). More refined thresholding methods such as remote sensing (based on statistical analysis, see [57]) can be used to reduce the variability of the results induced by the operator. The known limitation associated with EPMA implementations for shale and other fine-grained soils is that the small sizes of clay minerals that cannot be resolved by the volume of interaction related to the experiment. Consequently, the matrix of fine-size clays is determined as the remainder of the image after identifying the silt-size mineral phases. By doing so, one may risk to overestimate the volume fraction of clay minerals by including fine-grained inclusions that were not recognized through thresholding. However, this issue is expected to have small effects on the results for shale materials, since most inclusions are easily distinguished owing to their large grain size.

8.1.2 Evaluation of X-ray Diffraction (XRD)

X-ray diffraction is one of the most widely used methods to study the structure of crystalline materials. XRD testing is based on the analysis of the wavelengths of diffracted signals, which are functions of the spacing of interatomic planes in minerals. Given that no two minerals possess the same interatomic spacing, diffracted wavelengths can serve as tools for mineral identification. X-ray diffraction is particularly suitable for identification of clay minerals because each clay group exhibits unique interatomic spacings. The so-called powder method is well suited for the analysis of small size minerals. The use of the powder method ensures that some of the very large number of particles will be properly oriented to create measurable diffracted X-rays. For a composite powder, an intensity spectrum is obtained, with each peak associated to a particular mineral. Kaolinite, for example, exhibits a peak associated with 7 $\AA$, whereas illite and dried smectites have peaks associated with 10 $\AA$. Non-clay minerals can also be adequately identified.

Although XRD is widely accepted for the assessment of mineralogy, it involves some levels of uncertainty due to procedural flaws and differences in analysis methods. Mitchell [47] concluded that XRD is a semi-quantitative technique because of known differences in mass absorption coefficients of different minerals, particle orientations, sample weights, surface texture of samples, among other factors. Kahle [54] provided a thorough study of the different methodologies commonly used for the quantification of clay minerals in XRD, with an emphasis on methods using mineral intensity factors. He concluded that procedural differences such as sample preparation and instrument configuration may lead to different mineralogy quantifications. In addition, assumptions employed for data analysis may affect the accuracy of XRD assessments: a) that all phases present in a sample have been identified and sum to 100 %, b) that the orientation in a specimen is identical for all minerals, and c) that intensity factors are the same for all particles of one phase. Brindley [36] stated that crystalline components that exist in a material sample with more than 50 % by weight may be measured to an accuracy of 10 % of the determined value, whereas components present with less than 5 % by weight may be measured to an accuracy of 50 % of the determined value. Ottner [31] conducted a round robin test in which two clay samples were sent to 19 laboratories. The quantitative analyses of clay minerals showed large discrepancies among laboratories, whereas relatively little variability was observed in the quantitative results for non-clay inclusions (quartz, feldspar, calcite, and dolomite). The observed variabilities for clay minerals was attributed to the differences in pretreatment and sample preparation techniques. To verify the effect of analysis methods in XRD, the authors estimated the clay fraction based on three different methods after subjecting the sample to the same experimental conditions to eliminate the influence of pretreatment and sample preparation. The results showed that the choice of quantification method in XRD had a significant influence on the results. This discussion highlights the uncertainty associated with the application of XRD to assess the mineralogy of soil and rock samples, which are natural composites with very heterogeneous compositions and microstructures.

The quantitative analysis of the mineralogy of shale samples is commonly obtained through XRD, especially in oil and gas research and laboratory characterization. Table 3.1 summarizes the mineralogy data based on XRD experiments for the shale samples considered in this work. The mineralogy information can be used to calculate the volume fraction contributions of clay minerals and non-clay inclusions that are needed for material modeling. These volumetric quantities become critical inputs to e.g. mechanical models, as they weigh the contributions of the relevant chemical phases to the mechanical response of the composite materials across different length scales. Besides the mineralogy data, the determination of volumetric quantities requires as an input the total porosity, which can be determined through various experimental means (see Section 3.3). The variability in porosity estimates becomes another factor affecting the overall quantification of volume fractions for shale materials, in addition to the variability in mineralogy assessed by XRD, as previously discussed. Table 3.4 summarizes the volume fractions of clay minerals and non-clay inclusions derived from the provided XRD mineralogy information and porosity measurements. To obtain the volume fraction of the porous clay composite (see Section 2.2.2), which defines the scale of measurements in this study, the measured porosity is added to the solid volume fraction of clay minerals. The composition of shale based on XRD and porosity measurements in terms of volumetric amounts of clay and silt-size (non-clay) minerals will be used to benchmark the development of the grid WDS technique.

8.1.3 Validation

In this section, we compare the chemical compositions estimated from the proposed grid WDS methodology, X-ray image analysis, and XRD. The information is compared in terms of volume fractions for the major mineral families that can be captured by these techniques, namely silt-size inclusions (quartz, feldspar) and the clay matrix. In the grid WDS and image analysis techniques, the volume fractions are measured directly, whereas in XRD the volume fractions are derived from mineralogy and porosity measurements. For the comparison with image analysis and XRD experiments, we have selected the grid WDS experiments involving large grid sizes: S7-a, S3-a, S1-a (see Table 6.1). These particular applications of the grid WDS method will be shown to be the most relevant for assessing the overall composition of the material samples and capturing their heterogeneous microstructures. In a later section, a discussion on the effect of grid size on the resulting volumetric assessments of chemical constituents will be presented. Figures 8-1 through 8-6 show the comparisons between the results of the three techniques for shale samples S7, S3, and S1. Figures 8-1, 8-2, 8-3 display the comparisons as bar charts for the four major chemical components in shale by volume fraction: quartz, feldspar, other inclusions (siderite, pyrite, hematite and calcite), and the porous clay composite (the mixture of nanoporosity and solid clay). Figure 8-4, 8-5, 8-5 show cross-plots of the chemical assessments by XRD and image analysis compared to the results from grid WDS analysis (except for shale S1, for which imaging analysis results are not available).

Two trends emerge from the comparisons presented in Figures 8-1 through 8-6. First, the grid WDS results compare well with those obtained through image analysis. This trend may not be surprising given that both methods were performed using the same experimental technique (EPMA), and that the investigated areas are representative of the shale samples herein considered (see discussion in Section 8.2). The small differences observed in these results could be attributed to the sensitivity in thresholding or to the variability associated with the statistical analysis results from grid WDS data. In addition, the differences in volumetric estimates could be related to the heterogeneous nature of shale, which manifests itself as particular microstructures and chemical compositions spread over the material volume. Another trend that can be identified from Figures 8-1 through 8-6 is that the XRD results consistently display higher volumetric estimates for non-clay inclusions compared to the estimates from grid WDS and image analysis. Consequently, lower estimates for the porous clay are observed for the XRD compared to the two other techniques. For the different shales, the discrepancies between XRD and grid WDS estimates for the porous clay phase range between 6 % for experiment S1-a to 27 % for experiment S3-a. This trend may be explained by the large uncertainty associated with XRD analysis as outlined in Section 8.1.2.

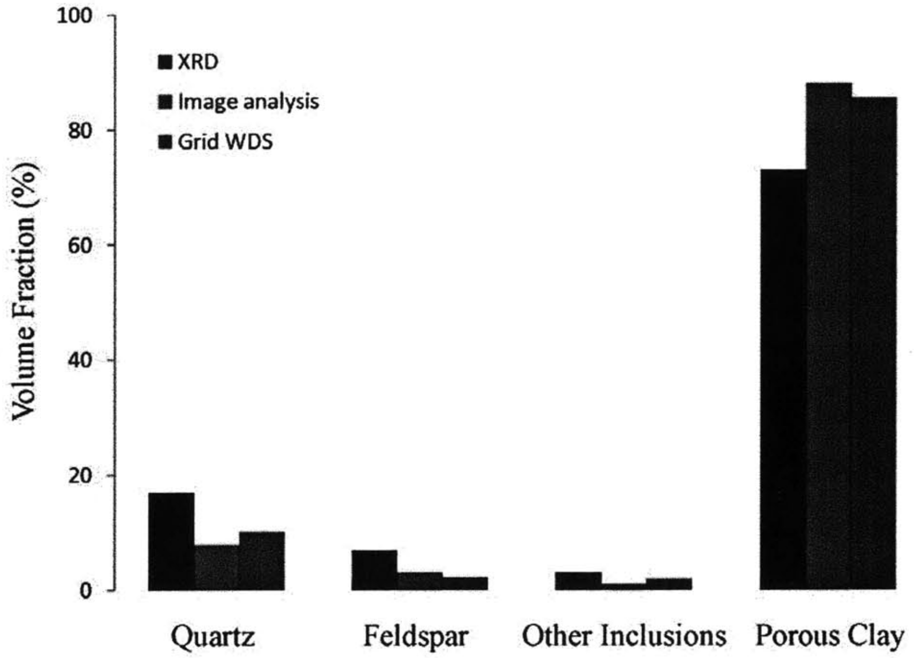

Figure 8-1: Comparison of the mineralogy results for sample S7 derived from XRD, image analysis, and grid WDS analysis for experiment S7-a. Other inclusions refer to siderite and pyrite.

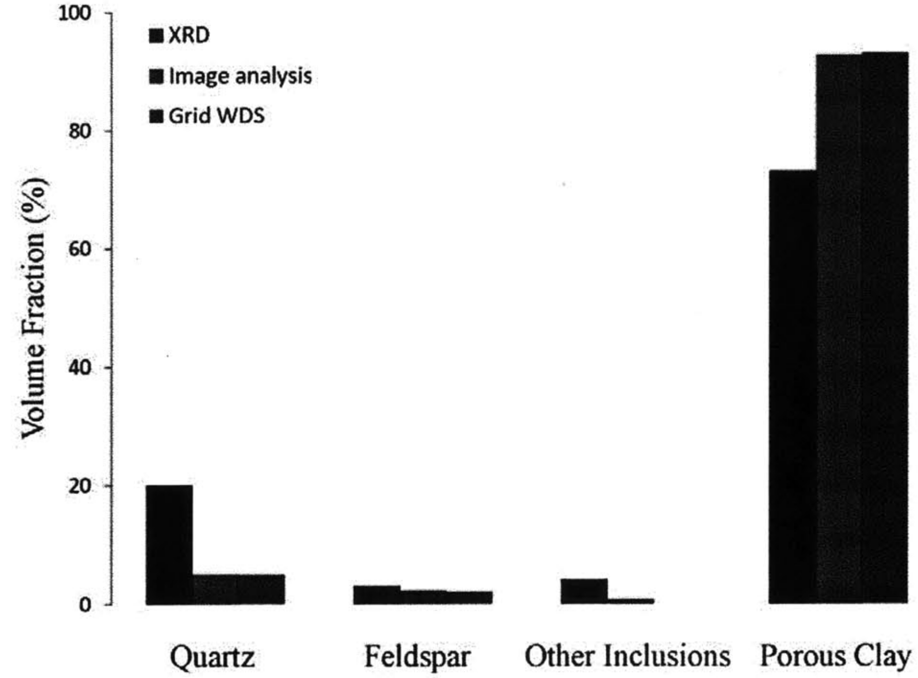

Figure 8-2: Comparison of the mineralogy results for sample S3 derived from XRD, image analysis, and grid WDS analysis for experiment S3-a. Other inclusions refer to calcite and hematite.

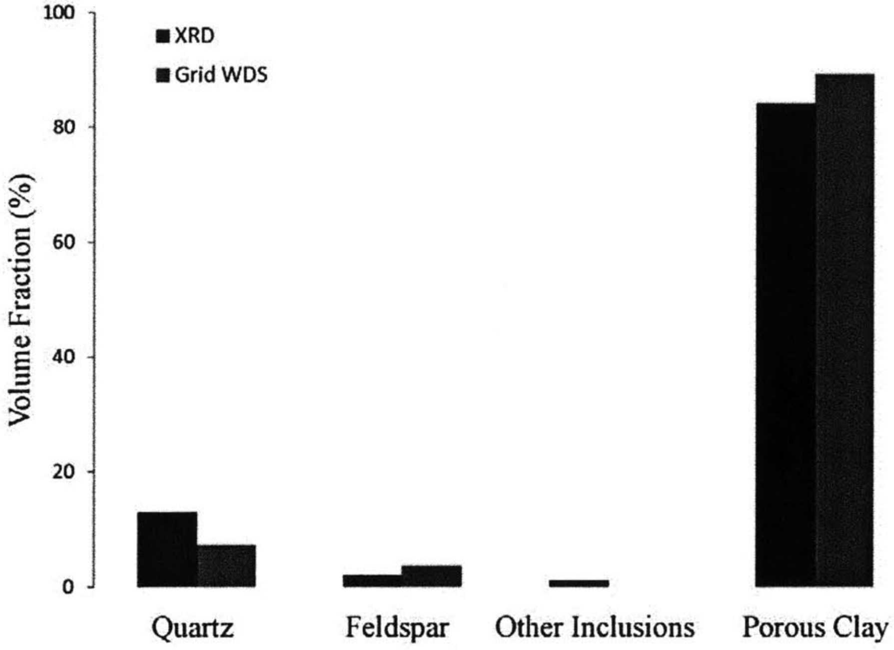

Figure 8-3: Comparison of the mineralogy results for sample S1 derived from XRD and grid WDS analysis for experiment S1-a. Other inclusions refer to siderite.

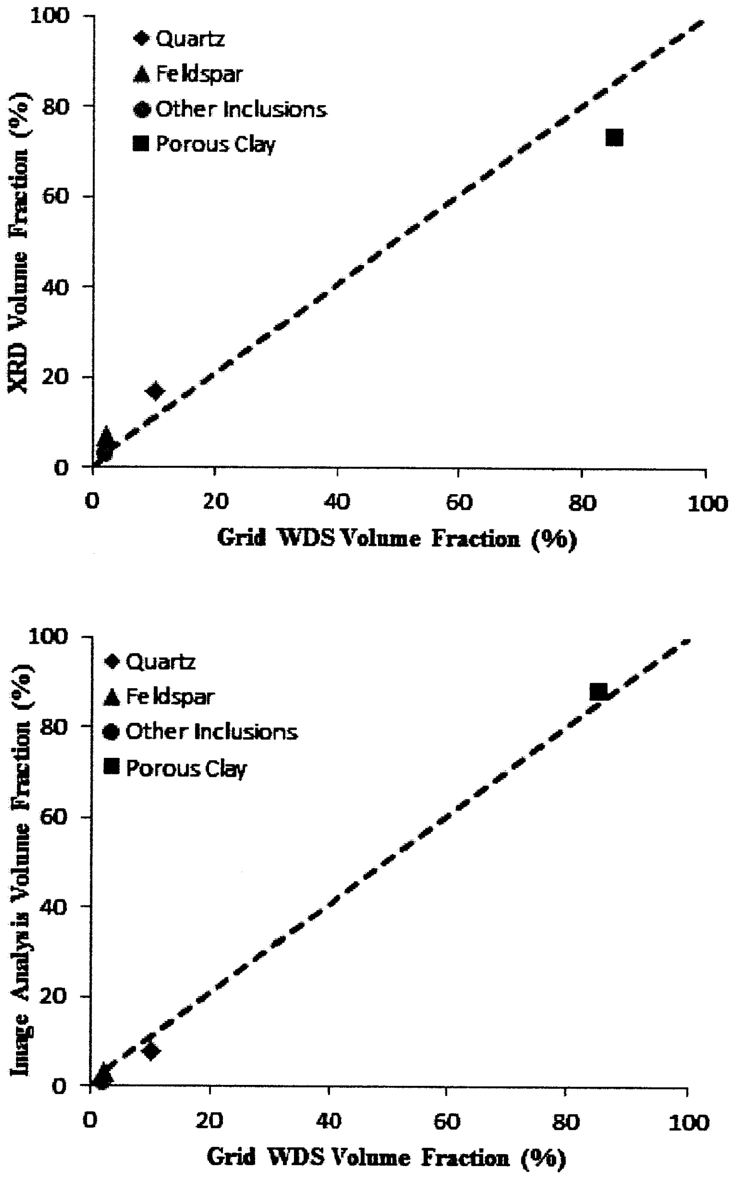

Figure 8-4: Comparisons of the volume fraction estimates obtained by grid WDS analysis for sample S7 and those obtained by (top) XRD and (bottom) X-ray image analysis.

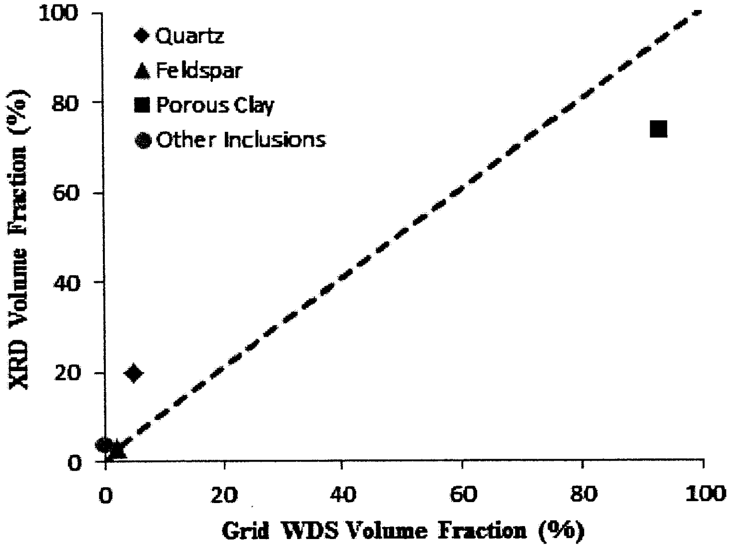

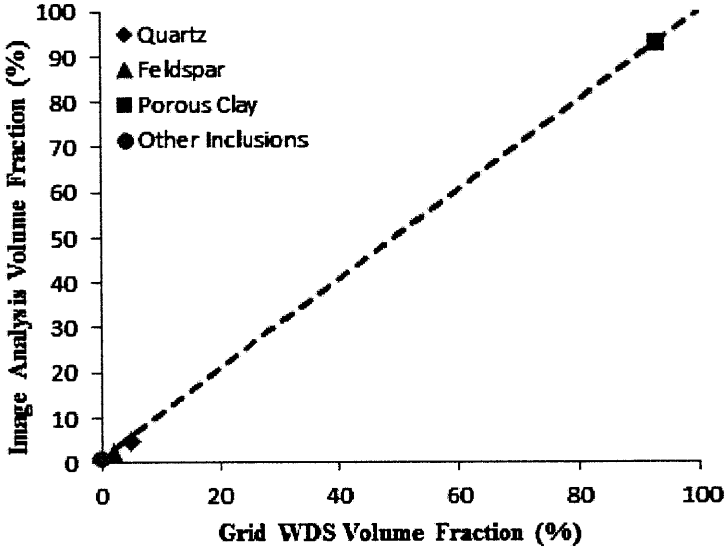

Figure 8-5: Comparisons of the volume fraction estimates obtained by grid WDS analysis for sample S3 and those obtained by (top) XRD and (bottom) image analysis.

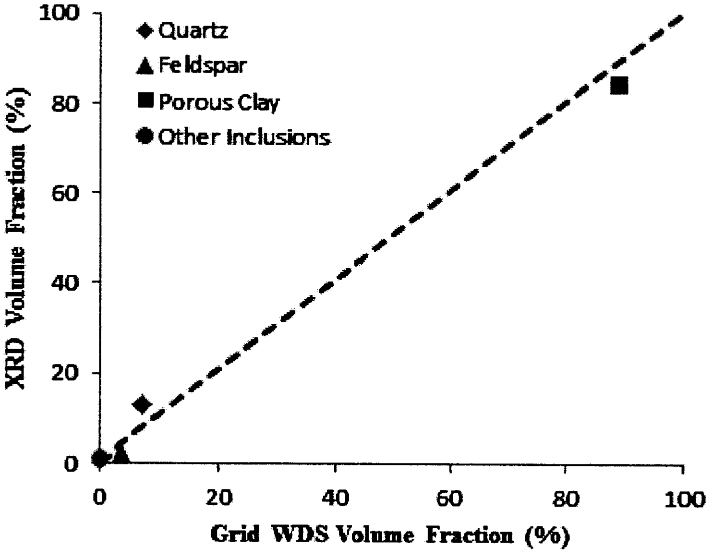

Figure 8-6: Comparisons of the volume fraction estimates obtained by grid WDS analysis for sample S1 and those obtained by XRD analysis.

8.2 The Effect of Grid Size on Grid WDS Chemical Assessment

The application of the grid WDS technique introduces two lengths scales in the chemical assessment of the heterogeneous material under investigation. The first length scale is related to the characteristic size of the microvolume being solicited by the electron beam during the EPMA experiment. That length scale limits the resolution of the technique with respect to minerals of small sizes. In the application to shale minerals, the length scale associated with the microvolume is approximately a few micrometers (Section 4.3.2). The other length scale related to the grid WDS technique is the grid size. In order to apply statistical tools for quantitative mineralogical assessment using WDS spot analyses, the size of the grid of experiments must be carefully designed to capture the heterogeneity of the sample. To avoid sampling effects, the grid size must be much larger that the largest heterogeneity in the sample; that is the largest grain present in the sample (see equation 4.4). In this section we address the following question: how large should the size of the grid WDS be relative to the size of the largest grain present in the sample? This issue will be pursued in light of the grid WDS results for shales S7 and S3. Two types of grids were employed for grid WDS assessment of these samples: large grids which provide chemical information from areas of 1 mm^2, and small grids for areas below 0.04 mm^2. The experiments performed in this study for shales S7 and S3 are tabulated in Table 6.1, which displays the grid size, number of spots, and the spacing between WDS spot analyses.

8.2.1 Grid Size Effect for S7

The grain size distribution of sample S7, presented in Figure 7-5, shows that the grains range in size from 4 μm to 200 μm. Furthermore, six grain families were identified through cluster analysis of the grain sizes that range in size from 5 μm to 59 μm.

Figure 8-7 shows a volume fraction comparison between the results of the grids that were performed for S7 sample. The results of image analysis, which are also presented in Figure 8-7 and Table 7.1, will be used as benchmark values as they correspond to large areas representative of the sample (approximately 7mm^2). Table 8.1 provides the numerical description of the results shown in Figure 8-7 along with the size of each grid performed on sample S7. Although the grid sizes are variable and differ across experiments, some grids compare well with the image

	Grid size (mm)	Quartz	Feldspar	Clay minerals	Other inclusions
Image analysis		8	3	88	1
S7-a	3 x 3	10	2	85	2
S7-b	1 x 1	24	1	75	1
S7-c	0.1 x 0.1	12	3	83	2
S7-d	0.2 x 0.2	7	2	90	1
S7-e	0.2 x 0.2	6	2	90	2

Table 8.1: Grid WDS experiments performed on sample S7, and estimated volume fractions for the main chemical constituents.

analysis results. Particularly, grids S7-a, S7-d, and S7-e show a good agreement with the results of image analysis. This trend could be explained by the following arguments:

- The results of experiment S7-a compare well with those of image analysis because the tests were performed over a large grid that samples the heterogeneity of the sample. Figure 8-8 shows the surface of sample S7 on which the experiment S7a was performed. The image shows that the size of the grid is large compared to the size of the largest heterogeneity on that surface. Consequently, this experiment yielded representative results of the sample.

- The remaining grids (S7-b, S7-c, S7-d, S7-e) are considered as relatively small grids compared to the size of the largest grain in sample S7 (approximately 200 μm). The observation that some of those grid experiments are in good agreement with the image analysis results could be attributed to sampling issues. Recall that six grain families were identified for S7 sample that range in size from 5 μm to 59 μm. Provided that these families are randomly distributed over the surface of the sample, a grid of small size may sample one family preferentially, introducing a bias in the results. To further expand this notion, Figure 8-9 shows the backscattered image of the surface of sample S7 in which experiment S7b was performed. The image clearly shows that the surface of the sample at that particular spot contains sizeable grain inclusions of quartz and feldspar. This helps explain the discrepancy between the grid WDS results for experiment S7b and those of image analysis.

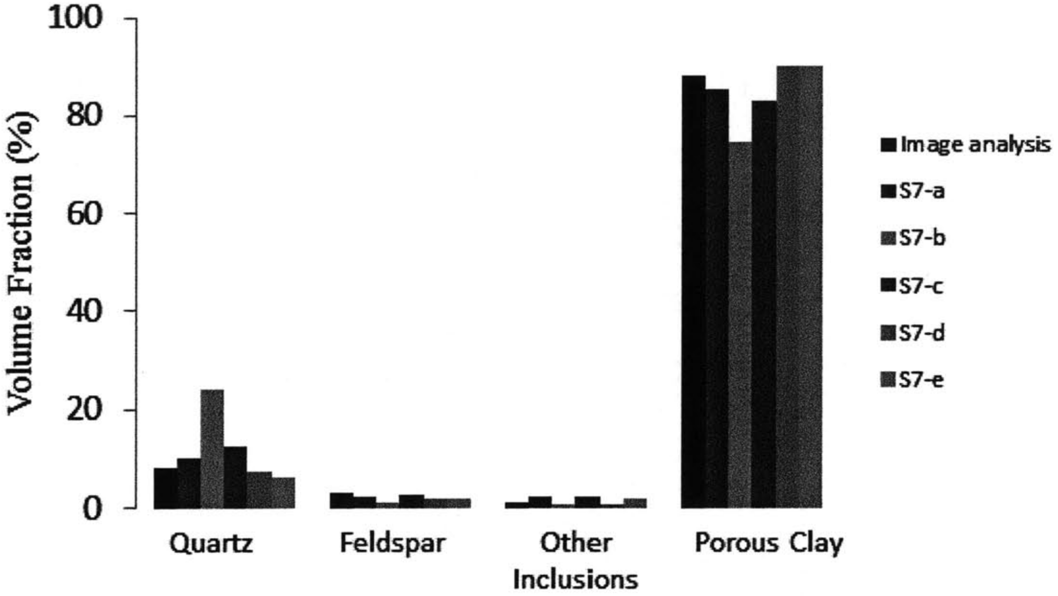

Figure 8-7: Volume fraction comparison between grid WDS and image analysis results for sample S7.

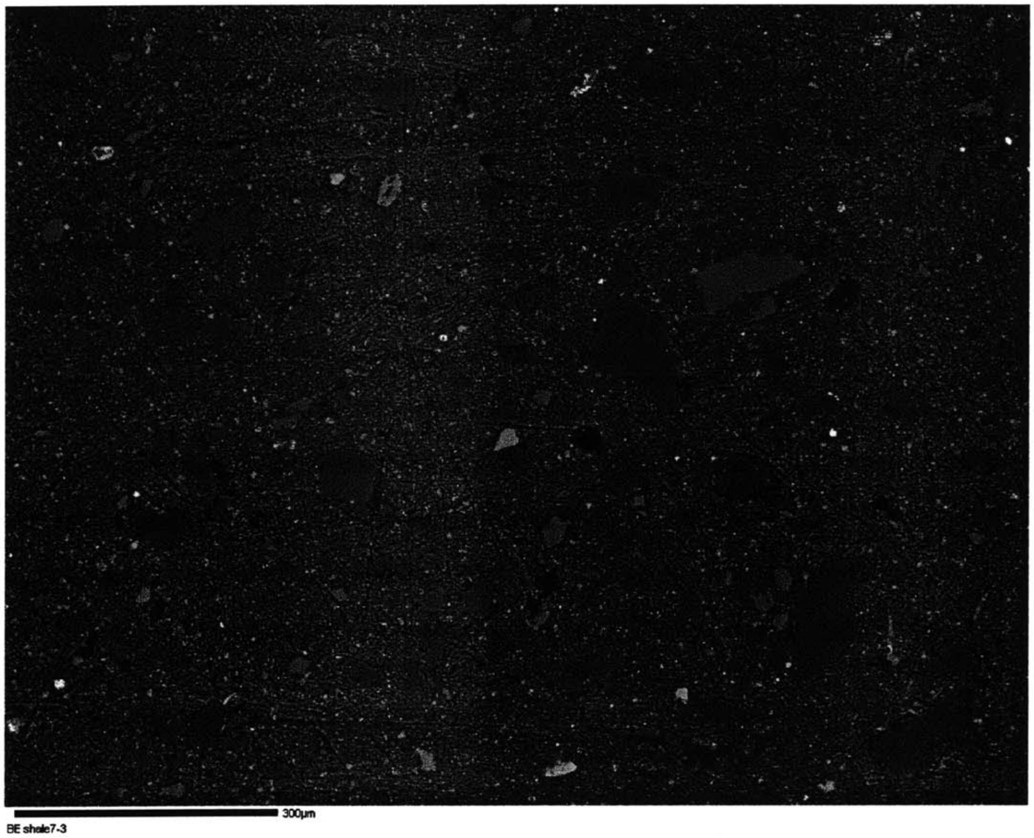

Figure 8-8: The surface of sample S7 where the experiment S7-a was performed. This image shows that the size of the grid is large compared to the size of the large grains in the sample.

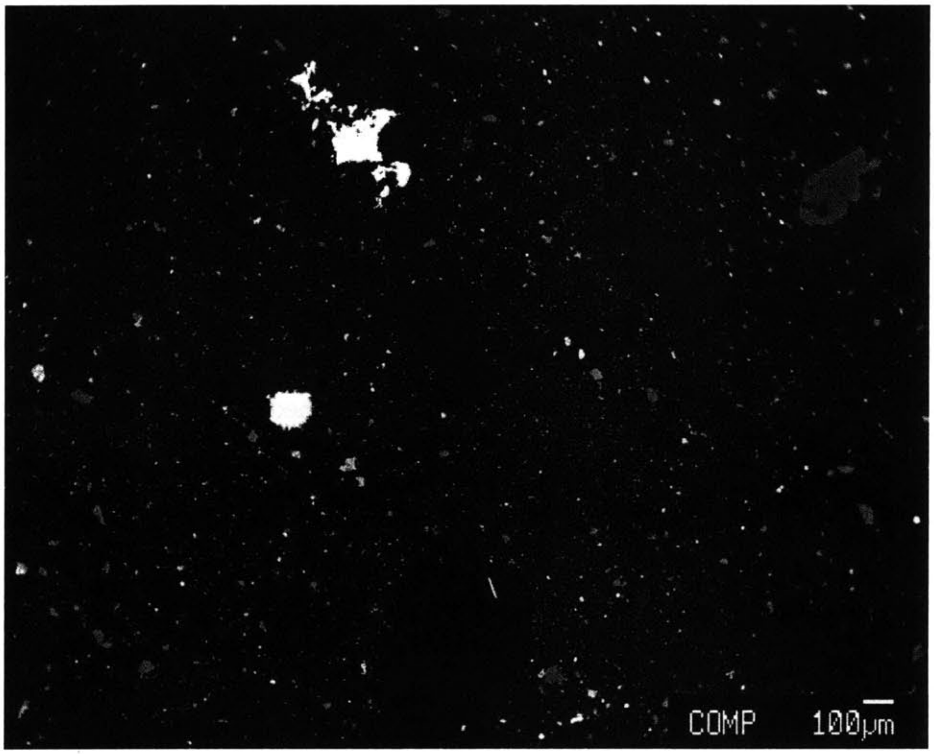

Figure 8-9: The surface of sample S7 where the experiment S7-b was performed. This image shows that the size of the grid is not large enough compared to the size of the large grains in the sample.

	Grid size (mm)	Quartz	Feldspar	Clay minerals	Other inclusions
Image analysis		5	2	92	1
S3-a	1 x 1	5	2	93	0
S3-b	0.1 x 0.1	12	6	82	0
S3-c	0.2 x 0.2	10	0	90	0
S3-d	0.2 x 0.2	5	1	94	0
S3-e	0.2 x 0.2	6	1	93	0

Table 8.2: Grid WDS experiments performed on sample S3, and estimated volume fractions for the main chemical constituents.

8.2.2 Grid Size Effect for S3

We now discuss the effect of grid size of sample S3 experiments using the grain size analysis provided in Figure 7-5. Four grain families were identified in the clustering of the grain sizes ranging from 3 μm to 19 μm. Figure 8-10 displays a volume fraction comparison between the grids that were performed for sample S3. Table 8.2 summarizes the mentioned data. The image analysis results presented in Table 7.2 will be used as benchmark values. The X-ray mapping was obtained over a large area (4 mm^2), which is deemed to be representative for the given sample.

Similar to S7 sample, grids of WDS spot analyses performed on S3 sample provided variable results. This trend may well be the result of sampling issues. The fact that the small grids (S3-b, S3-c, S3-d, S3-e) show a relative variability in the results could be attributed to the particular locations of the grids which are not representative of the entire mineralogy make-up of the sample. In contrast, experiment S3a with a large grid size compared to the largest heterogeneity (approximately 50 μm) provides a representative assessment of the sample, which is comparable with that of the image analysis. The backscattered image of the surface where experiment S3-a was performed, displayed in Figure 8-11, shows that the grid size is large compared to the individual silt grains.

8.2.3 Recommendations

The grid WDS aims at providing quantitative information about mineralogy composition of heterogeneous materials. Hence, the grid size must be large enough to provide representative information of the material of interest. This size of the grid depends mainly on the size of the

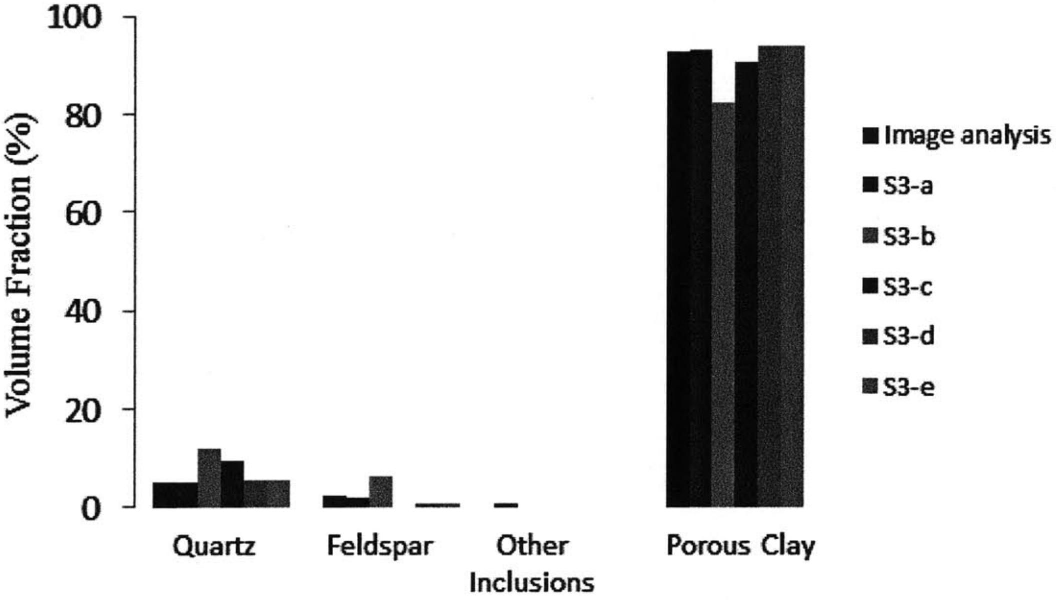

Figure 8-10: Volume fraction comparison between grid WDS and image analysis results for sample S3.

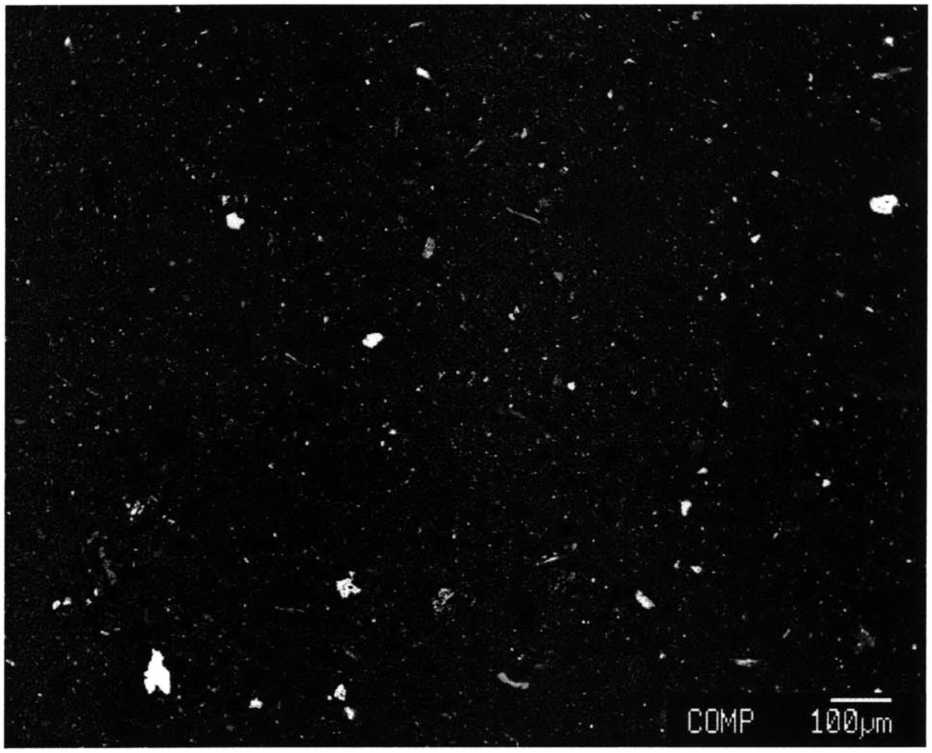

Figure 8-11: The surface of sample S3 where the experiment S3-a was performed. This image shows that the size of the grid is large compared to the size of the large grains in the sample.

largest heterogeneity in the sample. For the application of the technique, the grid size must be much larger than the largest heterogeneity to avoid sampling problems. For our development of the technique for shale materials, the previous analysis shows that the grid size requirement to provide representative mineralogy results for samples S7 and S3 is 3mm x 3mm and 1 mm x 1mm respectively. Keeping in mind that the largest grain size in samples S7 and S3 is approximately 200 μm and 50 μm respectively, we recommend that the grid sizes ought to be approximately 15 to 20 times the size of the largest grain in the sample.

8.3 Make-up of Clay Mineral Components

In this section, we focus on the components identified through clustering of grid WDS data which are associated with clay minerals. Table 6.24 summarizes the chemical components that were identified as clay phases in the three shale materials considered in our work. As it has been discussed, the resolution of WDS experiment exceeds the characteristic size of clay minerals, and therefore, the compositions of the clay phases identified through the grid WDS technique represent the on-average mineralogy of clay minerals within the probed microvolumes (see Section 4.3.2). A convenient way to resolve the clay mineralogy in shale determined through grid WDS can be the treatment of the overall clay signature measured in each WDS spot test as a combination of clay minerals involved in the mix. To accomplish this objective, we recall the mixture model developed in Section 4.3.4 to separate major clay families potentially present in the clay matrix. In particular, we aim to distinguish 1:1 clay minerals (kaolinite) from 2:1 clay minerals (illite, smectite, mixed layer clays). The specific identification of 2:1 clay minerals such as illite, smectite, and mixed layer clays cannot be accomplished using WDS measurements alone. Structural information about the minerals such as basal spacing would be required in addition to WDS experiment for their identification.

The mean compositions of the identified clay mineral components (see Table 6.24) are superimposed on the common clay minerals presented in Figure 4-16. This step helps in identifying clay mineral types from their relative positions in the atomic ratio projections adopted for clay minerals as shown in Figures 8-12, 8-13, and 8-14 for experiments S7-a, S1-a, and S3-a, respectively. Figure 8-12b shows that the average composition of the clay components for experiment S7-a is situated between the regions expected for 2:1 and 1:1 clays. This confirms the assumption that the grid WDS technique probes an on-average composition of clay minerals, since sample S7 contains both types of clay (see Table 3.1). This behavior is also observed in the Al-Si space as shown in Figure 8-12a. The relatively high aluminum content of the clay components obvious in this space may indicate the presence of other clay types. The same remark applies for experiment S1a as shown in Figure 8-13. In contrast, the average compositions of clay minerals components identified for sample S3-a are situated in the region expected for 2:1 clays and particularly montmorillonite as can be seen in Figure 8-14b. The same trend is obvious in the Al-Si space as shown in Figure 8-14a. This indicates that sample S3 is dominated by 2:1 clay minerals.

The application of the mixture model to clay minerals requires the identification of end anchor points and the element (X in equation 4.8) to be used in the mixture analysis. The element to be used in the mixture model must provide sufficient contrast between 1:1 clay and 2:1 clay. The combination K+Ca+Na serves this purpose since 1:1 clays contain minor amounts of these elements. To define the end anchor points, the common clay minerals data presented in Figure 4-16 is used. For 1:1 clay minerals, the average value of K+Ca+Na is approximately 0.1, whereas it is equal to approximately 2.76 for 2:1 clay minerals. This information is used to analyze clay minerals components identified for samples S7-a, S3-a, and S1-a. The application of mixture modeling follows the steps outlined in Section 4.3.4. The λ values are calculated based on the following formula:

$$X_{mix} = \lambda X_I + (1 - \lambda) X_{II} \tag{8.1}$$

where λ is the proportion of 1:1 clays (kaolinites) in the mix, X_{mix} represents the measured combination K+Ca+Na, X_I and X_{II} represent the the atomic ratios of K+Ca+Na for 1:1 and 2:1 clays respectively. These values are obtained from the data of common clay minerals as stated above. The calculated λ values are then clustered using the Mclust algorithm in which one variable was used in this case, λ. Finally, the clay types proportions of the mixture phase are separated according to the following formula:

$$V_I = \lambda_i v_{f,i} \tag{8.2}$$

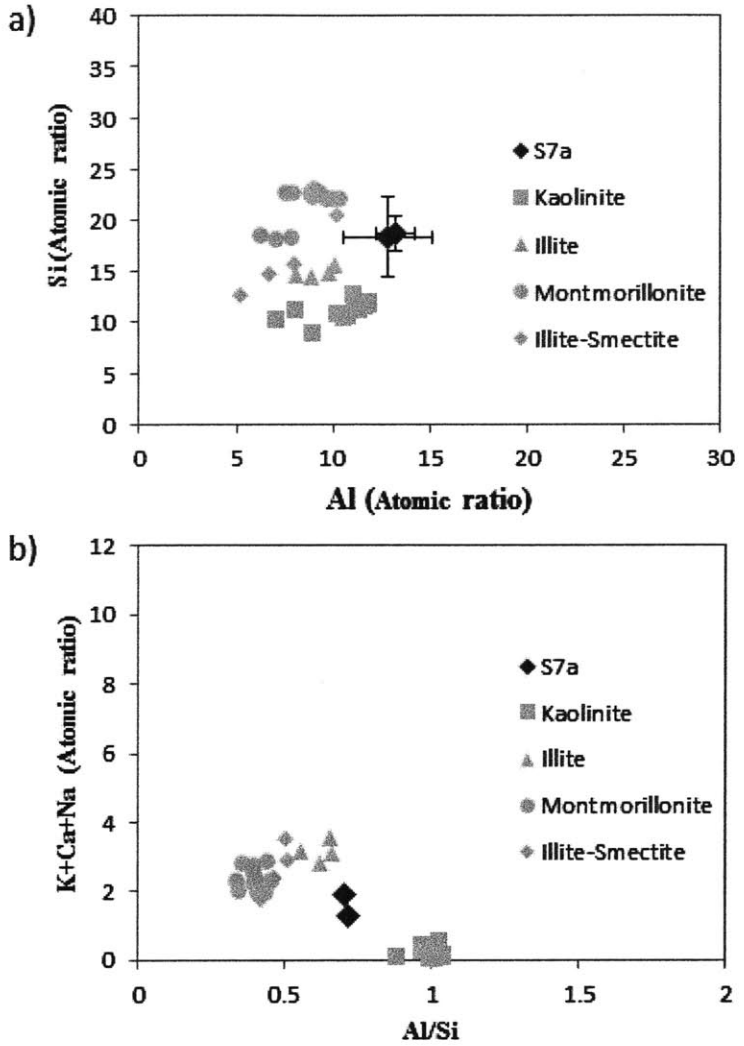

Figure 8-12: Average compositions of clay mineral components identified in experiment S7-a through cluster analysis of grid WDS data and displayed on the projections adopted for clay minerals; a) Si-Al space, and b) Al/Si-K+Ca+Na space. Data in gray color corresponds to the composition of common clay minerals shown previously in Figure 4-16.

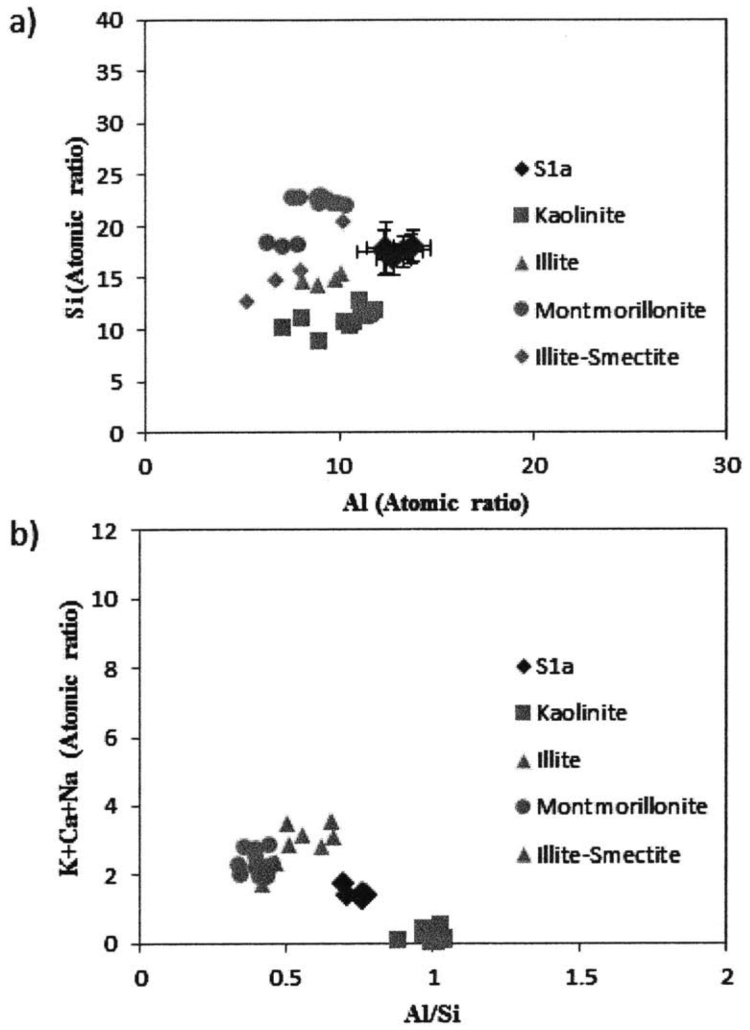

Figure 8-13: Average compositions of clay mineral components identified in experiment S1-a through cluster analysis of grid WDS data and displayed on the projections adopted for clay minerals; a) Si-Al space, and b) Al/Si-K+Ca+Na space. Data in gray color corresponds to the composition of common clay minerals shown previously in Figure 4-16.

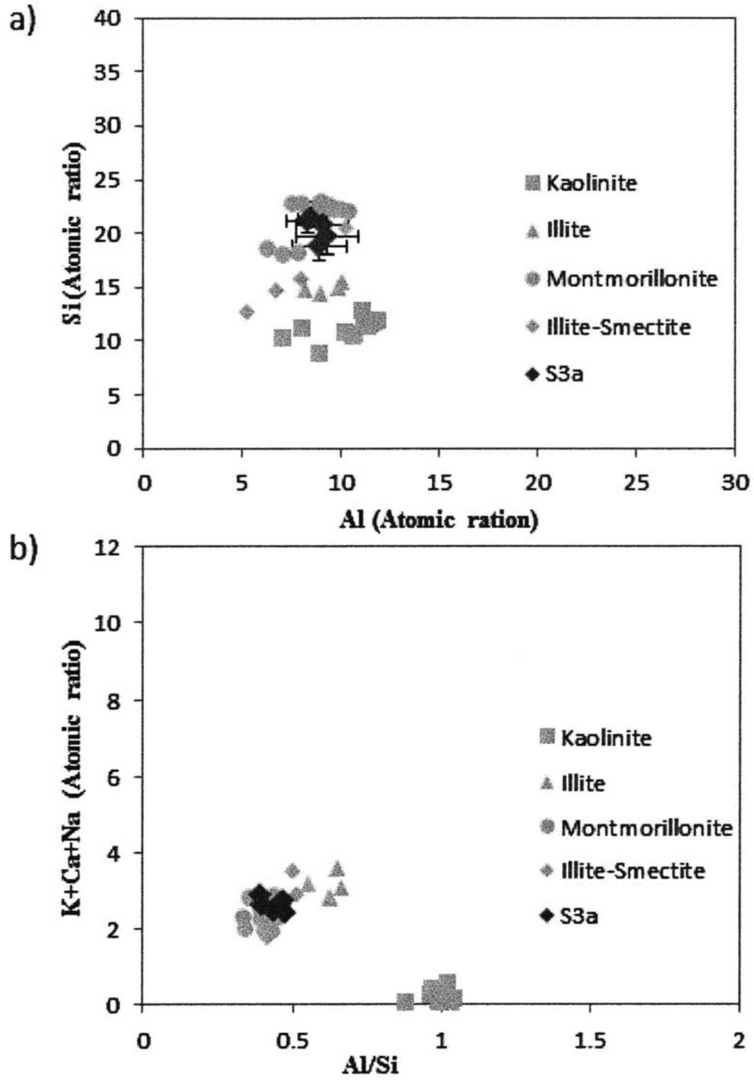

Figure 8-14: Average compositions of clay mineral components identified in experiment S3-a through cluster analysis of grid WDS data and displayed on the projections adopted for clay minerals; a) Si-Al space, and b) Al/Si-K+Ca+Na space. Data in gray color corresponds to the composition of common clay minerals shown in Figure 4-16.

	Component 1		Component 2		Component 3	
	λ_1	$v_{f,1}$	λ_2	$v_{f,2}$	λ_3	$v_{f,3}$
S7-a	0.39	0.50	0.55	0.50	-	-
S3-a	-0.30	0.05	0.05	0.91	0.44	0.04
S1-a	0.03	0.01	0.45	0.30	0.57	0.69
	1:1 clays	2:1 Clays				
S7-a	0.47	0.53				
S3-a	0.06	0.94				
S1-a	0.53	0.47				

Table 8.3: Results of the analysis of the clay components for experiments S7-a, S3-a, and S1-a. This table displays the clustering results vlaues.

	1:1 clays	2:1 Clays	1:1 - 2:1 Clay ratio
S7-a	27	30	0.9
S3-a	5	74	0.07
S1-a	33	29	1.14

Table 8.4: Volume fractions of 1:1 and 2:1 clays identified through mixture modeling.

$$V_{II} = (1 - \lambda_i) v_{f,i} \tag{8.3}$$

where V_I and V_{II} are the pure volume fractions of 1:1 and 2:1 clays, respectively. λ_i and $v_{f,i}$ represent the mean value and the volume fraction of component i identified in the clustering of λ values. Table 8.3 summarizes the mixture modeling results for the clay components identified in experiments S7-a, S3-a, and S1-a. Table 8.4 lists the final volume fractions of 1:1 and 2:1 clays derived from mixture modeling. The ratios of 1:1 - 2:1 clay minerals ratios determined by WDS are on the same order of magnitude compared to those determined by XRD (see Table 3.5).

8.4 Chapter Summary

In this Chapter, we validated the grid WDS technique for shale by comparing the mineralogy estimates with those obtained from two independent techniques: X-ray diffraction and image analysis. We showed that the results of grid WDS technique are in adequate agreement with those obtained by the alternative methods. In general, XRD estimates consistently display lower volumetric values for the porous clay component compared to the estimates obtained by grid

WDS and image analysis. We also studied the effect of grid size on the mineralogy information obtained by grid WDS. Based on our experimental campaign, a grid of size $15-20$ times the largest grain in the sample was deemed sufficient to appropriately capture the heterogeneity of shale samples. Finally, we applied the mixture modeling presented in Section 4.3.4 to analyze the make-up of clay mineral components identified by the grid WDS technique. This approach enabled the identification of clay families.

Part IV

Applications

Chapter 9

Applications

The grid indentation results of shale materials are interpreted solely based on mechanical arguments including mechanical behaviors of constituents, length scale consideration, and overall composition known a priori from mineralogy tests. The identified mechanical behavior of shale constituents at the micrometer and sub-micrometer scales are not yet linked to particular material chemistries. In this chapter we propose the chemo-mechanical coupling technique as a method to link shale mechanical behavior to composition at micrometer and sub-micrometer length scales. The chapter begins with a presentation of the motivation for the coupling technique. The next section discusses the results of grid WDS and grid indentation techniques separately. The discussion of the coupling of the chemical data inferred from grid WDS technique and the mechanical data inferred from grid indentation technique ends this chapter.

9.1 Motivation: Nanomechanics of Shale

To motivate the chemo-mechanical characterization of shale, the results of a comprehensive nanoindentation experimental program on various shale materials are recalled in Figure 9-1. The indentation data developed by Bobko et al. [10] were reanalyzed in [43] using the ML-EM clustering method, yielding similar modulus and hardness properties as those obtained by the deconvolution analysis in [10]. The shale materials characterized by the GeoGenome Industry Consortium cover a broad spectrum of compositional properties of shale (varying mineralogies and porosities). The indentation moduli M_1, M_3 for each material displayed in Figure 9-1 correspond to the cluster modeling of the mechanical porous clay from indentation and hardness data (see Section 5.7). With a focus on elasticity, the assessment of the porous clay (or phase 1) presented in Section 5.7 consistently applies to each indentation grid measured in both directions for each shale material considered in Figure 9-1. The indentation moduli properties scale with the clay packing density, which synthesizes the compositional and porosity information into one parameter: $\eta = f^c / (1 - f^{inc})$ (see Section 6.27). The scaling between the indentation moduli and the clay packing density emphasizes the effect of the nanoporosity (or $\varphi_0 = 1 - \eta$) as the main driver of the anisotropic elastic behavior of the porous clay. It is observed that increasing indentation modulus values correspond to increasing clay packing densities, tending to an apparent solid phase ($\eta \rightarrow 1$) that is anisotropic. In addition, a solid percolation threshold exists as packing densities approach 0.5, which hints towards a granular behavior of the porous clay composite.

The relationship between modulus-packing density implies that the particular mineralogy compositions of the seven shale materials in Figure 9-1 play a less significant role in defining the porous clay elasticity. For each shale material, the vertical error bars encompass the variability of indentation modulus properties as assessed by cluster modeling. The mentioned variability captures the mechanical variability observed from grid indentation data, which may be attributed to varying local porosities. In addition, the grid WDS data developed in this study hint towards the locally variable chemistry of the clay phases as another potential source for the observed range of modulus properties of the mechanical porous clay. The stiffness behavior of the porous clay phase inferred from statistical indentation represents the in situ response of the clay fabric in non-organic shale materials. The apparent solid clay phase implied in Figure 9-1 exhibits a smaller order-of- magnitude in elasticity compared to the measured elastic properties of single clay crystals (see review in [11]). This mechanical unit of clay incorporates the mechanical contributions of conglomerates of clay platelets, interlayer matter (absorbed water, hydrated cations), and interparticle contacts.

The previous discussion highlights the importance of the porous clay phase identified through the grid indentation technique in shale modeling. However, key questions remain about the indentation measurements on shale. Is the mechanical behavior of the porous clay in shale, i.e. average M, H data for the porous clay phase from grid indentation and cluster analysis, in fact

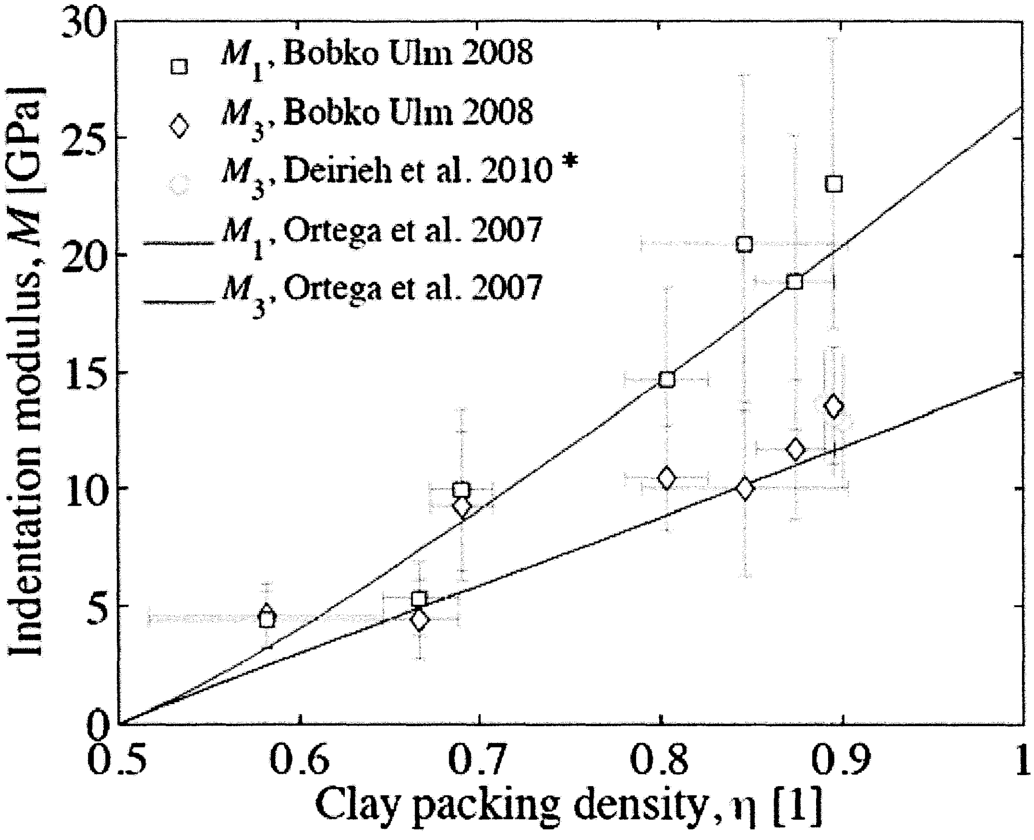

Figure 9-1: Indentation modulus values for seven shale materials of different origins and mineralogy compositions, detailed in [10]. For each sample, grid indentation experiments were performed parallel and normal to the natural bedding planes of the material (M_1, M_3, respectively). The indentation data was reanalyzed in [40]. The indentation data is presented as a function of the clay packing density whose variability depends on different experimental estimates of the porosity (MIP porosity versus porosity backcalculated from density measurements). The data points correspond to mean properties and vertical error bars to standard deviations assessed by the cluster analysis of the grid indentation data. Solid lines correspond to the micromechanics modeling of the porous clay phase developed independently of indentation data [41] [42]. *Data points correspond to experiments S3-C1I, S3-C2I and S3-C3I performed in this study.

associated with the clay fabric of shale from a strict chemical point of view? In what follows, we address this question by performing the chemo-mechanical coupling technique on two shale materials investigated in this work (S3, S7).

9.2 Chemo-Mechanical Coupling Technique

The chemo-mechanical coupling technique, which involves measuring mechanics and composition of a specified location of a sample, aims at establishing a link between mechanics and composition at fundamental length scales. This task is achieved through performing grid indentation and grid WDS experiments on the same surface of a sample. The indentation and WDS experiments were performed in square grids of properly chosen spacing to deliver the required information. The coupling technique starts by performing a grid indentation experiment on a specified location on a shale sample. The sample is then carbon coated to prevent charging in WDS testing. The grid of indentations can be located making use of ink marker and big indents that can be easily identified under the backscattered mode in EPMA. Once the indentations are precisely located, a grid of WDS spots is performed over the same area to provide the required link between mineralogy and mechanics. Finally, the experimental data obtained in both tests is interpreted with cluster analysis techniques.

An important consideration for the coupling of the indentation and WDS data is the adequate comparison between the material volumes probed in each technique. A Monte Carlo (MC) simulation of WDS experiment was performed using CASINO [19] and the experimental parameters described in Section 4.3.2. The average density of the simulated shale material corresponds to the experimental value $\rho = 2.55\ g/cm^3$ (see Table 3.2). The MC simulation shows depths of interaction between the material and accelerated electrons of approximately 2 μm. This characteristic length scale of the interaction volume in a WDS experiment matches that of the indentation experiment defined by the maximum indentation depth. Finite element simulations for indentation testing using a Berkovich probe show that the measured elastic response corresponds to a material volume that is roughly 3 times the depth of indentation [33] [60]. With average indentation depth of approximately $h_{\max} = 700 - 900$ nm for the indentation experiments performed in this study, the material domain sensed by indentation is on the order

Sample name	Grid size	Spacing	No. of points	Experiment
S3-C1W	25x25	5	625	WDS
S3-C1I	25x25	5	625	Indentation
S3-C2W	20x20	10	400	WDS
S3-C2I	20x20	10	400	Indentation
S3-C3W	31x31	5	961	WDS
S3-C3I	31x31	5	961	Indentation
S7-C1W	25x25	10	625	WDS
S7-C1I	25x25	10	625	Indentation

Table 9.1: Experimental program of the grid WDS/indentation experiments performed in the coupling analysis. A total of four surface locations in two samples (S7, S3) were employed for indentation and WDS tests. Two particular locations (S3-C3, S7-C1) containing a large sized inclusion were imaged by BSE images and X-ray maps. The letters I, W refer to either indentation or WDS experiments, respectively.

of $2-3$ μm. These results show that the microvolume probed by indentation is comparable to that probed by WDS.

9.3 Grid WDS/Nanoindentation Results

The implementation of the grid indentation and WDS techniques for the chemo-mechanical study of shale follows the experimental program detailed in Table 9.1. Each set of these experiments includes grid WDS and indentation experiments performed on the same spot, such as S3-C1W and S3-C1I, with the letters I and W corresponding either to indentation or to WDS experiments, respectively. Four coupled experiments were performed on two different shale samples (S7, S1). The first two experiments (S3-C1, S3-C2), which were performed on sample S3, will be used to reveal the chemical nature of the porous clay phases identified by grid indentation technique. The other two experiments (S3-C3, S7-C1) were performed on locations containing sizeable inclusions, and BSE images and X-ray maps were also obtained for these locations. These experiments will be used to study the nature of the so-called composite phases identified in grid indentation technique.

9.3.1 Grid WDS Results

The chemical assessment of the shale samples using the grid WDS technique follows the procedure outlined in Section 4.3.3. The chemical data collected by WDS spot analysis is interpreted using the multivariate clustering, in which the atomic ratios of the measured elements are used to find the most probable chemical families present in the sample. Once the data is clustered, the results are presented on 2-D elemental projections that provide means for visual interpretation of the data. The projections adopted in this study differentiate between silicates and carbonates. In the case of silicates, such as quartz, feldspar, and clay minerals, the projections Al–Si, and Al/Si–K+Ca+Na are adopted. The projections that can be used for the analysis of carbonates are: Ca–Mg, and Fe–Si. These projections help in identifying calcite, magnesite, dolomite, and siderite (see Figure 4-9 for an illustration of the identification process). The remainder of this section presents the interpretation of clustering results defined for grid WDS experiments in Table 9.1, which are displayed in Figures 9-2 through 9-9. The objective is to identify the poles and ligands associated with the main chemical components derived from the grid WDS experiments.

A pole is defined as a component with a relatively small standard deviation; that is an intense clustering of data points around a mean position, and, hence, interpreted as an approximately homogeneous phase. Three types of poles were identified in the analysis of grid WDS experiments listed in Table 9.1, that is quartz, feldspar, and clay mineral poles. These poles can be identified based on their positions on the relevant projections. Quartz poles, for example, are located in the region expected for quartz mineral (Figure 4-9). Thus, we interpret phases such as phases 9 and 10 in Figure 9-8, for example, as quartz mineral phases. Similarly, feldspar poles are situated in the region expected for feldspar minerals as shown in Figure 4-9. Phase 7 in Figure 9-6 represents an example of feldspar pole. In contrast, the identification of clay poles is complex owing to their highly heterogeneous chemical composition. This task is simplified using the database gathered form the literature and displayed in Figures 4-10 through 4-13, which account for the chemical variability of clay minerals. In particular the chemical data associated with the most common clay minerals presented in Figure 4-16 is the most important. This data set aids in identifying the clay minerals poles in the proposed atomic projections. Thus, we interpret phases located in the region expected for clay minerals, such as phases 1, 2, 3, 4, 5, and 7, in Figure 9-8. The spread in the clay phases is mainly due to the highly heterogeneous nature of clay minerals, and the fact that WDS probes an on-average composition of clay minerals (see Section 4.3.2).

Analysis total described in Section 4.3.3 is an important experimental parameter that can be used to strengthen the above findings of clays, quartz, and feldspar poles. In practice, the analysis total should be equal to 100 %; however, the application of WDS deviates from the given mark due to some minor elements not being measured and other experimental issues. The analysis totals corresponding to clay phases consistently displays lower values (95 %) compared to those of quartz and feldspar phases (100 %). This behavior is attributed to hydrogen, which present in clay minerals in the form of water or OH^-, and which is not measured in the WDS experiments because its low atomic number is outside the range of resolution of EPMA. For example, quartz phases, such as phase 10 in Figure 9-8, have analysis totals of approximately 100 %, while clay phases, such as phases 1 through 5 in Figure 9-8, have analysis totals of approximately 90 %.

Another prominent feature that is noticed throughout the chemical analyses presented in this Chapter is the presence of ligands between clays and other non-clay minerals (quartz, feldspars). Feldspar- and quartz-clay ligands are clearly visible, for example, in the chemical analysis of sample S3-C1W presented in Figure 9-2. These ligands are identified visually based on their end anchor points. Phase 9 connects the clays and quartz phases in the Al–Si projection (Figure 9-2a). This mixture phase spans between quartz anchor point ($\mathrm{Si} = 33.33$ and $\mathrm{Al} = 0$) and clay anchor point ($\mathrm{Si} \approx 15 - 20$,and $\mathrm{Al} \approx 5 - 10$). Phase 3 connects the clay and feldspar phases in the Al/Si–K+Ca+Na projection in Figure 9-2b. This mixture phase spans between feldspar anchor point (K+Ca+Na=7.7, Al/Si=0.33 – 1) and clay anchor point (K+Ca+Na=2–4, Al/Si=0.3-1). Table 9.2 compiles the chemical phases and their identifications for the grid WDS results presented in Figures 9-2 through 9-9. These results will be coupled with grid indentation results to reveal the chemical nature of the mechanical phases identified by grid indentation.

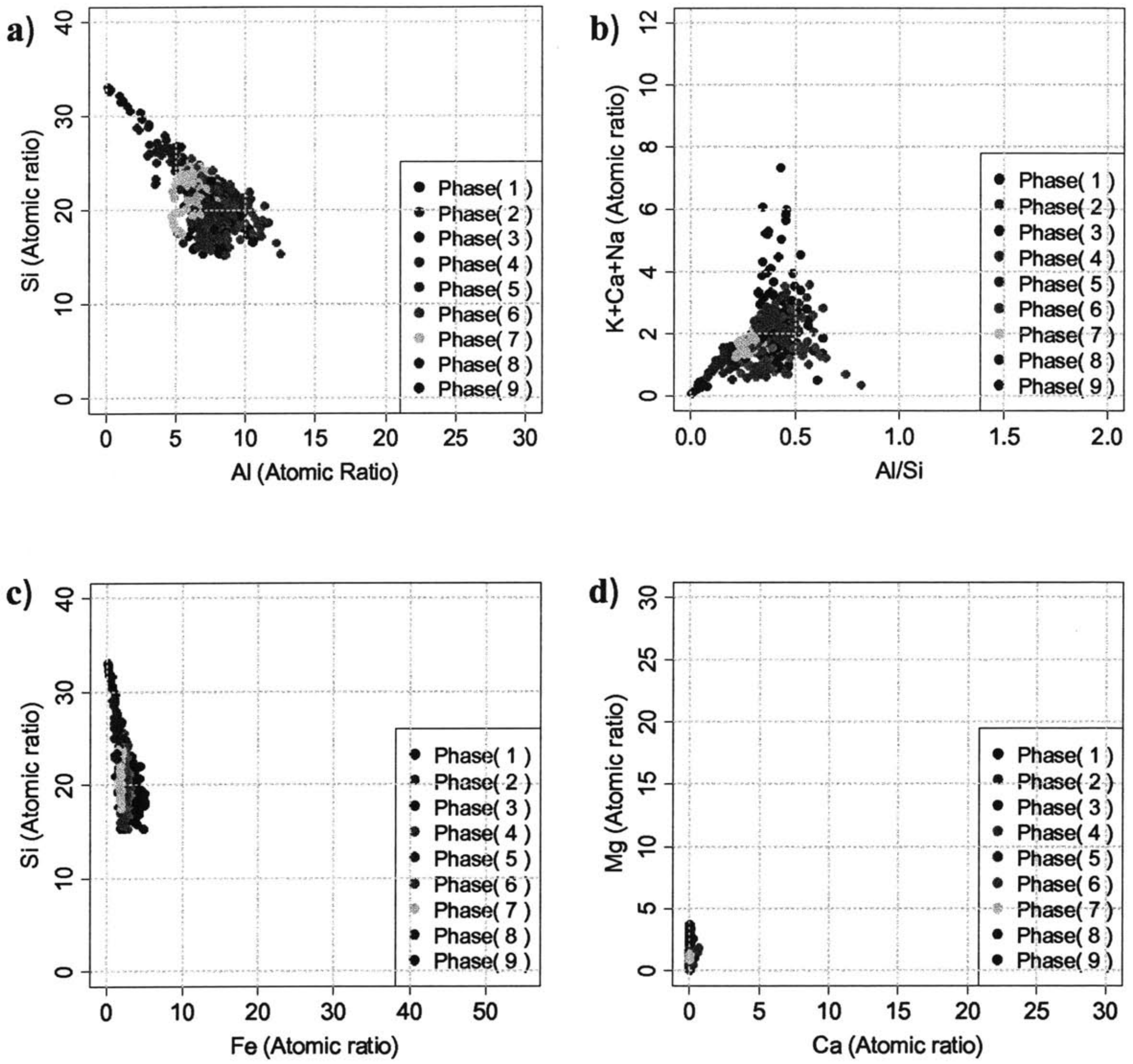

Figure 9-2: Multivariate cluster analysis of the grid WDS data for experiment S3-C1W. The identified phases are presented on 2-D projections for visual interpretation of the data: a) Al-Si space and b) Ca+Na+K-Al/Si space separate quartz, feldspars, and clay minerals. c) Fe-Si space and d) Ca-Mg space separate carbonate minerals; siderite, calcite, magnesite, ankerite, and dolomite.

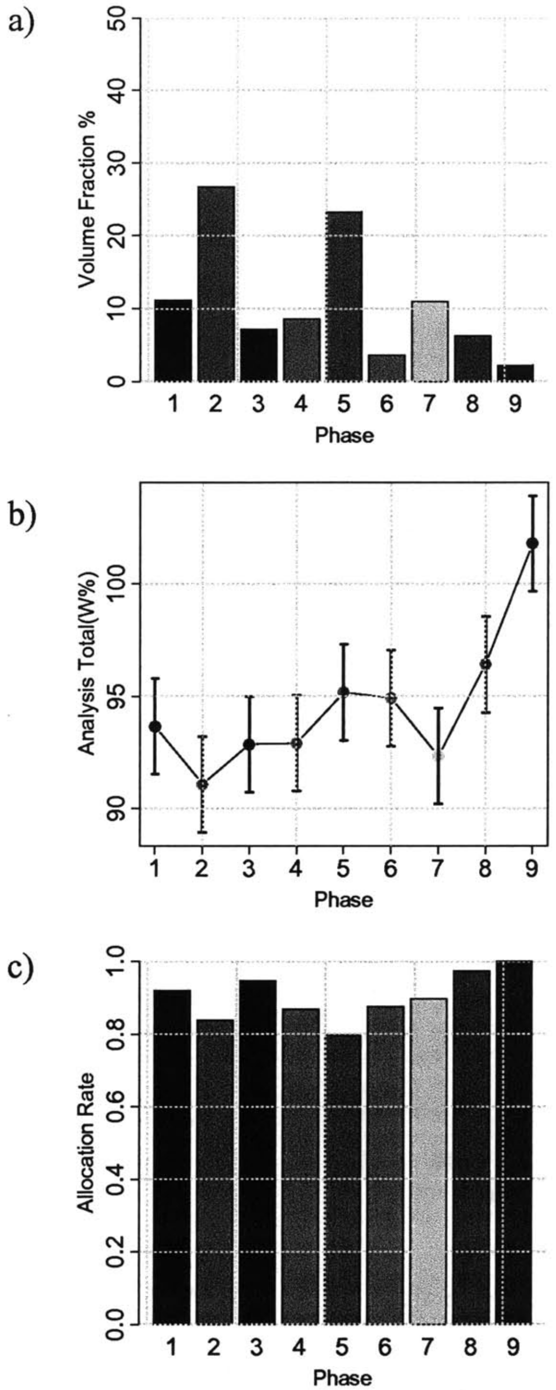

Figure 9-3: Graphical representation of clustering results presented in Table 9.8 for experiment S3-C1W. a) volume fractions, b) mean and standard deviation values of the analysis totals, and c) allocation rates for each of the phases displayed in Figure 9-2.

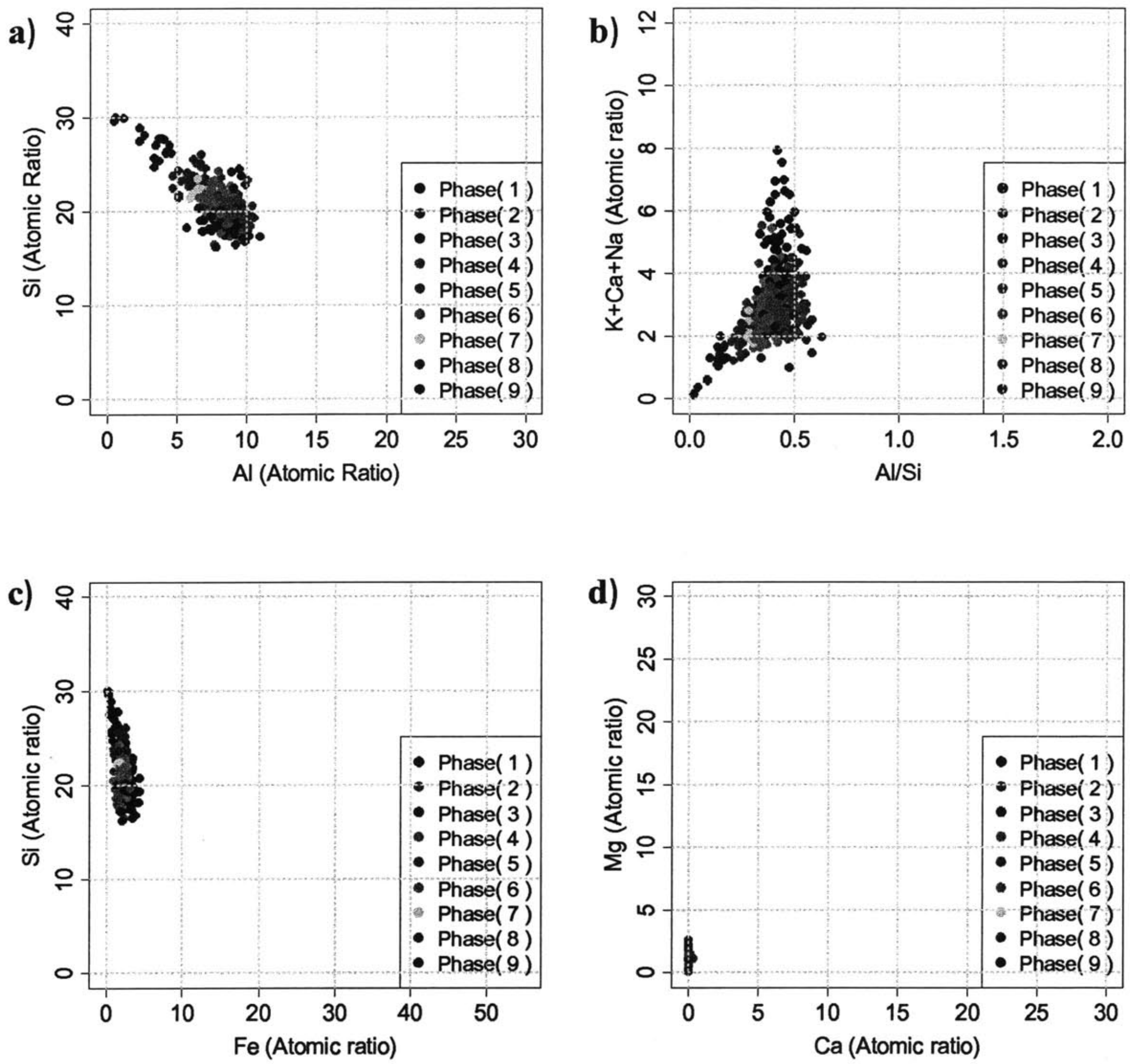

Figure 9-4: Multivariate cluster analysis of the grid WDS data for experiment S3-C2W. The identified phases are presented on 2-D projections for visual interpretation of the data: a) Al-Si space and b) Ca+Na+K-Al/Si space separate quartz, feldspars, and clay minerals. c) Fe-Si space and d) Ca-Mg space separate carbonate minerals; siderite, calcite, magnesite, ankerite, and dolomite.

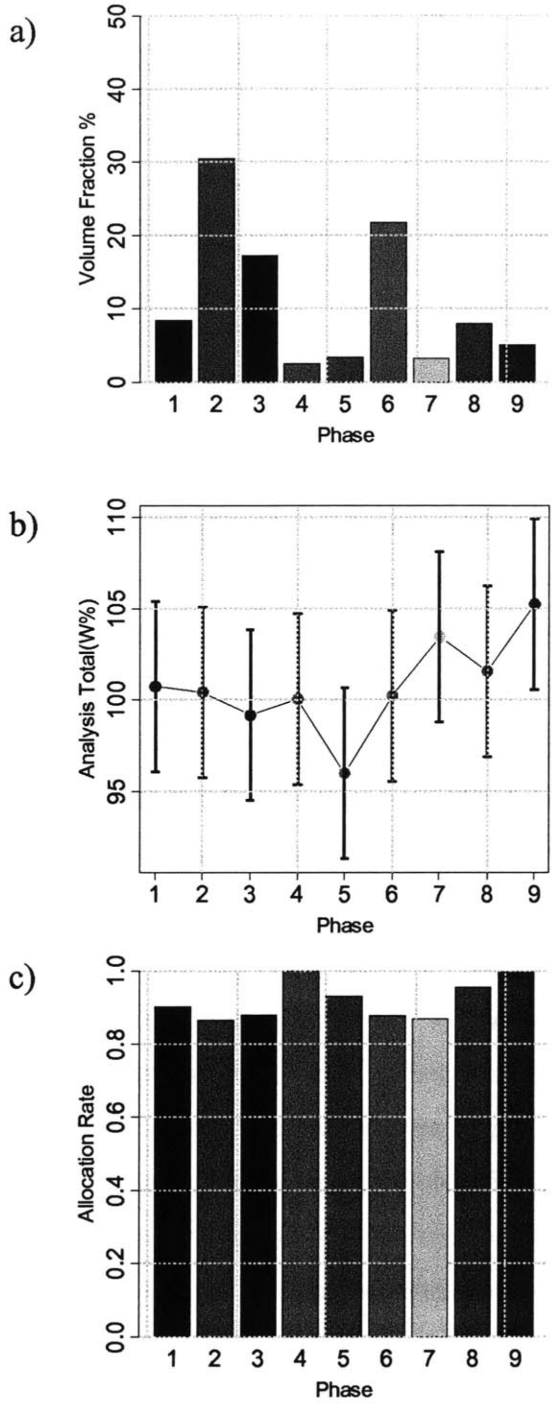

Figure 9-5: Graphical representation of clustering results presented in Table 9.10 for experiment S3-C2W. a) volume fractions, b) mean and standard deviation values of the analysis totals, and c) allocation rates for each of the phases displayed in Figure 9-4.

Sample	S3-C1W	S3-C2W	S3-C3W	S7-C1W
Quartz phases	9	-	-	10, 9
Clay phases	1, 2, 4, 5, 6, 7	2, 3, 4, 5, 6, 7	1, 2, 3, 5	1, 2, 3, 4, 5, 7
Feldspar phases	-	-	7	-
Quartz-clay phases	8	9, 8	10, 9	8
Feldspar-clay phases	3	1	4, 6, 8	6

Table 9.2: Identification of chemical phases based on cluster modeling of grid WDS experiments outlined in Table 6.1 and Figures 9-2 through 9-9.

9.3.2 Grid Indentation Results

The interpretation of the cluster analysis results of grid indentation experiments, listed in Table 9.1, is pursued based on the approach outlined in Section 5.7. This approach, previously presented in [10] [25], employs mechanical arguments, length scale considerations, and overall material composition known a priori from mineralogy tests (see Table 3.1) to evaluate the mechanical response of shale measured in grid indentation. Results of cluster analysis of M and H values for the grid indentation experiments, listed in Table 9.1, are displayed in Figures 9-10 through 9-13 and numerically summarized in Tables 9.3 through 9.6. The discussion of the grid indentation results is pursued based on the results of experiment S3-C1I displayed in Figure 9-10.

Four mechanical phases were identified from the clustering of indentation modulus and hardness measurements as shown in Figure 9-10 and Table 9.3 . It is worth noting that the term mechanical phase is understood as each of the mixture components recognized by the cluster model based on elasticity and hardness characteristics. A priori, these mechanical phases active in the response of shale at the micrometer and sub-micrometer scales are not yet linked to particular material chemistries. On-average modulus and hardness properties display increasing values ranging between those of phase 1 (lowest values) and phase 4 (highest values). Phase 4 corresponds to the dominant quartz inclusions determined from XRD mineralogy tests. This inclusion phase exhibit average indentation modulus and hardness values of approximately $M = 80 - 150$ GPa, and $H = 12 - 20$ GPa. These results match, in first order, the expected mechanical properties of quartz [20] [61] [53]. Phase 1 corresponds to the porous clay phase identified from its large volume fractions (Figure 9-10b) expected from the XRD mineralogy.

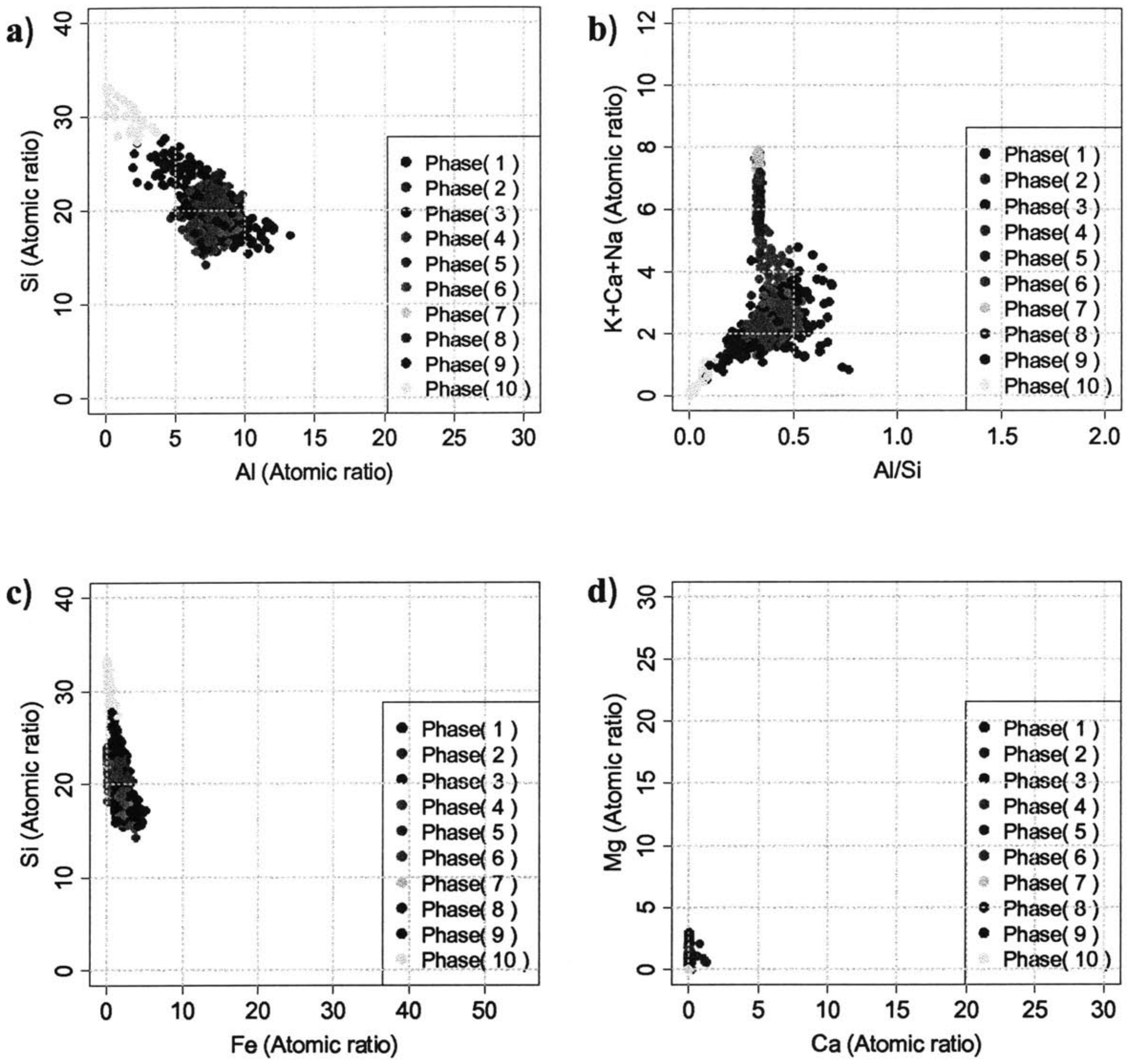

Figure 9-6: Multivariate cluster analysis of the grid WDS data for experiment S3-C3W. The identified phases are presented on 2-D projections for visual interpretation of the data: a) Al-Si space and b) Ca+Na+K-Al/Si space separate quartz, feldspars, and clay minerals. c) Fe-Si space and d) Ca-Mg space separate carbonate minerals; siderite, calcite, magnesite, ankerite, and dolomite.

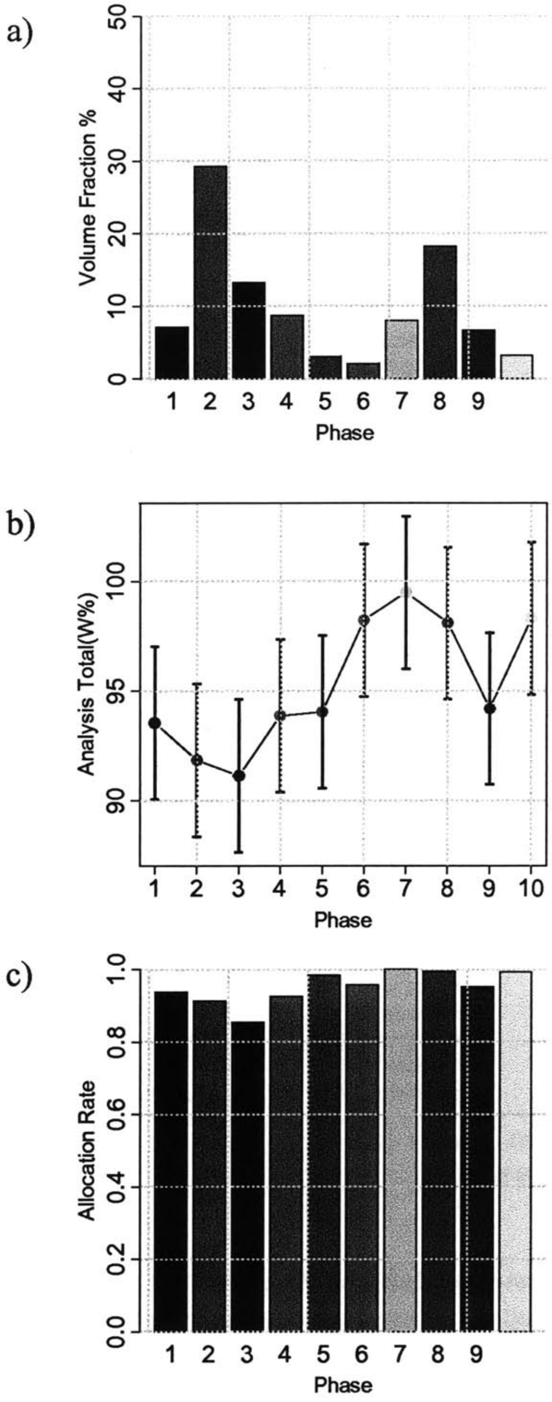

Figure 9-7: Graphical representation of clustering results presented in Table 9.12 for experiment S3-C3W. a) volume fractions, b) mean and standard deviation values of the analysis totals, and c) allocation rates for each of the phases displayed in Figure 9-6.

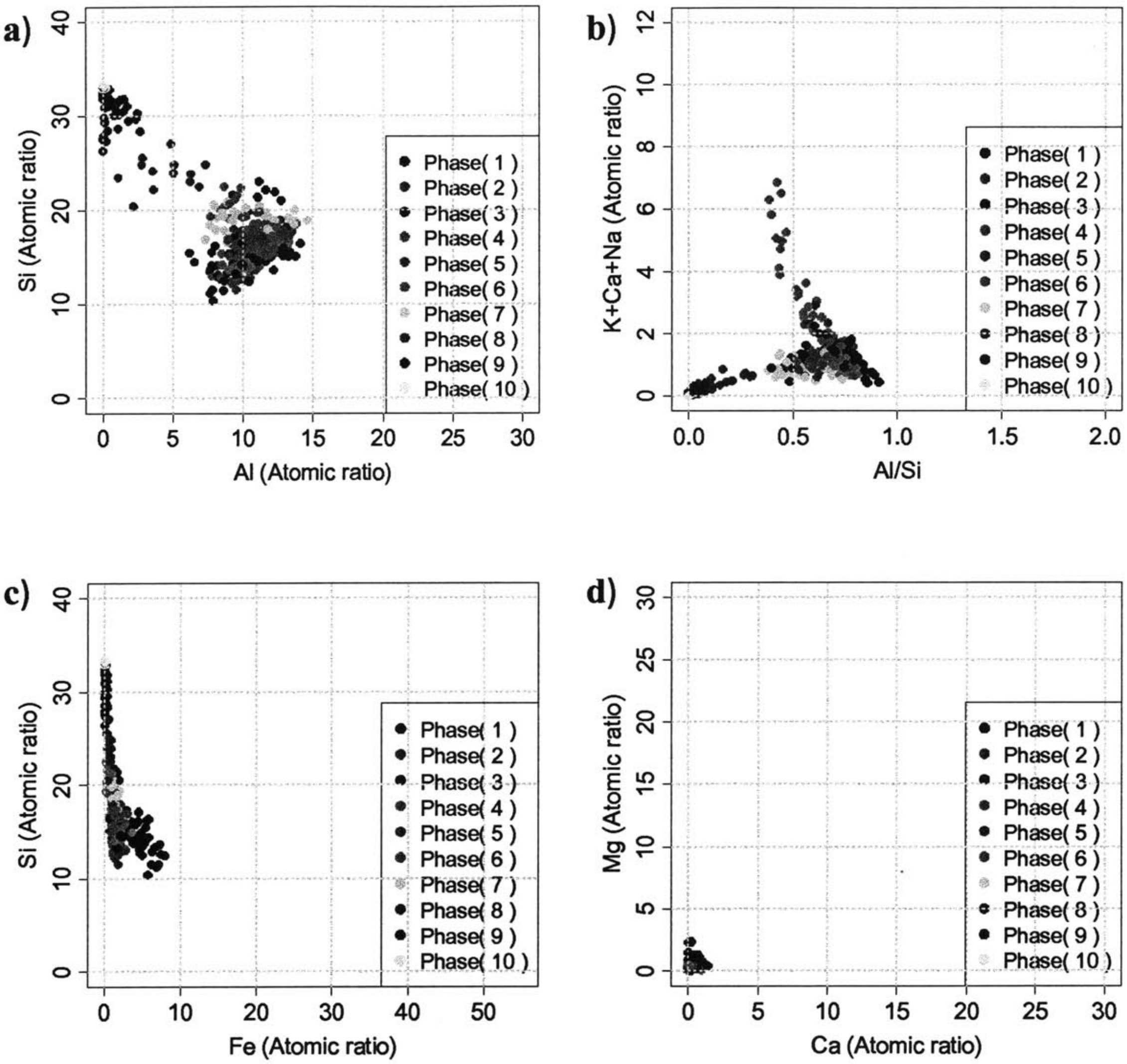

Figure 9-8: Multivariate cluster analysis of the grid WDS data for experiment S7-C1W. The identified phases are presented on 2-D projections for visual interpretation of the data: a) Al-Si space and b) Ca+Na+K-Al/Si space separate quartz, feldspars, and clay minerals. c) Fe-Si space and d) Ca-Mg space separate carbonate minerals; siderite, calcite, magnesite, ankerite, and dolomite.

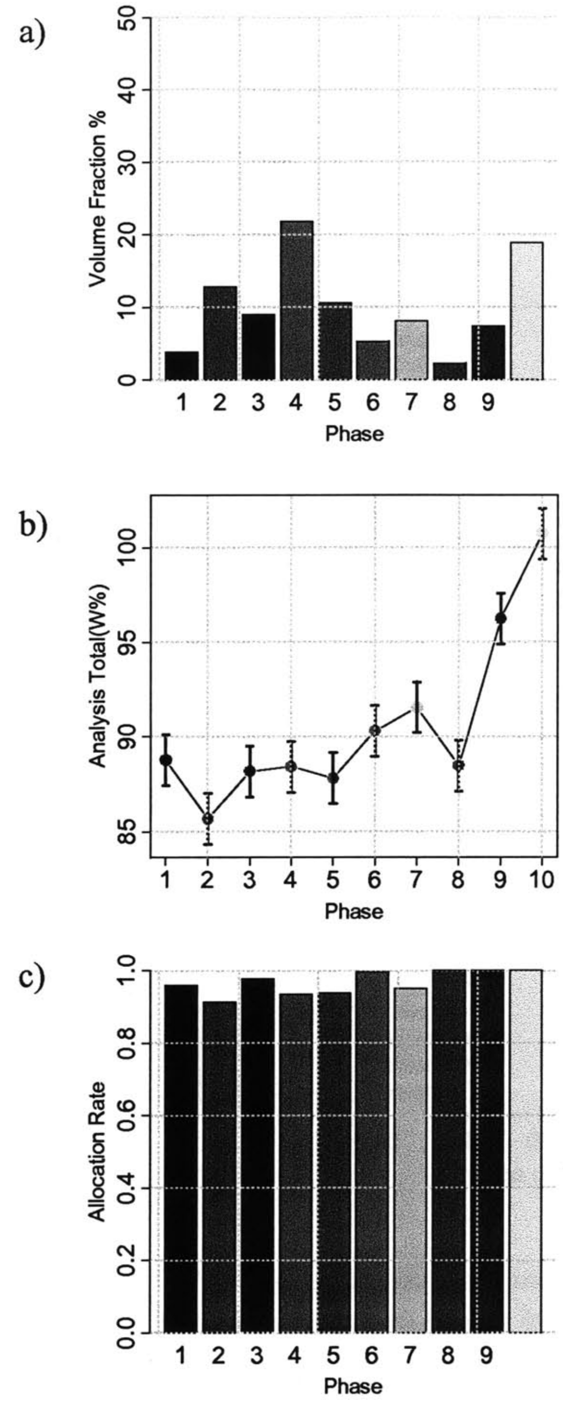

Figure 9-9: Graphical representation of clustering results presented in Table 9.14 for experiment S7-C1W. a) volume fractions, b) mean and standard deviation values of the analysis totals, and c) allocation rates for each of the phases displayed in Figure 9-8.

Furthermore, the porous clay phase is consistently identified with lower indentation modulus and high allocation rates (Figure 9-10d). Phases 2 and 3 correspond to phases with intermediate M and H values and lower volume fractions (Figure 9-10b). These phase are interpreted as composite phases. Figure 9-14 provides a compilation of the identified trends for the indentation experiments performed in this work.

The stiffness and hardness properties for the mechanical porous clay phase in shales S3 and S7 determined from the cluster analysis appears to be fairly consistent for the different grid experiments. Figure 9-15 displays the mean and standard deviation values for the indentation modulus and hardness of the porous clay phase for different experiments presented in this report. In addition, the data reported by Bobko [10] and reanalyzed using the EM-Ml method for cluster analysis [43], is presented in the figure. The indentation modulus and hardness properties compared adequately among experiments, attesting to the robustness of the grid indentation technique for shale employing the experimental parameters herein proposed. In what follows, these results are coupled with the grid WDS analysis to investigate the chemical nature of the porous clay phase and the so-called composite phases identified by grid indentation experiments.

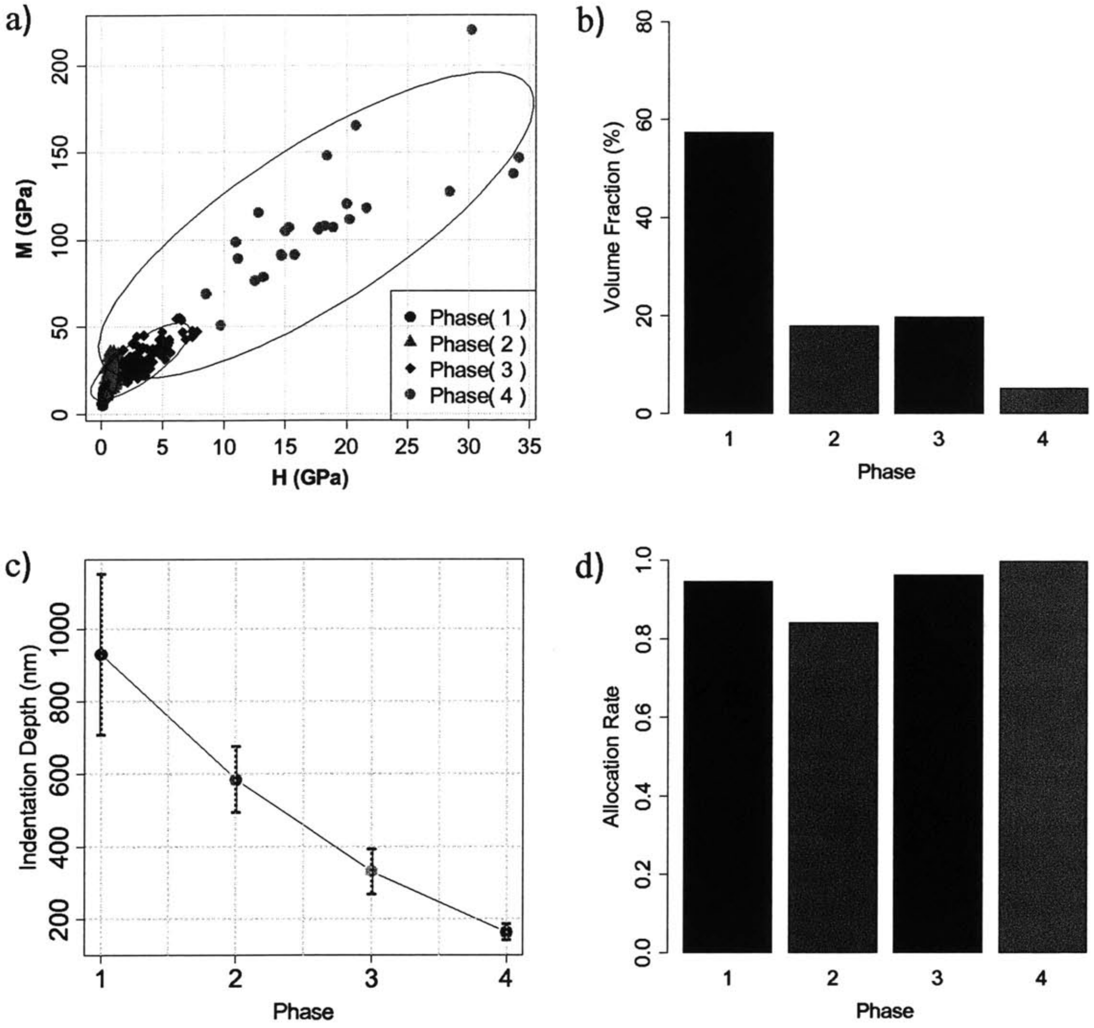

Figure 9-10: Cluster analysis results of the grid indentation data for experiment S3-C1I. a) Cluster analysis of the indentation modulus and hardness showing four mechanical phases. b) Volume fractions for each of the mechanical phases described by the cluster modeling in (a). c) Mean and standard deviation values of the maximum indentation depths for each mechanical phase measured in the grid indentation experiment.

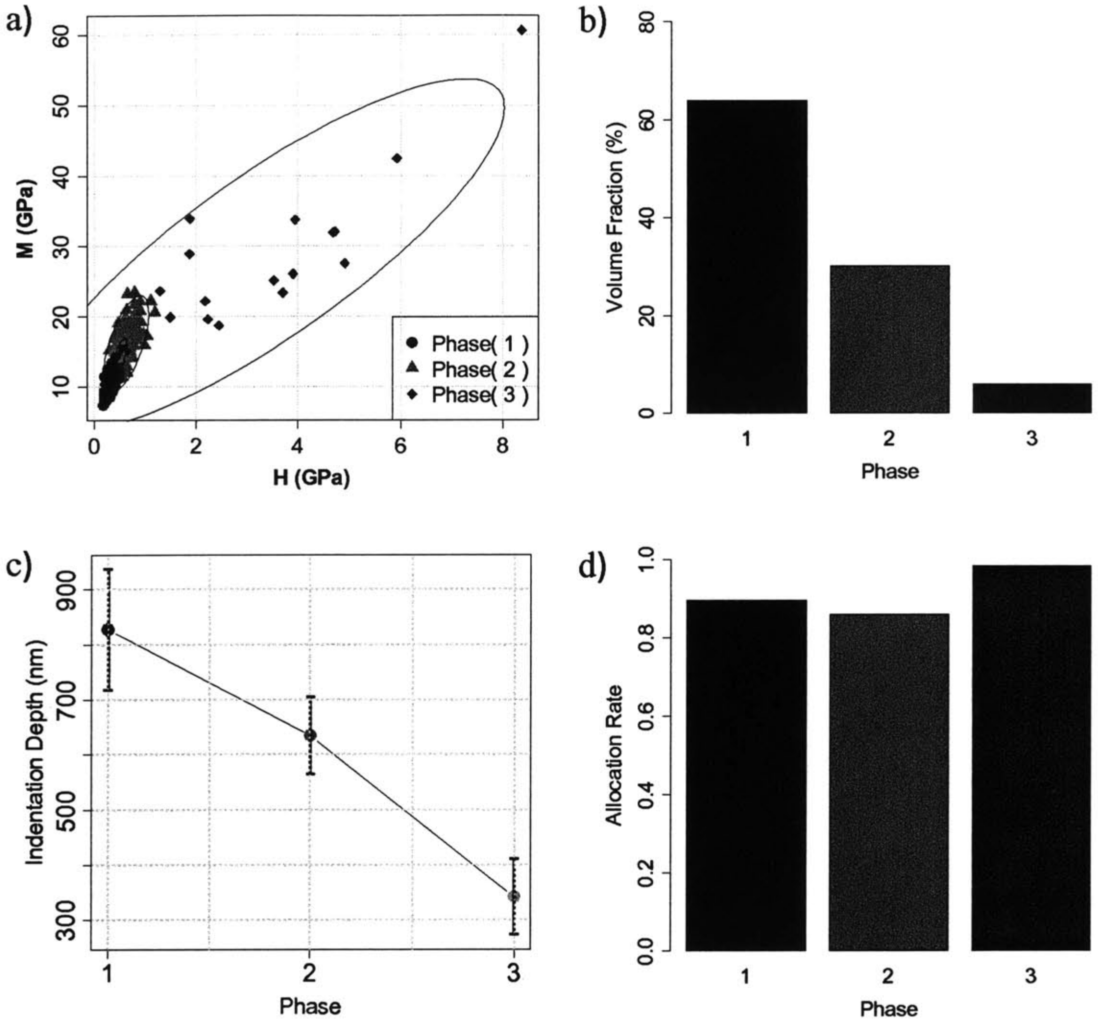

Figure 9-11: Cluster analysis results of the grid indentation data for experiment S3-C2I. a) Cluster analysis of the indentation modulus and hardness showing three mechanical phases. b) Volume fractions for each of the mechanical phases described by the cluster modeling in (a). c) Mean and standard deviation values of the maximum indentation depths for each mechanical phase measured in the grid indentation experiment.

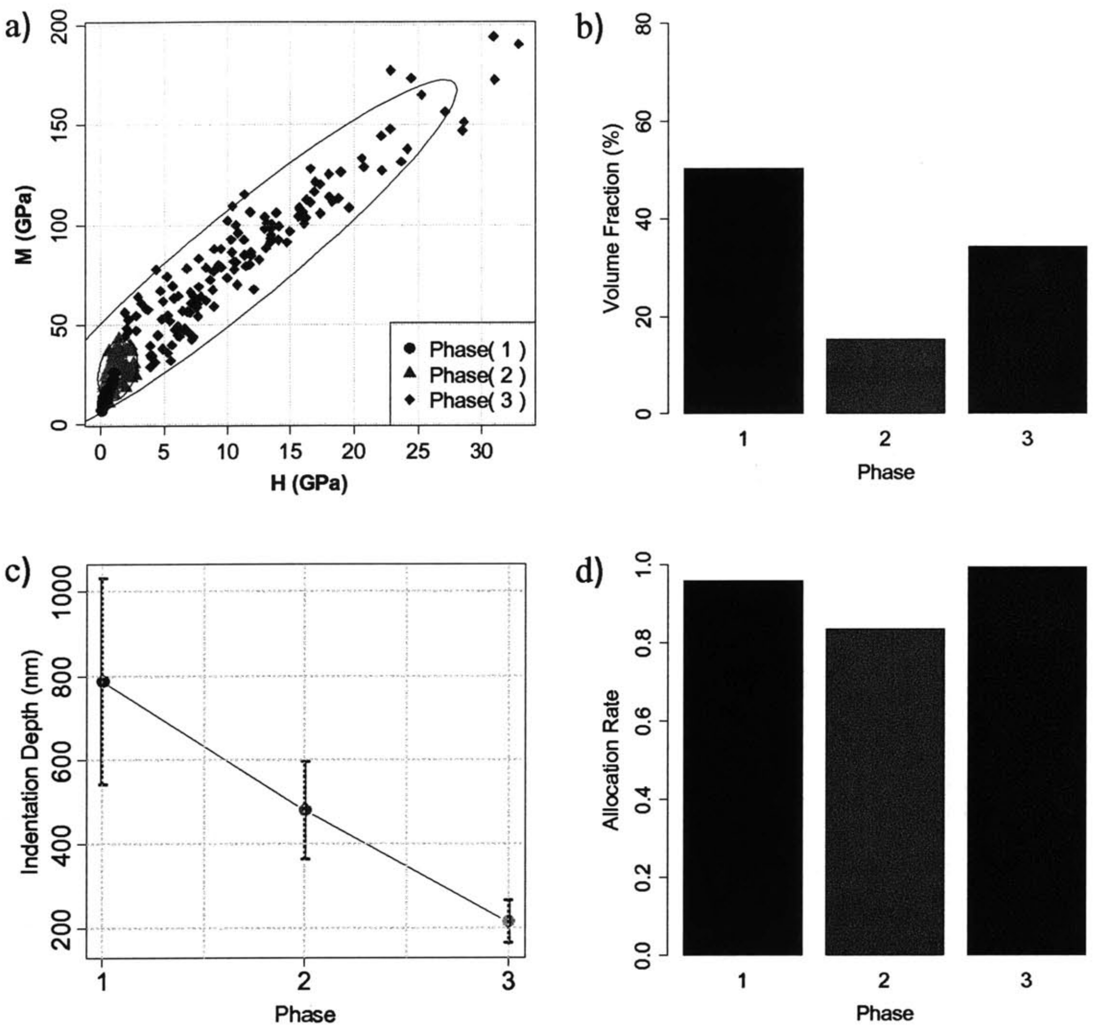

Figure 9-12: Cluster analysis results of the grid indentation data for experiment S3-C3I. a) Cluster analysis of the indentation modulus and hardness showing three mechanical phases. b) Volume fractions for each of the mechanical phases described by the cluster modeling in (a). c) Mean and standard deviation values of the maximum indentation depths for each mechanical phase measured in the grid indentation experiment.

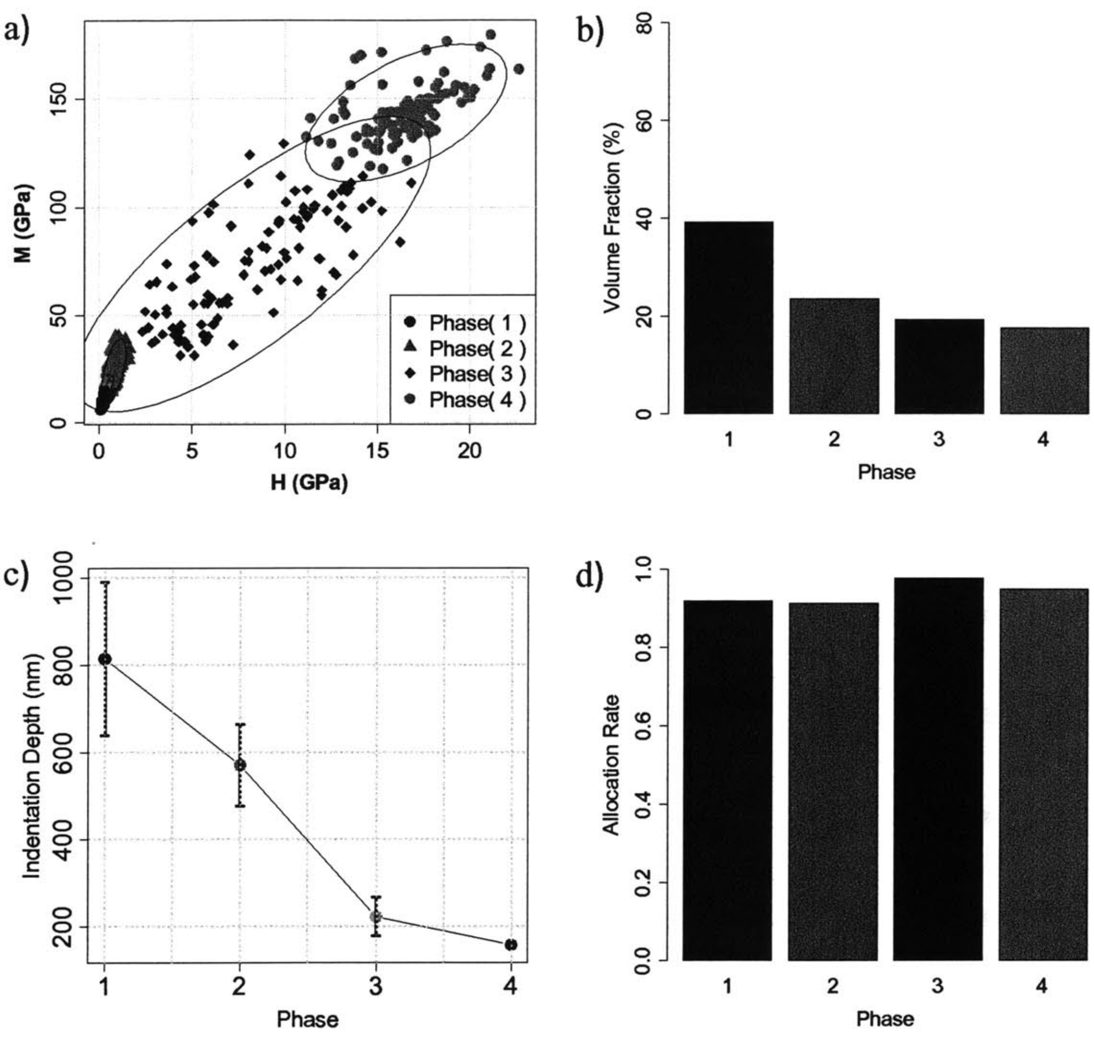

Figure 9-13: Cluster analysis results of the grid indentation data for experiment S7-C1I. a) Cluster analysis of the indentation modulus and hardness showing five mechanical phases. b) Volume fractions for each of the mechanical phases described by the cluster modeling in (a). c) Mean and standard deviation values of the maximum indentation depths for each mechanical phase measured in the grid indentation experiment.

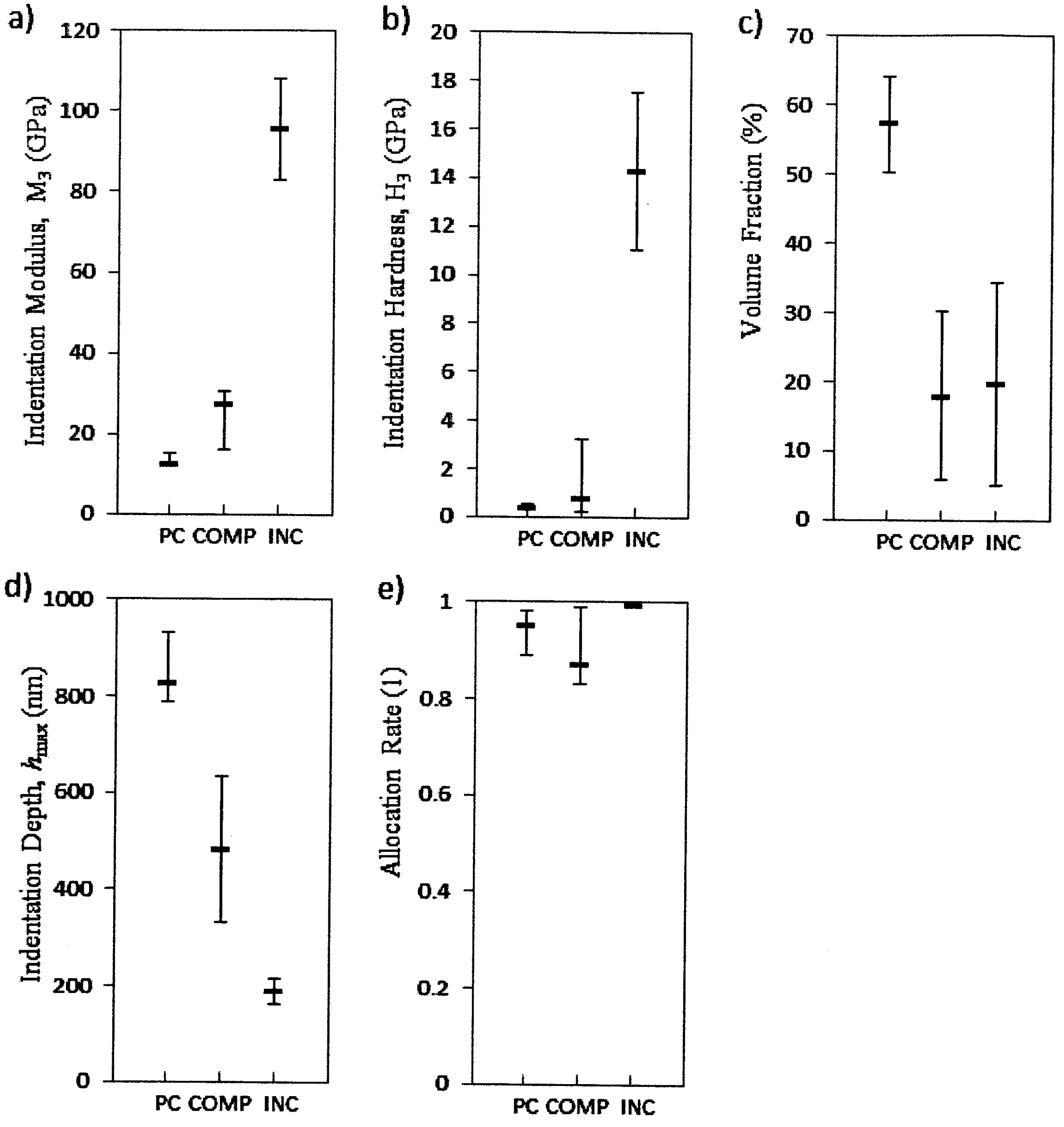

Figure 9-14: Compilation of results for cluster modeling of grid indentation data for shale S3. The cluster analysis modeling recognizes three mechanically active phases: the porous clay (PC) phase, a transition or composite (COMP) phase, and the inclusion (INC) phase. Figures a) through e) display the on-average properties established for each phase. The solid data point corresponds to the median and the error bars to the maximum and minimum (on-average) values determined for experiments S3-C1I, S3-C2I, and S3-C3I. The average properties for the three types of mechanical phases show distinctive features which facilitate the interpretation of the grid indentation data.

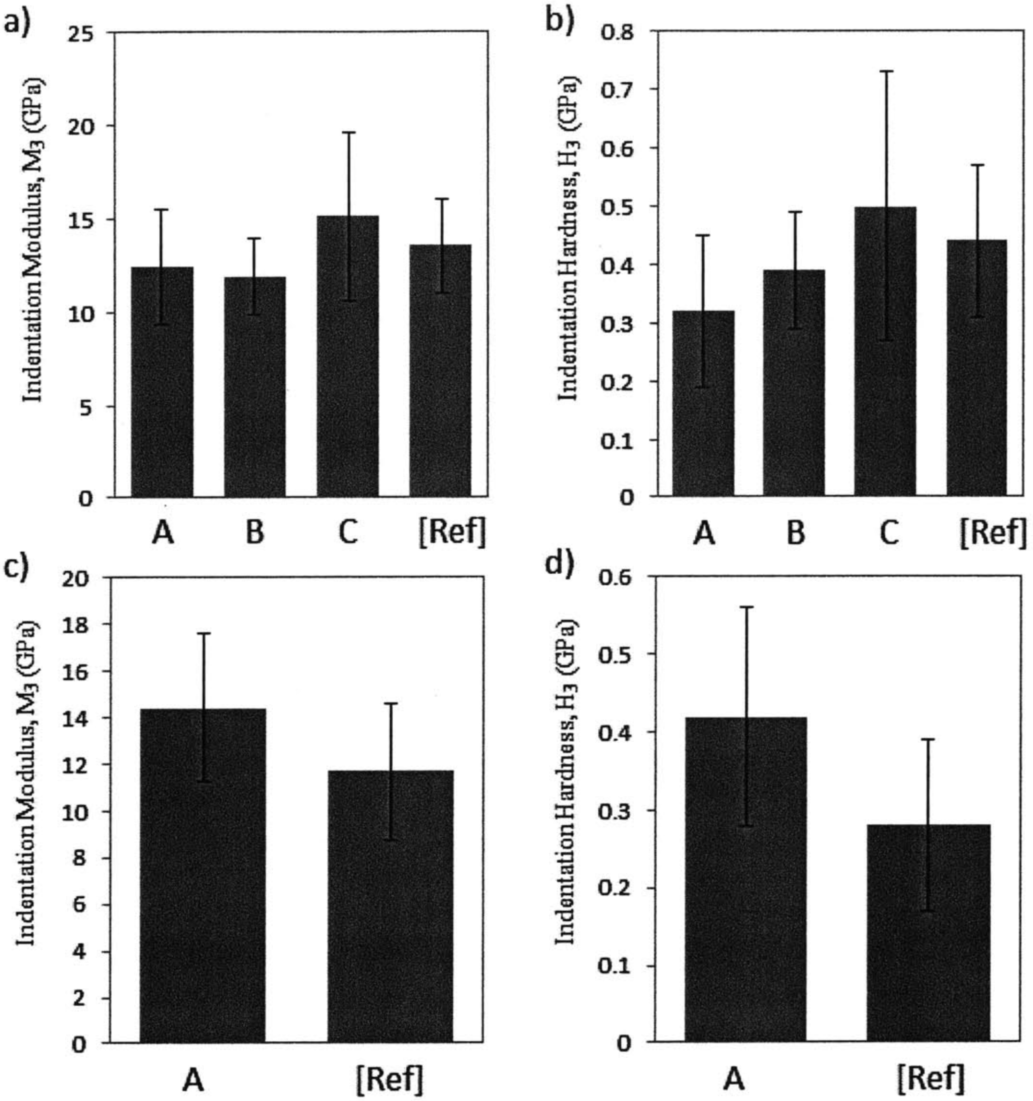

Figure 9-15: Comparison of the indentation modulus and hardness properties for the porous clay in shale inferred from cluster analysis of grid indentation experiments. The data is presented in bars representing the mean values, and error bars representing the associated standard deviations. Ref corresponds to the indentation data reported in [10] and reanalyzed using the EM-ML method for cluster analysis [43]. The results of experiments S3-C1I, S3-C2I, and S3-C3I were used in a) and b). The results of experiment S7-C1I were used in c) and d).

Phase	1	2	3	4
M_3, μ [GPa]	12.44	20.34	30.43	108.08
M_3, σ [GPa]	3.11	5.67	9.00	35.81
H_3, μ [GPa]	0.32	0.76	3.19	17.53
H_3, σ [GPa]	0.13	0.27	1.65	7.26
$h_{\max}$, μ [nm]	931.42	584.70	330.76	162.41
$h_{\max}$, σ [nm]	221.28	91.40	61.20	21.70
Vol. fraction (%)	57.29	17.89	19.66	5.16
No. data	305	88	93	25

Table 9.3: Cluster analysis results of the grid indentation data for experiment S3-C1I. The notations μ and σ correspond to the mean and standard deviation of the given property. The values for the number of measured data (No. data), indentation depth, volume fraction are also listed.

Phase	1	2	3
M_3, μ [GPa]	11.95	16.13	28.59
M_3, σ [GPa]	2.04	2.81	10.28
H_3, μ [GPa]	0.39	0.63	3.39
H_3, σ [GPa]	0.10	0.18	1.90
$h_{\max}$, μ [nm]	827.70	634.44	341.57
$h_{\max}$, σ [nm]	108.93	69.90	68.95
Vol. fraction (%)	63.93	30.15	5.92
No. data	196	77	16

Table 9.4: Cluster analysis results of the grid indentation data for experiment S3-C2I. The notations μ and σ correspond to the mean and standard deviation of the given property. The values for the number of measured data (No. data), indentation depth, volume fraction are also listed.

9.4 Chemo-Mechanical Analysis - Part I: the Porous Clay

The results from cluster modeling of the grid WDS data for experiments S3-C1 and S3-C2 are employed to reveal the chemical composition of the porous clay mechanical phase inferred from statistical indentation. Figure 9-16 displays a series of graphical representations of the grids of indentation and WDS experiments, in which each pixel represents a local measurement within the resolution of the grid (5-10 μm grid spacings). In Figures 9-16a and 9-16d, the data corresponding to the mechanical porous phase inferred from indentation analysis are displayed. The background in those figures represents the data associated with the remaining phases (composite and inclusion phases), as well as the data that was discarded from indentation analysis (defective load-depth curves). Similarly, Figures 9-16b and 9-16e show the data for

Phase	1	2	3
M_3, μ [GPa]	15.14	27.23	82.87
M_3, σ [GPa]	4.54	6.32	36.66
H_3, μ [GPa]	0.50	1.35	11.01
H_3, σ [GPa]	0.23	0.63	6.95
$h_{\max}$, μ [nm]	787.40	480.79	214.81
$h_{\max}$, σ [nm]	244.49	115.83	51.56
Vol. fraction (%)	50.31	15.31	34.37
No. data	214	66	139

Table 9.5: Cluster analysis results of the grid indentation data for experiment S3-C3I. The notations μ and σ correspond to the mean and standard deviation of the given property. The values for the number of measured data (No. data), indentation depth, volume fraction are also listed.

Phase	1	2	3	4	5
M_3, μ [GPa]	14.42	24.88	63.69	134.06	141.55
M_3, σ [GPa]	3.18	5.88	22.52	14.07	6.01
H_3, μ [GPa]	0.42	0.79	7.14	14.92	16.79
H_3, σ [GPa]	0.14	0.27	3.54	1.89	1.03
$h_{\max}$, μ [nm]	811.37	568.36	239.48	160.87	157.77
$h_{\max}$, σ [nm]	174.85	92.86	61.10	7.99	4.18
Vol. fraction (%)	40.34	22.44	15.97	8.68	12.58
No. data	250	127	93	44	84

Table 9.6: Cluster analysis results of the grid indentation data for experiment S7-C1I. The notations μ and σ correspond to the mean and standard deviation of the given property. The values for the number of measured data (No. data), indentation depth, volume fraction are also listed.

the clay phase defined from WDS cluster analysis, for which the background represents the data associated with the remaining phases (quartz-clay mixture, and discarded data with low yield totals). The grid representations previously described are employed to construct Figures 9-16c and 9-16f, in which for each sample the mechanical porous clay phase is matched with the chemical clay phase. The resulting chemo-mechanical porous clay data represents the set of indentation and WDS experiments on specific spots which are associated simultaneously to the mechanical and chemical clay phases. The coupled chemo-mechanical grids in Figures 9-16c and 9-16f display a satisfactory match of the mentioned phases, with 85% or more of the mechanical porous clay being matched by the chemical data (the mechanical data not matching the chemical description is also displayed in the figure). The results presented in Figure 9-16 formalize the conjecture about the porous clay phase at the scale of micrometers in shale being related to the mechanical phase with the largest volume fraction and low stiffness and hardness values probed by grid indentation. The coupled chemo-mechanical analysis thus shows that the mechanical porous clay corresponds in fact to the clay from a strict chemical description.

9.5 Chemo-Mechanical Analysis - Part II: Quartz-Clay Interfaces

Special studies were conducted with the objective of improving the understanding of the mechanical and chemical nature of the so-called composite phases inferred from grid nanoindentation experiments on shale. To this end, coupled grid indentation and WDS experiments were conducted on a particular region of the shale samples in experiments S3-C3 and S7-C1 containing a sizable inclusion. The regions of grid experiments were also imaged using BSE and X-ray mapping to obtain visual descriptions of the underlying microstructures. The latter techniques provide the baseline information for linking the spatial configuration of the material surface to the results of coupled indentation and WDS grids. The BSE image and X-ray maps were obtained based on the experimental parameters described in Section 7.2. The BSE and X-ray maps presented in Figures 9-17 and 9-18 show the microstructures associated with experiments S3-C3 and S7-C1, respectively, in which large grains of approximately 100 μm in characteristic size are clearly visible. The elements selected for X-ray mapping provided the sufficient means

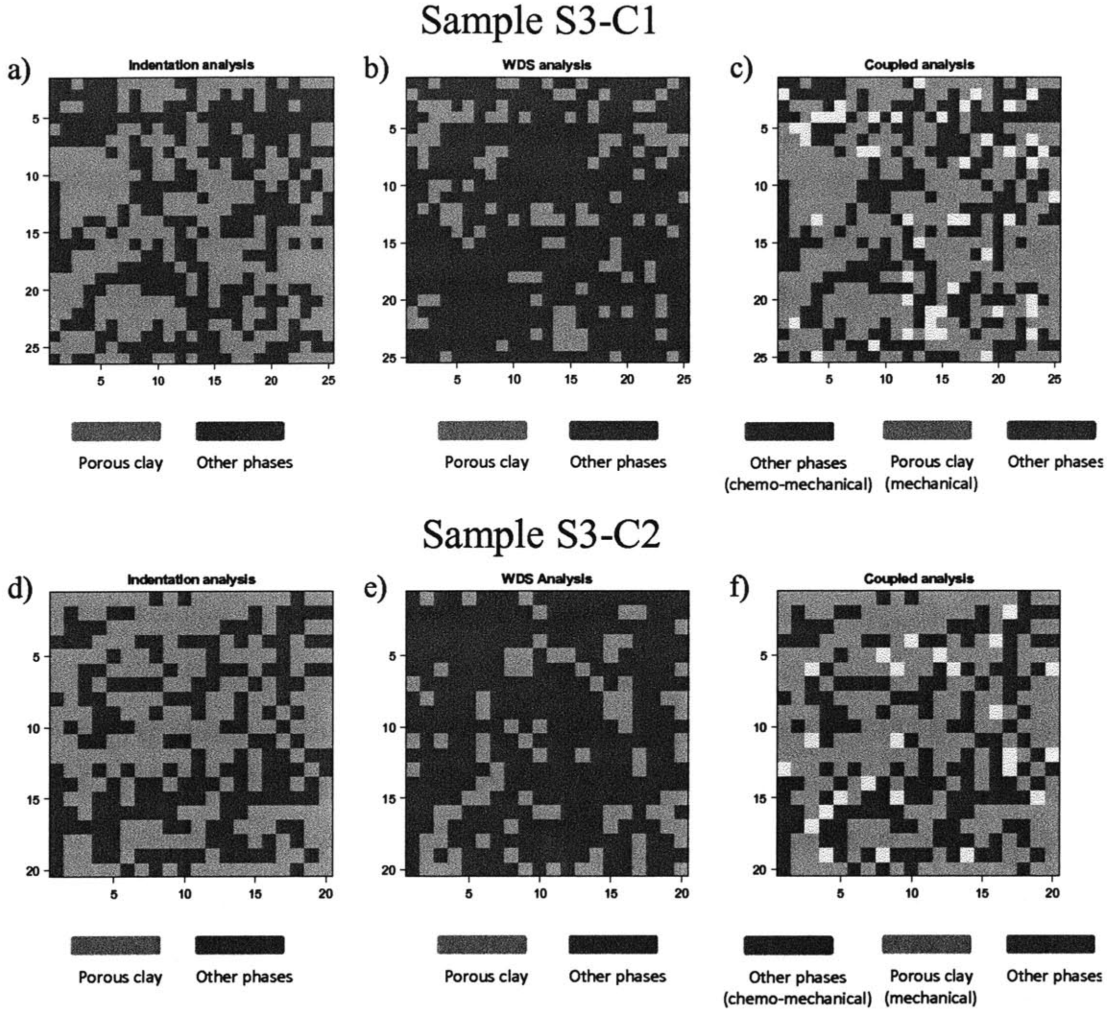

Figure 9-16: Coupled chemo-mechanical assessment of samples S3-C1 and S3-C2 identifying the constitution of the porous clay mechanical phase. For each sample, the figures represent the grid spatial distribution of the data associated with (a,d) the porous clay mechanical phase, and (b,e) the clay chemical phases (see Table 9.2). Figures (c,d) display the overlap of the data presented in the indentation and WDS grids, hence, establishing the porous clay (in red) understood from both analyses. The data for the mechanical porous clay not matching the chemical assessment is also displayed (in yellow). Other phases refer to the additional mechanical or chemical phases identified from cluster analysis, including the data discarded from indentation experiments and the data with low yield totals excluded from grid WDS analysis. Each pixel represents the grid spacing: 5 μm for experiment S3-C1 and 10 μm for S3-C2.

to qualitatively identify the major phases in the probed surface (see Section 7.2). Only elements that show contrast in chemical composition are presented in both experiments. The large grain in Figure 9-17 is recognized as feldspar, in accord with moderate concentrations of silicon and aluminum, as well as high concentrations of potassium (K-feldspar) and sodium (plagioclase). The concentrations of these elements result in two characteristic regions in the grain. A smaller plagioclase grain is observed in the upper-right corner of the images in Figure 9-17. Quartz grains are also identified by high concentrations of silicon and the absence of other elements. In contrast, the large grain in Figure 9-18 is identified as quartz in accord with the high silicon concentration and the absence of other elements. Feldspar grains are also identified from the information of potassium and sodium X-ray maps. The matrix in both figures corresponds to fine-grained clay minerals.

The same surfaces presented in Figures 9-17 and 9-18 were used for performing grid indentation and WDS experiments. The interpretation of the cluster analysis results of the associated WDS and indentation experiments are presented in Sections 9.3.1 and 9.3.2. The results of grid WDS experiments for experiments S3-C3W and S7-C1W, presented in Figures 9-6 and 9-9, respectively, are displayed spatially over the actual grids of measurements in Figures 9-19d and 9-20d. The phases identified through cluster analysis of the grid WDS data in these experiments provide a remarkable description of the local chemistry of the tested surfaces. The composite grain of feldspar in experiment S3-C3W (9-19d) is well delineated using the information from cluster analysis (phases 7 and 8 in 9-19c). Similarly, the quartz grain in experiment S7-C1W is well defined using the information from cluster analysis (phase 10 in Figure 9-20c). The clay phases in both experiments (see Table 9.2) surrounds the large inclusions and regions of small quartz and feldspar inclusions.

The analysis of the third battery of tests corresponding to grid nanoindentation is presented in Figures 9-12 and 9-13. Following the assessment outlined in Section 9.3.2, phase 1 in both experiments corresponds to the mechanical porous clay phase. Phase 4 in experiment S7-C1 (Figure 9-13) and phase 3 in experiment S3-C3 (Figure 9-12) correspond to the mechanical inclusion phases. Remaining phases with intermediate properties between the porous clay phases and the inclusion phases are regarded as mechanical composite (or transition) phases. The results from cluster analysis for experiments S3-C3 and S7-C1 are also displayed in Figures

9-19 and 9-20, which display the spatial arrangement of each indentation test and its associated mechanical group. The feldspar grain in Figure 9-19b is delineated by a series of phase 4 data points, which are associated in turn with high modulus and hardness values. Indentation experiments on orthoclase (a type of alkali feldspar) in metamorphic rocks rendered indentation properties of approximately $M = 89, H = 7$ GPa [22], which describe the lower range of our experimental values for the feldspar grain. The small feldspar grain in the upper-right corner of Figure 9-19b is also recognized by grid indentation. Similarly, the same trend is observed in Figure 9-20 in which the so-called composite phases (phases 2 and 3) surround the quartz and feldspar inclusions.

The presented experimental evidence offers the necessary elements to discern the nature of the so-called mechanical composite phases. Given the adequate delineation of the feldspar and quartz grains from grid indentation as observed in Figures 9-19b and 9-20b, the data for the mechanical composite phases (phases 2 and 3) is related spatially to the surroundings of the silt grains. To complement the information of the spatial location of the data for mechanical composite phases, coupled chemo-mechanical analysis of the grid indentation and WDS results reveals that 77% of the data encompassed in the mechanical composite phases correspond to the chemical clay phase inferred from WDS cluster analysis. These results properly define the mechanical composite phases found in grid indentation experiments of shale as tests performed on conglomerates of clay particles near stiffer (harder) inclusions of quartz or feldspar. The local mechanical behavior measured by nanoindentation is truly a composite response, in which the lower indentation properties of the clay fabric being probed are altered by the nearby presence of rigid grains. In contrast, measurements away from boundaries with quartz and feldspar grains provide consistent mechanical measurements that characterize the porous clay phase of shale.

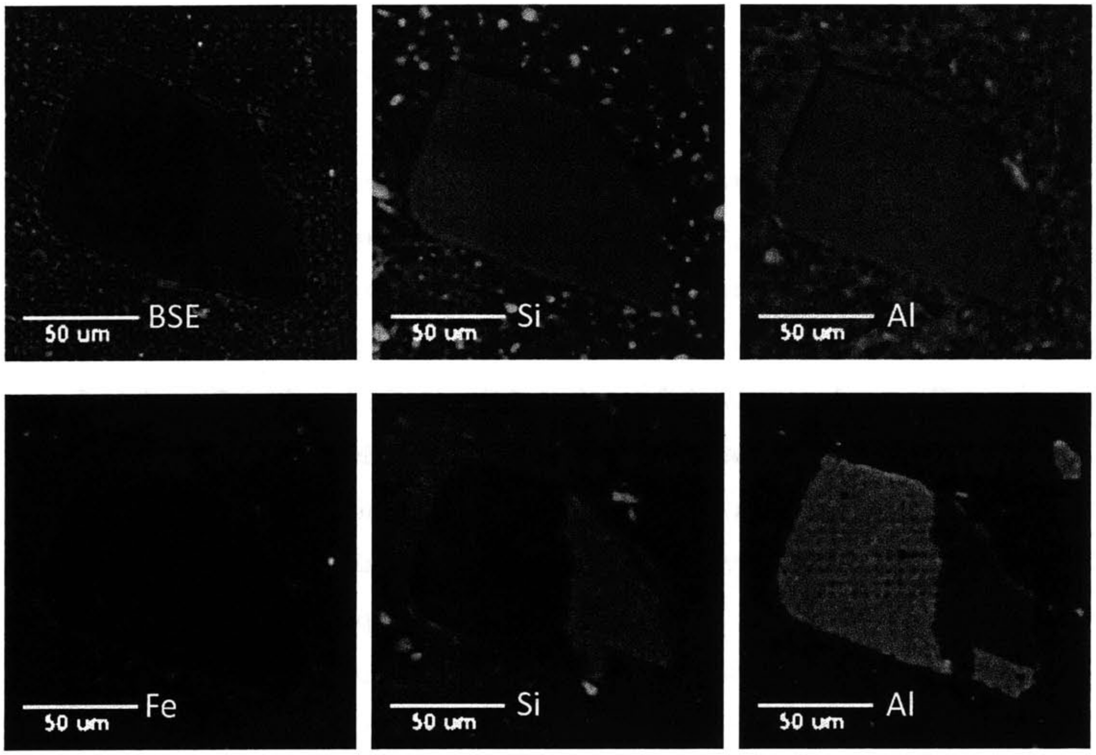

Figure 9-17: Backscattered electron (BSE) and X-ray maps obtained for experiment S3-C3. The particular spot for these EPMA images was chosen deliberately as it contains a sizable inclusion. The X-ray maps display the relative amount of the particular element in the material surface: the dark-to-light transition corresponds to a low -to-high concentration gradient. A qualitative analysis of the X-ray maps characterizes the inclusion as feldspar. The apparent matrix surrounding the inclusion contains clay minerals and some silt grains.

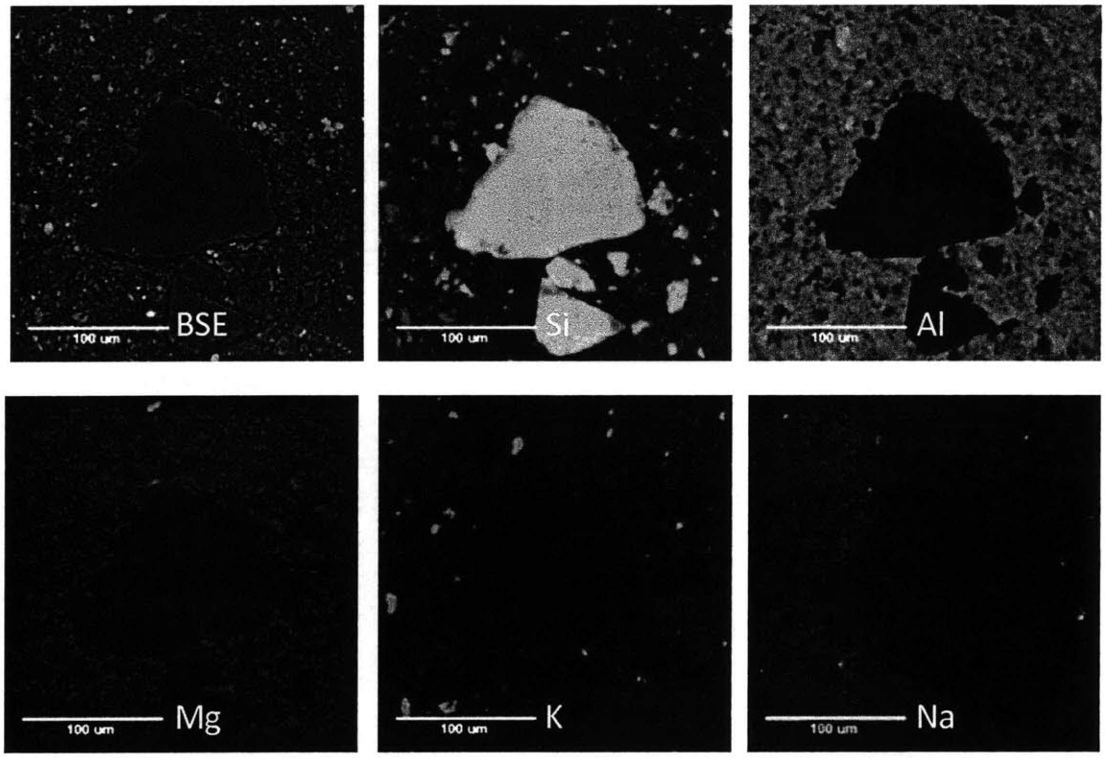

Figure 9-18: Backscattered electron (BSE) and X-ray maps obtained for experiment S7-C1. The particular spot for these EPMA images was chosen deliberately as it contains a sizable inclusion. The X-ray maps display the relative amount of the particular element in the material surface: the dark-to-light transition corresponds to a low -to-high concentration gradient. A qualitative analysis of the X-ray maps characterizes the inclusion as quartz. The apparent matrix surrounding the inclusion contains clay minerals and some silt grains.

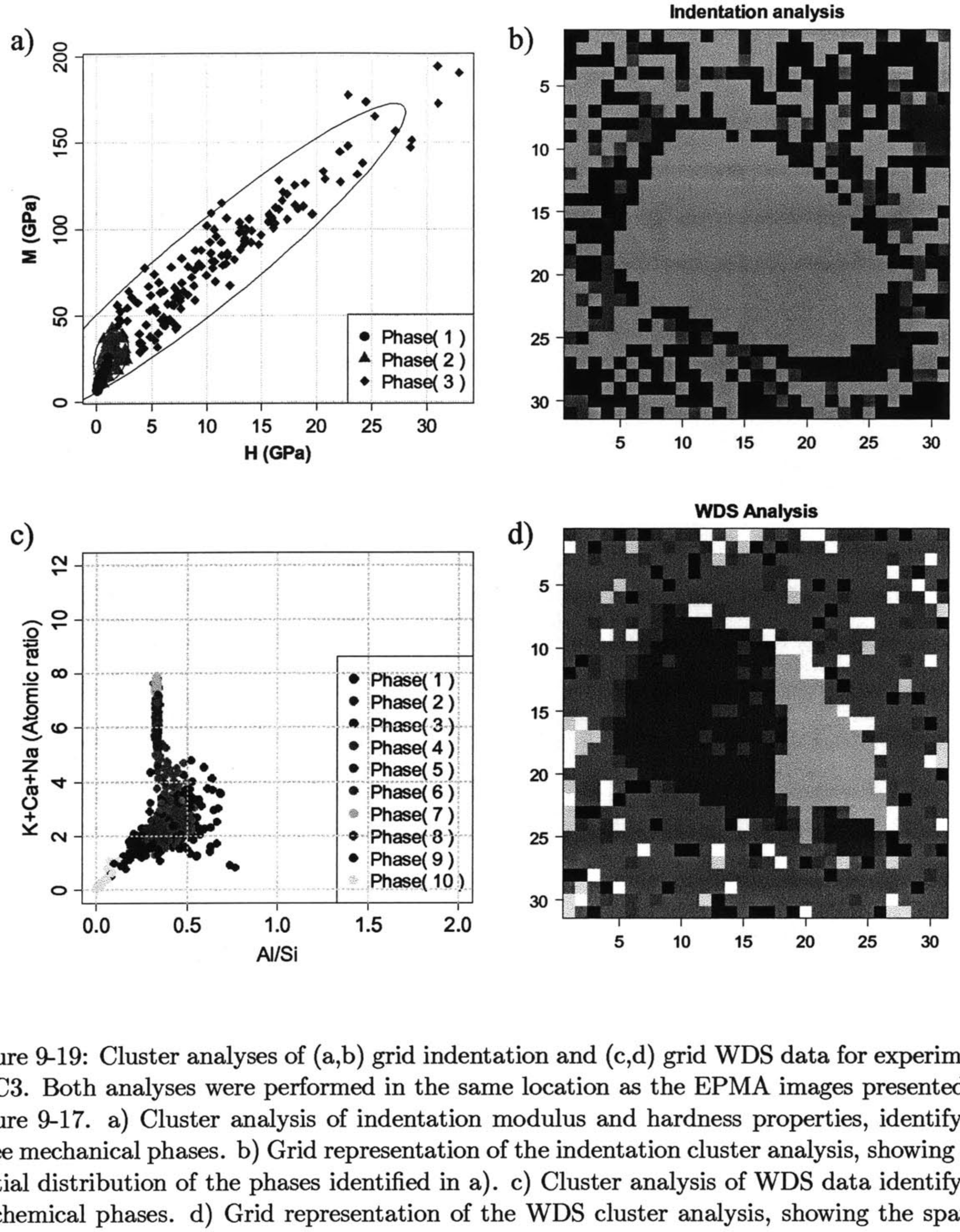

Figure 9-19: Cluster analyses of (a,b) grid indentation and (c,d) grid WDS data for experiment S3-C3. Both analyses were performed in the same location as the EPMA images presented in Figure 9-17. a) Cluster analysis of indentation modulus and hardness properties, identifying three mechanical phases. b) Grid representation of the indentation cluster analysis, showing the spatial distribution of the phases identified in a). c) Cluster analysis of WDS data identifying 10 chemical phases. d) Grid representation of the WDS cluster analysis, showing the spatial distribution of the identified phases in c). Clay phases are displayed in one color (light red). Each pixel represents the grid spacing (5 μm).

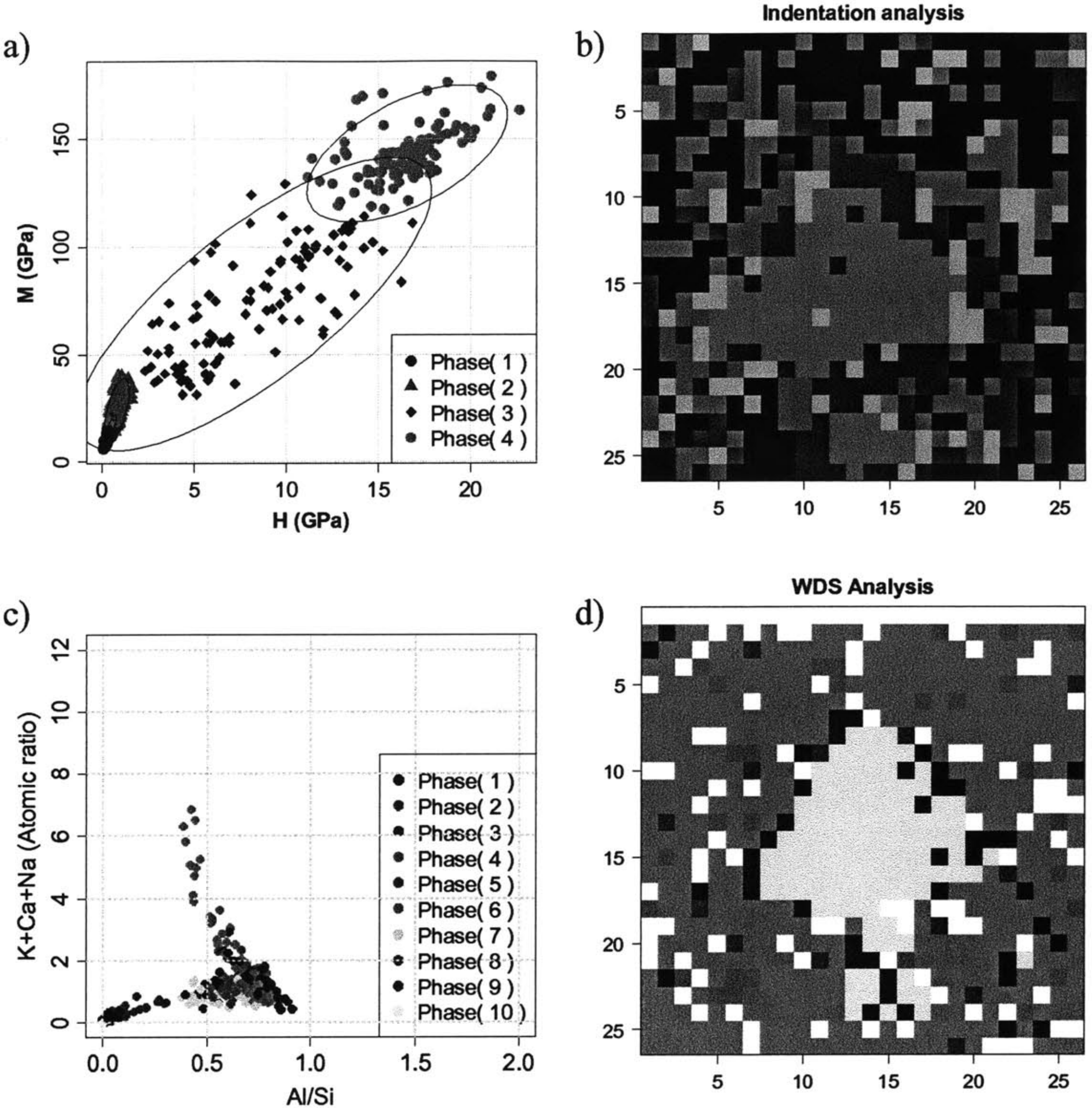

Figure 9-20: Cluster analyses of (a,b) grid indentation and (c,d) grid WDS data for experiment S7-C1. Both analyses were performed in the same location as the EPMA images presented in Figure 9-18. a) Cluster analysis of indentation modulus and hardness properties, identifying four mechanical phases. b) Grid representation of the indentation cluster analysis, showing the spatial distribution of the phases identified in a). c) Cluster analysis of WDS data identifying 10 chemical phases. d) Grid representation of the WDS cluster analysis, showing the spatial distribution of the identified phases in c). Clay phases are displayed in one color (light red). Each pixel represents the grid spacing (10 μm).

9.6 Chapter Summary

In this Chapter we presented the results of the chemo-mechanical coupling technique for shale materials. The direct coupling of grid WDS and grid indentation experiments revealed that the porous clay phase, inferred solely from the mechanistic interpretation of grid indentation experiments, is in fact related to the response of clay minerals. The chemo-mechanical coupling technique also established that clay minerals located nearby hard inclusions of quartz and feldspar exhibit enhanced mechanical properties due to a composite response as sensed by the indentation experiments. The experimental observations define the chemo-mechanical signature of shale at grain-scales, thus answering the scientific challenge posed in this thesis which is establishing the link between material composition and mechanical behavior at fundamental material scales.

Phase		1	2	3	4	5	6	7	8	9
Si	μ	17.14	18.72	19.73	19.83	20.33	20.66	22.13	26.30	31.47
	σ	3.02	1.73	1.55	1.62	1.59	2.39	1.80	1.60	1.15
Al	μ	7.94	9.06	6.86	7.94	7.95	7.01	6.44	4.17	1.02
	σ	1.32	1.63	0.45	0.75	0.78	1.01	0.99	1.12	0.80
K	μ	1.13	1.30	1.34	1.48	1.44	1.15	0.97	0.70	0.13
	σ	0.57	0.72	0.11	0.18	1.01	0.58	0.37	0.26	0.13
Ca	μ	0.02	0.01	0.01	0.02	0.04	0.32	0.02	0.01	0.02
	σ	0.01	0.01	0.01	0.01	0.02	0.19	0.01	0.00	0.06
Na	μ	1.74	0.50	1.16	0.64	0.80	1.17	0.52	0.37	0.13
	σ	1.59	0.15	0.60	0.16	0.40	1.14	0.14	0.16	0.08
Fe	μ	4.33	2.83	2.08	2.49	2.72	2.45	2.12	1.33	0.42
	σ	2.27	0.95	0.23	0.34	0.75	0.77	0.39	0.36	0.29

Table 9.7: Summary of the make up of the chemical phases identified by cluster analysis and displayed in Figure 9-2 for experiment S3-C1W. The notations μ and σ correspond to the mean and standard deviation of the given property. The standard deviation corresponds to the square root of the variance.

Phase	1	2	3	4	5	6	7	8	9
Volume fraction (%)	6.34	14.83	6.47	34.65	8.51	1.95	18.06	6.75	2.44
Analysis total μ	92.41	93.45	89.67	92.89	94.96	93.86	93.35	96.88	100.65
Analysis total σ	3.59	3.59	3.59	3.59	3.59	3.59	3.59	3.59	3.59
Allocation	0.91	0.85	0.87	0.86	0.87	1.00	0.83	0.98	1.00

Table 9.8: Volume fractions, analysis totals, and allocation rates for the chemical phases identified by cluster analysis and displayed in Figure 9-2 for experiment S3-C1W. The notations μ and σ correspond to the mean and standard deviation of the given property.

Phase		1	2	3	4	5	6	7	8	9
Si	μ	19.32	19.54	19.56	19.96	21.40	21.53	22.49	23.54	27.35
	σ	1.34	1.08	1.75	13.11	1.32	0.89	0.49	1.15	1.45
Al	μ	8.10	8.78	8.58	8.30	8.10	7.58	6.43	6.05	3.11
	σ	0.82	0.66	1.06	7.97	0.80	0.54	0.30	0.70	0.88
K	μ	1.51	1.71	1.54	1.44	1.52	1.41	1.27	1.16	0.60
	σ	0.34	0.28	0.45	3.35	0.34	0.23	0.12	0.29	0.37
Ca	μ	0.00	0.00	0.00	0.10	0.02	0.00	0.00	0.00	0.00
	σ	0.00	0.00	0.00	0.03	0.00	0.00	0.00	0.00	0.00
Na	μ	4.05	1.47	1.55	1.96	1.45	1.18	0.91	0.98	0.56
	σ	0.71	0.57	0.92	6.92	0.69	0.47	0.26	0.61	0.76
Fe	μ	2.23	2.14	2.83	2.06	2.34	2.03	1.67	1.72	0.90
	σ	0.44	0.35	0.57	4.29	0.43	0.29	0.16	0.38	0.47
Mg	μ	1.23	1.31	1.52	1.23	1.29	1.18	1.04	1.00	0.58
	σ	0.25	0.20	0.32	2.41	0.24	0.16	0.09	0.21	0.27

Table 9.9: Summary of the make up of the chemical phases identified by cluster analysis and displayed in Figure 9-4 for experiment S3-C2W. The notations μ and σ correspond to the mean and standard deviation of the given property. The standard deviation corresponds to the square root of the variance.

Phase	1	2	3	4	5	6	7	8	9
Volume fraction (%)	8.44	30.49	17.22	2.52	3.42	21.66	3.27	7.95	5.04
Analysis total μ	100.74	100.41	99.16	100.05	96.00	100.21	103.45	101.55	105.22
Analysis total σ	4.67	4.67	4.67	4.67	4.67	4.67	4.67	4.67	4.67
Allocation	0.90	0.87	0.88	1.00	0.93	0.88	0.87	0.96	1.00

Table 9.10: Volume fractions, analysis totals, and allocation rates for the chemical phases identified by cluster analysis and displayed in Figure 9-4 for experiment S3-C2W. The notations μ and σ correspond to the mean and standard deviation of the given property.

Phase		1	2	3	4	5	6	7	8	9	10
Si	μ	18.50	19.71	19.73	20.26	20.52	22.63	22.84	22.99	24.52	30.33
	σ	2.80	1.65	2.03	1.92	3.39	0.35	0.44	0.27	1.21	1.10
Al	μ	9.25	7.88	7.88	7.92	7.54	7.61	7.53	7.66	5.00	1.55
	σ	1.40	1.01	1.63	0.77	0.74	0.15	0.24	0.15	1.15	0.78
K	μ	2.10	1.60	1.39	1.36	2.59	0.05	3.69	0.06	0.97	0.29
	σ	0.89	0.29	0.28	0.52	3.44	0.05	0.16	0.05	0.25	0.18
Ca	μ	0.02	0.02	0.03	0.03	0.28	0.02	0.07	0.00	0.02	0.01
	σ	0.03	0.02	0.02	0.03	0.53	0.04	0.01	0.01	0.02	0.02
Na	μ	0.82	0.69	0.76	2.82	1.81	6.56	3.83	6.03	0.52	0.20
	σ	0.59	0.19	0.35	1.72	2.48	0.62	0.27	0.43	0.30	0.19
Fe	μ	2.56	2.08	2.02	1.39	1.21	0.28	0.13	0.10	1.27	0.40
	σ	1.64	0.37	0.41	0.75	1.57	0.16	0.05	0.05	0.35	0.30
Mg	μ	1.46	1.28	1.02	0.82	0.66	0.03	0.01	0.01	0.73	0.21
	σ	0.76	0.24	0.24	0.48	0.82	0.06	0.03	0.03	0.19	0.15

Table 9.11: Summary of the make up of the chemical phases identified by cluster analysis and displayed in Figure 9-6 for experiment S3-C3W. The notations μ and σ correspond to the mean and standard deviation of the given property. The standard deviation corresponds to the square root of the variance.

Phase	1	2	3	4	5	6	7	8	9	10
Volume fraction (%)	7.14	29.28	13.31	8.79	3.12	2.09	8.08	18.26	6.73	3.21
Analysis total μ	93.53	91.85	91.13	93.86	94.03	98.23	99.49	98.09	94.20	98.31
Analysis total σ	3.49	3.49	3.49	3.49	3.49	3.49	3.49	3.49	3.49	3.49
Allocation	0.94	0.91	0.85	0.93	0.98	0.96	1.00	0.99	0.95	0.99

Table 9.12: Volume fractions, analysis totals, and allocation rates for the chemical phases identified by cluster analysis and displayed in Figure 9-6 for experiment S3-C3W. The notations μ and σ correspond to the mean and standard deviation of the given property.

Phase		1	2	3	4	5	6	7	8	9	10
Si	μ	15.47	15.48	15.74	16.64	16.66	18.35	18.64	23.93	30.91	33.23
	σ	1.06	1.68	3.91	1.12	1.29	3.45	0.90	0.97	1.04	0.13
Al	μ	11.86	11.29	9.77	11.77	11.19	9.73	10.84	4.43	0.66	0.01
	σ	1.44	1.44	2.27	0.84	1.45	0.76	2.04	1.62	0.49	0.06
K	μ	0.51	0.51	0.51	0.51	0.82	2.29	0.54	0.26	0.06	0.00
	σ	0.26	0.14	0.22	0.07	0.30	1.99	0.14	0.12	0.13	0.01
Ca	μ	0.14	0.12	0.35	0.05	0.06	0.13	0.08	0.03	0.01	0.00
	σ	0.11	0.09	0.33	0.03	0.04	0.20	0.05	0.05	0.03	0.00
Na	μ	0.53	0.54	0.46	0.54	0.40	1.05	0.29	0.23	0.04	0.00
	σ	0.23	0.21	0.24	0.24	0.12	1.32	0.19	0.25	0.05	0.01
Fe	μ	2.56	1.74	3.58	1.23	1.30	0.87	1.42	0.60	0.16	0.05
	σ	1.32	0.78	2.76	0.13	0.26	0.43	0.44	0.28	0.18	0.03
Mg	μ	0.65	0.49	0.74	0.46	0.49	0.30	0.36	0.20	0.04	0.00
	σ	0.33	0.14	0.53	0.07	0.12	0.22	0.21	0.11	0.07	0.01

Table 9.13: Summary of the make up of the chemical phases identified by cluster analysis and displayed in Figure 9-8 for experiment S7-C1W. The notations μ and σ correspond to the mean and standard deviation of the given property. The standard deviation corresponds to the square root of the variance.

Phase	1	2	3	4	5	6	7	8	9	10
Volume fraction (%)	3.78	12.87	9.00	21.74	10.59	5.29	8.13	2.31	7.46	18.83
Analysis total μ	88.77	85.68	88.16	88.41	87.81	90.30	91.53	88.47	96.22	100.74
Analysis total σ	1.34	1.34	1.34	1.34	1.34	1.34	1.34	1.34	1.34	1.34
Allocation	0.96	0.91	0.98	0.93	0.94	1.00	0.95	1.00	1.00	1.00

Table 9.14: Volume fractions, analysis totals, and allocation rates for the chemical phases identified by cluster analysis and displayed in Figure 9-8 for experiment S7-C1W. The notations μ and σ correspond to the mean and standard deviation of the given property.

Part V

Conclusions and Perspectives

Chapter 10

Summary of Results and Perspectives

We started this investigation with the goal of answering the following question: what is the chemo-mechanical signature of shale at nanometer length scales? We employed a dual chemo-mechanical technique to assess the composition and mechanics of shale at sub-micrometer length scale. The direct coupling of both techniques enabled the evaluation of the mechanical responses of the major constituents of shale. This chapter represents a summary of the knowledge generated throughout the development and application of the grid WDS technique for assessing the chemistry of shale materials at a similar length scale compared to the mechanical microvolume probed by nanoindentation. In addition to the findings and contributions of this work some areas for future research directions are proposed.

10.1 Summary of Main Findings

This study generated the following scientific findings with respect to the links between composition and mechanical performance of shale:

- The implementation of the developed grid WDS technique for shale materials provides quantitative means to determine silt-size inclusions (mainly quartz and feldspars) and the clay matrix. This quantification is reported in terms of volume fractions and mean elemental compositions of the mentioned major chemical components. The identification of quartz and feldspar phases is conveniently achieved due to the relatively large sizes of the grains. In contrast, the heterogeneous nature of clay minerals, as well as their small characteristic size (which is below the resolution of the WDS spot measurements) resulted in the identification of clay-like phases forming the overall clay matrix. Mixture modeling was employed to separate the contributions of 1:1 and 2:1 clay minerals.

- A comparison of the mineralogy results obtained by grid WDS technique with those of image analysis and X-ray diffraction (XRD) showed that XRD consistently underestimates the volume fraction associated with the porous clay phase in shale. The alternative volume fraction determinations of clay and non-clay components in shale offered by grid WDS in addition to XRD could be used in models of shale poromechanics, in which the volumetric contributions of constituents are key elements to the successful modeling of macroscopic behaviors.
- The direct coupling of the grid WDS and the grid indentation techniques reveals that the porous clay phase, identified independently by the grid indentation technique, corresponds to the mechanical response of clay minerals. The chemo-mechanical coupling technique also shows that clay minerals located nearby hard inclusions of quartz and feldspars exhibit enhanced mechanical properties due to the composite action as sensed by the indentation experiment.

10.2 Research Contributions

Reaching the scientific findings required development, refinement, and implementation of experimental and analytical methods:

- Development of the grid WDS technique as a useful tool for in situ characterization of shale mineralogy. This development involved the evaluation of the experimental parameters that are required to properly characterize the heterogeneous shale materials. A comprehensive evaluation of the grid size effect on mineralogy results showed that a grid of size 15 - 20 times the size of the largest grain present in the material is appropriate to quantitatively describe the mineralogy of shale.

- The implementation of statistics to treat the multivariate chemical information obtained through grid WDS measurements. The proposed projections of clustering results into particular combinations of major chemical elements present in shale help in identifying the main constituents in shale. In addition, the use of atomic ratios was proven to enhance contrast between different elements, and hence, facilitate the cluster modeling of WDS measurements.
- Development of the chemo-mechanical coupling technique that involves the direct use of the grid WDS and the grid indentation experimental setups. This technique provides the means to link composition of shale materials to the mechanical performance at submicrometer length scales.

10.3 Industrial Benefit

The industrial benefit of our work is the assessment of chemistry and mechanics of shale at fundamental length scales. This information becomes crucial for the development of new multiscale models that aim to predict the macroscopic responses of shale materials. In particular, we expect that the two findings about the existence of a composite mechanical response between silt inclusions and clay near silt-grain boundaries will help refine the treatment of mechanical interfaces in homogenization models.

10.4 Areas of Improvement and Future Perspectives

The development of the grid WDS technique for shale materials recognizes some limitations. In the mineralogy assessment of shale materials, we relied heavily on the accuracy of wave dispersive spectroscopy (WDS). While this technique can provide accurate chemical compositions of some constituents that nearly matched laboratory values, the inherent limitations associated with the application of WDS on heterogeneous materials should be investigated in the future. This includes the chemical variability as a result of roughness and the application of matrix corrections on a heterogeneous material.

In previous studies, it has been postulated that the mechanical behavior of the porous clay composite is independent of clay mineralogy. Having developed the chemo-mechanical coupling technique, we now have the sufficient tools in place to precisely study the effect of the particular clay mineralogy on the measured properties of the porous clay composite.

For the chemo-mechanical coupling technique, the chemical and mechanical data were analyzed separately using cluster analysis methods. In principle, we should be able to use the cluster analysis methodology to analyze a synthesized chemical-mechanical dataset. That is, the combined use of the chemical data (elemental atomic ratios) and mechanical data (modulus and hardness values) to identify the relevant phases of shale materials. More developments in the engineering practice to locate grids in the WDS and indentation experimental setups are needed.

Finally, the grid WDS technique, developed in this study, was applied to shale materials that contain minor amount of organic content. The application of this new technique to the investigation of organic shales could be a fascinating future research topic. This would require the careful consideration of the experimental parameters of the grid WDS technique to properly account for the organic content. Furthermore, a more refined cluster methodology would be necessary to capture the major constituents of organic shale materials.

Bibliography

[1] A. C. D. Newman, Chemistry of Clays and Clay Minerals. Harlow: Longman Scientific & Technical, 1987.

[2] A. Delafargue, "Material invariant poromechanics properties of shales," S.M. Thesis, Massachusetts Institute of Technology, 2004.

[3] A. Delafargue and F.-J. Ulm, "Explicit approximations of the indentation modulus of elastically orthotropic solids for conical indenters," International journal of solids and structures, vol. 41, pp.

[4] A. Dilks and S.C. Graham, "Quantitative mineralogical characterization of sandstones by back-scattered electron image analysis," Journal of Sedimentary Research, vol. 55, p. 347, 1985.

[5] A. Gasgupta and A.E. Raftery, "Detecting features in spatial point processes with clutter via model-based clustering.," Journal of the American Statistical Association, vol. 93, 1998.

[6] A. Klute, Methods of soil analysis. Part 1. Physical and mineralogical methods. American Society of Agronomy, Inc., 1986.

[7] B. E. Hornby, L. M. Schwartz, and J. A. Hudson, "Anisotropic effective-medium modeling of the elastic properties of shales," Geophysics, vol. 59, no. 10, pp. 1570-1583, Oct. 1994.

[8] B. Gathier, "Multiscale strength homogenization: application to shale nanoindentation," Master thesis, Massachusetts Institute of Technology, Cambridge, 2008.

[9] C. Bobko, "Assessing the mechanical microstructure of shale by nanoindentation: The link between mineral composition and mechanical properties," PhD thesis, Massachusetts Institute of Technology, 2008.

[10] C. Bobko and F.- J. Ulm, "The nano-mechanical morphology of shale," Mechanics of Materials, vol. 40, no. 4-5, p. 318–337, 2008.

[11] C. Bobko, J. A. Ortega, and F.-J. Ulm, "Comment on Elastic modulus and hardness of muscovite and rectorite determined by nanoindentation," Applied clay science, 2009.

[12] C. E. Weaver, The Chemistry of Clay Minerals. Amsterdam: Elsevier Scientific Pub. Co, 1973.

[13] C. Fraley and A.E. Raftery, "MCLUST: Software for model-based cluster analysis," Journal of Classification, vol. 16, pp. 297–306, 1999.

[14] C. Fraley and A.E. Raftery, "Model-based methods of classification: using the mclust software in chemometrics," Journal of Statistical Software, vol. 18, pp. 1–13, 2007.

[15] C. Fraley and A.E. Raftery, "Model-based clustering, discriminant analysis, and density estimation," Journal of the American Statistical Association, vol. 97, pp. 611–631, 2002.

[16] C. M. Rojas and R. E. Van Grieken, "Electron microprobe characterization of individual aerosol particles collected by aircraft above the Southern Bight of the North Sea," Atmospheric Environment. Part A. General Topics, vol. 26, no. 7, pp. 1231–1237, 1992.

[17] C. M. Sayers, "Seismic anisotropy of shales," Geophysical Prospecting, vol. 53, no. 5, p. 667–676, 2005.

[18] D. A. Saucy, J. R. Anderson, and P. R. Buseck, "Cluster analysis applied to atmospheric aerosol samples from the Norwegian Arctic," Atmospheric Environment, vol. 21, no. 7, p. 1649–1657, 1987.

[19] D. Drouin, A. R. Couture, D. Joly, X. Tastet, V. Aimez, and R. Gauvin, "CASINO V2. 42—A fast and easy-to-use modeling tool for scanning electron microscopy and microanalysis users," scanning, vol. 29, no. 3, pp. 92–101, 2007.

[20] D. Han, A. Nur, and D. Morgan, "Effects of porosity and clay content on wave velocities in sandstones," Geophysics, vol. 51, no. 11, pp. 2093–2107, 1986.

[21] D. H Krinsley, K. Pye, S. Boggs, and N. K. Tovey, Backscattered scanning electron microscopy and image analysis of sediments and sedimentary rocks, Cambridge Univ Pr, 1998.

[22] D. L. Whitney, M. Broz, and R. F. Cook, "Hardness, toughness, and modulus of some common metamorphic minerals," American Mineralogist, vol. 92, no. 2-3, pp. 281, 2007.

[23] D. Tabor, "A simple theory of static and dynamic hardness," Proceedings of the Royal Society of London. Series A, Mathematical and Physical Sciences, vol. 192, pp. 247–274, 1948.

[24] F.-J. Ulm, G. Constantinides, A. Delafargue, Y. Abousleiman, R. Ewy, L. Duranti, and DK. McCarty, "Material invariant poromechanics properties of shales," Poromechanics III—Biot Centennial (1905–2005): AA Balkema, p. 637–644, 2005.

[25] F.-J. Ulm and Y. Abousleiman, "The nanogranular nature of shale," Acta Geotechnica, vol. 1, no. 2, pp. 77–88, 2006.

[26] F.-J. Ulm, M. Vandamme, C. Bobko, J. A. Ortega, K. Tai, and C. Ortiz, "Statistical indentation techniques for hydrated nanocomposites: Concrete, bone, and shale," Journal of the American Ceramic Society, vol. 90, no. 9, pp. 2677–2692, 2007.

[27] F.M. Borodich, L.M. Keer, and C.S. Korach, "Analytical study of fundamental nanoindentation test relations for indenters of non-ideal shapes," Nanotechnology, vol. 14, pp. 803, 2003.

[28] F.M. Borodich and B.A. Galanov, "Self-similar problems of elastic contact for non-convex punches," Journal of the Mechanics and Physics of Solids, vol. 50, pp. 2441–2461, 2002.

[29] F. M. Borodich, "Similarity methods in Hertz contact problems and their relations with the Meyer hardness test," Department of Mathematics, Glasgow Caledonian University, Glasgow G, vol. 4, 1998.

[30] F.M. Borodich, "Hertz contact problems for an anisotropic physically nonlinear elastic medium," Strength of Materials, vol. 21, pp. 1668–1676, 1989.

[31] F. Ottner, S. Gier, M. Kuderna, and B. Schwaighofer, "Results of an inter-laboratory comparison of methods for quantitative clay analysis," Applied Clay Science, vol. 17, no. 5-6, pp. 223–243, 2000.

[32] F.P. Ganneau, G. Constantinides, and F.J. Ulm, "Dual-indentation technique for the assessment of strength properties of cohesive-frictional materials," International journal of solids and structures, vol. 43, pp. 1727–1745, 2006.

[33] G. Constantinides, K.S. Ravi Chandran, F-.J. Ulm, and K.J. Van Vliet, "Grid indentation analysis of composite microstructure and mechanics: principles and validation," Materials Science and Engineering: A, vol. 430, pp. 189–202, 2006.

[34] G. Constantinides, F.-J. Ulm, and K. Van Vliet, "On the use of nanoindentation for cementitious materials," Materials and Structures, vol. 36, no. 3, pp. 191–196, 2003.

[35] G.I. Barenblatt, Scaling, self-similarity, and intermediate asymptotics, Cambridge Univ Pr, 1996.

[36] G. W. Brindley, "Identification of clay minerals by X-ray diffraction analysis." Clay and Clay Technology. Available: http://www.clays.org/journal/archive/volume%201/1-1-119.pdf.

[37] I. I. Bondarenko et al., "Determination of the phase homogeneity of samples of Bi-Pb-Sr-Ca-Cu-O ceramics by clusterization of electron probe microanalysis data," Journal of the Less Common Metals, vol. 164, pp. 620–627, 1990.

[38] I.N. Sneddon, "The relation between load and penetration in the axisymmetric Boussinesq problem for a punch of arbitrary profile," International Journal of Engineering Science, vol. 3, pp. 47–57, 1965.

[39] I.N. Sneddon and I.C.F.M. Sciences, Application of integral transforms in the theory of elasticity, Springer, 1975.

[40] J. A. Ortega, "Microporomechanical modeling of shale," PhD thesis, Massachusetts Institute of Technology, Cambridge,2010.

[41] J. A. Ortega, F.-J. Ulm, and Y. Abousleiman, "The effect of the nanogranular nature of shale on their poroelastic behavior," Acta Geotechnica, vol. 2, no. 3, pp. 155–182, 2007.

[42] J. A. Ortega, F.-J. Ulm, and Y. Abousleiman, "The nanogranular acoustic signature of shale," Geophysics, vol. 74, no. 3, pp. D65, 2009.

[43] J. A. Ortega, F.-J. Ulm, and Y. Abousleiman, "The effect of particle shape and grain-scale properties of shale: A micromechanics approach," International Journal for Numerical and Analytical Methods in Geomechanics, vol. 34, no. 11, pp. 1124–1156, 2010.

[44] J.D. Banfield and A.E. Raftery, "Model-based Gaussian and non-Gaussian clustering," Biometrics, vol. 49, pp. 803–821, 1993.

[45] J. Goldstein, Scanning Electron Microscopy and X-Ray Microanalysis, 3rd ed. New York: Kluwer Academic/Plenum Publishers, 2003.

[46] J.J. McGee and K. Keil, "Application of electron probe microanalysis to the study of geological and planetary materials," Microscopy and Microanalysis, vol. 7, pp. 200–210, 2001.

[47] J. K. Mitchell, Fundamentals of Soil Behavior, 3rd ed. Hoboken, N.J: John Wiley & Sons, 2005.

[48] J. Vanzo, "A nanochemomechanical investigation of carbonated cement paste," Master thesis, Massachusetts Institute of Technology, Cambridge, 2009.

[49] K. Bandyopadhyay, "Seismic anisotropy: Geological causes and its implications to reservoir geophysics," PhD thesis, Stanford, 2009.

[50] L. A. G. Aylmore and J. P. Quirk, "Domain or turbostratic structure of clays," Nature, vol. 187, pp. 1046-1048, 1960.

[51] L.A. Galin, H. Moss, I.N. Sneddon, N.C.S.U.R.S.O.P. SCIENCES, and A. MATHEMATICS, Contact problems in the theory of elasticity, Dept. of Mathematics, School of Physical Sciences and Applied Mathematics, North Carolina State College, 1961.

[52] L. Dormieux, D. Kondo, and F.-J. Ulm, Microporomechanics, Chichester, West Sussex, England: Wiley, 2006.

[53] M. E. Broz, R. F. Cook, and D. L. Whitney, "Microhardness, toughness, and modulus of Mohs scale minerals," American Mineralogist, vol. 91, no. 1, pp. 135, 2006.

[54] M. Kahle, M. Kleber, and R. Jahn, "Review of XRD-based quantitative analyses of clay minerals in soils: the suitability of mineral intensity factors," Geoderma, vol. 109, no. 3-4, pp. 191–205, 2002.

[55] M. Klepka et al., "Combined XRD, EPMA and X-ray absorption study of mineral ilmenite used in pigments production," Journal of Alloys and Compounds, vol. 401, no. 1-2, pp. 281–288, 2005.

[56] M. Vandamme, "The nanogranular origin of concrete creep: a nanoindentation investigation of microstructure and fundamental properties of calcium-silicate-hydrates," PhD thesis, Massachusetts Institute of Technology, Cambridge, 2008.

[57] N.K. Tovey and D.H. Krinsley, "Mineralogical mapping of scanning electron micrographs," Sedimentary geology, vol. 75, pp. 109–123, 1991.

[58] N.K. Tovey, D.H. Krinsley, D.L. Dent, and W.M. Corbett, "Techniques to quantitatively study the microfabric of soils," Geoderma, vol. 53, pp. 217–235, 1992.

[59] P. E. Potter, J. B. Maynard, and W. A. Pryor, Sedimentology of Shale: Study Guide and Reference Source. New York: Springer-Verlag, 1980.

[60] P. L. Larsson, A. E. Giannakopoulos, E. Soderlund, D. J. Rowcliffe, and R. Vestergaard, "Analysis of Berkovich indentation," International Journal of Solids and Structures, vol. 33, no. 2, p. 221–248, 1996.

[61] P. Heyliger, H. Ledbetter, and S. Kim, "Elastic constants of natural quartz," The Journal of the Acoustical Society of America, vol. 114, pp. 644, 2003.

[62] S. Boggs, Petrology of Sedimentary Rocks, 2nd ed. Cambridge: Cambridge University Press, 2009.

[63] S. Cariou, F.J. Ulm, and L. Dormieux, "Hardness-packing density scaling relations for cohesive-frictional porous materials," Journal of the Mechanics and Physics of Solids, vol. 56, pp. 924–952, 2008.

[64] S. Diamond, "Mercury porosimetry:: An inappropriate method for the measurement of pore size distributions in cement-based materials," Cement and Concrete Research, vol. 30, no. 10, pp. 1517–1525, 2000.

[65] S.I. Bulychev, V.P. Alekhin, M.K. Shorshorov, A.P. Ternovskii, and G.D. Shnyrev, "Determination of Young's modulus according to the indentation diagram," Industrial Lab, vol. 41, pp. 1409–1412, 1975.

[66] S.J.B. Reed, Electron microprobe analysis and scanning electron microscopy in geology, Cambridge Univ Pr, 2005.

[67] S. Y. Lee, L. K. Hyder, and P. D. Alley, Microstructural and mineralogical characterization of selected shales in support of nuclear waste repository studies. Oak Ridge National Lab., TN (USA), 1988.

[68] W. A. Deer, R. A. Howie, and J. Zussman, Rock-Forming Minerals, vol. 3. London: Longmans, 1962.

[69] W. A. Deer, R. A. Howie, and J. Zussman, An Introduction to the Rock-Forming Minerals, 2nd ed. Harlow, Essex, England: Longman Scientific & Technical, 1992.

[70] W. A. Deer, R. A. Howie, J. Zussman, and L. L. Y. Chang, Rock-Forming Minerals, 2nd ed., 5 vols. London: Geological Society, 1997.

[71] W. A. Van Borm and F. C. Adams, "Cluster analysis of electron microprobe analysis data of individual particles for source apportionment of air particulate matter," Atmospheric Environment (1967), vol. 22, no. 10, pp. 2297–2307, 1988.

[72] W.C. Oliver and G.M. Pharr, "Improved technique for determining hardness and elastic modulus using load and displacement sensing indentation experiments," Journal of materials research, vol. 7, pp. 1564–1583, 1992.

[73] W. R. Bryant, R. H. Bennett, P. J. Burkett, and F. R. Rack, "Microfabric and physical properties characteristics of a consolidated clay section: ODP Site 697, Weddell Sea," The Microstructure of Fine-Grained Sediments, from Mud to Shale, pp. 73, 1991.

[74] Y.T. Cheng and C.M. Cheng Zheng Zhemin, "Scaling relationships in conical indentation of elastic-perfectly plastic solids," International Journal of Solids and Structures, vol. 36, pp. 1231–1243, 1999.

[75] Y.T. Cheng and C.M. Cheng, "Scaling approach to conical indentation in elastic-plastic solids with work hardening," Journal of Applied Physics, vol. 84, pp. 1284–1291, 2009.

[76] Y.T. Cheng and C.M. Cheng, "Scaling, dimensional analysis, and indentation measurements," Materials Science and Engineering: R: Reports, vol. 44, pp. 91–149, 2004.